EUROPEAN ORGANIZATION FOR NUCLEAR RESEARCH

Experiment Proposal
for
PUMA: antiprotons and radioactive nuclei

The PUMA collaboration[1]

September 29, 2019

CERN-SPSC-2019-033 / SPSC-P-361
29/09/2019

Contact: Alexandre Obertelli
Email: aobertelli@ikp.tu-darmstadt.de

[1]See section 12.1

Executive Summary

Antiprotons as a probe to study short-lived isotopes remain unexploited despite past pioneering works with stable nuclei [1–4]. In particular, low-energy antiprotons offer a very unique sensitivity to the neutron and proton densities at the annihilation site, i.e. in the tail of the nuclear density. Such studies with short-lived nuclei and low-energy antiprotons are the first motivation of the proposed antiProton Unstable Matter Annihilation (PUMA) experiment. Today, no facility provides a collider of low-energy radioactive ions and low-energy antiprotons: PUMA aims at transporting one billion antiprotons from CERN/ELENA to CERN/ISOLDE to perform the capture of low-energy antiprotons by short-lived nuclei, and probe in this way the so-far unexplored isospin composition of the nuclear-radial-density tail of radioactive nuclei.

The present proposal follows a Letter of Intent [5] and a Memorandum [6] previously submitted in December 2017 and June 2018, respectively, in which the physics case and concept of PUMA were developed. In the minutes of the 59$^{\text{th}}$ meeting of the INTC [7], the committee "strongly endorses the current physics programme: although very ambitious, the outcome and impact could be significant and its future progress will be regarded with interest". In the minutes of the 131$^{\text{st}}$ SPS and PS Experiments Committee (SPSC) meeting [8], "the SPSC looks forward to receiving, when ready, a proposal with more details, that demonstrates the feasibility of the project by addressing solutions for the above mentioned technical challenges. The Committee encourages the collaboration to consider the possibility of a more compact design, and the option of separating the transport and detection devices, and to look for potential locations at the AD". On June 19, 2019, the SPSC published a call for proposals for projects at the AD after the second LHC long shutdown (LS2) [9]. This call aims at reviewing ideas of existing experiments at the AD hall and future projects which propose to make use of low-energy antiprotons.

In this document, we propose to the SPSC that PUMA becomes a CERN experiment. If accepted, PUMA will continue to be developed at TU Darmstadt and will be installed at ELENA in 2021. It is planned that PUMA, stays first at ELENA to develop the trapping of 10^9 antiprotons and to perform reference measurements on site with stable nuclei. We will also benchmark the transportation of antiprotons and qualify the half-life of the antiproton plasma stored in PUMA. Measurement proposals and requests for beam time at ISOLDE will be submitted to the INTC for approval at a second stage.

We propose to build a fully-transportable experimental setup composed of a 28-cm-large bore 4 Tesla solenoid, with active and passive shielding, a Penning trap for storing antiprotons and ions and charged-particle trackers composed of a time-projection chamber and a plastic scintillator barrel for the detection of annihilation products. Diagnostics for the antiproton plasma will also be included in the system. The trap will be composed of two zones, a storage zone and a collision zone.
The main challenge of PUMA is related to the extreme high vacuum required for a long term storage of the antiprotons with a half-life of thirty days corresponding to twenty residual gas molecules per cm^3 or about 10^{-17} mbar at 4 K. As the objective of PUMA is to inject low-energy ions into the antiproton plasma, the antiproton trap needs to be open to the beam lines at ISOLDE.
Once the antiprotons are trapped, the entire system will be transported in operation from ELENA to ISOLDE. At ISOLDE, low-energy Radioactive Ion Beams will be introduced into the PUMA trap and mixed with antiprotons to favor the formation of antiprotonic atoms, followed by annihilation.
The ratio of the number of annihilated neutrons to the number of annihilated protons will be evaluated by measuring the charged pions produced from annihilation. The basic principle of PUMA relies on the electric charge conservation of the annihilation process: the total charge of pions is -1 for a neutron annihilation and 0 for a proton annihilation. The determination of this ratio requires a correction of final state interactions, acceptance and detection efficiency. Complementary X-ray measurements from the decay of the formed antiprotonic atoms are also considered for future plans.

In Chapter 1, an overview of the proposed experiments, its objectives and the explanation of the planned technical solutions are presented. Chapter 2 describes in some details the annihilation mechanism when a low-energy antiproton interacts with a nucleus. The focus is set on the treatment of final state interactions after the annihilation from the re-interaction of produced pions with the residual nucleus. The sensitivity of the proposed method is discussed. We propose an analysis method which will provide the ratio of neutron-to-proton annihilations at a precision better than 10 %, providing an unprecedented constraint on neutron-to-proton densities at the nuclear surface. After an overview of the experimental setup in Chapter 3, the key components of the experiments are described: the vacuum (Chapter 4), the solenoid (Chapter 5), the trap and trapping procedure, as well as the plasma diagnostics (Chapter 6), the detection for radiations following annihilations (Chapter 7). We show that, on the technical side, the PUMA concept can be successfully achieved. In Chapter 8, the foreseen operation at ELENA is described. The transportation procedure from ELENA to ISOLDE is detailed in Chapter 9. Operations at ISOLDE are the object of Chapter 10. Since the development of PUMA will be first performed at TU Darmstadt, the foreseen infrastructure is described in Chapter 11. Finally, the organisation of the project in terms of collaboration, work packages and timeline as well as the cost estimate are given in Chapter 12.

Contents

Chapter 1

Physics objectives and concept

1.1 Neutron skins and halos

The occurrence of neutron halos was discovered in light-mass nuclei at the limit of nuclear existence, i.e. at the neutron drip line [10]. Historically ^{11}Li was the first halo nucleus discovered [1] whose structure is understood as a ^{9}Li core surrounded by two neutrons with a large radial extension. Halos are truly a fascinating manifestation of quantum physics. They belong to a subset of clustering [11] for which most of the probability to find the halo neutrons extends to a region of space that is classically forbidden. In other words, the neutrons are well beyond the range of the neutron-core potential [12–15] and owe their existence to quantum tunneling. Their properties show universal aspects of few-body systems such as scaling laws [16, 17], i.e. they do not encode details of the strong force. This makes atomic nuclei, and more particularly exotic neutron-rich systems, a unique laboratory to study universal few-body phenomena. That said, universal features do not void physicists to reach a true understanding of nuclear halos. This requires both a precise description of nuclear correlations and an accurate accounting of large-distance behavior. Unfortunately, this coincides with one of the greatest challenges of contemporary physics: a problem of multiple scales. While modeling efforts are being deployed in this direction, our understanding will only improve by challenging theory with a more complete representation of halo systems from new experimental probes.

Several halos have been identified and characterized, when possible, from complementary observables such as reaction cross sections, neutron transfer, charge and matter radii, elastic and inelastic scattering, Coulomb excitation and femtoscopy measurements [19, 20]. An overview of the so-far observed (or claimed) halo nuclei is given in Fig.1.1. Today, only light halo nuclei up to mass A=8 (^{8}He) can be calculated via *ab initio* techniques where the Schrödinger equation is solved fully with realistic nucleon-nucleon interactions. While only *s*-wave halos have been observed so far, *p*-wave neutron halos have also been recently claimed to appear in very neu-

[1] In reality, the simplest case of halo is the deuteron, a stable binary halo, which exhibits a large central depletion and an anomalously large radius.

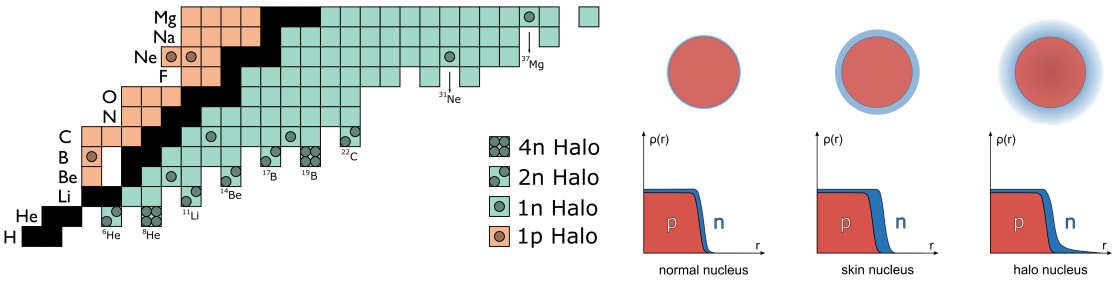

Figure 1.1: (Left) Low mass region of the nuclear chart. Isotopes marked with a circle correspond to nuclei which show indications of a proton or a neutron halo. The figure is taken from [18]. (Right) Schematic representation of proton and neutron radial densities for stable nuclei, halo nuclei and in case of a neutron skin. Depending on the situation, the ratio of the neutron and proton densities in the tail of the matter density distribution are very different.

tron rich Ne and Mg isotopes from breakup cross section measurements [21, 22]. A more direct measurement is needed to verify these conclusions.

Proton halos are expected to exist and some candidates have been explored experimentally. The tail of the wave function should be more suppressed at larger distances than for an angular momentum barrier. This makes halo formation more difficult and will prevent it altogether for nuclear charges above ten or twenty. The most prominent cases are the one-proton halo ^{8}B [23–25] and the two-proton halo ^{17}Ne [26]. Theoretical proton and neutron radial densities for ^{17}Ne are shown in Fig. 1.2.

For medium mass nuclei, the appearance of halos is predicted by several effective models with varying outcome from one to another [27–31]. As an illustration, predictions from [31] of neutron halos in medium-mass neutron-rich nuclei quantified through a halo factor N_{halo} are shown in Fig. 1.3. N_{halo} is defined as the amount of neutrons in a nucleus where the one-body matter density of the core nucleus, composed of A-1 nucleons, is less than 10% of the halo density, following the definition $N_{\mathrm{halo}} = \int_{r_0}^{\infty} \rho(r) r^2 dr$ where r_0 is the radius of the core. Calculations were performed for spherical nuclei, near shell closures, with the Sly4 Skyrme effective nucleon-nucleon interaction [32]. Except some work within the Nilsson-diagram framework [33–35], the role of deformation has been barely studied so far and no data firmly support the existence of deformed halos.

A large neutron excess at the nuclear surface is not necessarily a halo and can take the form of a neutron skin. Neutron skins, corresponding to a neutron density higher than the proton density at the surface of the nucleus, have been evidenced in stable nuclei. Neutron skins are so far mostly quantified via their thickness defined as the difference between the neutron and proton distribution rms radius

$$\Delta r_{np} = \langle r_n^2 \rangle^{1/2} - \langle r_p^2 \rangle^{1/2} \tag{1.1}$$

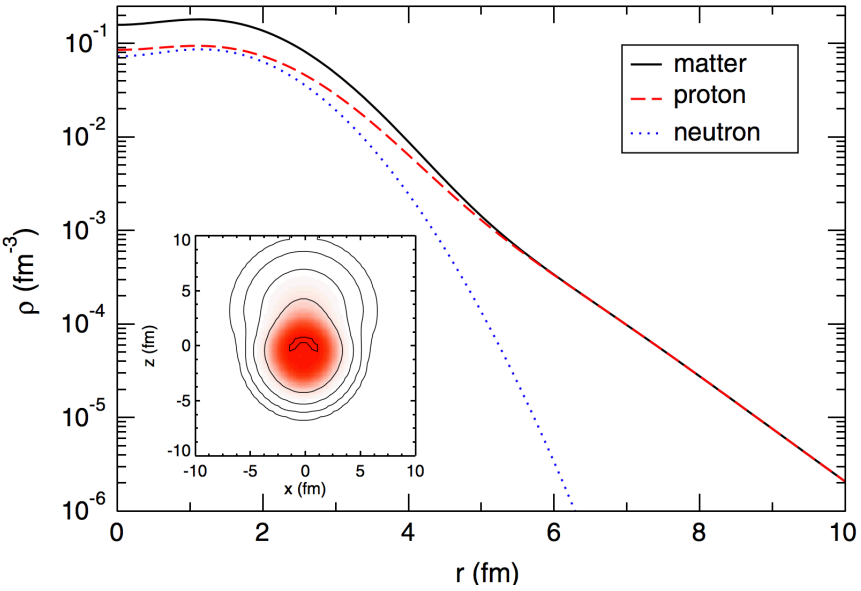

Figure 1.2: Theoretical matter, proton, and neutron density distributions for the ground state for ^{17}Ne. The Fermionic Molecular Dynamics (FMD) approach reproduces well the large charge radius of ^{17}Ne, whose description is consistent with a two-proton halo bound to a ^{15}O core. Figure taken from [26].

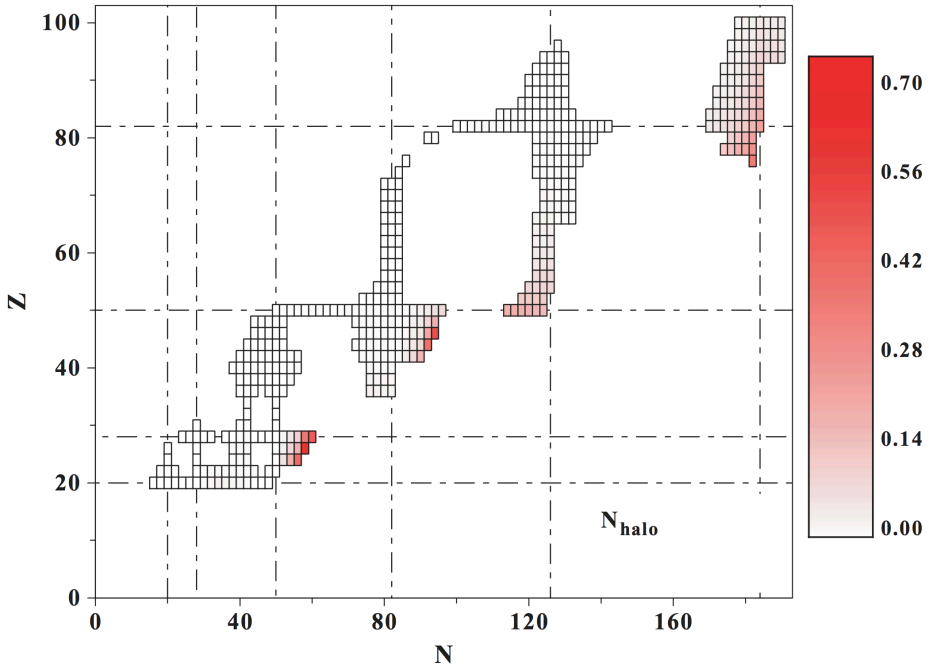

Figure 1.3: Halo factor N_{halo} characterizing the amount of neutron halo in medium-mass neutron-rich nuclei. Calculations were performed at the mean-field level in the Hartree-Fock-Bogolyubov framework withe the Sly4 effective interaction. Figure from [31].

Thick neutron skins, i.e. thicker than ∼0.3 fm, were observed in light neutron rich nuclei. Microscopic models predict the development of thick neutron skins in very neutron rich medium mass nuclei [36–44] but no experimental evidence exists so far. An illustration of the spread of predictions by using different Skyrme nucleon-nucleon functionals is shown in Fig. 1.4. Such thick neutron skins would represent a unique occurrence of low-density pure neutron matter in the laboratory. Using all experimental techniques presently available, it has not yet been possible to determine the neutron skin accurately enough in order to discern the best microscopic theories for proton and neutron distributions. Characterizing the evolution of the neutron skin along isotopic chains towards large neutron excess will represent a new constrain to nuclear structure theories.

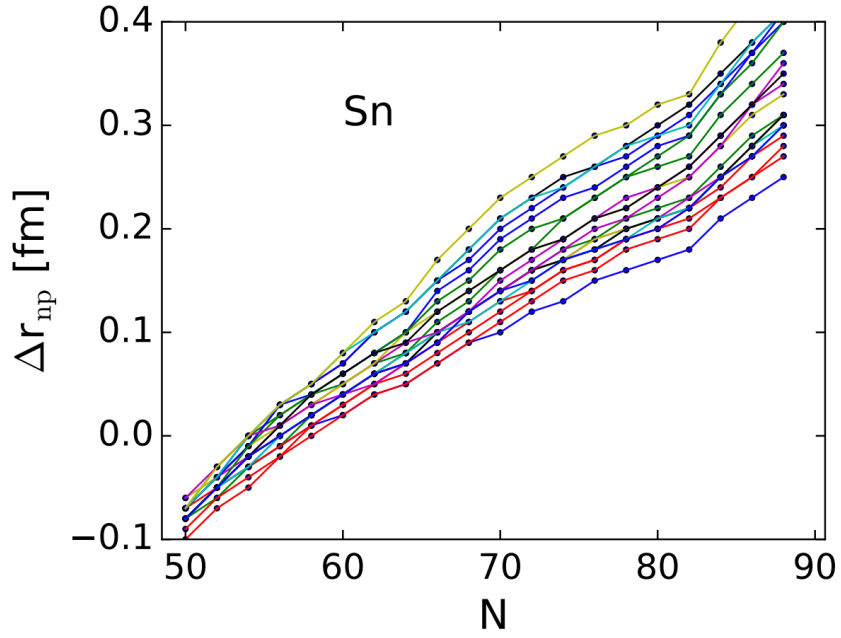

Figure 1.4: Neutron skin thickness Δr_{np} calculated for tin isotopes with twenty-three different Skyrme interactions. Figure from [43].

In addition to the many body problem, the study of neutron skins has been motivated by the nuclear equation of state, a driving component of the structure of neutron stars. In heavy stable nuclei, the difference between the neutron and proton radii is of the order of few percent [45]. The determination of the neutron skin thickness is indeed precious to learn about the equation of state at low density ($\rho < \rho_0$), to give information on the isospin dependence of the nuclear force and to constrain our description of neutron stars [46, 47]. The larger the pressure of neutron matter, the thicker is the skin as neutrons are pushed out against surface tension. The same nuclear pressure supports neutron stars against gravity, therefore correlations between neutron skins of neutron-rich nuclei and various neutron star properties are naturally expected. The density dependent symmetry term $\varepsilon(\rho)$ of the equation of

state gives the cost in energy to separate neutrons and protons. A strong correlation between the so-called slope coefficient of the symmetry energy $L = 3\rho_0 \partial\varepsilon/\partial\rho|_{\rho_0}$ and the neutron-skin thickness has already been shown [40] and is illustrated in Fig. 1.5. According to this correlation, one can constrain the symmetry-energy term of the equation of state. In addition, the magnitude of neutron skins gives insight into the nature of three-body forces in nuclei, the position of nuclear drip lines, and collective nuclear excitations related to the isospin degree of freedom. Best constraint on nuclear forces would come from a systematic study of neutron skins along isotopic chains and for very neutron rich systems.

The nature of neutron skins in nuclei may not be as simple as described by mean

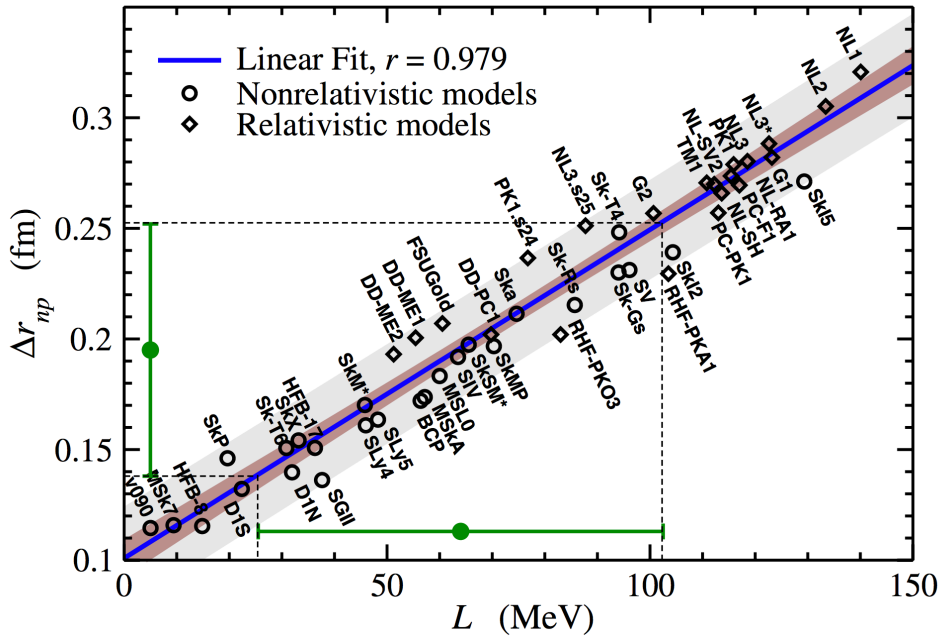

Figure 1.5: Calculated neutron skin thickness of ^{208}Pb against the slope L of the symmetry energy for different effective nucleon-nucleon interactions at the mean field level. Figure from [40].

field approaches. Parity-violating electron scattering analysis [45] as well as predictions from a data-constrained dispersive optical model analysis [48] favor thicker neutron skins than other *ab initio* predictions and than most most microscopic predictions, as well as compared to strong-probe extracted values [49,50]. We still have a lot to learn about the nuclear surface properties. Spatial correlations including alpha clustering are predicted to take place at sub-saturation densities and therefore at the nuclear surface. It is expected that clustering and the formation of inhomogeneous matter at low densities modifies the tail of the proton density [51]. If such correlations are confirmed experimentally, it would modify our understanding of the symmetry energy of the nuclear equation of state, as compared to calculations assuming a uniform uncorrelated spatial distribution of constituents [52]. Recently *ab initio* calculations have been extended to medium mass nuclei. Calculated binding

energies and matter radii of stable nuclei show a systematic discrepancy compared to experiment when the coupling constants of the input two- and three-body interactions are fixed to scattering data and three-body nuclei only. These discrepancies indicate limitations of the most recent *ab initio* theories to grasp enough of the relevant many-body effects in the current power counting schemes of the pertubative expansion [53].

For the above reasons, the outer part of the nuclear density in neutron-rich isotopes is of capital interest, although difficult to access experimentally. Indeed, all current techniques to investigate neutron skins and halos are sensitive to the entire density or, in the case of hadronic probes, to the nuclear surface where $\rho \sim \rho_0/2$. In the case of neutron skins and halos, the relevant region of neutron excess takes place in the *tail* of the nuclear density, i.e. beyond the surface where $\rho \sim \rho_0/2$, a region unexplored so far. The use of low-energy antiprotons as a probe should remedy this lack of experimental information, as further detailed below. As an illustration of the difference between the radial sensitivity of annihilation following antiproton capture and direct nuclear reactions such as nucleon knockout at high beam energies, we illustrate in Fig. 1.6 the theoretical mean radial annihilation position for both processes. While the nuclear reaction is sensitive to the surface of the nucleus, the annihilation is sensitive to its tail where the skin and halo phenomena prevail. These studies with radioactive ions were first proposed by Wada and Yamazaki in 2004 [54].

1.2 Antiprotons and nuclear structure

The first nuclear structure experiment with antiprotons was performed at Brookhaven National Laboratory, USA in the 1970s [55]. Low energy antiprotons were sent onto targets made of different solid materials (C, Ti, Ta, Pb) and charged pions from annihilation were measured in a bubble chamber where the targets were inserted. Since the electric charge is conserved during the annihilation process, the measurement of the ratio of positive and negative pions should be related to the annihilated neutron-to-proton ratio. Detection efficiency was considered in the analysis, as well as the difference of annihilation probability with protons and neutrons. The later correction term was estimated with ^{12}C as reference. The obtained normalised neutron-to-proton annihilation ratios show values significantly larger than N/Z for all cases, where N is the number of neutrons and Z is the number of protons. The relative excess compared to N/Z was interpreted as an excess of neutrons in the tail of the nuclear density and quantified as a so-called *halo factor*. In the case of ^{208}Pb, 2.3(5) times more neutron annihilations were observed compared to what one could expect from N/Z. Since this pioneer study, antiprotons have been used to investigate the nature of the tail of the nuclear density in stable nuclei.

The initial interpretation of this first work clearly suffered from the lack of a detailed treatment of final state interactions, as well as the lack of theoretical un-

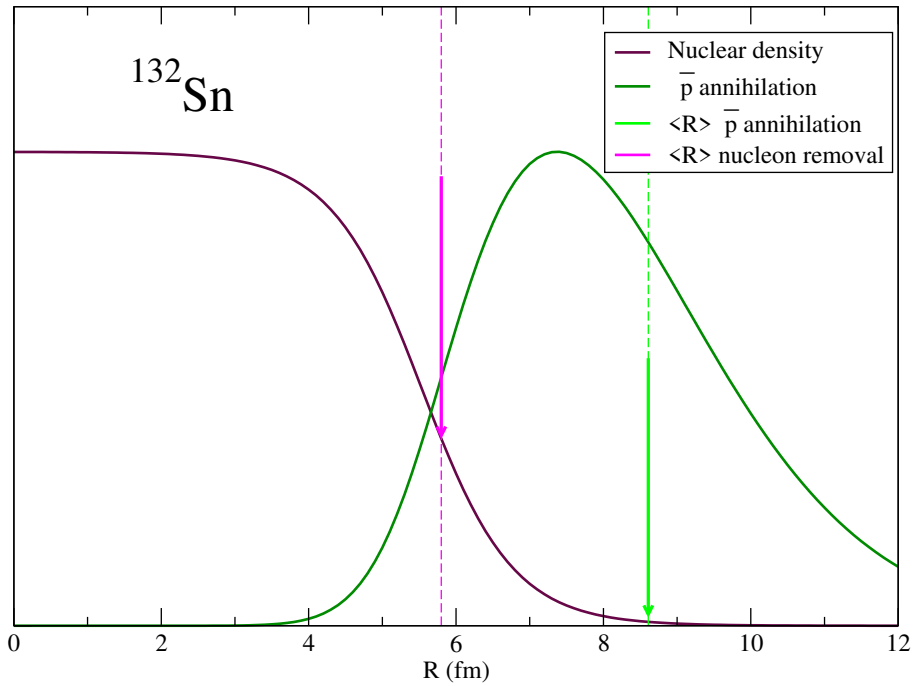

Figure 1.6: Matter density distribution of ^{132}Sn (black), obtained from extrapolation of optical model. The theoretical mean radius for nucleon stripping from quasifree scattering (pink arrow) and the expected site of annihilation after antiproton capture (green arrow) are shown. For this estimate, the annihilation profile corresponding to a mixture of antiprotonic orbitals with quantum numbers ($n = 8$, $\ell = 7$) at 90% and ($n = 9$, $\ell = 7$) at 10% (green curve) is considered.

derstanding for the site of the annihilation. These points were partly addressed in the interpretation of later works at the Low Energy Antiproton Ring (LEAR) and the Antiproton Decelerator (AD) at CERN, where the annihilation process from nucleon- and nucleus-antiproton collisions were mostly studied. The sensitivity of low-energy antiprotons to the nuclear density tail of nuclei was demonstrated [56], although a fully microscopic and consistent treatment of the antiproton-nucleus many-body problem still remains to be developed. The major part of nuclear structure studies with antiprotons relied on the detection of X rays from the decay of antiprotonic atoms [57–59] and γ rays from the residual nuclei [4, 60]. Several of these works aimed at determining the neutron skin thickness of stable nuclei in a model dependent way. As detailed in Chapter 2, PUMA aims at characterizing the tail of the nuclear density of radioactive nuclei from the measurement of low-energy-annihilation products.

As of today, no accelerator complex provides low-energy antiprotons to be used as probes for unstable nuclei. Indeed, the use of antiprotons with unstable nuclei requires two large scale facilities, one for the antiproton production and one for radioactive-ion beams (RIB), or a way to bring antiprotons to a RIB facility. This was proposed for FAIR as the FLAIR project [61] but has not been included in the

Start Version of FAIR. There is no RIB-antiproton collider today. The experiment detailed in the Letter of Intent and this addendum aims at bringing stored antiprotons from ELENA to the ISOLDE facility [62] at CERN. Its results may provide the necessary inputs to advocate for a low-energy antiproton-radioactive ion collider at CERN or GSI which, in return, may open new perspectives to study nuclear systems.

1.3 Objectives

The first objectives of the PUMA experiment are

- to provide a new observable for radioactive nuclei that characterises the neutron-to-proton asymmetry of their density tail, namely the neutron-to-proton annihilation ratio,
- to characterize the density tail of known halos and neutron skins with this new method,
- to evidence new proton and neutron halos,
- to understand the development of neutron skins in medium-mass nuclei along isotopic chains.

The proposed method is indeed first an unambiguous discovery tool for halos: annihilation from a neutron halo nucleus should lead to a neutron-to-proton annihilation ratio exceeding by an order of magnitude the N/Z ratio of the nucleus (following qualitatively the halo definition proposed in [30]), annihilation from a proton halo, on the contrary, should lead to a neutron-to-proton annihilation ratio significantly smaller than unity. Neutron skins could be characterized by a neutron-to-proton annihilation ratios larger than N/Z. To illustrate the sensitivity of the n/p-annihilation ratio to neutron skins, we calculated the expected value for two tin isotopes with realistic proton and neutron densities: in the case of the stable ^{124}Sn, the expected neutron-to-proton annihilation ratio is 2.13, while it is close to unity for the neutron-deficient ^{104}Sn, 2.35 for the neutron rich ^{132}Sn. These values are to be compared to $N/Z = 1.48$, 1.08 and 1.64, respectively. This example illustrates that a relative accuracy of 10% or better for the neutron-to-proton annihilation ratio is sufficient to provide first quantitative information on the neutron-skin growth as a function as neutron number. The expected range of neutron-to-proton annihilations are summarized in Tab. 1.1.

	n/p-annihilation ratio
Neutron halo	$\geq 10 \times N/Z$
Proton halo	$\ll 1$
Neutron skin	$> N/Z$

Table 1.1: Expected neutron-to-proton annihilation ratios in the case of a neutron halo, a proton halo or a neutron skin.

The foreseen studies are expected to provide new information on the nuclear many-body problem, which may eventually shed light on our understanding of neutron(-rich) matter at low density. Note that the observable PUMA will provide is the ratio of neutron-antiproton annihilations and proton-antiproton annihilations after antiproton capture. This quantity is to be connected to the neutron-over-proton density ratio integrated over the region of annihilation sites, i.e. in the tail on the nuclear radial density. PUMA is then complementary to measurements aiming at neutron-skin thickness determination and is sensitive to the tail of the radial density distribution, so far unexplored.

Several physics cases have been identified to be suitable for the investigation of the neutron and proton composition of the nuclear density tail in radioactive nuclei. They will all be measured in the exact same experimental conditions and are summarized in Table 1.2. It is important to note that (i) reference measurements with stable nuclei will first be done at ELENA and will provide benchmark data for the response function of the device (detection and tracking efficiencies, signal-to-background determination,...), as well as benchmarks for theory and the foreseen interpretation method, (ii) the analysis of high statistics reference measurements at ELENA might lead to new prospects for PUMA (see below), (iii) measurements along isotopic chains are believed to be important since they will allow studies which may provide more (relative) accuracy than individual measurements. Note that at both ELENA and ISOLDE Multi-reflection time-of-flight (MR-TOF) devices will be used to provide isotopically pure ions.

Regarding to the program at ELENA, in addition to the above reference measurements with stable nuclei, we intend to perform specific development studies which might improve or expand the physics program with PUMA:

- detection of the heavy-ion recoil after annihilation along the solenoid axis for a direct tagging of an annihilation with a heavy-ion. This might lead to a strong enhancement of the signal over background ratio, particularly important for the most exotic cases.
- capture from antiprotons trapped in the collision zone at high velocity (~ 100 eV), also supposed to improve the signal over background ratio.
- measurement of gamma-rays from the electromagnetic decay of heavy-ion residues from the annihilation.
- measurement of X-rays emitted during the decay of the antiprotonic atom.

1.4 Concept of PUMA

As stated in the earlier Letter of Intent [5], the PUMA project aims at transporting one billion antiprotons from ELENA to ISOLDE to perform the capture of low-energy antiprotons by short-lived nuclei. The PUMA ion Penning-Malmberg trap will consist of a storage zone (S trap) dedicated to the storage of a large amount of

	Nuclei	Objectives
ELENA	p	Detection efficiency, benchmark of simulations, experimental response for pure proton annihilation
	d	benchmark of method on simplest nucleus, extract response for neutron annihilation
	^{3}He, ^{4}He	isotopic study, comparison to *ab initio* predictions
	^{16}O, ^{40}Ar, ^{132}Xe	benchmark for analysis with medium-mass nuclei, evolution of final state interactions with nucleon number
	$^{112-124}$Sn	neutron-skin isospin dependence along the isotopic chain of stable Sn nuclei
ISOLDE	^{4,6,8}He, ^{7,9,11}Li	1) neutron skin and halos as a function of isospin 2) (high statistics) study of annihilation process
	^{8}B, ^{17,18}Ne	search for proton halos
	$^{26-31}$Ne, ^{28,33}Mg	1) neutron skin in light isotopic chains 2) search for (p-wave) neutron halos
	$^{14-22}$O, $^{104-138}$Sn	1) evolution of neutron skins with isospin 2) exclusive final state population (when detection of γ rays from nuclear de-excitation is included)

Table 1.2: Proposed first physics cases at ELENA (top) and ISOLDE (bottom). Among the raised cases, the most neutron-rich Ne, Mg and Sn isotopes may not be produced at enough rates for a possible measurement. Current available intensities at ISOLDE are given in Chapter 10. The capabilities of the method will depend on the signal-over-background (including effects from production rate, lifetime of isotopes, vacuum and number of antiprotons in the trap) in the measurement and the reached relative energy between antiprotons and radioactive nuclei in the trap (the capture probability evolves as a function of the inverse of the relative velocity).

antiprotons, and a collision zone (C trap) dedicated to the interaction of antiprotons with unstable ions. 10^9 antiprotons will be stored at ELENA in the S trap. The entire system will be transported on a truck to ISOLDE. There, typically, 10^7 to 10^8 antiprotons will be transfered to the C trap from the S trap. Both zones will be located in a 4 T magnetic field provided by a superconducting solenoid. Pions issued from annihilations will be detected by a cylindrical time projection chamber surrounding the C trap. The curvature of the charged pions in the magnetic field of the trap will allow to identify the charge of the measured pions. After the corrections from final-state interactions, we will determine the ratio of neutron-antiproton annihilations and proton-antiproton annihilations following the antiproton capture. This is the core observable to be provided by PUMA. A sketch of the setup is shown in Fig. 1.7. A realistic view of the full setup in its frame is presented in Chapter 3.

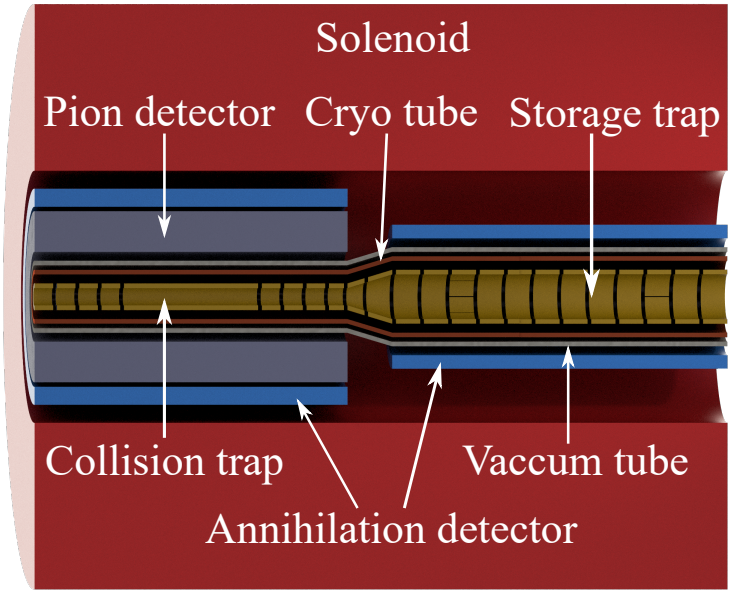

Figure 1.7: Schematic view of the PUMA pion detection and trap setup.

A proposed operation scheme of the system is presented in Fig. 1.7. The scheme will consist of five key techniques: a pulsed drift tube (PDT) to slow down antiprotons and ions at the entrance of the two traps, a rotating wall drive for the antiproton cloud shaping, sympathetic electron cooling, fractional extraction of antiprotons from the reservoir, and nested potential to trap positively-charged ions in the same region. Details on the devices to be built are given in Chapters 4, 5, 6 and 7.

Although the details of each experiment at ISOLDE should be described in later individual proposals to the INTC, we give here an estimate of the counting rate expected from annihilations in PUMA so that orders of magnitude can be grasped by the reader. The annihilation probability of an individual nucleus with stored antiprotons is estimated to reach 10^6 barns at 100 eV relative energy [63]. Antiprotons annihilate with both protons and neutrons. The decay channels are composed of energetic pions with conservation of the initial charge and momentum of the antiproton-nucleon system.
Assuming an antiproton capture cross section of 10^{-16} cm^{-2}, and assuming an antiproton plasma of thickness 10^8 cm^{-2}, every ion at 100 eV will fly through the antiproton cloud 2×10^6 times when trapped for a 1 s total duration. In the case of a stable or long-lived nucleus introduced in a bunch of 10^4 ions into the antiproton plasma, the corresponding annihilation rate will be 100 Hz. A high-statistics measurement with stable ions will therefore last few minutes, the limiting factor being the acquisition rate the detector readout can handle (about 1 kHz with the considered electronics).
In the case of the most exotic short-lived nuclei such as ^{11}Li, the number of nuclei introduced per cycle is smaller and the time the nuclei spend in the antiproton plasma is limited by their half life. We assume that nuclei produced at 1000 s^{-1} are trans-

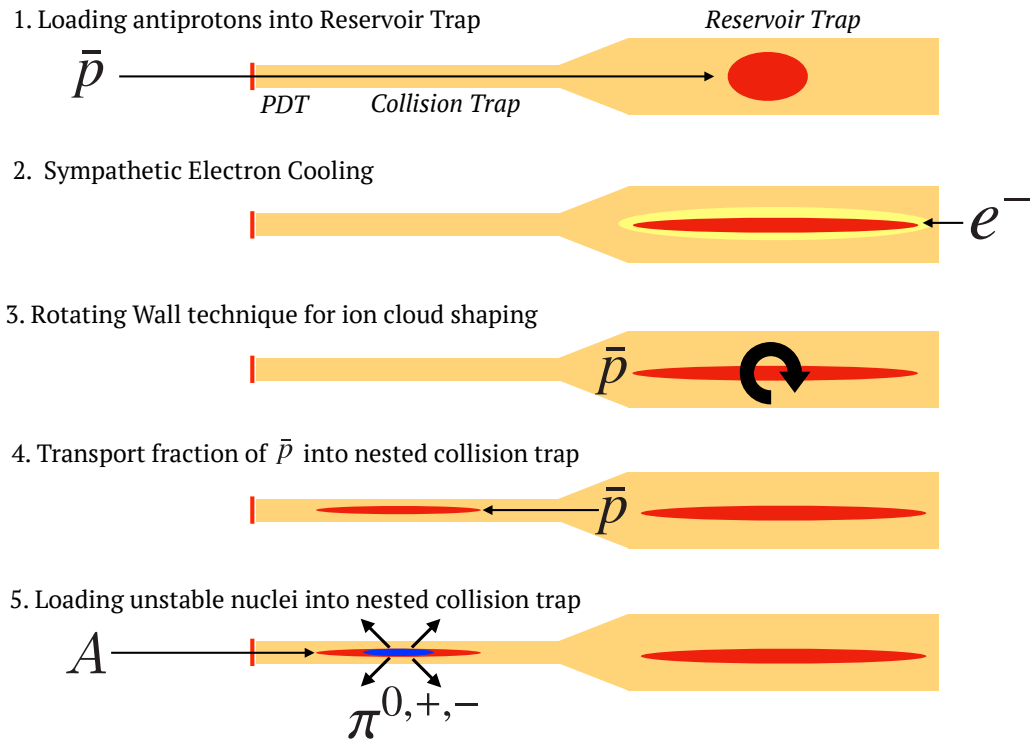

Figure 1.8: Operation scheme of PUMA. The trap entrance is equipped with a pulse drift tube (PDT) to adjust the energy of the ions when injected into the trap.

mitted to PUMA in bunches at 10 ms cycles. Every ion at 100 eV will fly through the antiproton cloud 2×10^4 times when trapped for a 10 ms total duration. In this extreme case, the corresponding annihilation rate will be 10 per minute. To achieve this sensitivity, the design and conception of PUMA requires an extra-high vacuum for the trap to minimize the background from residual-gas-induced annihilations.

Chapter 2

Method

2.1 Interaction between low-energy antiprotons and atoms

Antiprotonic atoms are especially suited to probe the nuclear density at the nuclear periphery, since the antiproton-nucleus annihilation is estimated to take place at about 2 to 2.5 fm outside the half-density radius, as deduced from the LEAR/CERN PS209 X-ray experiment [58]. The annihilation of the antiprotons is followed by meson emission, dominated by the emission of pions. The reconstruction of the total charge of the emitted pions allows for the determination of the charge of the annihilated particles, 0 in the case of antiproton-proton annihilation and -1 in the case of antiproton-neutron annihilation. Thus, the distribution of protons and neutrons in the nuclear periphery can be explored through the charge distribution of the emitted pions.

In order to obtain the neutron-to-proton annihilation ratio from the emitted pions, the whole process leading to and after antiproton annihilation must be considered. This process follows three differentiated steps:

- Capture of the antiproton by the atom in an orbital with high energy, after which the antiproton follows a decay cascade until it reaches the nuclear surface.
- Annihilation of the antiproton with one of the nucleons in the nuclear surface, resulting in the emission of mesons, mostly pions.
- Final-state interactions of the emitted pions with the nucleus, which may modify the detected pion distribution.

These steps and their current understanding are described in the following.

2.1.1 Atomic capture

Atomic capture of negatively charged mesons and baryons is known to be a complicated process since it is a many-body problem involving the long-range Coulomb

interaction at low energies. Therefore it has a highly quantum-mechanical nature. Numerous works have explored the capture process, which is similar for all heavy negatively charged particles ($\mu, K^-, \bar{p}, ...$), starting with the early works of Fermi and Teller [64], up to recent semiclassical [63], quantum-mechanical [65] and hybrid calculations [66]. A recent report on capture of exotic particles can be found in [67].

Despite being theoretically challenging, the physics of the capture process is believed to be relatively simple: an antiproton with an energy close to the ionization energy of an atom interacts strongly via Coulomb interaction with the most weakly-bound (valence) electron of the atom, resulting the ejection of the valence electron from the atom, due to the large mass difference between the electron and the antiproton. The antiproton is left in a bound state with a binding energy similar to that of the ejected electron, which corresponds to a principal quantum number of $n_c \sim n_0 = \sqrt{M^*/m_e} n_e$, where M^* is the reduced mass of the antiproton-nucleus system and n_e is the principal quantum number of the valence electron. The angular momentum of the captured antiproton l is in general assumed to follow an almost statistical distribution ($P(l) = (2l+1)e^{\alpha l}$, $\alpha \leq 0.2$) [68]. This shows qualitative but not quantitative agreement with recent theoretical calculations, as shown in the left panel of Fig. 2.1, which corresponds to the capture of muons by Ne.

State-of-the-art theoretical calculations [69] (shown in the right panel of Fig. 2.1) predict non-negligible capture cross sections for energies above the ionization potential of the colliding atom, the cross section increasing with its number of protons. This process can be understood as the antiproton colliding with multiple electrons before capture and losing more energy than with only one collision. Unfortunately, the dependence of the capture cross section on the collision energy has not been experimentally determined. Given the expected energies of the ion beams to be used with PUMA, the capture cross section energy dependence may introduce some uncertainties in the yields obtained. As a first approximation to adress the capture cross section energy dependence, a parametrization of the results in [63] for radioactive ions as a function of energy E and atomic number Z will be employed. This parametrized energy-dependent cross section will be convolved with the expected energy distribution between antiprotons and ions in order to obtain the optimal energy range for the ion beams, within the limitations of the beam settings. Conversely, the yields from PUMA may provide currently missing experimental results for the energy dependence of the capture process in the range of 10s-100s of eV.

2.1.2 Atomic cascade through the electron cloud

After capture, the antiproton cascades to lower levels through the electron cloud by successive Auger and radiative transitions. The value of n_c at this stage is large ($n_c \sim 100$), so annihilation of the antiproton by the nucleus is negligible. Due to the large value of n_c, the most likely transitions $n_c \rightarrow n_c - 1$ are Auger transitions, which result in the emission of low-energy electrons, difficult to measure, so this step of the cascade is difficult to characterize experimentally, and there are extremely few experimental publications on the Auger spectra at this stage of the cascade [71].

The LEAR/CERN PS175 experiment has been able to measure the intensity of

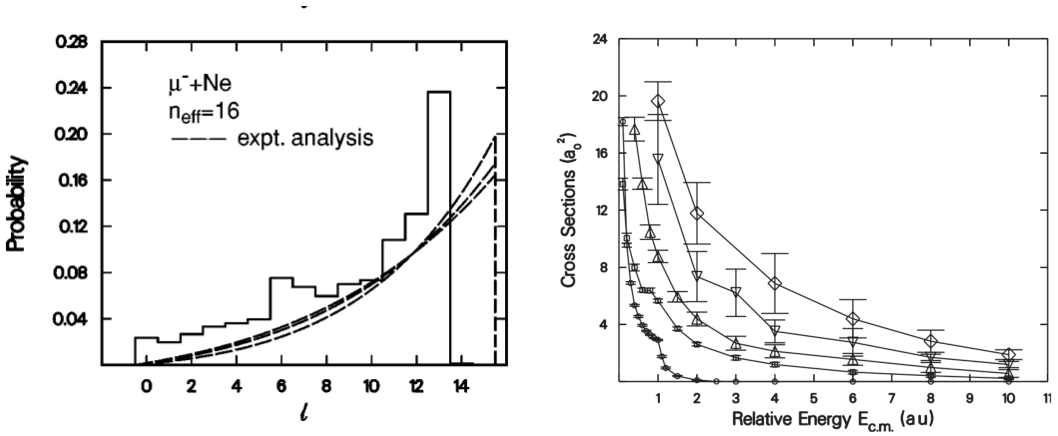

Figure 2.1: (Left) $P(l)$ distribution from semiclassical calculation (bins) and phenomenological fit (dashed line). Figure taken from [70]. (Right) Antiprotonic capture cross sections as function of center of mass energy for He (circles), Ne(squares), Ar(up triangles), Kr(down triangles), Xe(diamonds). Figure taken from [69].

various X-ray spectra of three noble gases: Ar, Kr and Xe, in the energy region corresponding to this stage of the cascade [72]. The occurrence of Auger transitions could be observed indirectly by the variation of the intensity of the peaks, while the peaks were found to correspond to transitions between orbits embedded in the electronic cloud via comparison with multiconfiguration Dirac-Fock (MCDF) calculations.

The findings in this experiment are relevant for the PUMA project, as both consider low-density environments, where the refilling (capture of electrons from surrounding atoms and "refill" of vacancies left by ejected Auger electrons) can be neglected. Refilling is known to play an important role in the population of the different antiprotonic orbitals so experimental data in a similar electron refilling regime set a useful benchmark for the calculations to be performed for PUMA.

2.1.3 Atomic cascade after the electron cloud

After going through the electron cloud ejecting most electrons in the atom, the antiproton continues to cascade down, mostly through radiative transitions.

It is relevant to note that radiative transitions with $\Delta n_c > 1$ lead to an increase in population of the so called "circular states" $(n_c, l = n_c - 1)$ [73], which reduces the sensitivity to the previous distribution of states $P(n_c, l)$ populated through capture and the previous steps of the cascade. This stage of the cascade is dominated by high-energy X rays which can be measured very precisely, so a robust understanding of this stage has been developed, with codes able to reproduce it with significant precision [74, 75]. A member of PUMA was involved in the development of [74], which was used in the analysis of the experiment LEAR/CERN PS209 [58]. For this analysis, the initial population distribution was assumed to have the quasi-statistical shape $P(n_c, l) = (2l + 1)e^{\alpha l}$. n_c was taken to be 20, far from the K-shell electron orbitals. The parameter α was established to be 0.1-0.2 for the studied nuclei, with

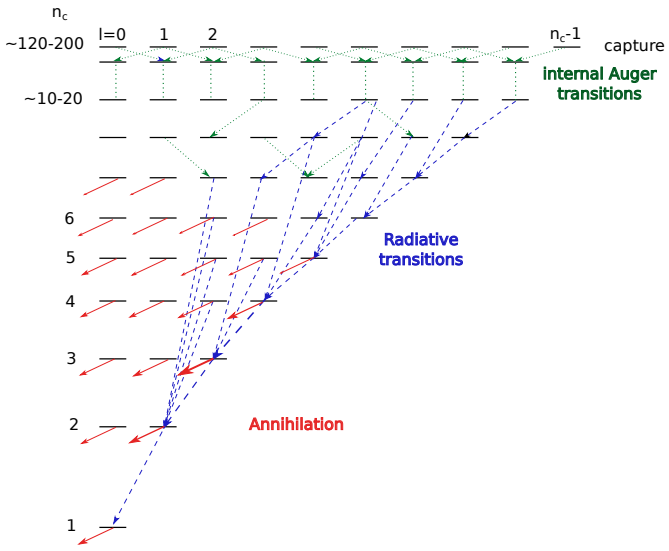

Figure 2.2: Scheme of the antiprotonic decay in a light Z atom. Figure inspired from that in [73].

a 10% statistical uncertainty. As mentioned above, PS209 showed antiproton annihilation to explore distances 2-2.5 fm beyond the nuclear surface, with a systematic difference between proton and neutron radii across the nuclear chart. A schematic of the overall cascade process is presented in Fig. 2.2.

Based on the previous analysis, we plan to perform cascade calculations using the recently constructed cascade code by T. Koike [76] together with the code [74], which will be updated by a member of the PUMA collaboration, who was involved in the original version of the code.

In the current, first stage of the project, we will use the conventional local form for the antiproton-nucleus potential $V_{\rm opt}$ [77]:

$$2\mu V_{\rm opt} = -4\pi \left(1 + \frac{\mu}{M}\frac{A-1}{A}\right)[b_0(\rho_n + \rho_p) + b_1(\rho_n - \rho_p)], \tag{2.1}$$

where μ is the reduced mass of antiproton and nucleus, A the nuclear mass number and M the nucleon mass. ρ_n and ρ_p are the neutron and proton densities, normalized to the neutron N and proton Z numbers rescpectively. The same parameters b_0 and b_1 from PS209 [58] are used, to study the "halo factor", heavily explored in PS209 [68]:

$$f_{\rm halo} = \frac{N(\bar{p}n)}{N(\bar{p}p)}\frac{Z}{N}\frac{{\rm Im}(a_{\bar{p}p})}{{\rm Im}(a_{\bar{p}n})}. \tag{2.2}$$

Here, the first factor is the ratio of annihilation events for neutrons divided by the annihilation events for protons, while the third one is the ratio of the imaginary part of the scattering lengths for antiproton-proton and antiproton-neutron interaction,

corresponding to $b_0 - b_1$ and $b_0 + b_1$ respectively. We expect this parametrization of the annihilation process not to be sensitive to the nature of the nuclear cascade, so the parameters from PS209 should be applicable for PUMA.

Other inputs in the calculation are:

1. $P(n_c, l)$: the initial distribution of the antiproton
2. Auger transition rates
3. Refilling rates

For 1., the quasistatistical distribution will be assumed, as in PS209 [68], analyzing the effect of parameter α, which could be modified due to the different refilling rates in PUMA and PS209. As for 2. and 3., both are expected to be small in the low-density environment in PUMA. The effect of the differences in density between PS209 and PUMA on the halo factor must be assessed. As well, the consistency between the halo factor obtained from this model and that produced from the final detection of the pions will be checked. In case significant differences are found, a unified analysis of cascade, annihilation and final-state interaction will be developed, to ensure consistency in the analysis of the different steps.

2.1.4 Annihilation

The antiproton nucleon annihilation is a complex QCD process [78]. The final state results mostly in the production of pions. Branching values of final states after antiproton-nucleon annihilation have been measured [79, 80]. The main decay channels are listed in Tab. 2.1.

2.1.5 Final state interactions

Since the annihilation takes place in the vicinity of the nucleus, pions produced after the annihilation may re-interact with the residual nucleus before being detected with a variety of processes including absorption and charge exchange, generally labelled as Final State Interactions (FSI) [81]. The interaction probability of the pions in the final state with the residual nucleus depends follows a geometrical solid-angle dependence [82].

This implies that, even assuming 100% detection efficiency for charged pions, the total charge determination will be biased if FSI are not accounted for.

2.2 Pion detection: analysis method and sensitivity

2.2.1 Overview

With PUMA, we will measure and identify the charge and the multiplicity of charged pions emitted from annihilations. From these data, we will determine the neutron-to-proton ratio of annihilations. These observables, with their uncertainties stemming

antiproton-proton		antiproton-neutron	
Pion final state	Branching	Pion final state	Branching
$\pi^0\pi^0$	0.00028	$\pi^-\pi^0$	0.0075
$\pi^0\pi^0\pi^0$	0.0076	$\pi^-k\pi^0(k>1)$	0.169
$\pi^0\pi^0\pi^0\pi^0$	0.03	$\pi^-\pi^-\pi^+$	0.0023
$\pi^+\pi^-$	0.0032	$\pi^-\pi^-\pi^+\pi^0$	0.17
$\pi^+\pi^-\pi^0$	0.069	$\pi^-\pi^-\pi^+k\pi^0(k>1)$	0.397
$\pi^+\pi^-\pi^0\pi^0$	0.093	$\pi^-\pi^-\pi^-\pi^+\pi^+$	0.042
$\pi^+\pi^-\pi^0\pi^0\pi^0$	0.233	$\pi^-\pi^-\pi^-\pi^+\pi^+\pi^0$	0.12
$\pi^+\pi^-\pi^0\pi^0\pi^0\pi^0$	0.028	$\pi^-\pi^-\pi^-\pi^+\pi^+k\pi^0(k>1)$	0.066
$\pi^+\pi^-\pi^+\pi^-$	0.069	$\pi^-\pi^-\pi^-\pi^-\pi^+\pi^+\pi^+k\pi^0(k\geq 0)$	0.0035
$\pi^+\pi^-\pi^+\pi^-\pi^0$	0.196		
$\pi^+\pi^-\pi^+\pi^-\pi^0\pi^0$	0.166		
$\pi^+\pi^-\pi^+\pi^-\pi^0\pi^0\pi^0$	0.042		
$\pi^+\pi^-\pi^+\pi^-\pi^+\pi^-$	0.021		
$\pi^+\pi^-\pi^+\pi^-\pi^+\pi^-\pi^0$	0.019		

Table 2.1: Pion final states for antiproton-proton [79] and antiproton-neutron [80] annihilation. Not all decay channels are shown and the total sums of the above branching ratios do not reach 100%.

from the FSI corrections, are the experimental output of PUMA which later on should be compared to theoretical predictions. On the theoretical side, as already mentioned in this chapter, the neutron-to-proton annihilation ratio depends intuitively on the ratio of neutron and proton densities at the site of the annihilation. The site of annihilation comes from the decay path of the antiproton after its capture and the competition between QCD annihilation, and QED electromagnetic and conversion-electron decays. An overview of the main elements in the measurement and the interpretation of the data is summarised in Fig. 2.3.

Here we discuss the analysis method and sensitivity to extract the ratio of neutron-to-proton annihilations from the measurements of charged pions in the final state. The development of this analysis tool and its benchmark on intra-nuclear cascade simulated data, as well as on reference measurements at ELENA is an important part of the project.

Our method is based on the following philosophy:

- Parameterize the FSI with a model. At this stage we use the four-parameter ($\omega^{\pm}$, $\lambda^{\pm}$) model as described in Ref. [83].
- Simulate the detector response for pions, protons, and neutrons coming from annihilations after FSI.
- Iterate following until convergence.
  - Train a neural network to recognise neutron and proton annihilations

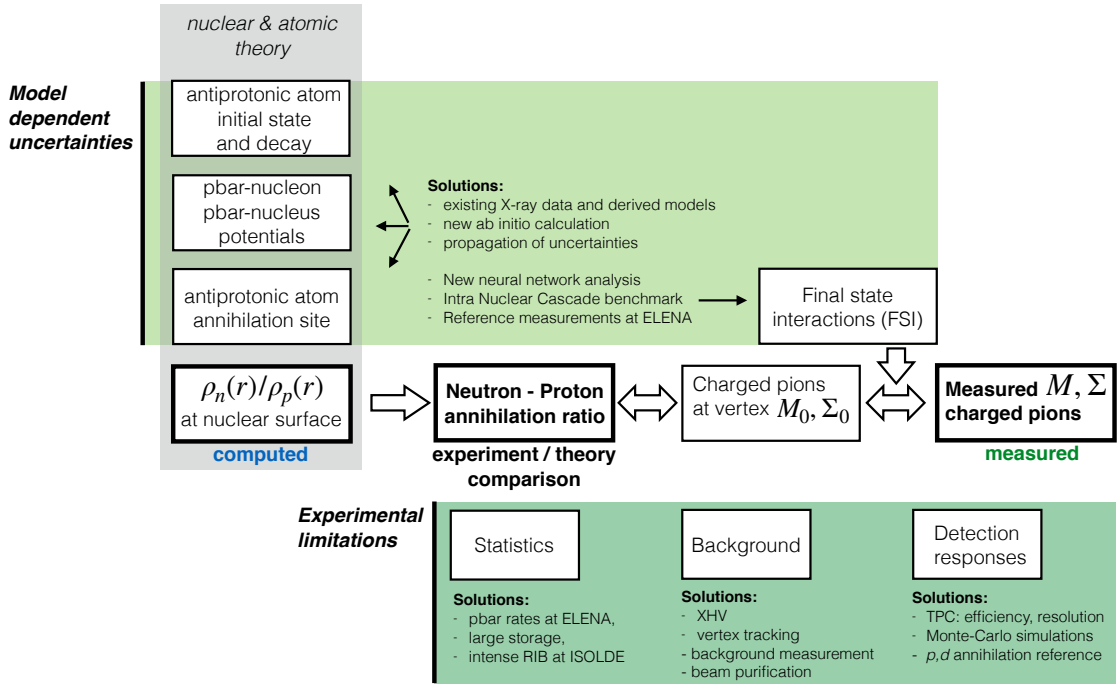

Figure 2.3: Schematics of the connection between measurement, observables and comparison with theory.

based on the simulated total charge of detected pions and their multiplicity.

  - Apply the neural network on data.
  - Use the difference between the data and best estimate of the model to further improve the neural network.

- Apply the neural network on data to obtain the neutron-to-proton annihilation ratio.

First developments show that the method is sensitive to the neutron-to-proton annihilation ratio at the level of 5% for the statistics of 10^3 annihilation events. The sensitivity has been drastically improved by two orders of magnitude better than the previous study [83]. This new approach will be tested on intra-nuclear cascade simulated data and the theoretical uncertainties quantified. The method will be further benchmarked on light stable nuclei for which the neutron and proton densities are believed to present less theoretical uncertainties when computed and for which exhaustive scattering data are available.

2.2.2 Parameterized model of FSI

We recall here the main ingredients of the method developed in Ref. [83]. Note that the model was developed by S. Wycech, a collaborator of PUMA. The original idea

was proposed by Y. Yamazaki, former team leader of ASACUSA and M. Wada, member of the PUMA collaboration.

The model assumes that the interaction of pions with the residual nucleus resumes in four processes which can be accounted for by four parameters which characterise the probability of an produced pions to encounter the related process:

- the absorption or charge exchange probabilities $\omega^{\pm}$ of $\pi^{\pm}$ by the residual nucleus,
- the charge exchange probabilities $\lambda^{\pm}$ of π^{0} to $\pi^{\pm}$.

The double charge exchange reactions can be ignored and, so far, we neglect two-step processes. In this simple model, the size of the residual nucleus is not considered as a parameter. The effect of FSI resulting from a choice of parameters $\omega^{+} = \omega^{-} = \lambda^{+} = \lambda^{-} = 0.1$, is illustrated in Tab. 2.2 and Tab. 2.3.

$M\backslash\Sigma$	-5	-4	-3	-2	-1	0	$+1$	$+2$	$+3$	$+4$
0	0	0	0	0	0	2993	0	0	0	0
1	0	0	0	0	0	0	0	0	0	0
2	0	0	0	0	0	40239	0	0	0	0
3	0	0	0	0	0	0	0	0	0	0
4	0	0	0	0	0	52118	0	0	0	0
5	0	0	0	0	0	0	0	0	0	0
6	0	0	0	0	0	4650	0	0	0	0
7	0	0	0	0	0	0	0	0	0	0
8	0	0	0	0	0	0	0	0	0	0
9	0	0	0	0	0	0	0	0	0	0

Table 2.2: Simulated histogram of the multiplicity of primordial charged pions (M) and the total charge (Σ) for 10^5 $\bar{p} + p$ events.

A first simulation of the effect of FSI on measured charge (Σ) and multiplicity (M) is shown in Fig. 2.4, as a function of different assumptions for the charge exchange ($\lambda^{\pm}$) and absorption ($\omega^{\pm}$) probabilities. Fortunately, the FSI can be corrected from the redundancy of the measurement: the observable from PUMA will be the two-dimensional matrix giving the number of events as a function of M and Σ. The matrix contains both the information on the neutron-to-proton annihilation ratio and FSI effects. At this stage the expected accuracy of these simulations is 5% on the neutron-to-proton annihilation ratio from 5×10^5 antiprotonic atoms assuming 80% detection efficiency of charged pions (See Chapter 7).

2.2.3 Machine learning

We use a simple neural network to determine the initial neutron-to-proton annihilation ratio from M-Σ data matrices. The neural network is illustrated in the left

$M\backslash\Sigma$	-5	-4	-3	-2	-1	0	$+1$	$+2$	$+3$	$+4$
0	0	0	0	0	0	1697	0	0	0	0
1	0	0	0	0	2913	0	2982	0	0	0
2	0	0	0	945	0	22641	0	993	0	0
3	0	0	107	0	11372	0	11414	0	132	0
4	0	16	0	1457	0	28930	0	1502	0	6
5	0	0	63	0	4668	0	4582	0	70	0
6	0	1	0	249	0	2574	0	247	0	1
7	0	0	6	0	203	0	217	0	6	0
8	0	0	0	0	0	4	0	0	0	0
9	0	0	0	0	0	0	0	0	0	0

Table 2.3: Simulated histogram of the multiplicity and the total charge with the final state interactions. $\omega^{\pm} = \lambda^{\pm} = 0.1$.

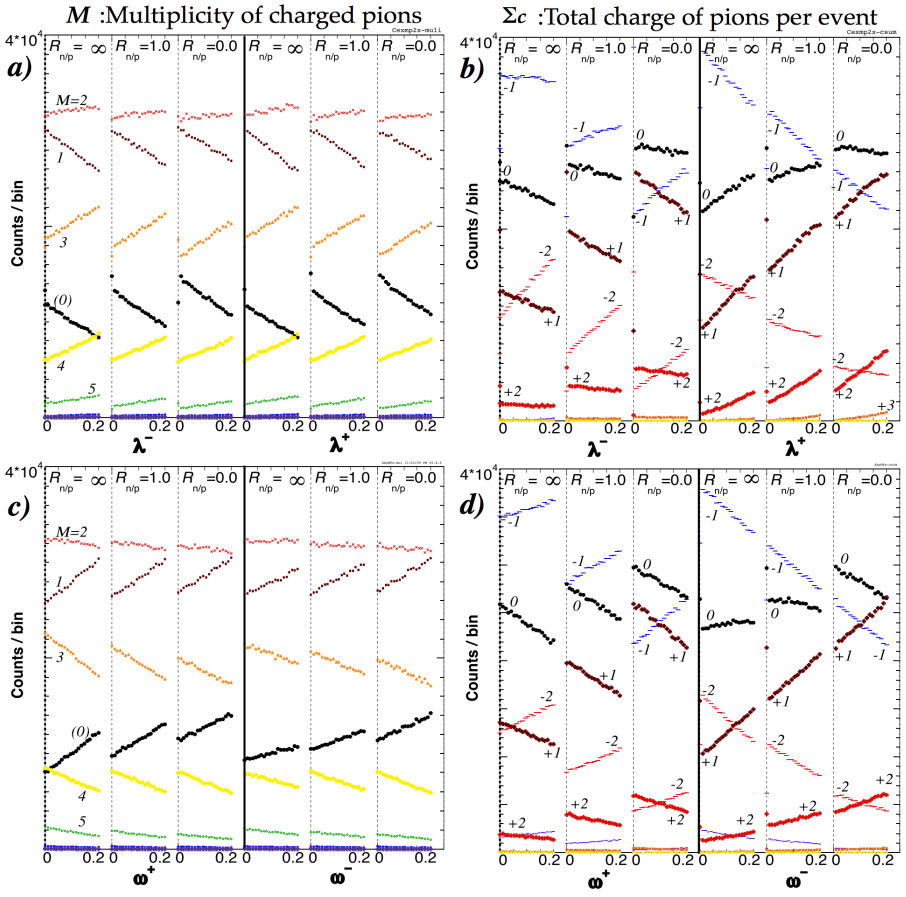

Figure 2.4: Distortions of the charged-pion production as a function of charge exchange, absorption and proton-over-neutron density ratio. The figure is taken from [83].

part of Fig. 2.5: it consists of an input layer with 100 nodes (a_i) corresponding to 10×10 elements of a M-Σ matrix, one hidden layer with 100 nodes (b_i), and

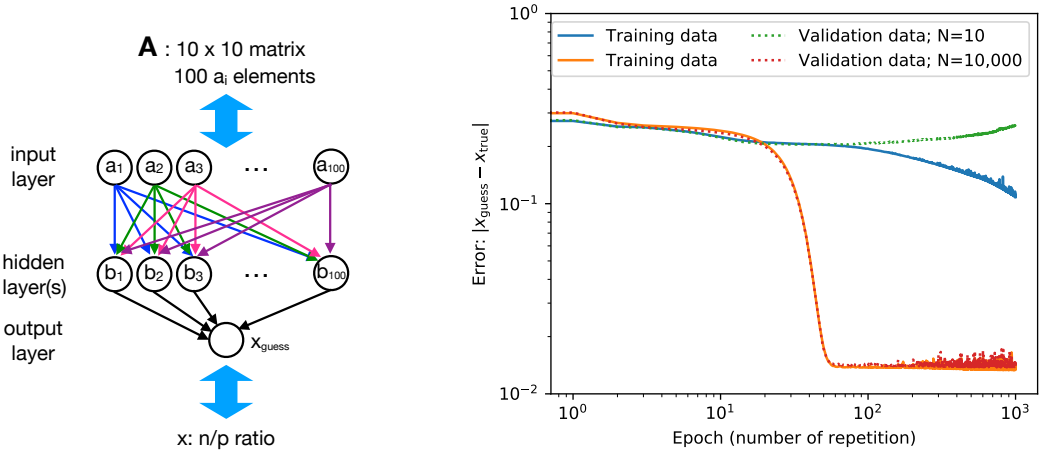

Figure 2.5: (Left) Scheme of the adopted neural network. The input matrix **A** is the two-dimensional M-Σ matrix characterizing the measured charged pions. (Right) Convergence of the training procedure to fit the function that links the M-Σ matrix to the deduced n/p annihilation ratio (x_{guess}), to be compared to the exact value x_{true} with the number of training repetitions.

an output layer with one node (x_{guess}) providing the neutron-to-proton ratio. Each node is calculated as

$$\begin{aligned} b_i &= \sum_{j=1}^{100} w_{ij} a_j, \\ x_{\text{guess}} &= f(\sum_{j=1}^{100} w'_{ij} a b_j), \end{aligned} \tag{2.3}$$

where $f(x)$ is a so-called activation function which allows the neural network to solve non-trivial problems. The neural network has parameters of about 10^4 (weights w_{ij} and w'_{ij} in Eqs. 2.3). These parameters are determined through the training using the 10×10 M-Σ matrices with different n/p ratios.

The neural network is implemented by using the deep-learning library TensorFlow [84] and the high-level neural networks API Keras [85]. The so-called Adam optimizer [86] is used for faster convergence. We observe a convergence of the fitting procedure after $\sim 10^2$ repetitions. The convergence is illustrated on the right part of Fig. 2.5. It shows, for example, that when the neural network is trained with matrices with a statistics of 10000 simulated annihilations, the fitted function finds the proper n/p ratio with a precision better than 98%. Note that this accuracy is for a test data set simulated with the same model and parameters as the training samples.

One can first investigate to what accuracy the n/p annihilation ratio is obtained by applying the trained neural network. This is shown on the left panel of Fig. 2.6: already with 100 annihilation events, the n/p annihilation ratio is found with a precision of 85% for the set of parameters and detection efficiency considered above. For a statistics of 10^4 events, the precision reaches 99%.

The principal limitation of this method is the uncertainty coming from the model dependence of the FSI. We investigated the dependence of these parameters for variations of ±100% around the values $\omega^{\pm} = \lambda^{\pm} = 0.1$. The dependence is found to be relatively small: by varying one parameter by ±100%, the precision of the n/p-ratio extraction varies a maximum of 20%, as illustrated for a variation of ω^{+} on the right panel of Fig. 2.6.

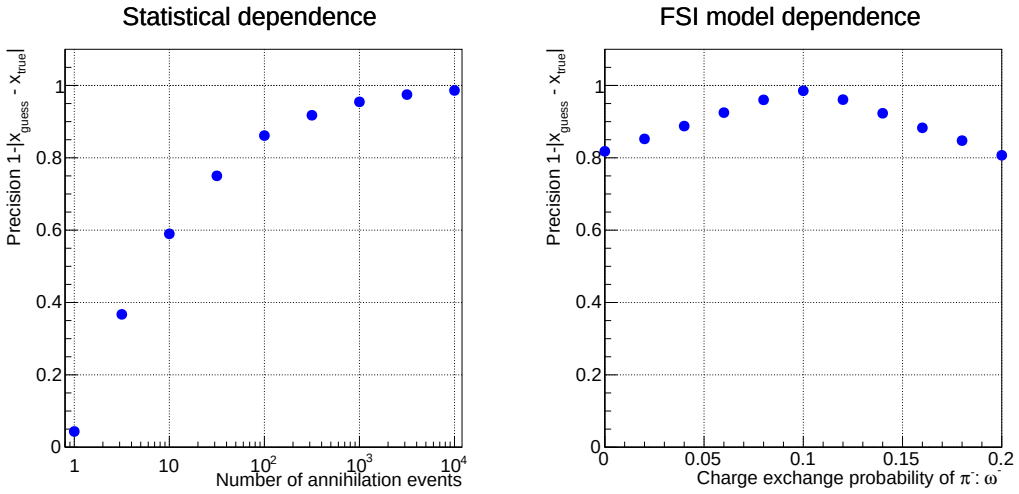

Figure 2.6: (Left) Mean standard deviation of the extracted n/p ratio from the analysis compared to the initial value, as a function of the statistics of the analysed sample. Initial data and the training sample were simulated with the same model. (Right) Illustration of the sensitivity to model parameters. In the shown case, the data sample was simulated with 10^4 annihilation events, model parameter ω^{+} is varied from 0 to 0.2. All other parameters were taken as the training samples, i.e. $\omega^{-} = \lambda^{\pm} = 0.1$.

2.2.4 Recursive machine learning (ongoing)

The neural network is trained by using the Monte-Carlo samples based on the four-parameter model described above. The model parameters $\omega^{\pm}$ and $\lambda^{\pm}$ are empirically determined by fitting the experimental data. These parameters have a typical uncertainty of 100% coming from a disagreement of the data. As discussed above, this uncertainty results in 20% error in the estimation of the neutron-to-proton ratio. Figure 2.7 shows the estimation of the neural network for data generated with two different sets of model parameters. If the model parameters used for the training of the neural network are close to those used for the evaluation, the error in the calculated neutron-to-proton ratio has no dependence on the true value of the neutron-to-proton ratio used for generating the Monte-Carlo samples. However, the error in the calculation has large correlation with the true value, and of course becomes large, if the different model parameters are used for the training and the evaluation. It is important to find realistic model parameters for the training in order to minimize the error in the calculation of the neutron-to-proton ratio.

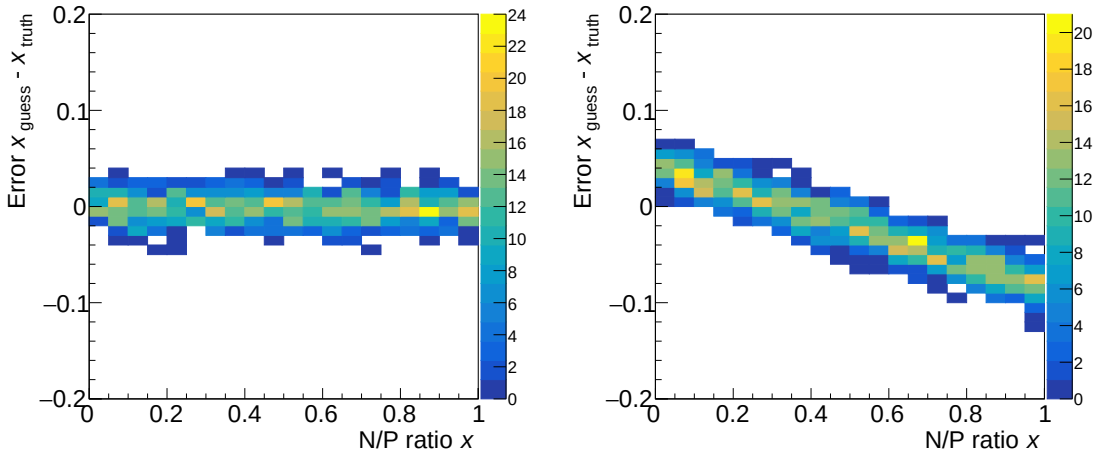

Figure 2.7: (Left) The error of the evaluation of the neutron-to-proton ratio by the neural network. The horizontal axis shows the neutron-to-proton ratio. The neural network is trained with Monte-Carlo samples with parameters of $\omega^{\pm} = \lambda^{\pm} = 0.1$ and its performance is evaluated with the same parameters. (Right) The performance is evaluated with samples with parameters of $\omega^{+} = \lambda^{+} = 0.1$, $\omega^{-} = \lambda^{-} = 0.2$.

The model parameters $\omega^{\pm}$ and $\lambda^{\pm}$ cannot be directly determined from the experimental data because they are not observable. However, they can be indirectly obtained from the obtained M-Σ matrix since it contains all the information of the FSIs as well as the neutron-to-proton ratio. If the model parameters are not realistic, the model cannot reproduce the experimentally-obtained M-Σ matrix. Thus, it is expected that the model parameters can be determined without any *a priori* information by minimizing the difference between measured and predicted M-Σ matrices. The M-Σ matrices generated with different model parameters are shown in Tab. 2.4 as an example.

$M\backslash\Sigma$	-5	-4	-3	-2	-1	0	$+1$	$+2$	$+3$	$+4$
0	0	0	0	0	0	1384	0	0	0	0
1	0	0	0	0	2696	0	4079	0	0	0
2	0	0	0	1403	0	18331	0	2188	0	0
3	0	0	284	0	12946	0	13783	0	280	0
4	0	27	0	2993	0	23029	0	2035	0	18
5	2	0	313	0	6414	0	4189	0	111	0
6	0	21	0	634	0	2116	0	232	0	3
7	0	0	20	0	312	0	142	0	5	0
8	0	0	0	3	0	4	0	0	0	0
9	0	0	0	0	0	0	0	0	0	0

Table 2.4: Simulated histogram of the multiplicity and the total charge with the final state interactions. $\omega^{+} = \lambda^{+} = 0.1$, $\omega^{-} = \lambda^{-} = 0.2$.

The model parameters for the training are improved by minimizing the "distance" Δ between the experimental data and the model. Herein the Euclidean distance is employed for the simplicity:

$$\Delta = \sqrt{\sum_{i,j} \left| a_{ij} - a'_{ij} \right|^2}, \tag{2.4}$$

where a_{ij} and a'_{ij} respectively represents the elements of the M-Σ matrices obtained experimentally and the one predicted by the model.

The experimental data are imitated by the Monte-Carlo simulation with the parameters of $\omega^{\pm} = \lambda^{\pm} = 0.1$, the neutron-to-proton ratio of 0.5, and the number of annihilation events of 10^4. The Δ distribution as a function of ω^- and λ^- is shown in Fig. 2.8. The Δ has a minimum at $\omega^- = \lambda^- = 0.1$. It is demonstrated that the model parameters are determined within the error of 10%, corresponding to the uncertainty of the neutron-to-proton ratio of 2%.

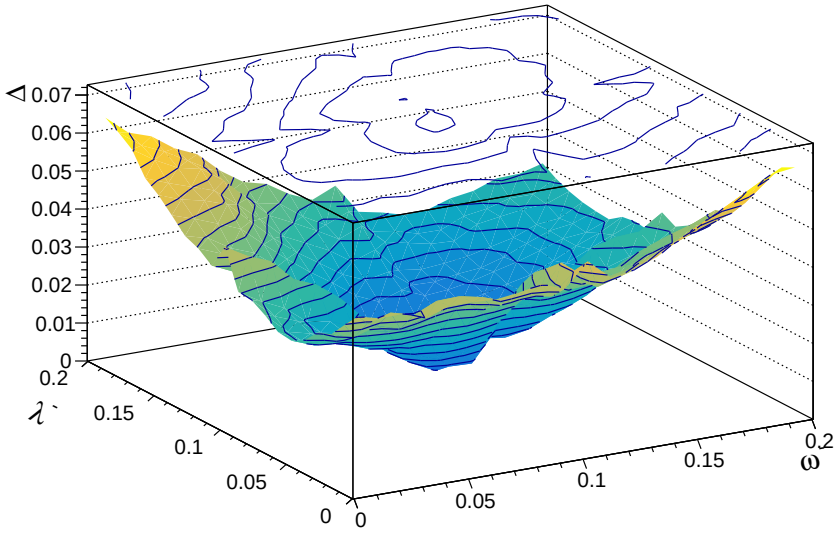

Figure 2.8: The distance Δ distribution as a function of ω^- and λ^-. Other parameters are fixed as $\omega^+ = \lambda^+ = 0.1$

.

This method will be further benchmarked by using more realistic event generator based on the intra-nuclear cascade calculation described below. At this stage, we are confident that the proposed together with the high tracking efficiency of PUMA will allow an uncertainty on the neutron-to-proton annihilation ratio better than 10% for a statistics of few thousand annihilations, the target of PUMA.

2.2.5 Intra-nuclear annihilation model

Antiproton-induced reactions with heavy ions have already been implemented to intra-nuclear cascade codes [87–89]. At our knowledge, there is no available simu-

lation code today for antiproton-nucleus annihilation at rest. We implemented this feature inside the Intra-Nuclear Cascade of Liège (INCL) developed over the past decades [90–92], mostly for spallation studies at intermediate energies.

The initial conditions are set as follows:

- the loci of annihilation are drawn in a pre-defined range, for example between 2 and 3 fm
- the user can decide if the annihilation should occur with a proton or a neutron. A data sample with a given n/p annihilation ratio can be obtained by mixing proton and neutron annihilation events
- the annihilation occurs with the nucleon closest to the randomly chose annihilation radius
- the decay channel is chosen according to experimental tables for $\bar{p}p$ and $\bar{p}n$ annihilations
- the resulting pions ($\pi^{\pm}$'s and π_0's) are randomly emitted in the phase space ensuring energy conservation

The final state interactions are taken care by the INCL version we used, without any modification on our side. In INCL, the pion-nucleon interactions are defined from experimental data. An example of the quality and momentum dependence is shown in Fig. 2.9 where the π^+ production from the interaction of antiprotons at 900 MeV/c with a nucleus of ^{12}C is shown.

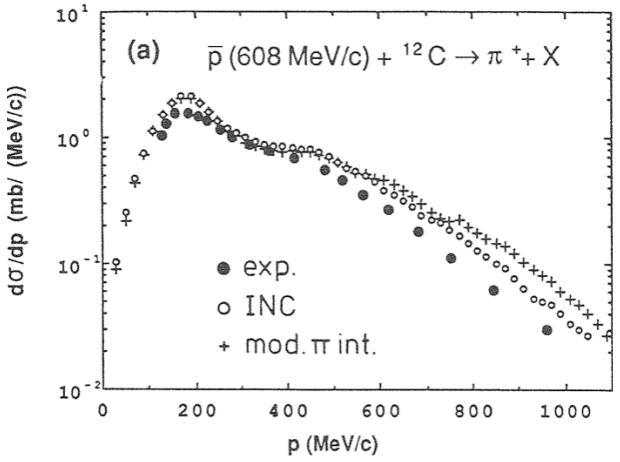

Figure 2.9: Inclusive π^+ production cross section from $\bar{p}$ + ^{12}C at 608 MeV/c. The cross section is given as a function of the pion energy in the final state. Data are compared with two INC calculations. Figure taken from [88].

2.3 Foreseen developments

2.3.1 Model and analysis tools

Treatment of final state interactions

- The parameterized model used to teach the machine learning algorithm will be further developed, in particular by the addition of the nucleus-mass dependence of the FSI following the work of [82].
- An analysis method to extract the net annihilation charge from measured pions total charge and multiplicity will be developed and benchmarked on test cases (e.g. light N=Z nuclei, where neutron and proton charge distribution are expected to be the same). To do so, the implementation of antiproton annihilation on nuclei has been recently added into the INCL intranuclear cascade code. Realistic simulations with the design of the PUMA trap will be performed and the accuracy of the developed method to recover the initial proton-to-neutron annihilation ratio will be estimated. A postdoctoral fellow will be hired from September 2018 to focus specifically on this aspect.
- The algorithm, that can be based on standard fit or more refined neural-network techniques will be implemented using simulated data. The annihilation simulation will be coupled to a realistic simulation of pion detection within the GEANT4 framework. Later on, the algorithm can be applied to extract the ratio of proton over neutron charge for annihilation on light N=Z nuclei (α, ^{12}C), where the ratio is expected to be close to unity. Note that data on different isotopes will allow relative comparison and reduce systematic uncertainties.

Uncertainty coming from the background

- The amount of the residual hydrogen and helium gases can be comparable with that of the target nuclei. This will introduce an additional uncertainty in the neutron-to-proton ratio. A very preliminary estimation shows this uncertainty is comparable with the other ones if the signal-to-noise ratio is better than 1. This will be further investigated with the realistic simulations of PUMA including the surrounding equipment.

2.3.2 Ab-initio antiproton-nucleus interaction models

On the theory side, collaborators will contribute to PUMA in developing several aspects related to antiproton-nucleus systems, as detailed below in the order of increasing difficulty.

- As a first step, we aim to compare the existing N$\bar{\text{N}}$ interaction models. They may be classified in two main groups depending on the way they treat the annihilation process: the optical models or the unitary coupled-channel approach

were annihilation is taken into account by including explicit meson-meson channels coupled to $N\bar{N}$ in a unitary scheme. From the optical models side, these are: Dover-Richard [93], Khono-Weise [94], the updated (2009) version of the Paris potential [95] and the recently developed chiral-effective theory inspired potential by Haidenbauer and collaborators [96].

An alternative to the optical model approach is the unitary coupled channel model which can lead to substantial differences in the short range parts of wave functions. We have at our disposal this model developed in another context [97, 98], which will be updated for the low energy physics case.

The main interest of this initial step is to understand the stability of the theoretical predictions in describing the annihilation process in the simplest system including antiparticles: protonium [99]. This implies computation of lower $\bar{\text{p}}$-p orbits with the different potentials as well as the corresponding annihilation densities $\gamma_\alpha(r)$ for the lowest states $\alpha = \{LSJ\}$ [99]. These quantities are related to the spatial distribution of the annihilation process, whereas their overlap integrals provide the total width of the state. They can be obtained in terms of the state wave function Ψ_α and the annihilation interaction. In the optical model, it reads

$$\Gamma_\alpha = \int dr\ \gamma_\alpha(r) \qquad \gamma_\alpha(r) = \text{Im}\left[V_{N\bar{N}}(r)\right] \mid r\Psi_\alpha(r) \mid^2 . \tag{2.5}$$

- A second step consists in computing the $\bar{\text{p}}$-A (antiproton-nuclei) Coulomb orbits in the few lightest nuclei for which an exact numerical *ab-initio* solution is accessible. To this aim the Faddeev-Yakubovsky [100, 101] equations in configuration space will be solved. Our present technology allows us to solve A=2,3,4 and 5 problems [101] accounting for the different asymptotic channels. This limits the Faddeev-Yakubovsky approach to the following stable nuclei: ^{2}H, ^{3}H, ^{3}He and ^{4}He. The first results in the $\bar{p} -^2 H$ case, showed however that the calculations are very challenging and it is not clear that this full program could be achieved using the last approach.

After obtaining the exact solution in a few test nuclei, we will make use of another *ab-initio* computation technique for scattering and continuum states, based on the No-Core Shell Model [102]. This method has been successful in describing reactions of a neutron (proton) impinging on a light to medium mass nuclei, up to $A \sim 12$ [103]. This will allow us to study the evolution of low-energy antiproton-nucleus towards heavier and exotic systems aimed by the PUMA project.

At the end of this step we will have computed a set of nuclei for which the widths of the antiprotonic Coulomb orbits can be directly computed with no

other approximation than the ones included when developing fundamental models of the $\bar{N}N$ interaction.

- Having at our disposal the exact solution for the simplest nuclei, the third and crucial step will consist in validating the results of the $\bar{p}$-nucleus ($\bar{p}$-A) optical potential approach [68, 104, 105], which is one of the key points of the PUMA project. This approach is indeed based on the assumption that the $\bar{p}$-A optical potential is directly related to the nuclear density $\rho(r)$ by means of expressions like

$$V(r) = \frac{2\pi}{\mu_{pA}}\, a_{\bar{p}p}\, \rho(r) \tag{2.6}$$

where $a_{\bar{p}p}$ is the scattering length and the μ_{pA} denotes the reduced mass of the $\bar{p}$-A system. Furthermore, it assumes that a $\bar{p}$-A potential constructed in this way is able to reproduce the corresponding antiprotonic widths.

It is worth to emphasize that this ansatz has never been tested in the case where all the terms can be exactly computed. To confirm or infirm the validity of (1), and eventually determine what kind of corrections would be required, will constitute a major contribution to the PUMA project.

2.3.3 Antiprotonic decay

Concerning the decay of the antiprotonic atom, the following steps will be performed:

- Setting and running the existing cascade code, first by the use of an antiproton optical potential with relatively simple, tentatively phenomenological, nuclear surface density distributions. LEAR data will be used to benchmark this step.
- Recent potential forms and parameters from [77] will be used to further refine the model.
- Improving the simple nuclear surface density distributions by the use of other microscopic density predictions, especially on the proton and neutron contents of the nuclear surface. The uncertainties stemming from the antiprotonic atom formation and decay will be evaluated, first assuming $\bar{p} - A$ potentials of the existing literature.
- If sensitivity to the inputs for the potentials is found to be strong a unified analysis of cascade, annihilation and final-state interaction will be developed to ensure consistency.

Chapter 3

Device overview

Before describing in more details each part of the PUMA experiment, we give here a short overview of the setup. PUMA will integrate several functions in one transportable device: solenoid and traps for storage and devices, vacuum pumps, electronics for the trap operation and plasma diagnostics, annihilation detection and its electronics, compressors and cold heads for the solenoid and trap, UPS, batteries and chiller to cool the compressors during transport. All these functions are integrated into two frames:

- A main frame containing the solenoid, trap and all function necessary to the operations of PUMA.

- An annex frame for the UPS, batteries and chiller.

The full system is 5.5 meter long, 2.7 meter height and 1.9 meter wide. The two frames can be disconnected. The main frame is 3.5 meter long, while the annex frame is 2 meter long. The dimensions are fixed by external constrains: the length of 5.5 meter is limited by the delivery zone of ELENA and ISOLDE. The height of 2.7 meter is the standard height of containers. It is limited by the roof height of the experimental zone at TU Darmstadt and by the crane operations at ELENA. The total weight of PUMA is estimated to 7.5 tons decomposed as follows: 4.5 tons of solenoid (mostly the passive shielding), 1.5 tons of devices and 1.5 tons of frame. The total electrical power consumption of the device is estimated to 45 kW with a maximum consumption of 70 kW. The devices (trap not included) to be incorporated inside the frame are listed in Tab. 3.1.

The PUMA experiment consist of one solenoid and one double trap inside a unique 4 K cryostat. We underline this point because the SPSC [8] suggested to investigate the option of having two separate traps in two separate solenoids, one for collisions and one for storage and transport. Historically, the two-solenoid option was first investigated in 2014 at the birth of the PUMA idea and was abandoned quickly: it is indeed believed that one unique system has several advantages which we summarize here and which will find further justifications in the following chapters:

- Both the antiproton storage and the annihilation measurement require a vacuum of 10^{-17} mbar. One unique 4 K cryostat separated by a conductance reduction pipe guarantees the best experimental conditions for PUMA.
- For safety during transport and flexibility of operation, we chose a cryogen-free option. This implies that the transport frame hosts, in addition to the solenoid, compressors and electronics, an UPS, batteries and a chiller for cooling. The gain of switching from one large solenoid to a smaller one dedicated to transport only would not make the experiment small.
- The use of two solenoids would require an additional XHV transfer line between them, additional XHV efforts to create two separate regions at 10^{-17} mbar for transport and collisions, as well as additional alignment efforts between the two traps.

Frame	Content	Power (kW)	Weight (kg)
Main: $1.9 \times 3.5 \times 2.7\,\mathrm{m}^3$	Solenoid cryostat and cryocoolers, magnet power supply and quench detectors, trap electrodes and cryostat (inside the solenoid bore), trap cryocoolers and HV supplies, rotating wall drive, waveform generators, trap control crate, vacuum pumps, TPC detector and electronics, gas bottle	50	5500
Annex: $1.9 \times 2.5 \times 2.7\,\mathrm{m}^3$	Chiller, UPS, batteries, power supply panel	20	1500
Total	-	70	7000

Table 3.1: Description, power consumption and weight of the main devices inside the PUMA frame.

A conceptual 3D representation of the full PUMA system is shown in Fig. 3.1.

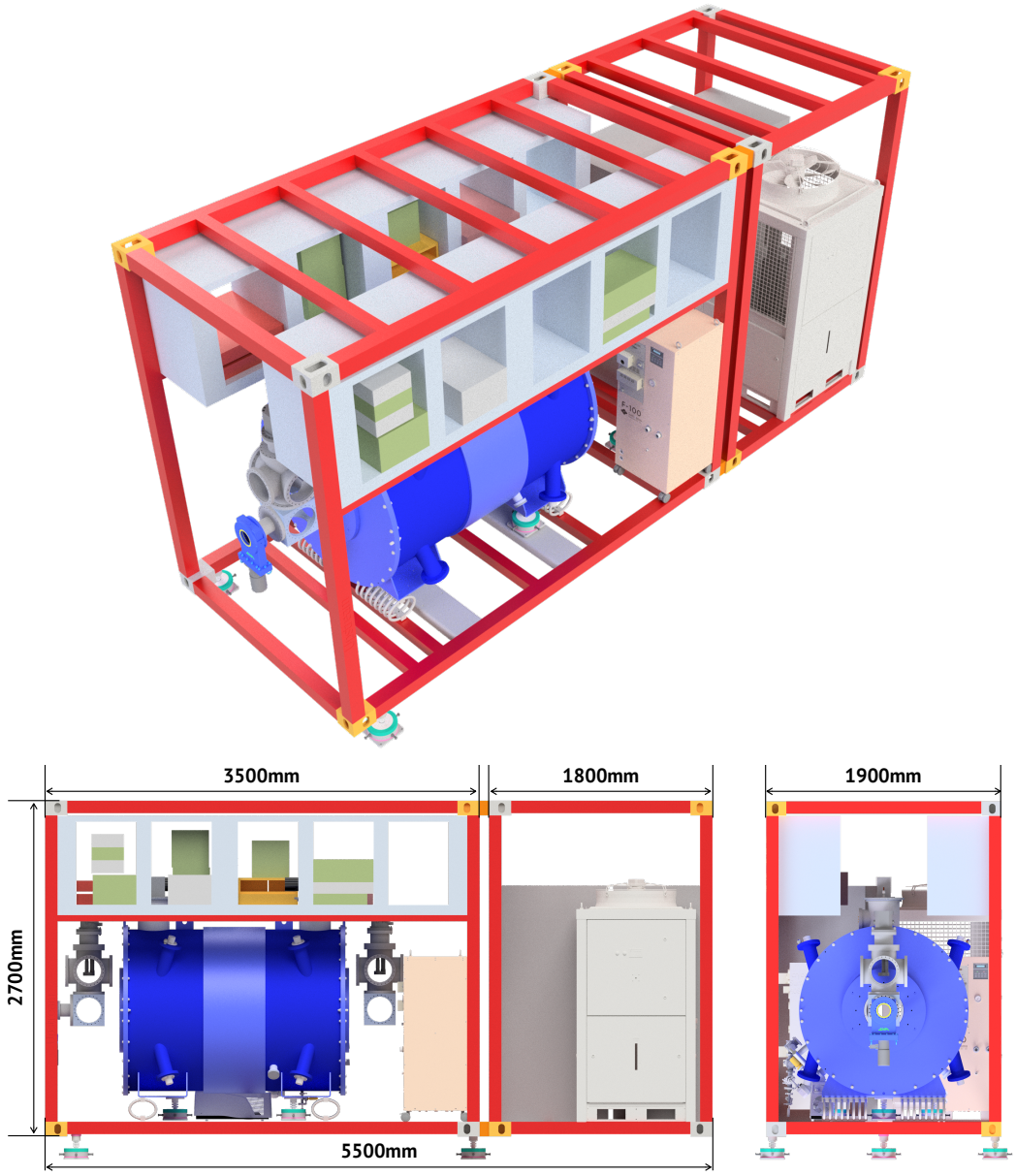

Figure 3.1: Conceptual 3D view of PUMA. The two frames can be separated. The dimensions of PUMA are 5.5 m × 2.7 m × 1.9 m.

Chapter 4

Vacuum

PUMA aims at storing one billion antiprotons with a plasma half life in the storage trap better than 30 days, the typical duration of an experimental cycle of trapping at ELENA, transport to ISOLDE and performing physics experiments with radioactive ions at ISOLDE. To achieve this, an extremely high vacuum (XHV) of about 10^{-17} mbar, corresponding to a residual gas density of $n_{\mathrm{gas}} \approx 20\,\mathrm{cm}^{-3}$ in the storage trap is targeted. The XHV will be obtained by cryopumping. In addition, the vacuum level in the collision trap, where the interaction between antiprotons and the radioactive ions will take place, should also reach the same level of vacuum to prevent background from annihilation with the residual gas.
After a short reminder of XHV considerations, we discuss in this chapter the hydrogen isotherms at low pressure, the key physics ingredient for the PUMA vacuum concept, and its parameterisation. First simulations of the vacuum in the PUMA trap are then detailed.

4.1 Vacuum concepts

4.1.1 Lifetime of the antiproton plasma

The lifetime of the antiprotons plasma and the molecular density in the trap are related. We assume the following capture cross section of antiprotons on molecular hydrogen, which is likely to be the dominant process in a cryogenic vacuum system [106–108]

$$\sigma = 3\pi a_0^2 \sqrt{\frac{27.2\ \mathrm{eV}}{E}}, \tag{4.1}$$

where $a_0 = 5.3 \times 10^{-11}$ m is the Bohr radius of the hydrogen atom and E the kinetic energy of the antiproton in the centre-of-mass system. The annihilation probability Γ is given by [108]

$$\Gamma = \frac{1}{\tau} = n_{\mathrm{gas}} v \sigma, \tag{4.2}$$

where $v = \sqrt{2E/m_{\mathrm{p}}}$ is the antiproton velocity. The lifetime τ of the antiproton plasma relates to the residual gas density via [108]

$$n_{\mathrm{gas}} = \frac{1}{\tau}\left(3\sqrt{2}\pi a_0^2 \times \sqrt{\frac{27.2\ \mathrm{eV}}{m_{\mathrm{p}}}}\right)^{-1} \approx \frac{1}{\tau}\left(5.2 \times 10^8\right)\ \mathrm{s}\cdot\mathrm{cm}^{-3}. \tag{4.3}$$

Considering the equation of state for ideal gases $PV = nRT$, one gets equivalence of τ, n_{gas} and P of Tab. 4.1. According to Tab. 4.1, we would need a pressure of at least 10^{-16} mbar to keep the antiproton plasma for 30 days. However, as described along this chapter, a more realistic pressure to be achieved for the antiproton plasma at 4 K is 10^{-17} mbar, corresponding to $n_{\mathrm{gas}} = 20\ \mathrm{cm}^{-3}$, which is the maximum amount of gas particles we should allow to achieve a low rate of residual-gas-induced annihilations. The half life of the antiproton plasma after which half of the initial amount of antiprotons has annihilated relates to the lifetime through the relation $t_{1/2} = \ln(2)\tau$.

n_{gas} (cm^{-3})	τ (days)	P (mbar)
200	30	10^{-16}
20	300	10^{-17}

Table 4.1: Equivalence between the pressure P, the molecular volumic density n_{gas} at 4 K and the lifetime τ of the antiproton plasma. The density and lifetime have been rounded to the closest decade.

4.1.2 Cryopumping

To satisfy the above requirements, the concept of PUMA is based on cryopumping on the 4 K surface of the trap electrodes and cryostat. The extreme vacuum is maintained as long as the surface density of adsorbed molecules on the walls of the trap does not exceed a critical value given by the H_2 isotherm at the temperature of the trap.

Cryopumping relies on two main pumping mechanisms: cryocondensation and cryosorption. Cryocondensation is based on the intermolecular Van der Walls forces which are strong enough to maintain molecules bound together when the temperature is low enough (see Fig. 4.1). The key property is the saturated vapour pressure P_{v}, i.e. the pressure of the gas phase in equilibrium with the condensate at a given temperature. The lowest pressure attainable by cryocondensation is limited by the saturated vapour pressure. Among all gas species, only Ne, H_2 and He have P_{v} higher than 10^{-11} mbar at 20 K. The saturated vapour pressure of H_2 at the liquid He boiling temperature is in the 10^{-7} mbar range at 20 K, and is 10^{-12} mbar at 1.9 K. The quantity of gas that may be cryocondensed is very large and limited only by the thermal conductivity of the condensate. Cryosorption, on the other hand, is based on the attraction between gas molecules and the substrate. The interaction forces

with the substrate are much stronger than those between similar molecules [109]. As a result, providing the adsorbed quantity is lower than one monolayer, the sojourn time is much longer and gas molecules are pumped at pressure much lower than the saturated vapour pressure. A significant quantity of gas may be pumped below one monolayer if porous materials are used; for example, in one gram of standard charcoal for cryogenic application, about 1000 m^2 of surface are available for adsorption. Carbon coating increases the effective surface of a metal substract by a factor one hundred [110].

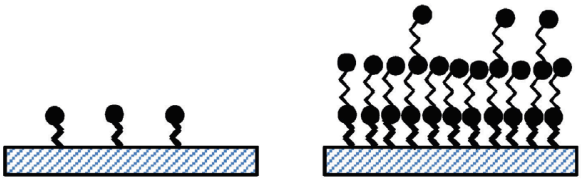

Figure 4.1: Schematic drawing depicting (left) submonolayer cryosorption, where the pumping is based on molecule-substrate interactions; and (right) cryocondensation, where the leading mechanism is intermolecular interaction. Figure from [111].

One technical objective of PUMA is to minimize the number of gas molecules entering the croystat and keep the system in the sub-monolayer regime as long as possible. To do so, the design of the cryostat of the trap is crucial. A conduction reduction and a "cryogenic gate" (see section 4.5) at the entrance of the cryostat will be used to limit the rate of residual gas molecules entering the trap, while at the entrance of the cryostat we aim at a pressure of 10^{-11} mbar.

4.2 Isotherms

At equilibrium, the residual gas density in the cryostat depends on three main factors: the temperature of the cold surface, its effective area and geometry, and the molecular occupation of this surface. The partial pressures of all relevant gas species at temperature levels of liquid Helium ($T = 4.2\,\mathrm{K}$), achieve the saturation vapor pressures of $P_\mathrm{v} < 10^{-12}\,\mathrm{mbar}$, except for hydrogen and helium. All gas species heavier than hydrogen and helium are pumped by cryocondensation.

The isotherm for a specific molecule on a specific substrate gives the relation of the surface coverage and the vapour pressure. If the surface coverage ratio $\Theta = S/S_\mathrm{m}$ between the actual surface coverage S and the maximum monolayer capacity S_m is lower than unity, the pressure at equilibrium will be lower than its saturation pressure. This ratio depends only on the surface temperature and the surface coverage. This relationship is described by an adsorption isotherm depending on S_m and P at a constant temperature. At $\Theta \approx 1$ the given pressure rises up to its temperature

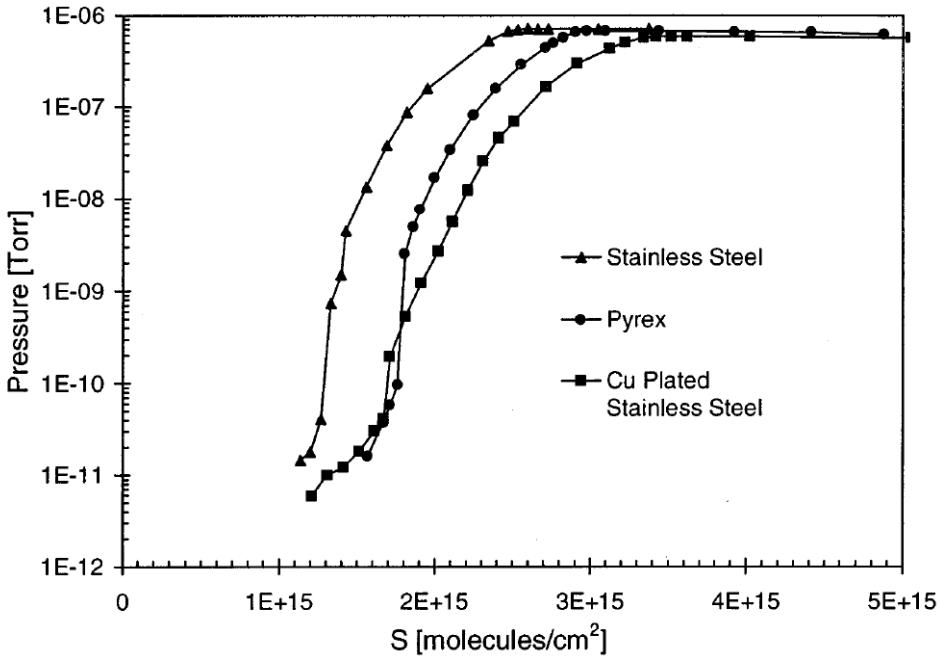

Figure 4.2: H_2 adsorption isotherms at 4.2 K on Pyrex, Stainless Steel, and Cu plated Stainless Steel. Figure from [124].

dependent saturation vapor pressure [112].

There are different models for adsorption isotherms. Examples are Henry's law [113,114], the Freundlich equation [115] and the Brunauer-Emmet-Teller (BET) isotherm equation [116, 117], which all describe the isotherms for different temperatures and different pressures. The physisorption isotherms for low temperatures in the submonolayer region are described by the Dubinin-Radushkevich-Kaganer (DRK) equation [118–122], which is

$$\ln(\Theta) = -D\left[k_{\mathrm{B}} \cdot T \cdot \ln\left(P_0/P\right)\right]^2 \tag{4.4}$$

where T is the temperature, k_{B} is Boltzmann's constant and D is an empirical constant depending on the given adsorbent-substrate system. Furthermore P corresponds the equilibrium pressure and P_0 is the saturated vapour pressure. D has an energy unit (eV^{-2}) and is linked to the vaporization heat of the adsorbate [113] and is also called the "DR energy" (Dubinin-Radushkevich energy) [123].

The adsorption isotherms of H_2 on pyrex, stainless steel, and Cu plated stainless steel measured at CERN [124] are shown in Fig. 4.2. All three isotherms in this figure can be divided into three parts: a plateau area, where the isotherms reach the saturated vapour pressure, a cliff area where the isotherms have a steep rise, and, at lower pressure, the DRK region where the DRK equation is considered the best model to extrapolate the isotherms at pressures lower than $\sim 10^{-9}$ mbar.

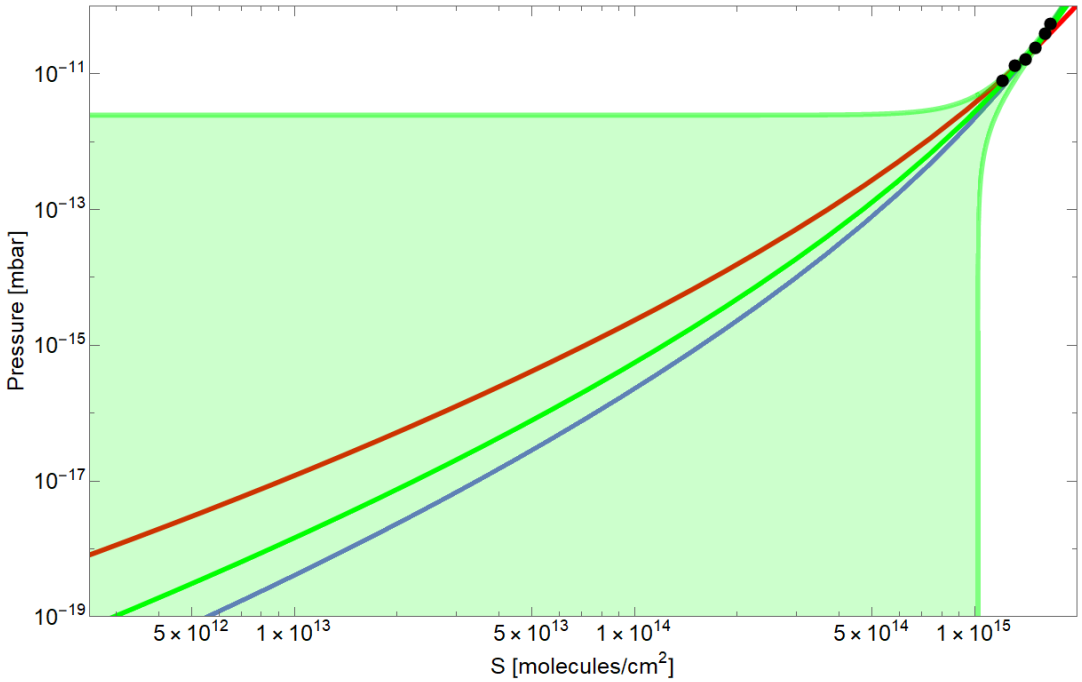

Figure 4.3: DRK model fit at 4.2 K of the last four points (red), five points (green) and six points (blue) from Fig. 4.2 for Cu plated stainless steel. The uncertainty band due to the extrapolation with the DRK model is shown by the green band.

In cryopumped XHV systems (below 10^{-12} mbar), hydrogen is typically the most dominant residual gas. For PUMA, we consider the H_2 isotherm data points measured at 4.2 K by Wallén [124] for Cu plated stainless steel and extrapolate the values to lower pressures. Data have been measured to 10^{-11} mbar and do not cover our XHV region of interest. To calculate the pressure P depending on the surface coverage S for the extrapolation, Eq. (4.4) can be reformulated as:

$$P = P_0 \cdot \exp\left[-\frac{\sqrt{-\ln\left(S/S_\mathrm{m}\right)}}{\sqrt{D}\cdot k_\mathrm{B}\cdot T}\right]. \tag{4.5}$$

The result of the extrapolation with Eq. (4.5) are pictured in Fig. 4.3 where fits considering the last four (red), last five (green) and last six points (blue) from Fig. 4.2 for Cu plated stainless steel are shown together with the uncertainty bands (light green area) coming from the fit with five points. Pictured is the confidence level of one standard deviation which leads to large uncertainties. Although the fits indicate a maximum of $\sim 3 \cdot 10^{13}$ molecules cm^{-2} on the cold surface of the trap electrodes and cryostat, the uncertainties are too large to be conclusive.

We therefore used instead data measured by Chill, Wilfert and Bozyk at GSI [112]. They measured H_2 adsorption isotherms in a temperature range between 7 K and 18 K. Their data (straight curves) are pictured in Fig. 4.4, where it is easily seen that all pressure measurements saturate below $P < 4 \cdot 10^{-10}$ mbar, showing limitations in the measurement. The high quality of the data allows to extrapolate an isotherm

at 4.2 K. A vapour pressure of $P_0 = 4.25 \times 10^{-7}$ mbar for H_2 was used [125], and an effective monolayer surface density $S_m = 6.45 \times 10^{14}\,cm^{-2}$ and $D = 1.29 \times 10^{41}\ J^{-2}$ (corresponding to $B = 3075\,eV^{-2}$) from reference [112] were used.

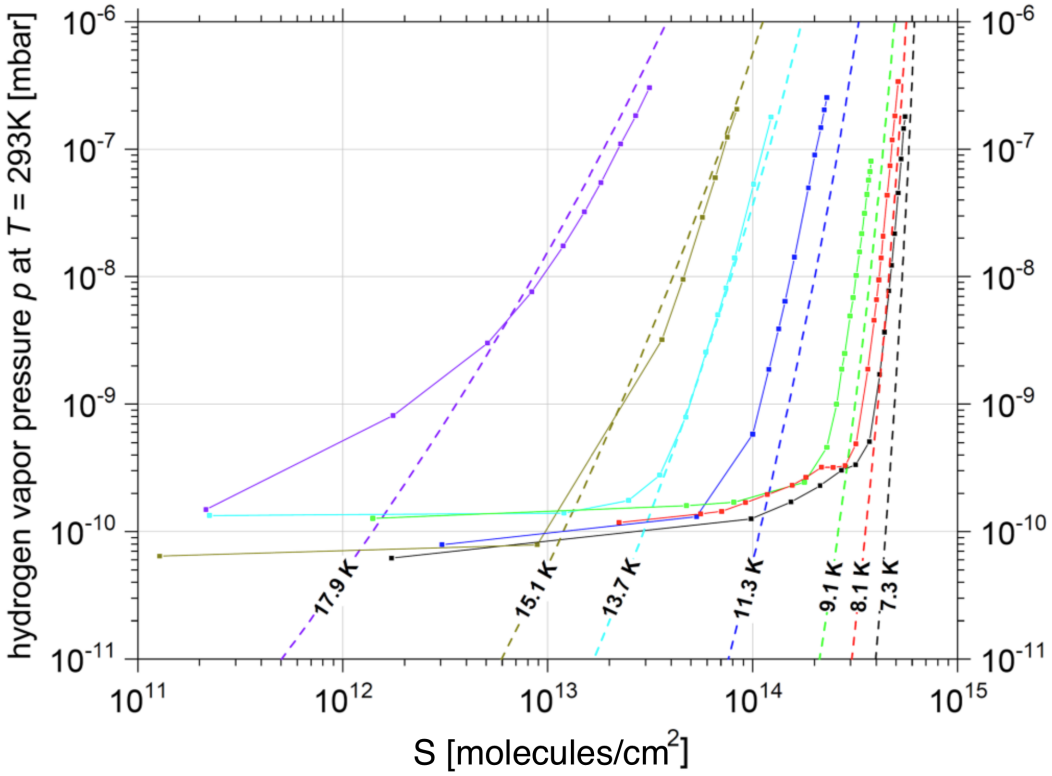

Figure 4.4: Measured adsorption isotherms of H_2 on an electropolished stainless steel surface for temperature 17.9 K, 15.1 K, 13.7 K, 11.3 K, 9.1 K, 8.1 K and 7.3 K (straight curves). The dashed curves are fitted theoretical isotherms calculated according to the DRK model. Figure from [112].

The extrapolation down to 10^{-17} mbar still generates large uncertainties which will lead to uncertainties in the lifetime of the antiproton plasma for a given cryostat geometry. It is therfore essential to measure the isotherms at lower pressure.

4.3 Initial conditions and outgassing

The phenomena of diffusion and outgassing are important throughout the pressure range we are operating in PUMA. Adsorbed particles, can migrate into a solid by skipping to interstitial sites or lattice defects or by moving along grain boundaries of crystallites. This effect is temperature dependent, because the particles require energy for every position change an activation energy E_{dif}. Diffusion is caused by a concentration gradient dn_{dis}/dx and features after Fick's fist law a particle flow rate

j_{dif}:

$$j_{\text{dif}} = -D\frac{\mathrm{d}n_{\text{dis}}}{\mathrm{d}x}. \tag{4.6}$$

Here, n_{dis} is the density of dissolved particles and x the path length. D is the so-called diffusion coefficient. The amount of absorbed gas particles can be much larger than the amount of adsorbed gas particles, because the number of sites available inside the solid is clearly much larger than on the surface of the solid [114]. During steel production a large amount of H_2 from the atmosphere dissolves in the steel [126]. This hydrogen in stainless-steel vacuum systems diffuses out and is the main source of residual gas in baked-out, ultra-high vacuum systems [114]. According to Kiuchi and McLellan [127], the hydrogen diffusion in steel can be expressed as a Arrhenius law following

$$D = D_0 \cdot \exp\left(-\frac{E_{\text{dif}}}{RT}\right) \tag{4.7}$$

where R denotes the ideal gas constant, T the temperature, with $D_0 = 7.3 \times 10^{-8}$ $\mathrm{m}^2 \cdot \mathrm{s}^{-1}$ and $E_{\text{diff}} = 5.69$ kJ/mol. According to Eq. (4.7), one gets $D \sim 10^{-40}$ $\mathrm{cm}^2 \cdot \mathrm{year}^{-1}$ for hydrogen in steel at 4 K. One can therefore legitimately consider that outgassing at 4 K is negligible. On the other hand, one may wonder what is the resulting surface coverage of the cryostat after the cooling phase.

In the following, we propose an order-of-magnitude estimate which shows that the residual gas present in the cryostat at the beginning of the cooling phase leads to a negligible contribution to the surface coverage. We assume the following cryostat conditions while cooling: a pressure of 10^{-7} mbar, volume $V = 5$ l, an effective inner surface $S = 0.5\,\mathrm{m}^2$. At equilibrium and considering the perfect gas relation, this pressure corresponds to an amount of molecules in the volume of

$$N = \frac{PV}{k_{\mathrm{B}}T} \sim 2 \times 10^{12}, \tag{4.8}$$

where $T = 300\,\mathrm{K}$, before cooling, is taken.

If one considers this amount of molecules to contribute uniformly to the surface of the cold surface when cooled to 4 K, one gets a surface density of 10^8 molecules per cm^2, very small compared to the value corresponding to 10^{-17} mbar, as extrapolated from the H_2 isotherm. We therefore conclude that the contribution of the initial residual gas molecules present in the cryostat before cooling is negligible for PUMA.

4.4 Simulations

The storage time of the antiprotons inside the trap is a function of the residual gas flow entering the cryostat and the cryo-pumping capacity of the trap. To limit the amount of residual gas molecules in the cryostat, a conductance pipe will be implemented. The dimensions of the conductance pipe are first considered to be

$L = 10\,\text{cm}$ (length) and $D = 1\,\text{cm}$ (diameter). These dimensions are not optimized yet and should be further tuned to the beam emittance at ISOLDE. For these dimensions the transmission probability α will be [128]

$$\alpha = \frac{1}{1 + \frac{3}{4} \cdot \frac{L}{D}} = 0.12 \approx 12\,\%. \tag{4.9}$$

We consider incoming molecules at $T = 300\,\text{K}$ at the entrance of the pipe. The rate of molecules J entering the conductance pipe from outside can be calculated as

$$J = \frac{P}{\sqrt{2\pi \cdot M \cdot k_\text{B} \cdot T}} \cdot S, \tag{4.10}$$

where k_B denotes the Boltzmann's constant, $M = 2 \cdot m_\text{p}$ the mass of the entering H_2 molecules, $S = \pi \cdot (D/2)^2$ the surface area of the entrance and $P = 10^{-11}\,\text{mbar}$ the pressure outside the cryostat. With the given values, the rate of molecules per unit area can be calculated as

$$\frac{J}{S} \approx 10^{14}\ \text{s}^{-1} \cdot \text{m}^{-2}. \tag{4.11}$$

By using the ideal gas law $PV = Nk_\text{B}T$ it is possible to calculate the particle generation rate Q at the entrance of the conduction pipe for the simulations which is comparable to a pressure of $10^{-11}\,\text{mbar}$ outside the cryostat. For the given values, Q can be calculated as

$$Q = \frac{J}{S} \cdot S \cdot k_\text{B} \cdot T = 3.48 \cdot 10^{-10}\ \frac{\text{mbar} \cdot \text{l}}{\text{s}} \tag{4.12}$$

This particle generation rate was used in the following simulations.

For a first rough estimate of the time necessary to reach a pressure of 10^{-17} mbar at equilibrium in the cryostat, we assume

- the residual gas molecules entering the cryostat are uniformly distributed over the inner surface,
- a sticking factor of unity for the molecules hitting the wall,
- an inner surface of 0.5 m^2 for the cryostat.

Under these assumptions, considering the above rate of incident particles of $\alpha J = 7.8 \times 10^9$ molecules per second and that 5×10^{14} molecules per cm^2 (extrapolated from the DRK model with the above-considered parameters from [112, 125]) correspond to an equilibrium pressure of $10^{-17}\,\text{mbar}$, one gets a time period of 10 years until $10^{-17}\,\text{mbar}$ is reached. This value is much larger than the PUMA core objective of 30 days.

Although this first estimate gives an indication that the PUMA concept for the vacuum is realistic, it is simplistic in several aspects and realistic simulations are therefore necessary. To estimate if the vacuum concept for PUMA can satisfy the requirements of the experiment, Monte Carlo simulations with Molflow+ [129, 130] and COMSOL Multiphysics [131] were performed.

4.4.1 Molflow+ Simulations

The Monte-Carlo software Molflow+ allows to calculate the pressure in a complex geometry when a molecular flow regime is met, i.e. when the mean free path of gas molecules is so long compared to the geometry size that collisions between the molecules can be neglected. In this case, the gas molecules fly independently, which makes this phenomena particularly suitable for Monte Carlo simulations. Desorption and reflection directions are generated in the same manner following the cosine law. The absorption on a surface is driven by a *sticking parameter* to be given as an input of the simulation.

Simulations with Molflow+ were performed to obtain the time at which the limit surface density corresponding to 10^{-17} mbar is reached, estimated from the H_2 isotherm extrapolation at 4 K. The Molflow simulations do not allow the inclusion of isotherms at varied time steps.

For the Molflow+ simulations a simplified geometry of the cryostat was used, pictured in Fig. 4.5. This cryostat is divided in three areas: The conductance pipe, the collision trap region and the storage trap region. All three parts in the simulation are simplified as cylinders with different diameters. The dimensions of the areas are not entirely fixed and depend on the results of the calculations and simulations which are ongoing.

To estimate the maximum lifetime of antiproton plasma in the cryostat the impingement rate given in $m^{-2} \cdot s^{-1}$ along the inner surface of the cryostat was computed. The lifetime is calculated by considering the highest value for the impingement rate in the whole cryostat. For the simulations, a sticking factor of 1, 0.9, 0.8 or 0.5 for collision and storage trap is used. At low surface coverage, a sticking factor of 0.5 is expected [132]. The sticking factor in the conductance pipe was taken as zero, assuming that the walls of the pipe would saturate very fast and a strong drop of the sticking factor in this region is expected soon after the start of operations.

A temperature of 4 K for the cryostat, and a particle generation rate at the entrance of the conductance pipe of 3.48×10^{10} mbar $\cdot$ l $\cdot$ s^{-1}, comparable to a pressure of 10^{-11} mbar at the entrance of the cryostat, has been implemented. The simulations computed the maximum time in days until the number of molecules equivalent to a pressure of 10^{-17} mbar and 10^{-18} mbar cover the surface. In Fig. 4.6 the impingement rate as a function of position in the collision area is pictured. The incoming particles enter the collision area from the left hand side. The highest impingement rate is measured at $x = 20$ mm (9×10^{10} $cm^{-2} \cdot s^{-1}$), which was expected for the simulated conditions: incoming particles with a uniform momentum distribution from the conductance pipe with a sticking factor of zero, enter the collision region and hit the walls very close to its entrance, which has a sticking factor of one. First results are given in Tab. 4.2.

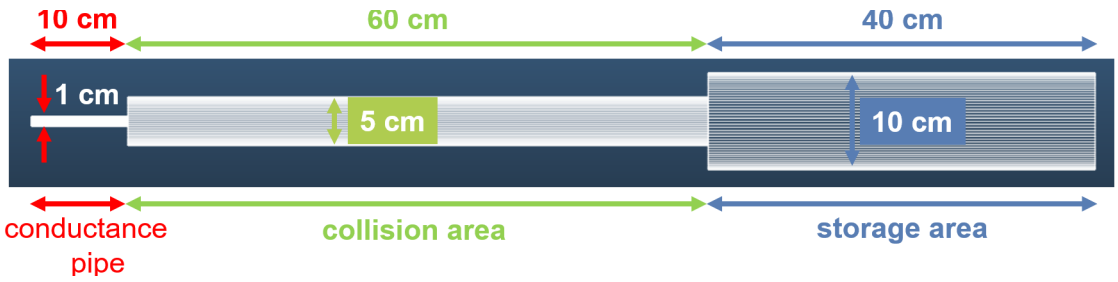

Figure 4.5: Dimensions of the cryostat which were used for Molflow+ simulations.

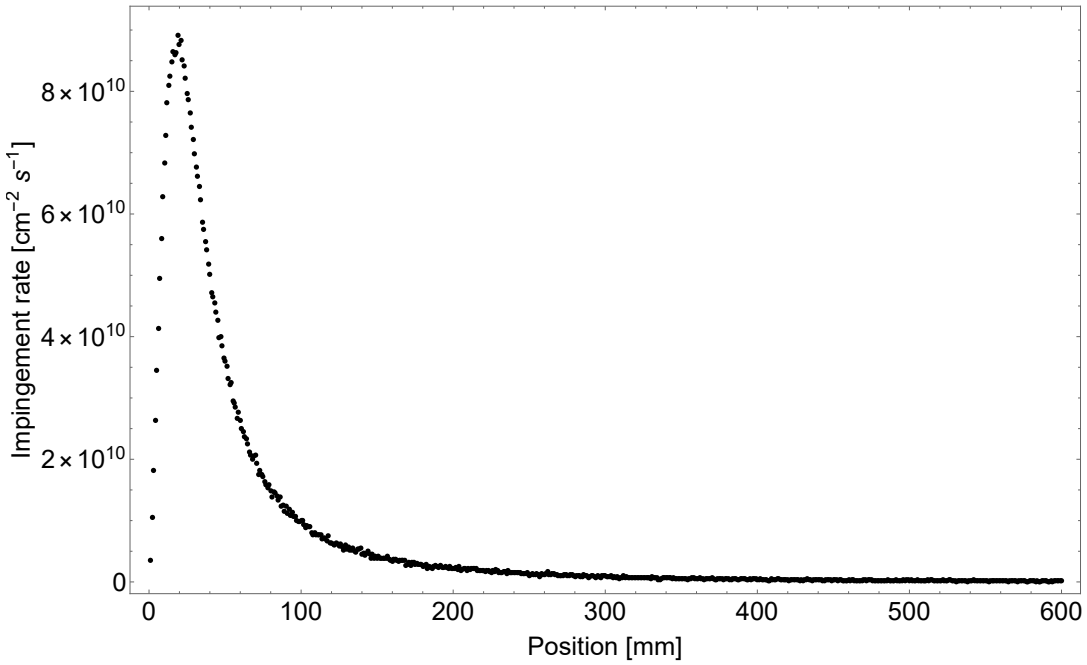

Figure 4.6: Impingement rate as a function of position in the collision area (x = 0 mm corresponds to the exit of the conductance pipe). Particles enter from the left hand side with sticking factor unity for collision trap.

	Sticking factors	Max. imping. rate ($cm^{-2} \cdot s^{-1}$)	Max. time (days) 10^{-17} mbar	Max. time (days) 10^{-18} mbar
Cylindrical conductance pipe, no electrodes	0-1-1	$9 \cdot 10^6$	635	603
	0-0.9-0.9	$8 \cdot 10^6$	716	681
	0-0.8-0.8	$8 \cdot 10^6$	722	685
	0-0.5-0.5	$8 \cdot 10^6$	847	804

Table 4.2: Molflow+ simulations of the maximum impingement rate on the cold surface of the cryostat and of the time period for which vacua of 10^{-18} mbar and 10^{-17} mbar can be maintained with a trap geometry as shown in Fig. 4.5. Sticking Factors are given in the order of Conductance Pipe - Collision Area - Storage Area.

Conductance pipe with sawtooth structure

To minimize the number of incoming particle a so-called "sawtooth structure" will be installed in the conductance pipe. The idea is that incoming particles impinging on the structured surface of the pipe will have an anisotropic emission angle towards the entrance caused by the surface structure. A sketch of the considered sawtooth structure is shown in Fig. 4.7. The final shape of the structure itself is not yet optimized. Results for the simulations with the sawtooth structure a given in Tab. 4.3.

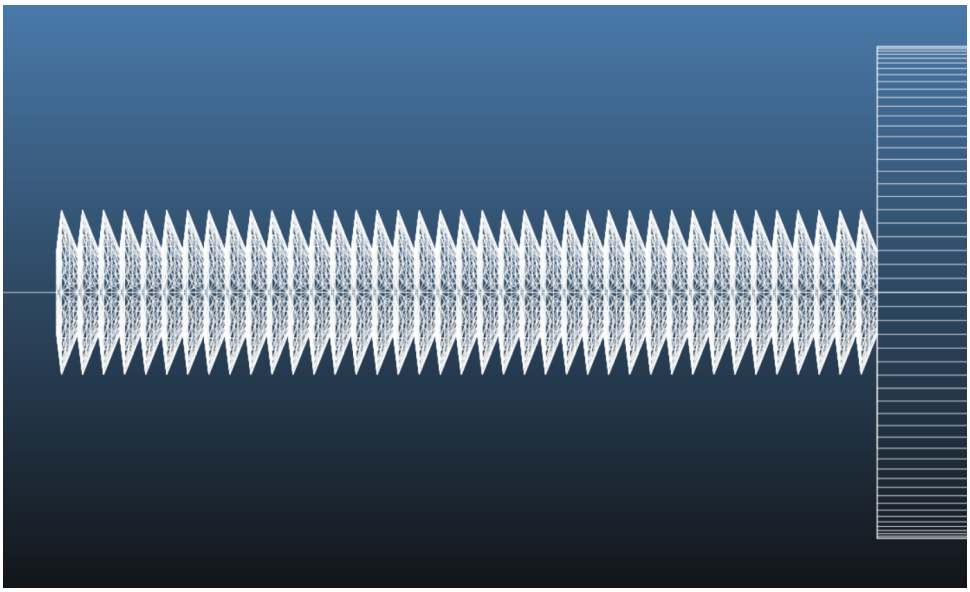

Figure 4.7: Shape of the sawtooth structure at the conductance pipe. The inner diameter of the conductance pipe is still 1 cm and is not changed by the sawtooth structure.

Cryostat and electrodes

The same simulations are made with the electrodes inside the cryostat. For further details of the electrodes inside the cryostat see Chapter 6. Here we give just a short overview of the dimensions of the electrodes we used in the simulations.

The length of the electrodes in the collision area (see Fig. 4.8) is 458 mm with an inner radius of 20 mm and an outer radius of 30 mm. In the storage area the electrodes have a length of 543 mm and an inner radius of 40 mm and an outer radius of 50 mm. The dimensions of the cryostat are slightly different from previous simulations. The collision area is 660 mm long with a diameter of 60 mm, the storage area is 540 mm with a diameter of 120 mm. The dimensions of the conductance pipe remain unchanged. Simulations show that the different sizes of the two cryostats

Geometry	Sticking factors	Max. imping. rate ($cm^{-2} \cdot s^{-1}$)	Max. time (days) 10^{-17} mbar	Max. time (days) 10^{-18} mbar
Electrodes	0-1-1	$3 \cdot 10^7$	192	182
Sawtooth, electrodes	0-1-1	$1 \cdot 10^7$	482	458
	0-0.9-0.9	$1 \cdot 10^7$	479	455
	0-0.8-0.8	$9 \cdot 10^6$	542	515
	0-0.5-0.5	$9 \cdot 10^6$	611	580

Table 4.3: Molflow+ simulations of the maximum impingement rate on the cold surface of the trap electrodes and of the time period for which vacua of 10^{-17} mbar and 10^{-18} mbar can be maintained with a trap geometry as shown in Fig. 4.8. Simulations with a cylindrical conductance pipe and a sawtooth-structure conductance pipe (see text) are compared.

have just marginal effects on the results and can be neglected. Table 4.3 shows the results of the simulations with the electrodes inside the trap.

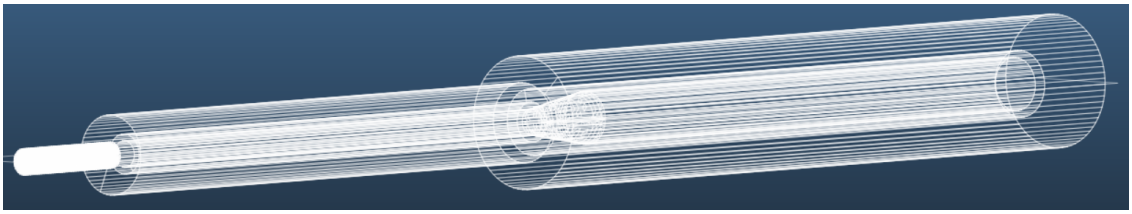

Figure 4.8: Electrodes inside the cryostat. The size of the cryostat is negligible bigger than without the electrodes.

Results and discussion

The peak of impingement values for all simulations were near the entrance of collision area. In simulations with electrodes inside the cryostat, the highest impingement rate is on the inner part of the electrodes, on the side closer to the particles entrance. In the cases without electrodes, the highest value is on the inside of the cylinder of the collision area.

Table 4.2 shows the result of the simulations with the cylindrical normal conductance pipe and without any electrodes and Table 4.3 shows the results with the electrodes inside the trap and the sawtooth structure at the conductance pipe. In both cases we variegate the sticking factor between 0.5 and 1 at the collision and storage trap.

- The PUMA concept can achieve a 10^{-17} mbar for nearly 200 days under the assumption of the isotherm extrapolation from available data [112]. This is

the case with the electrodes inside the trap, but no sawtooth structure at the conductance pipe.

- The sawtooth structure of the conductance-reduction pipe allows to double the time until a pressure of 10^{-17} mbar is reached.
- The inclusion of the electrodes inside the cryostat lowers significantly the time at which the limit molecular surface density is reached.
- The influence of the sticking factor for the electrodes and cryostat is rather big (up to more than 100 days) when values from 0.5 to 1 are considered (in the Molflow simulations).

Our main conclusion at this stage is that the requirements for PUMA are achievable with the proposed concept and no additional features, but the uncertainties are large, in particular on the isotherm extrapolation. It is essential to reduce the uncertainties by measuring isotherms at lower pressures (see also section 4.7.1). It should be stressed that the values were calculated for the highest impingement rate, which describes the worst-case scenario. These maximum values appear only on one single spot at the wall of the trap. The impingement rate is lower in the rest of the volume which implies a lower density and a longer time until coverage is reached.

As it will be detailed later, other features could be added to PUMA (cold gate valve, carbon layer inside the cryostat) which will contribute maintaining a vacuum lower than 10^{-17} mbar for longer period of time. The above calculations do not consider the isotherm and evolution of pressure with surface density as time evolves. This cannot be done with Molflow+ but with COMSOL Multiphysics, presented in the following section.

4.4.2 COMSOL Multiphysics simulations

The following COMSOL Multiphysics simulations take into account the DRK isotherm $\ln\theta = -(T/T_0 \ln(P/P_0))^2$ and evolution of pressure with surface density as time evolves. The isotherm was used under the approximation of quasi-static equilibrium was used

$$\left|\frac{1}{P}\frac{\partial P}{\partial t}\right| \ll s\frac{A}{V}\frac{\bar{v}}{4}, \tag{4.13}$$

where $\bar{v}$ is the mean velocity of the gas molecules in the system, s the sticking probability, A the surface of the cryostat, and V its volume [133]. The relationship between the pressure P and the surface coverage Θ is given by the adsorption isotherm. The application of this isotherm is reasonable if adsorption and desorption rates are in equilibrium. Therefore rapid changes in pressure and temperature should be avoided [114].

The dimension of the cryostat used for the simulations are slightly different from Molflow+ simulations. For the conductance pipe a diameter of 1 cm and a length of 10 cm were used and for the trap the diameter was 5 cm and the length was 100 cm.

The sticking factor was set to s = 1, and the pressure at the entrance of the conductance pipe was considered to be $P = 10^{-10}$ mbar and $P = 10^{-11}$ mbar at 300 K. Also, no beaming effect was considered at the entrance of the conductance pipe, but an isotropic distribution as it was done in the Molflow+ simulations.

The limits of the lifetime of the antiproton plasma corresponding to $n_{\text{gas}} = 20\,\text{cm}^{-3}$ (one year of lifetime; blue line) and $n_{\text{gas}} = 200$ cm^{-3} (one month of lifetime; orange line) (calculated in section 4) are shown in Fig. 4.9 where the plots show the dependence of the density and the z-coordinate of the cryostat for different time steps (1, 30, 100 and 365 days). The density is pictured at $z < 0.1$ m for the conductance pipe and at $z > 0.1$ m for the trap. Note that close to the entrance of the trap no particles can geometrically reach the wall, therefore no density can be calculated for this region.

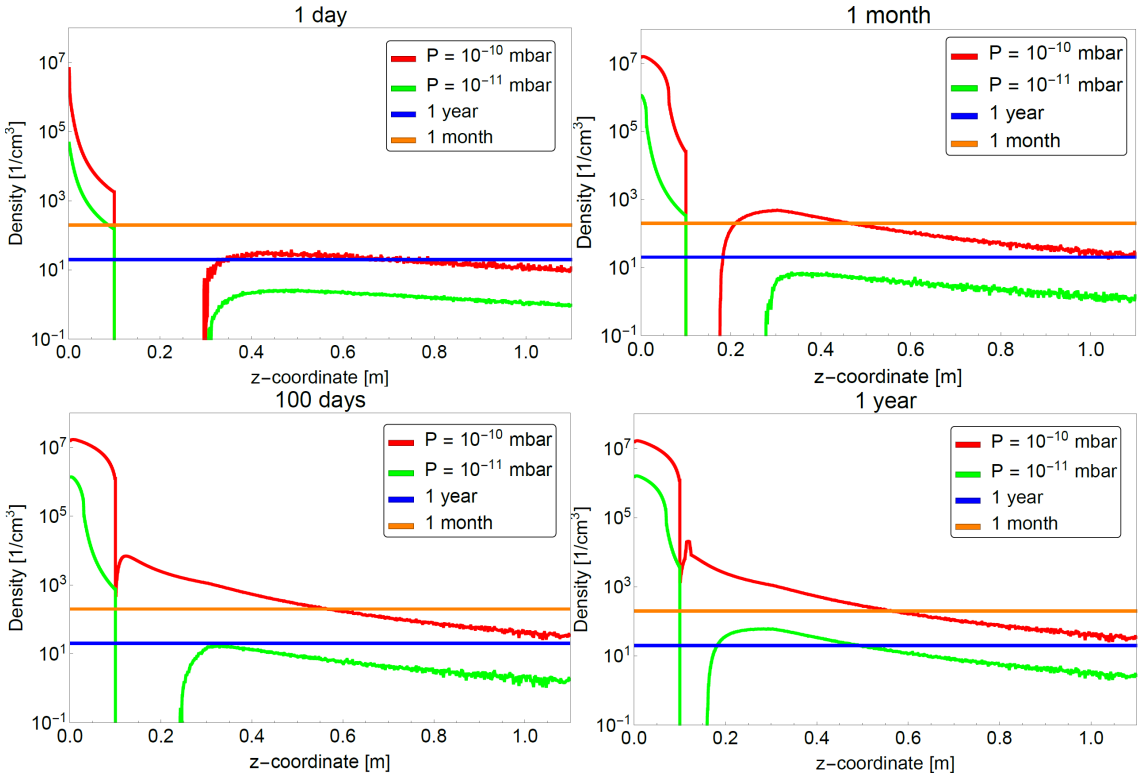

Figure 4.9: COMSOL Multiphysics Simulations of the residual hydrogen gas density along the trap axis at $T = 4.2\,\text{K}$, different pressures (10^{-10} mbar and 10^{-11} mbar) at the entrance of the cryostat and for different time steps: after one day (top left), one month (top right), one hundred days (bottom left) and one year (bottom right).

- With $P = 10^{-11}$ mbar and no beaming effect (isotropic distribution), the PUMA requirements are satisfied in the collision and storage trap at least for more than one month.

- At all four time steps in the simulation it is possible to store the antiproton plasma in the collision and storage trap for one year with $P = 10^{-11}$ mbar and for longer than a year in the storage trap alone.

These points imply that the requirements for PUMA are achievable with the described concept. Note that no electrodes were included, which will decrease the maximum storage time, as the Molflow+ simulations show. The results from COMSOL are in qualitative agreement with those obtained with Molfow. In addition no surface treatment and no "satwooth structure" were implemented at the conduction pipe. Both will increase the maximum lifetime.

4.5 Cryogenic gate

We will develop a cold gate valve to be positioned at the entrance of the conductance pipe to reduce strongly the conductance in the absence of beam. An artistic view of the gate valve, under design, is shown in Fig. 4.10.

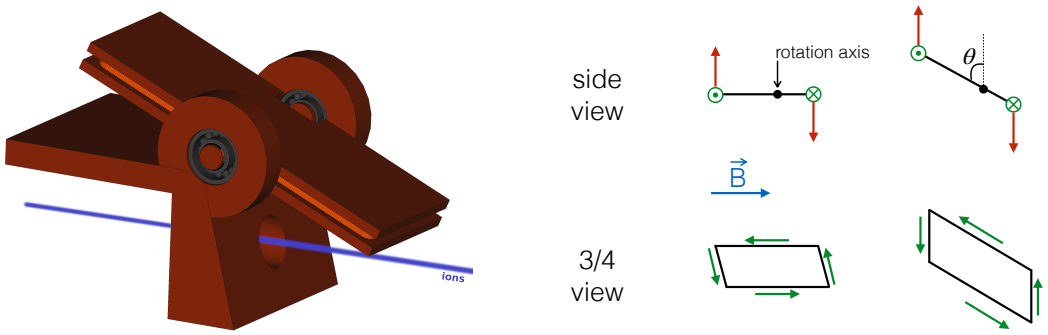

Figure 4.10: (Left) Three-dimension view of the cryogenic gate valve to be placed in front of the 4-K cryostat. (Right) Lorentz forces (red arrows) from the action of a magnetic field on a current loop (green arrows).

The opening and closing of the gate will be driven by a current loop inside the magnetic field of the magnet. The Lorentz force acting on the current loop will create a torque which will be used to open and close the gate. An illustration is given in the right panel of Fig. 4.10. The concept allows in principle a fast opening and closing (less than a second) of the valve with minimum heat losses, compared to a mechanical valve.

We quantify here the kinematics of the gate operation. We consider a rectangular loop of current I. The rectangle has an area $2A$. The torque τ created by a magnetic field B around the axis of the gate as sketched in Fig. 4.10 is given by

$$\tau = IAB\sin(\theta), \tag{4.14}$$

where θ is the inclination angle of the gate as shown in Fig. 4.10. We are considering a cold gate valve normally closed when there is no current in the loop and open when a current is applied. Once the current is switched off, the closing of the gate naturally takes place through gravity when the rotation axis is off-centered as illustrated in Fig. 4.10. First estimates for a copper gate of dimensions $(60 \times 25 \times 3)\,\mathrm{mm}^3$ and a weight of 15 g give a typical opening time of 200 ms for a 1 A current. The closing time from gravity is estimated to $\sim$ 500 ms. It can be speed up by inverting the current in the loop. The current loop will be built out of a superconducting NbTi wire and several turns will be used so that a current of 100 mA can be used. The superconducting wire will be cooled from the thermal contact with the 4 K cryostat. Ceramic bearings that can operate at cryogenic temperature will be used. The gate valve is currently under design and a prototype will be built at TU Darmstadt.

4.6 Vacuum environment

4.6.1 Beam vacuum at ELENA

According to the current status, the pressure in the transfer line LNE51 is expected around 10^{-10} mbar. The main limitation on the vacuum in the PUMA experiment at ELENA will come from from (i) the pulsed drift tube chamber (hereafter denoted PDT chamber, see Chapter 8 for details about the principle and electrode design) and (ii) the ion source of PUMA to be used for stable-nuclei annihilation measurements. The pumping systems will be designed accordingly to satisfy the 10^{-11} mbar vacuum requirement at the entrance of the PUMA trap. The option to use NEG coating over the entire surface of the PDT chamber will be considered.

The preliminary design of the PDT chamber is based on a standard DN250CF with length $L = 1.335$ m made of stainless steel. A preliminary design of its integration with electrodes and vacuum components, based on the design of the PDT built for the GBAR experiment, is shown in Fig. 4.11.

An ion source will be installed in the PUMA experimental zone. The vacuum at the nozzle of the source is 10^{-7} mbar. The source will be connected to a traps for bunching and mass selection. The ensemble will be separated from PUMA by a differential pumping section, similar to the one to be developed for ISOLDE (see next section). A vacuum better than 10^{-11} mbar at the entrance of PUMA will be guaranteed.

4.6.2 Vacuum at ISOLDE

The vacuum level in the ISOLDE transfer line is known to be around 10^{-6} mbar. Such pressure is obviously not compatible with the extreme high vacuum requirements (10^{-11} mbar) at the entrance of the PUMA trap. Although the design of the ISOLDE beamline is under discussion, it is foreseen that several devices will be

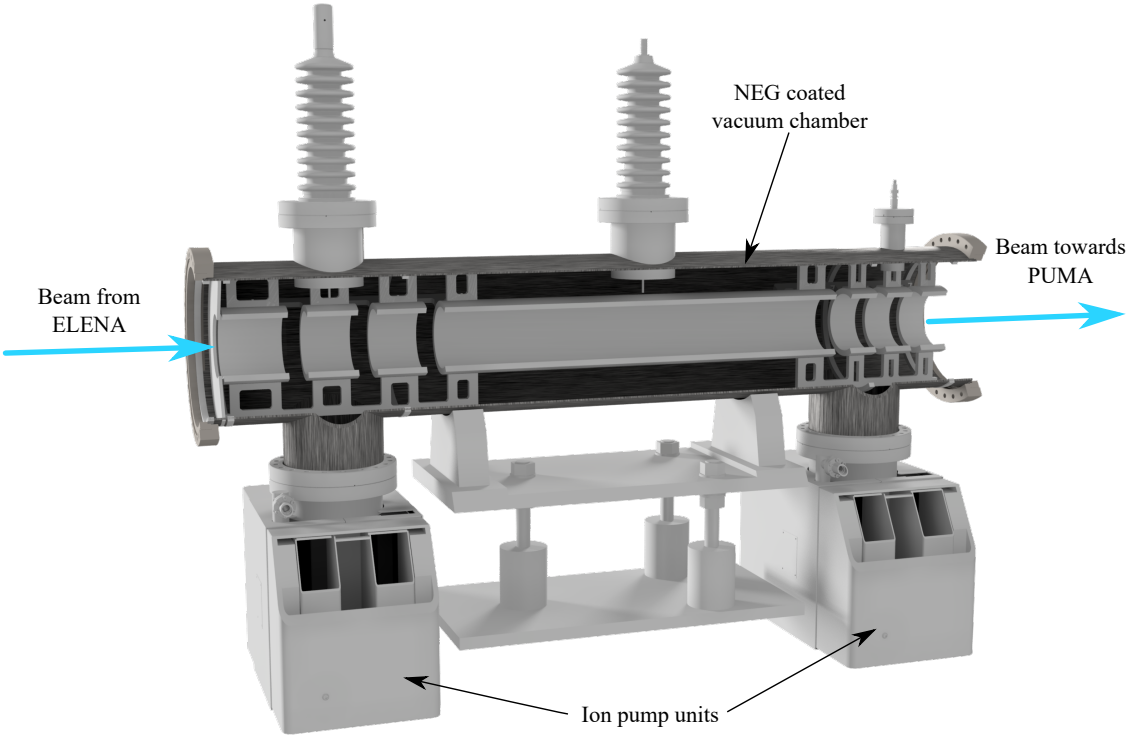

Figure 4.11: Preliminary design of the Pulsed Drift Tube chamber.

placed between the ISCOOL cooler and PUMA (see Section 10.2), in particular a 30 kV MR-TOF system for beam purification and improvement of emittance properties. These devices, because of their own requirements in terms of vacuum, will lead to a vacuum better than 10^{-7} mbar in front of PUMA. We therefore propose to implement a dedicated differential vacuum isolation system to limit the impact of residual gas on the trap vacuum quality. The system is mainly based on a differential pumping stage made of three successive sections separated by conductance reducers. A careful selection of the length and diameter of the conductance reducers leads to evaluate the pressure in the final cavity to few 10^{-10} mbar without considering the pumping equipment at the entrance of the trap. Preliminary studies show that this emerging concept could be improved to reach 10^{-11} mbar pressure in the last chamber considering the possibility to use NEG coating in the intermediate section as exposed in Figure-4.12. Outgassing, not implemented in the above estimates, should be considered with care in the final design of the differential pumping section.

Similarly to the pulsed ion source, neutral elements are generated by in-flight interactions with residual gas in the transfer lines at ISOLDE. This later could reduce the lifetime of the antiproton plasma inside the PUMA trap and impact the vacuum quality. Operations of the PUMA trap in direct sight with the ISOLDE transfer lines is then not a solution. In addition to the differential pumping scheme, we propose to develop an asymmetric differential pumping device where both input and output reducers are not aligned to avoid direct transport of the neutrals through

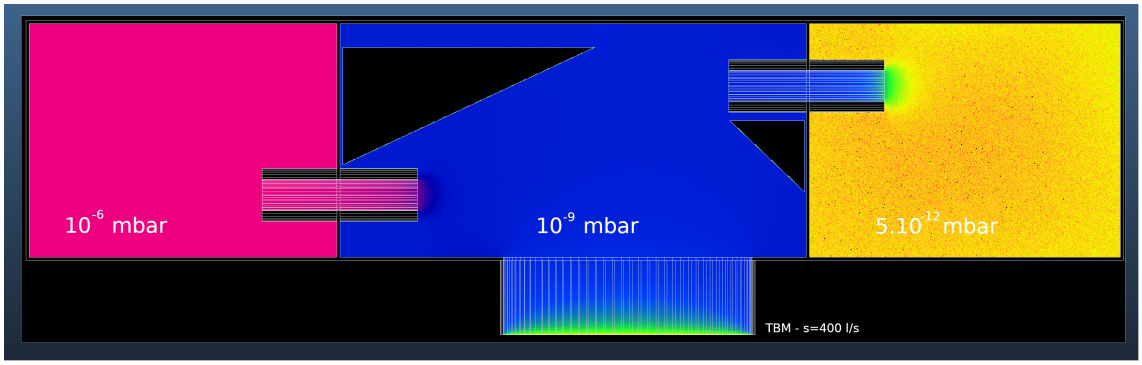

Figure 4.12: Molflow+ simulation of the ISOLDE vacuum separation. The black triangles represent reflectors limiting direct reflection of re-emitted gas through the conductance reducers. Outgassing of materials in the chamber is not taken into account in the simulation.

the chambers. Such device is composed of two electrostatic deflectors as presented on Fig. 4.13. The first deflector deviates the charged particle from the neutrals. Neutrals are then dumped in the back part of the chamber close to the pumping elements of the chamber. In the meantime, the ions of interest are guided through the exit conductance reducer by a second deflector.

4.7 Foreseen developments

In the following, we give the developments to be performed to enable adequate vacuum conditions for PUMA.

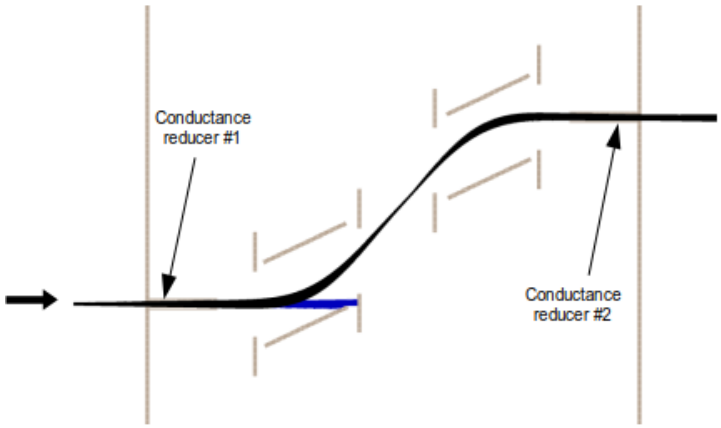

Figure 4.13: Preliminary SIMION simulation of the deflecting system in the vacuum separation. The black trajectories correspond to the ion of interest and the blue trajectories correspond to neutrals. On both side of the simulation, the conductance reducers are simulated to study the transmission through them.

4.7.1 Measurements of the Isotherms

A large uncertainty in the predictions for the PUMA vacuum lies in the extrapolation of the H_2 isotherm at 4 K. To reduce these uncertainties, we aim at the following:

- measure the H_2 and He isotherms from 10^{-8} mbar to 10^{-13} mbar (or better, if achievable) on stainless steel,
- extend the measurements to copper, gold plated copper and copper covered by a layer of carbon (see section 4.7.2),
- measure isotherms with high precision at higher temperature (10 K) for a better extraction of the isotherm fitting parameters.

These measurements will be performed at CERN where an isotherm measurement setup and a gauge (down to 10^{-14} mbar) are available together with the necessary expertise.

4.7.2 Surface treatment

A ~ 100 nm carbon layer, a technique mastered at CERN, inside the cryostat would increase the effective surface for cryo-pumping. At least an improvement of factor 10 for cryosorption could be expected after the process. A similar surface treatment could be applied to the ~ 60 K shield.

4.7.3 Cryogenic gate

Realistic simulations for the cold gate valve remain to be done. The system should then be developed and tested in different conditions. First tests should be made at room temperature and ambient pressure followed by tests at lower temperatures and pressures, until working conditions are reached. The evolution of the vacuum during the operation of the gate valve (opening and closing) will be studied in details.

4.7.4 Differential Pumping System

A differential pumping system to separate the vacuum from ELENA and (most importantly) from ISOLDE to PUMA has to be further designed and developed.

4.7.5 Simulations

Simulations have to be extended to realistic geometries and to the full vacuum system (not only the cryostat) to characterize consistently and realistically the residual gas density inside the trap. The following aspects should be implemented:

- COMSOL Multiphysics simulations with electrodes inside the cryostat and the "sawtooth structure" at the conductance pipe,

- inclusion of the $\sim 60\,\mathrm{K}$ shielding, mechanics geometry, realistic temperature conditions, and differential vacuum system in the simulations,
- realistic Molflow+ simulations,
- optimization of cryostat design.

4.7.6 Vibrations and Shocks

An unknown of PUMA remains the desorption due to vibrations and shocks. Especially during the transport from ELENA to ISOLDE vibrations and shocks cannot be prevented. Because PUMA will be the first project where a cryostat with extremely high vacuum will be transported on a truck, a specific study will be performed along the following steps:

- measure the frequency spectrum encountered by the trap during the transfer from ELENA to ISOLDE,
- design and perform a series of measurements of vacuum degradation as a function of vibration frequency and amplitude in the relevant range,
- develop a model for vibration-induced desorption.

Chapter 5

The solenoid

5.1 Magnetic Design

5.1.1 Requirements on the magnetic field

The cylindrical Penning trap is a key component for PUMA to trap antiprotons and ions. Charged particles in the trap are confined axially by electrostatic potentials, and radially by a strong magnetic field. The magnetic field is provided by a superconducting solenoid, which will be further detailed in this section. The solenoid will create a homogeneous magnetic field of 4 Tesla along 900 mm in a 280-mm diameter horizontal warm bore with active shielding to reduce the stray field outside the magnet. The dimensions are dictated by the requirements for a good tracking efficiency for pions (see Chapter 7) and the two-trap geometry. Furthermore a passive shield is required to comply with the safety regulation during the transportation. Bilfinger Noell was contracted in December 2018 to build the solenoid. This section summarizes the main results from the optimization of the PUMA solenoid design with both a superconducting active shield and a passive shield. Requirements on the magnetic field provided by the solenoid are summarized in Tab. 5.1. Field homogeneity constraints of less than 0.2 % at each trapping region (cylindrical volume 1 and 2) and less than 5 % at overall volume (cylindrical volume 3) are set. The constraint on the stray field was set to be below 2×10^{-4} T at three meters away from the center both axially and radially to satisfy the safety regulations during transportation and handling of magnet. The constraints are also useful in the experimental area not to interfere with surrounding devices and other experiments. A functional design report for the PUMA magnet has been released in March 2019 [134] and the magnet is currently under construction. The delivery to TU Darmstadt is expected in May 2020.

5.1.2 Coil design

The PUMA magnet system was first optimized without the passive shield to determine the coil layout and to estimate the coil parameters to create the trapping volumes according to the requirements. Important physical parameters such as ho-

Requirements	Values
Nominal field strength of the magnet	4.0 T
Field stability	better than 10^{-4} in time
Field homogeneity in cylindrical volume 1[1]	$\lvert B - B_0\rvert/B_0 < 0.2\,\%$
Field homogeneity in cylindrical volume 2[2]	$\lvert B - B_0\rvert/B_0 < 0.2\,\%$
Field homogeneity in cylindrical volume 3[3]	$\lvert B - B_0\rvert/B_0 < 5\,\%$
Axial stray field 3 m from center	less than 0.2 mT
Radial stray field 3 m from center	less than 0.2 mT

[1] Volume 1: length of (-450, -100 mm) along the axis and diameter of 50 mm
[2] Volume 2: length of (+100, +500 mm) along the axis and diameter of 50 mm
[3] Volume 3: length of (-500, +500 mm) along the axis and diameter of 220 mm
In this table the origin is the center of the solenoid, and the axis is the solenoid axis.

Table 5.1: The requirements for a solenoid.

mogeneity of the magnetic field, load lines, conductor type and length, stray field, inductance and stored energy are considered during the optimization. Subsequently, the dimensions of the passive shield are optimized to minimize the total weight, while avoiding the saturation and keeping the shielding effect. The parameters such as shielding length, thicknesses of the cylinder and end plates were considered. Finally the coil configurations are optimized again together with the passive shield to meet all the requirements. The optimization was performed by N. Marsic, W. Müller and H. de Gersem at the Institute for Accelerator Science and Electromagnetic Fields (TEMF) of TU Darmstadt [135].

5.1.3 Magnetic field without passive shield

The solenoid consists of seven coils made of NbTi superconducting wire: a main coil, a pair of booster coils, a pair of active shielding coils and a pair of shim coils. The current density in all coils will be 125 A.mm^{-2}. All the coils have the same operation current to share a single power supply and to share one pair of current leads. The magnetic field obtained by the simulation is plotted in Fig. 5.1. The field strength along center axis is plotted in red solid line, cylindrical surface of diameter 25 mm in blue solid line, and cylindrical surface of diameter 110 mm in brown solid line. According to simulations the homogeneity $|B - B_0|/B_0$ within volume 1 and 2 is 0.087 % which is less than half of the required 0.2 %. The homogeneity $|B - B_0|/B_0$ within volume 3 is 2.37 % which is also less than half of the required 5 %. Concerning the impact of the stray field on the surrounding area, the 0.2 mT line is roughly at a radius of 3 m, and the 5 mT line is at a radius of 1.5 m.

5.1.4 Magnetic field with a passive shield

The passive shields consist of a cylinder and two end plates with 20 mm thickness. A ring with 20 mm thickness and 500 mm length is arranged outside the middle surface of the outer cylinder. A ring with 30 mm thickness and 200 mm width is added

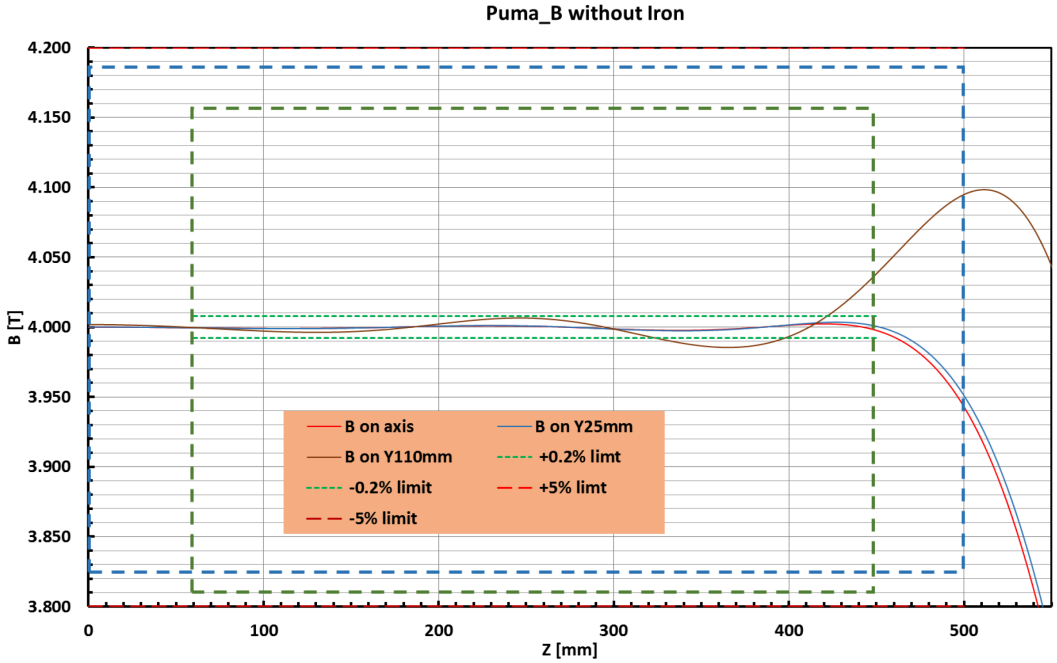

Figure 5.1: The magnetic field distribution in z-direction without a passive shield. In this figure the field lines are plotted from the center of the solenoid (Z = 0 mm) towards the end of solenoid (Z = 500 mm) since the simulation is symmetric around the center.

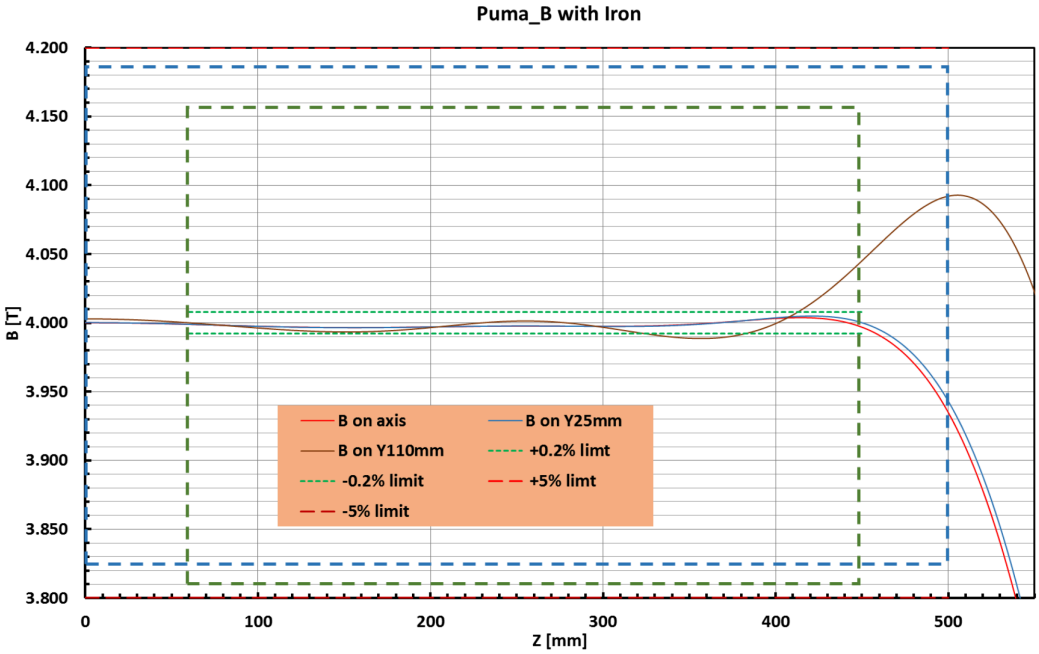

Figure 5.2: The magnetic field distribution in z-direction including a passive shield. In this figure the field lines are plotted from the center of the solenoid (Z = 0 mm) towards the end of solenoid (Z = 500 mm) since the simulation is symmetric around the center.

to each end plate to avoid saturation. The total weight of the presented passive shield is 1950 kg. 1010 steel is used for the designing of the passive shield. The magnetic field obtained by the simulation is plotted in Fig. 5.2. The field strength along center axis is plotted in red solid line, cylindrical surface of diameter 25 mm in blue solid line, and cylindrical surface of diameter 110 mm in brown solid line. According to simulations the homogeneity $|B - B_0|/B_0$ within the volume 1 and 2 is 0.122 % and $|B - B_0|/B_0$ within the volume 3 is 2.3 %. Which is only a slight deterioration of the homogeneity of the initial field without passive shielding and is still well within the requirements. The stray field of PUMA including the passive shield is shown in Fig. 5.3. The 0.3 mT line is about 1.8 m along the z-axis and about 1.1 m along the radial direction, it is indicated by a blue line in Fig. 5.3. The 0.5 mT line is just outside the cryostat along the radial direction, and about 1.25 m along the axial direction, as indicated in red in Fig. 5.3.

5.1.5 Power supply and quench detector

A power supply for the coils will be provided by an external company. The requirements on the power supply are summarized in Tab. 5.2. The coils are protected by cold diodes. In total, 6 sub-circuits divide the coil arrangement into sections

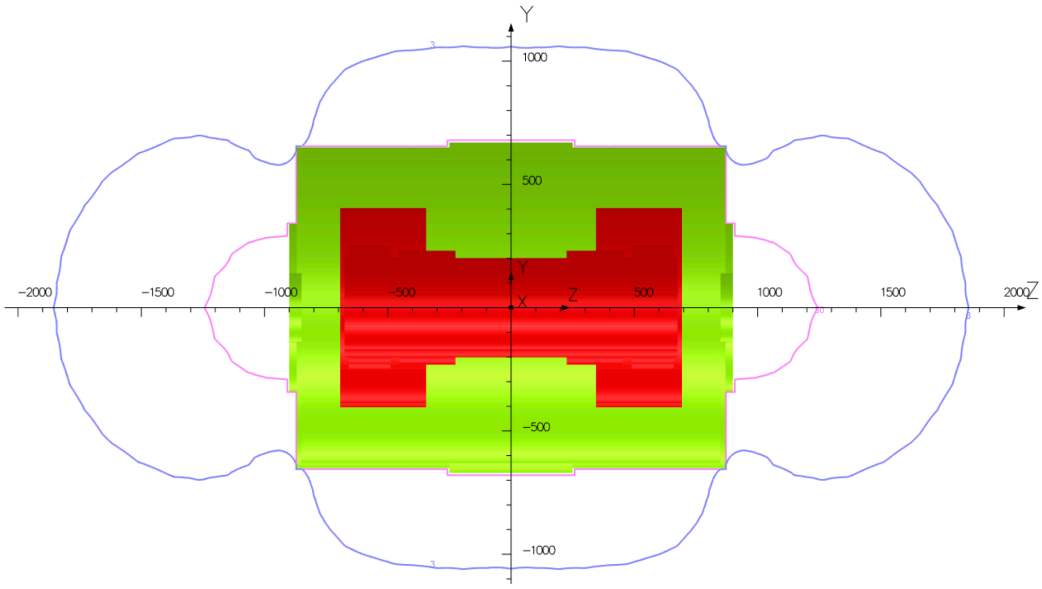

Figure 5.3: The stray field of the magnet arrangement including both the active and passive shield. The blue line indicates the 0.3 mT (3 Gauss) limit and the pink line indicates the 5 mT limit. Distances are given in mm.

with reduced voltage during quenching. A quench detector monitors the voltages across the coils. The quench detector has two independent circuits being connected to different parts of the coil arrangement. After detecting a voltage imbalance due to resistive voltage drop caused by a quench, the quench detector triggers a quench heater power supply to instantaneously fire quench heaters which are attached to the coils. The quench heater power supply contains capacitors to enable high heating power for the quench heaters with a very moderate power drawn from the grid.

Requirements	Values
Output type	DC
Operation mode	Constant current
Minimum output voltage	±5 V at terminal clamp
Output current	0 to +200 A with 0.01 A resolution
Output power	1000 W
Ramp rate	0 to ±50 mA/s with 0.5 mA resolution

Table 5.2: Requirements of the power supply for powering the magnet.

5.1.6 Magnetic field measurement

After reception of the solenoid at TU Darmstadt, we plan to measure the magnetic field and its homogeneity using a Hall and a NMR probe depending of the applicable field gradient. A test-bench with a motor driven carriage will be used to carry out the measurement. Hall probes can be placed on the central axis of the magnet or at

a radial offset from the center on the carriage. The measurement system will allow a linear scan and data acquisition with adjustable step size.

5.2 Mechanical design

5.2.1 Cryostat design

The cryostat is a horizontal bore vacuum vessel, housing the cold mass and the thermal radiation shield. The outer cylinder wall as well as the end plates of the vacuum vessel are made from soft magnetic steel. The bore tube is nonmagnetic and made from aluminum. The warm bore tube has an inner diameter of 280 mm, the cryostat flanges have an outer diameter of 1400 mm. The total length of the cryostat is 1800 mm. The exterior of the cryostat is presented in Fig. 5.4. The weight of the completed cryostat is about 4000 kg. The cold mass is suspended from the vacuum vessel by titanium tie rods. The suspension system is designed such that there is no radial shift of the cold mass between warm and cold conditions despite the thermal dilatation of both the cold mass and the tie rods.

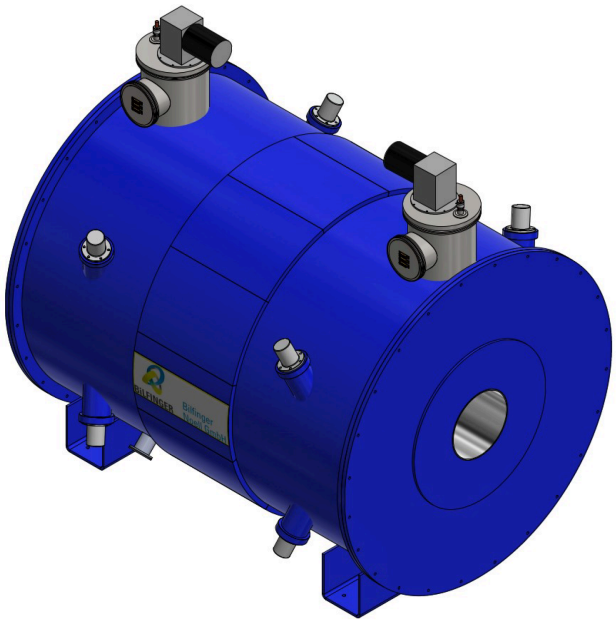

Figure 5.4: CAD representation of the cryostat design.

5.2.2 Thermal shielding

The cryostat has a thermal shield made from aluminum that intercepts all heat sources between the warm cryostat wall and the cold mass. The shield is thermally anchored to the first stage of the cryocoolers at around 50 K.

5.2.3 Insulation vacuum

The turbo molecular vacuum pump for the insulation vacuum is mounted to the cryostat on the lower side. The turbo molecular pump has a rotary vane pump as roughing pump. As such cryostats are not regularly and continuously pumped, the pumps and gate valves are operated by hand.

5.2.4 Cryogenic cooling

The solenoid is designed to be a completely cryogen-free system, and all the necessary cooling power is provided by two cryocoolers. There is one cryocooler attached at each end of the cryostat, connected to the thermal shield on the first stage and to the cold mass on the second stage. The stainless steel turrets housing the cryocoolers provide a flange for the instrumentation feedthroughs. The cryocoolers are Gifford-McMahon type RDK-408D2 cold heads with F-50 compressors from Sumitomo Cryogenics. Cooling water is provided by the experiment infrastructure during normal operation.

5.2.5 Alignment foot

The alignment of the PUMA system with respect to the beam line at ISOLDE or the AD will be guaranteed by an alignment foot. The foot has adjustment pins to correct the horizontal position and vertical height. The feet position will be adjustable up to ± 10 mm in both horizontal directions, and ± 15 mm in the vertical direction. This vertical range is well suited to the maximum fluctuations of floor flatness measured at ELENA. A conical pin at the center bolt allows smooth coupling with the hole prepared on the frame as indicated in Fig. 5.5. It can be directly bolted into the ground of the experimental area and thus reproducibly put back into the aligned position once the PUMA frame is moved.

5.2.6 Target marker for fiducialisation

The cryostat has a target marker for laser alignment. The target will be installed at both end caps and at all eight turrets of the cold mass suspension. The dimensions are compliant with the CERN standard and given in Fig. 5.5.

5.2.7 Damping system

A damping system is foreseen to reduce accelerations and shocks exerted on the superconducting magnet during transportation and related operations. This is of particular importance during road transportation and setting down to ground by the crane. The damping system will be attached to the bottom of the frame (indicated as damping system on Fig. 5.6). It is composed of several semi-rigid metallic springs, made to adsorb the shocks and vibrations. The system is routinely used by the supplier Bilfinger Noell.

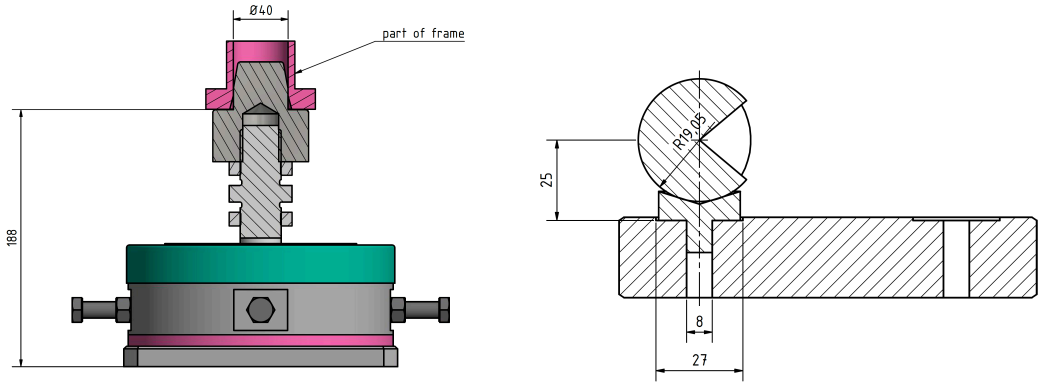

Figure 5.5: (Left) Side view of a support and alignment foot. The same feet will be used to position the solenoid in the frame and the frame at experimental sites. (Right) Half cut view of a target marker foreseen on the solenoid for optical alignment at experimental sites.

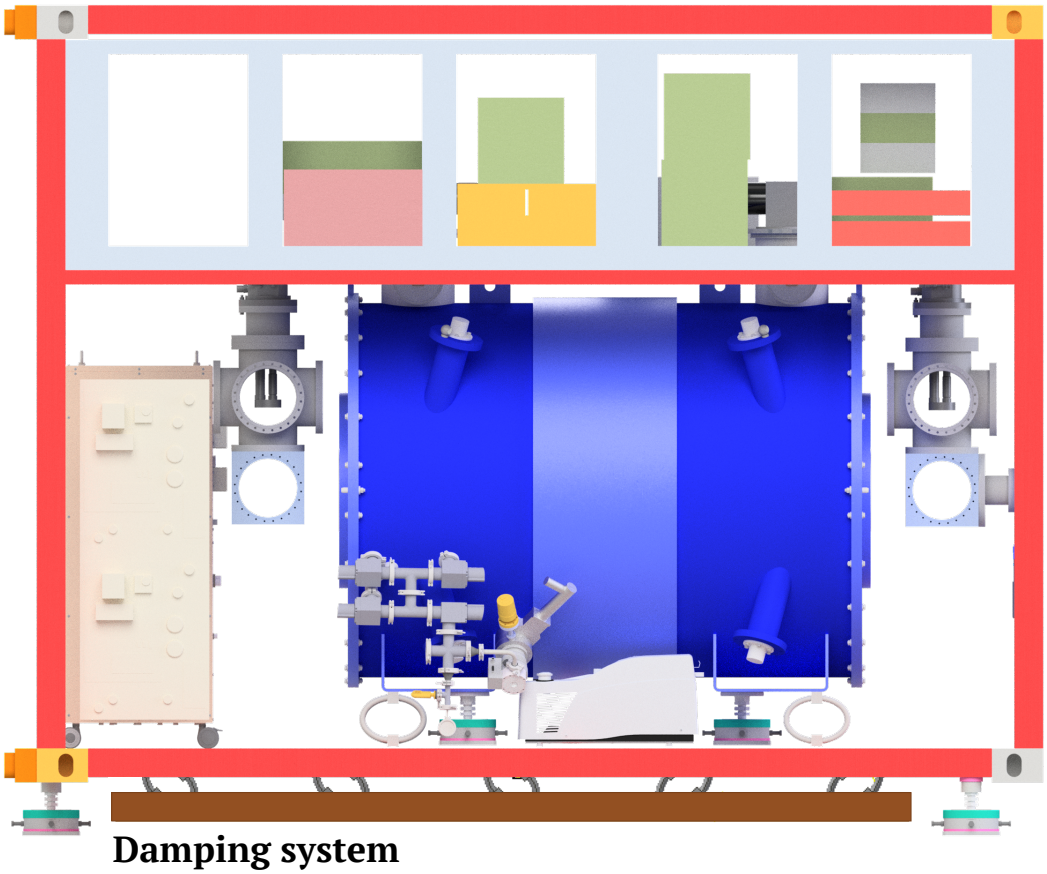

Figure 5.6: The damping system of PUMA will be located below the frame. The annex frame will be damped in the same way (not shown).

The damping system will efficiently reduce the accelerations exerted on all components on the frame. The transportation procedures will be as follows. The first step is to adjust the alignment-feet height lower so that the whole system rest on the damping mechanism. This is particularly important to absorb the shocks caused by the crane operation when touching down on the ground or the truck. The second step is the transportation. When on the truck, the brown sub-frame in Fig. 5.6 is fixed to the basis of the truck. The final step is to put the frame back in position with certain alignment. For this purpose, the alignment feet, fixed on the ground, are used to bring the frame back into its target position and height. During this procedure, the relative orientation of all components on the frames will stay unchanged.

Chapter 6

Trapping antiprotons and ions

6.1 Overview

PUMA aims at storing, transporting, and performing antiproton annihilations with ions. A portable Penning trap will be used for this purpose. To meet the requirements of the experiment, the PUMA trap consists of two trap zones. One is a large-diameter Malmberg-Penning trap to store antiprotons (Storage trap), and the other is a Malmberg-Penning trap with nested potential to capture antiprotons and oppositely charged ions at the same time (Collision trap). In either trap, charged particles are radially confined by a 4 T magnetic field, and axially by electrical potentials from cylindrical electrodes. The Malmberg-Penning trap has been widely used in AD experiments [136–138] to store many antiprotons, and eventually to generate antihydrogen. A pulsed drift tube (PDT) will be placed at the entrance of the trap to adjust the energy of the incoming ion beam to capture charged particles. A CAD drawing is presented in Fig. 6.1. The choice of one unique trap for all functions (storage, transport, collisions) is motivated by the necessity to maintain a constant magnetic field inside the storage trap during all operations and a perfect alignment of the traps with the magnetic field.

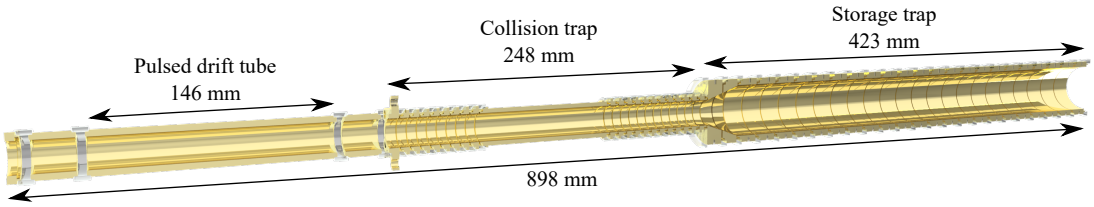

Figure 6.1: CAD half-cut view of the PUMA ion traps.

6.1.1 Cryogenic ion trap

We propose to build an ion trap that can store antiprotons for more than a month. This long-term storage can be achieved by avoiding losses from annihilation with the residual gas, as demonstrated by AD experiments [136–140]. The lifetime of the

antiprotons is determined by the vacuum in the trap (see Chapter 4). This extreme high vacuum (XHV) is achieved by keeping the whole ion trap at liquid helium temperature and using the ion trap itself as a cryopump. The ATRAP and the BASE collaborations demonstrated that one can achieve a vacuum level of better than 1×10^{-17} mbar by using this technique [136,139]. For this purpose, both storage and collision trap are maintained at the same XHV and cryogenic temperatures in a single vacuum tube.

6.1.2 Antiproton accumulation

The first stage of PUMA is to accumulate a large number of antiprotons at ELENA. ELENA will provide bunched antiprotons with expected operation cycle of 100 sec with 0.45×10^{7} antiprotons per bunch [141]. Accumulation scheme in accordance with the ELENA operation cycle will be developed. One accumulation cycle will consist of slowing down with a PDT, catching with fast-switched electrode, and cooling down to ambient temperature, in the present case 4 K, by sympathetic electron cooling. The cooling process will take the longest time, thus developing a fast cooling technique will be the key to establish an efficient accumulation cycle. Such attempts have already been made, for an example, by the ATRAP collaboration [142]. Bunched antiprotons from AD (up to 3×10^{7} /bunch) were captured, cooled down, and stacked by repeating the cycle. From a single bunch of antiprotons, 0.7 % were captured, and 60 % out of the captured were successfully cooled down. They made a successful cycle, and stacked more than 0.4 million antiprotons from 32 bunches. Electrons used for the sympathetic cooling will be provided by a cold field-emission electron source. As larger number of antiprotons are trapped, it is more difficult to keep them confined due to space charge effects. Actually it is known that a large number of charged particles confined in a Penning trap bears properties of a non-neutral plasma [143]. There has been a well-established way to control the behavior of non-neutral plasma called a rotating-wall technique [144–148]. This technique uses sine wave applied to a radially segmented electrode, which is seen from trapped particles as a rotating multipole field, to compress the particle cloud. The rotating-wall technique has been successfully extended to a multispecies non-neutral plasma containing antiprotons and electrons [149,150]. In case of a multispecies non-neutral plasma, additional difficulty of centrifugal separation must be dealt with [150, 151]. The rotating-wall technique eventually enables one to keep antiprotons confined for infinite time, besides other contributions such as vacuum. A design of the storage trap will be discussed to perform the series of operations with sufficient degree of freedom.

6.1.3 Diagnostics

Diagnosing the properties of the antiproton plasma is essential for PUMA. It is particularly important to know the properties of the antiproton plasma without losing them. Such diagnostics can be made using a non-destructive detection circuit. The circuit is designed to detect the charge from the plasma induced on a pick-up elec-

trode. It has been demonstrated that the induced signal from certain excited modes of the plasma contains useful information [152–155]. Using this diagnostics, shape, relative temperature, and number of charged particles contained in the plasma can be measured. It is known that the antiproton annihilation rate can be used to extract the number of trapped antiprotons [156]. A plastic scintillator barrel surrounding the storage trap will be used to measure the antiproton annihilation rate, and to cross check the number of trapped antiprotons. Along with the non-destructive diagnostics, the PUMA trap will be equipped with standard charged-particle detectors, a micro-channel plate (MCP) with phosphor screen readout and a Faraday cup. The MCP will be primarily used to image the cross-sectionally projected profile of the antiproton plasma. A custom-made MCP will be used to operate under a strong magnetic field. In order to meet with the demanding vacuum requirements, the MCP will be located outside the 4-K cryostat, in front of the pumping barrier, on a vertical action ladder. A similar design has already been developed by the Alpha collaboration [157], as shown in Fig. 6.2. The usage of a Faraday cup for antiprotons

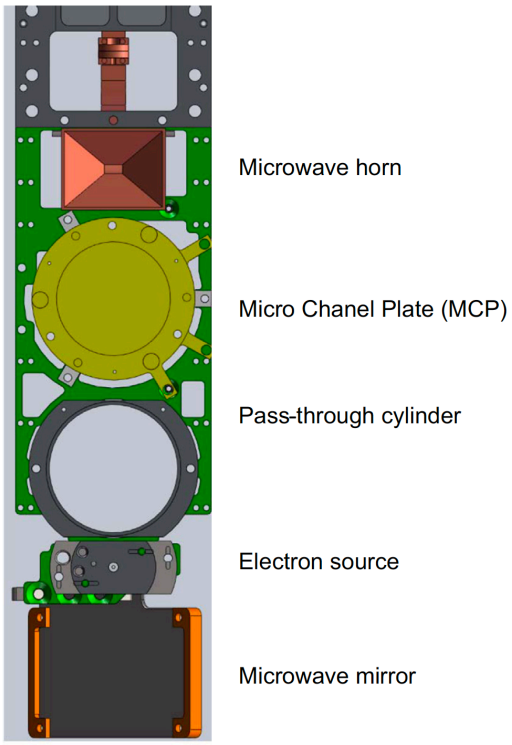

Figure 6.2: A vertical moving ladder used to host multiple devices at the end of the cylindrical Penning trap developed by the Alpha collaboration. Figure taken from [157].

is limited due to the charge carried out by the annihilation pions. However it is useful to make relative measurements, and to measure normal charged particles. The

Faraday cup can also be used to measure the energy of the charged particle by DC biasing the Faraday cup electrode. Employing segmented electrodes is optionally considered to extract the position and the energy of the confined particle. Further details and specification of the diagnostics will be discussed.

6.1.4 Simultaneous trap of antiprotons and ions

Once a sufficient amount of antiprotons are trapped and cooled in the storage, a fraction of antiprotons is extracted into the collision trap to annihilate with short-lived ions. A partial extraction technique has been established by the BASE collaboration based on an adiabatic voltage ramping [158]. PUMA will develop fractional extraction based on the same method. Following the fractional extraction, about 1 $\times 10^7$ antiprotons will be stored in the collision trap. The collision trap is designed so that the antiprotons can be confined for sufficient period of time to perform annihilation measurement. The same method as used at the storage trap, rotating wall and sympathetic electron cooling, will be applied. Also the same diagnostics will be used. Trapping oppositely charged antiprotons and ions will be realized by the a nested potential. Such scheme has been developed to trap particle and antiparticle simultaneously [159, 160]. The collision trap will be equipped with a sufficient number of electrodes to form the nested potential. One measurement cycle will consist of loading ions into the collision trap, detecting annihilations, and, where necessary, removing the remaining ions and annihilation product from the collision trap. The ions will be first decelerated by the PDT in front of the collision trap, and then captured by fast switching the trapping potential. Annihilations will be detected by the surrounding detectors. Shortly after the annihilations, the remaining ions and annihilation products will be removed by fast switching the trapping potential again. At certain time interval when the measurement is hindered, rotating wall and sympathetic electron cooling will be applied to the antiprotons to keep them trapped. Right before the measurement, the electrons will be removed by particularly fast switching the trapping potential.

6.2 PUMA ion trap

The PUMA trap is composed of two individual particle traps, the storage trap and the collision trap. The storage trap is dedicated for accumulating up to 10^9 antiprotons, while the collision trap will be used to confine a bunch of short-lived ions and a fraction of the stored antiprotons from the storage trap simultaneously. This section summarizes the design of those two traps while focusing on the material and geometry of the traps as well as the related electronics.

6.2.1 Electrode design

To confine and store the antiprotons and short-lived ions, the particles have to be axially trapped in an electromagnetic field. In our case, the confinement is provided

by two cylindrical multi-ring traps (MRT), which are based on the concept of a classical Penning trap. A constant axial magnetic field arises from the solenoid will confine the charged particles radially, while the electrostatic potential is provided by multiple ring electrodes. Here, we focus on the mechanical and electrostatic design of these ring electrodes for both the storage and the collision trap.

Electrostatic design

Due to the different purposes and foreseen particle numbers, the ring electrodes of the two traps have an individual geometrical design. In the storage trap, we expect to store up to 10^9 antiprotons, while the sum of short-lived ions and antiprotons in the collision trap will be typically in the order of 10^7 particles. Since we aim at a maximum charge density of 10^8 cm^{-3} to avoid significant space charge effects on the plasma, this difference in particle number has an impact on the required trap geometry, leading to a larger inner electrode radius r_{str} in the storage trap with $r_{\mathrm{str}} = 20$ mm compared to the smaller radius of the collision trap electrodes $r_{\mathrm{col}} = 10$ mm. The lengths of the two different electrode types were chosen to comply with a length-to-radius ratio of $l_{\mathrm{str}}/r_{\mathrm{str}} = 0.85$ and $l_{\mathrm{col}}/r_{\mathrm{col}} = 0.7$, respectively, leading to storage trap electrode length of $l_{\mathrm{str}} = 17$ mm and a collision trap electrode length of $l_{\mathrm{col}} = 7$ mm. The length-to-radius ratios were chosen based on a comparison of the design values of other MRT experiments, which are typically in a range of 0.7 to about 1.0 [161, 162]. Besides the basic cylindrical trap electrodes we also use a total of four azimuthally-segmented electrodes (two for the collision trap and two for the storage trap), which have the same inner diameter and length as the normal trap electrodes. For both traps we implement one four-fold segmented electrode and for the storage trap an additional eight-fold segmented electrode, which will be used for applying the rotating-wall technique, which is specified in the section about non-neutral plasmas. For the storage trap, a total of 22 electrodes (20 cylindrical + 2 segmented) will be used for shaping the harmonic potential well. Effectively, out of these 22 electrodes only 18 will be used for the actual potential well, while the two segmented electrodes and two additional electrodes directly next to the segmented electrodes will be kept at ground for excitation and for picking up the induced charge of the plasma in the trap. The voltages that can be applied to the electrodes range from - 500 V to + 500 V. For the storage trap we plan to use a harmonic axial potential, since it provides good confinement for small particle numbers up to high density ensembles. In the storage trap this harmonic potential will be provided by the 14 inner electrodes, which are surrounded by the pick-up and the segmented electrodes as well as four electrodes for catching the incoming particles (two on each end of the storage trap). The resulting potential is shown in Fig. (6.3) together with a schematic drawing of the stacked electrodes. The exact potential shape of the collision trap in contrast will not have a continuous shape, as it has to be adjusted to each individual ion species. An additional complexity arises from the opposite charges of the negatively charged antiprotons and the positively charged short-lived ions. Due to this, a nested potential will be necessary, which allows to store both positively and negatively charged particles in the same region of

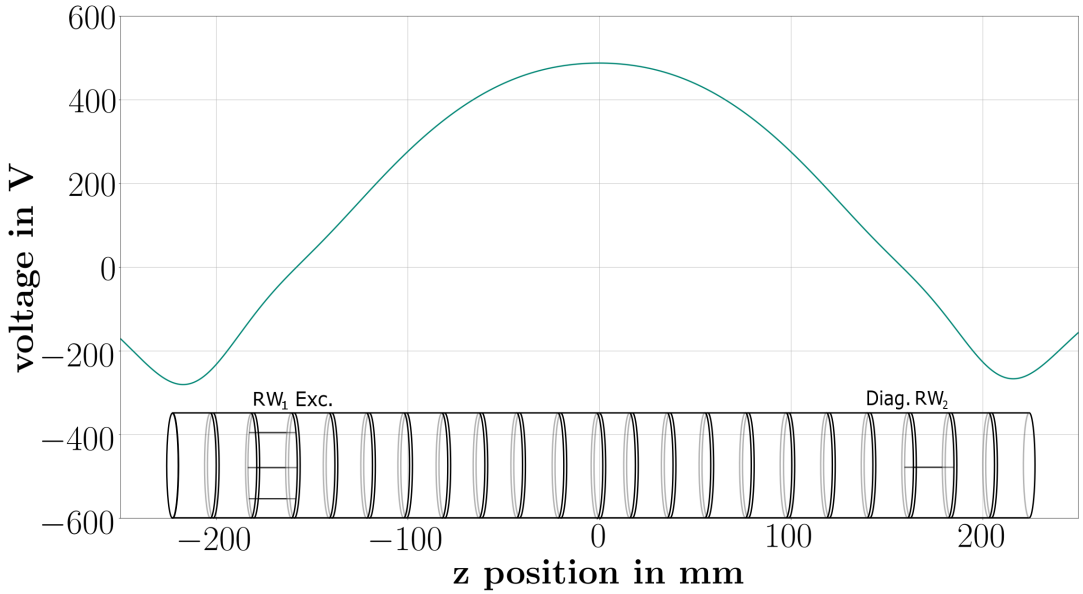

Figure 6.3: Electric potential on the trap center axis of the storage trap as calculated by SIMION. A schematic drawing of the ordering of the electrode types is added for orientation.

the trap. A preliminary plot of the on-axis potential for the collision trap is shown in Fig. 6.4. A more dedicated potential shape will be investigated with the test setup, where the storage of electrons and light positive ions will be tested.

Mechanical electrode design

In contrast to the individual geometrical and electrostatic design of the electrodes for the collision and the storage trap, the mechanical design for all electrodes is equal. The operation at an extreme high vacuum and at cryogenic temperatures strongly limits the choices for the electrode material and the material of the insulators between neighboring rings. The most important features of the required materials are a high thermal conductivity, low magnetic susceptibilities of all materials and low outgassing rates in vacuum. Comparing the thermal conductivity of different conductors and insulators (see Fig. 6.5), high-purity oxygen-free OFE copper (UNS 10100, 99.999 %) was chosen for the electrodes and pure sapphire (Al_2O_3) for the insulator rings [163, 164].

To avoid large asymmetries over the full stack of electrodes, all electrodes and copper rings have to be machined within a deviation of at maximum 20 µm from the nominal values. This precision is most important for the fitting of the electrodes with the insulator rings, because loose fittings might lead to a bending of the trap main

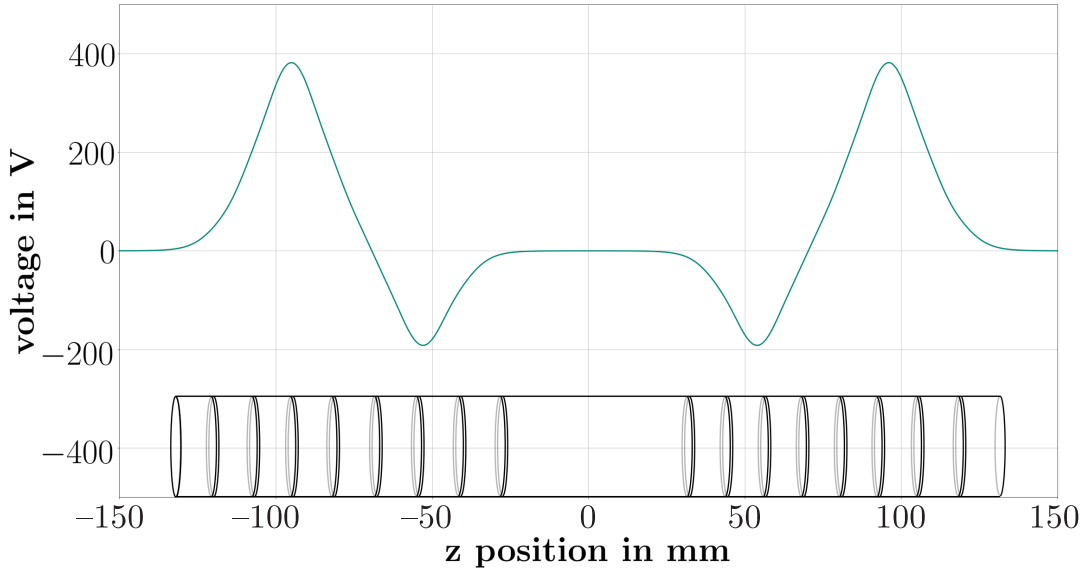

Figure 6.4: Preliminary trapping potential on the trap center axis of the collision trap as calculated by SIMION. A schematic drawing of the ordering of the electrode types is added for orientation.

axis, making a highly precise alignment of the trap with the magnetic field difficult. In addition, the precision is crucial for a successful operation of the segmented electrodes, whose segments are separated by sapphire balls of 1.5 mm diameter.

The first set of 22 copper electrodes is manufactured by the fine mechanics workshop at TU Darmstadt from a tube of OFE copper (see Fig. 6.6). An additional step to reduce the impact of patch potentials on the electrodes is to plate the electrodes first with a thin layer of silver (5 µm) and secondly with a thicker layer of gold (25 µm). Before the electrodes can be galvanically plated, the surfaces of the copper electrodes have to be high-gloss polished, so that the silver and the gold layer are evenly applied to all surfaces. The thin silver layer is necessary to avoid an immigration of the gold atoms into the copper, which tends to occur at high temperatures during baking. It is expected, that the first set of plated electrodes will be available in October 2019.

Trap alignment

The alignment of the trap center axis with the magnetic field lines of the solenoid is crucial for a proper operation of the trap. A misalignment of both center axes gives rise to azimuthal asymmetries in the electric field of the trap, which break the symmetry of the ideal setup and lead to a distortion of the particle motion in the trap. In a single particle picture, this results in a change of the eigenfrequencies. Considering a misalignment angle θ between the magnet field and the trap axis, the axial bounce frequency ω_z of the ideal trap gets reduced to a real trap frequency $\tilde{\omega_z}$

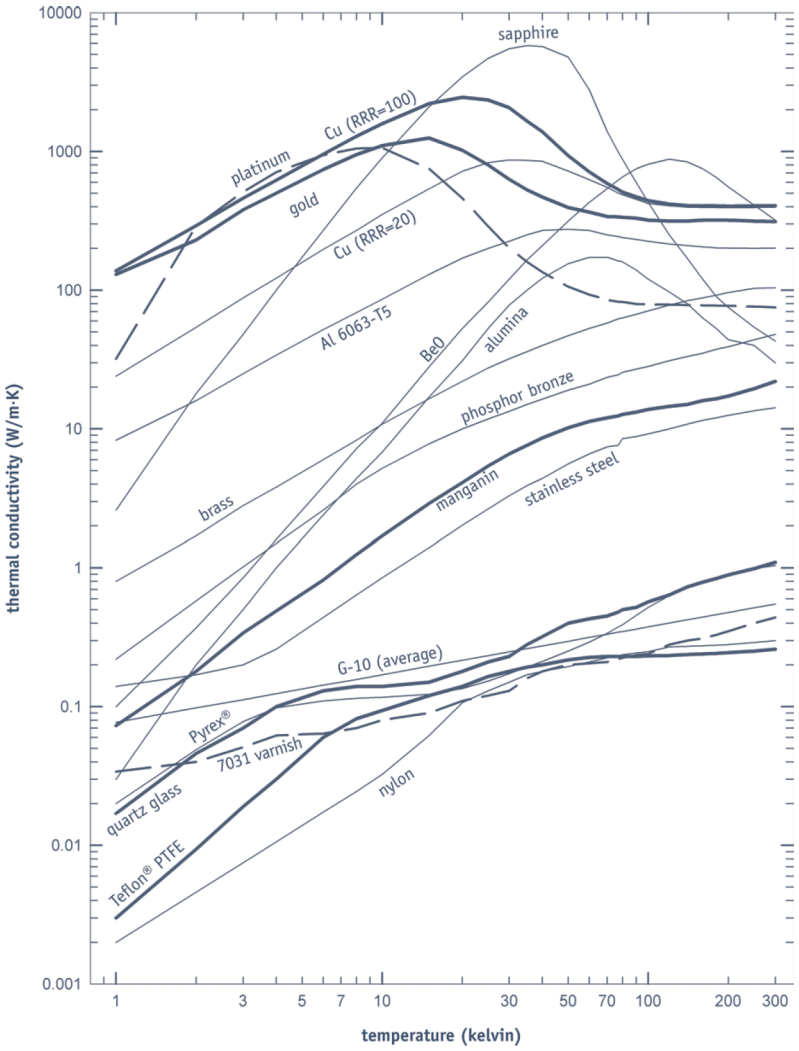

Figure 6.5: Plot of the thermal conductivity of different metals and insulators for temperatures from room temperature down to 1 K [165].

given by:

$$\tilde{\omega_z}^2 \approx \omega_z^2 \left(1 - \frac{3}{2}\theta^2\right). \tag{6.1}$$

In the case of a dense ensemble of particles however, some particles tend to be pushed to higher radii, where the impact of the field inhomogeneities become more relevant. This leads over time to a reduction of the plasma's angular momentum and thereby to a radial expansion up to particle losses on the trap wall [166]. The effect is usually modeled by a drag torque, which is introduced in the upcoming section about non-neutral plasmas. In addition, a misaligned magnetic field can cause problems for the destructive diagnostics, as it leads to a radial displacement depending on the misalignment angle θ and the distance to the Faraday cup or microchannel

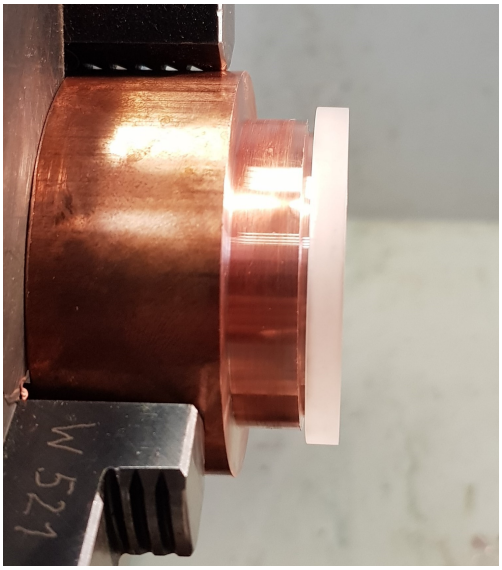

Figure 6.6: Image of a copper test electrode and a sapphire insulator ring to determine the proper dimensions for a tight fit. Here, the sapphire ring is just loosely attached to avoid that it gets stuck and cannot be detached again.

plate [154]. To reduce the impact of this torque it is helpful to align the trap and the magnet up to an angle of at maximum mrad or below. Generally, it is favored to achieve an angle of mrad down to µrad, as the lifetime of the ensemble in the trap can be significantly improved [166].

To ensure such a precise alignment, the PUMA trap assembly will be mounted to a precisely adjustable support frame which itself will be connected to the PUMA solenoid to avoid alignment shifts during the transportation process. It will be held by a set of four feet, which all are adjustable in height with a 100 µm precision, leading to the possibility to tune the angle between the magnetic field lines and the trap axis also in the order of mrad to µrad over the full length of about 1 m. To evaluate the precision of the alignment we plan to use low-energetic electrons and a microchannel plate (MCP), which is detailed in section 6.4.3. As electrons tightly follow the magnetic field lines in the 4 T field, the position of the electrons on the MCP relative to the projection of the trap center axis on the MCP allows the determination of the misalignment angle. The alignment will be performed iteratively to maximize the lifetime of electron plasma. By consecutive measurements the alignment and therefore the lifetime of the plasma can be improved.

6.2.2 Electronics design

The PUMA trap requires customized specifications for electronics. Series of operations to capture, trap, transfer, and manipulate charged particles require programmable fast control of the electronics. We are developing a programmable system based on PXI express (PXIe) developed by National Instruments. The PXIe-based

systems have been widely used in the trap control, such as at GBAR [167]. The schematic view of the trap electronics is shown in Fig. 6.7. Command sequence programmed by LabView is first processed by PXIe-8840 controller, and then distributed via digital analog converter (DAC) and other input/output (I/O) modules to each electronics. For operations that require fast synchronization to external trigger, such as capturing of antiprotons and ions where 100 ns switching is necessary, fast control modules are also prepared.

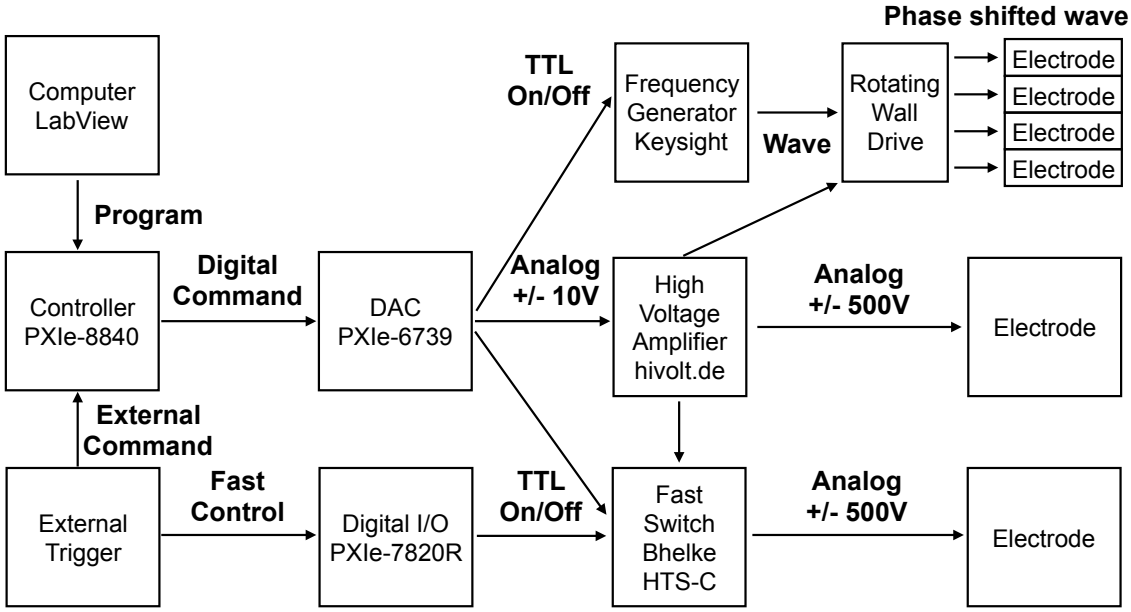

Figure 6.7: PUMA ion trap electronics and control.

Voltage supply

A high voltage amplifier is used to supply trapping potential to each electrode. A precision high voltage amplifier, HAR-8X8A provided by hivolt.de GmbH & Co. KG, will be employed. The amplifier has fixed gain of $50\pm0.3\,\%$, and amplifies input voltage of ±10 V, thus provides ±500 V to each electrode. The slew rate is 20 V/µs, and the noise level is 3 $\mathrm{mV_{RMS}}$, at capacitive load of 500 pF. The specification is comparable to similar devices used at AD experiments, AEgIS for example [161]. The amplifier chassis has high density design ideal for transportation, and directly controllable via National Instruments PXIe-6739 DAC.

Frequency generator

Frequency generators are used to provide sine waves to rotating wall and drive particles. PUMA employees the Keysight 31000 series. They are widely used among the ion trap community, and satisfies our requirement of frequency range up to GHz, accuracy of ±1%, and controlability through external trigger.

Rotating wall drive

A rotating wall drive will provide phase-shifted sine waves to the segmented electrodes. In order to cover a sufficient frequency and voltage range for the development, we employed a custom rotating wall drive made by Stahl electronics. The device will provide eight 45°-phase shifted sine waves on top of DC offset voltage. Covered frequency range is 0.8 to 10 MHz with maximum wave amplitude of $2V_{pp}$.

Fast switches

Fast switches are used to turn on and off trapping voltages to load and unload particles from the trap. In the case of loading and unloading the electrons, for example, the voltage should be lowered for very short period of time, typically in order of 50 ns. This operation is performed by push-pull transistor switch HTS series made by Behlke electronic GmbH. The switch has a minimum output pulse rise time of 50 nsec depending on capacitive load. The electrode circuit with the switch will be tuned to suppress transmitted noise and transition time.

6.3 Non-neutral plasma

To store up to 10^9 antiprotons over a timescale of several months within the storage trap, the dynamics of the antiproton ensemble has to be known precisely to avoid inadvertent particle loss. In contrast to a very small ensemble with only a few charged particles, where the dynamics of each particle can be assumed to be guided fully by the trap fields, the particle-particle interactions cannot be neglected in the case of a dense ensemble with large particle number. If the density is high enough and the temperature is low enough so that the Debye length $\lambda_D = \sqrt{\epsilon_0 k_B T/nq^2}$ is small compared to the typical dimensions of the particle ensemble, the dynamics of the particle cloud can be described based on the concept of a non-neutral plasma [168]. The Debye length represents a characteristic length over which external electric fields are screened inside a plasma and has values of $\lambda_D \approx 10$ - 50 µm assuming an antiproton density of $n \approx 10^{14}$ m^{-3} for PUMA. As the Debye length is much smaller than the estimated antiproton ensemble dimensions in the storage trap, which will be in the order of a few millimeters to centimeters, a description of the ensemble as a non-neutral plasma is appropriate. In this case, the antiproton plasma has a characteristic spheroidal shape with an aspect ratio $\alpha = z_e/\rho_e$ as the ratio of the axial length z_e and the length of the radial main axis ρ_e (see Fig. 6.8) [169, 170]. Inside the plasma, the particle density $n(r)$ is constant, while on the plasma edges it drops to zero on the scale of about a Debye length [144, 171].

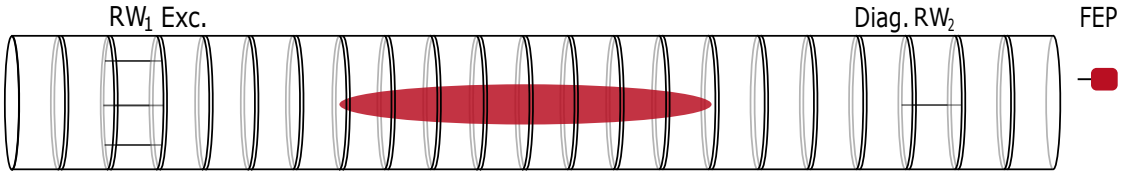

Figure 6.8: Schematic picture of a prolate ($\alpha > 1$) electron plasma in the PUMA storage trap, where the elctrons are provided by a cold field-emission point (FEP).

As the antiproton plasma tends to screen external electric fields from its inside, the dynamics of the particles inside the plasma are guided by their Coulomb interaction. Macroscopically, the plasma undergoes a bulk $\vec{E} \times \vec{B}$-drift around the trap center axis in the crossed magnetic and electric fields [168, 172]. The antiproton plasma creates a non-negligible space charge potential, which arises from the dense cloud of equally charged particles. This space charge potential deconfines the plasma and can lead to axial particle losses, if it overcomes the trap potential of the electrodes. Considering the estimated antiproton density of $n \approx 10^{14}$ m^{-3} for PUMA, the resulting space charge potential is in the order of about 30 V, leading to a stable axial confinement. To calculate the rate of the bulk drift of the plasma in the trap, the electric field caused by the space charge potential $\vec{E}_\mathrm{s}$ has to be taken into account, leading to a drift velocity $\vec{v}_\mathrm{D}$ of

$$\vec{v}_\mathrm{D} = \frac{\left(\vec{E}_\mathrm{t} + \vec{E}_\mathrm{s}\right) \times \vec{B}}{|B^2|} \tag{6.2}$$

In an ideal trap, the additional radial confinement of the plasma is characterized by a conservation of the total angular momentum [173, 174], which is given by:

$$L_\Theta = \sum_{i=1}^{N} \left(m\omega_i \rho_i^2 - \frac{1}{2} qB\rho_i^2 \right) = \text{const.} \tag{6.3}$$

Due to the small mass of the antiprotons the first term, which represents the mechanical angular momentum of each particle, is typically several orders of magnitude smaller than the second term corresponding to the canonical angular momentum. By approximating the total angular momentum by the canonical angular momentum

$$L_\Theta \approx -\sum_{i=1}^{N} \frac{1}{2} qB\rho_i^2 = -\frac{1}{2} qBN\langle\rho^2\rangle \tag{6.4}$$

it is shown that the mean square radius of the plasma is conserved. For the typical case of a plasma radius which is about an order of magnitude smaller than the trap electrode radius, this conservation of the mean square radius can be translated to an almost infinite storage time with respect to radial losses. However, in a real trap the cylindrical symmetry of the trap is slightly broken due to small misalignments of the trap electrodes with respect to the magnetic field or minor fabrication errors of the electrodes, leading to a slow reduction of the magnitude of the total angular

momentum and therefore an increase of the mean square radius of the plasma. Over time, this increased mean square radius eventually leads to radial particle losses, limiting the storage time to timescales of minutes up to a few hours. This reduction of the magnitude of the total angular momentum can be modeled by the negative background torque $\mathcal{T}_\mathrm{B}$ [173, 175]. To overcome the limitation of the radial confinement time it is necessary to compensate this background torque by a positive torque, which co-rotates with the plasma drift. In our case, this positive torque $\mathcal{T}_\mathrm{r}$ will be provided by an azimuthally rotating electric field, which is generated by the azimuthally segmented trap electrodes [144–146, 149, 150, 162]. On each electrode segment we apply a radio-frequency (RF) voltage with a small amplitude V_0 and the frequency ω_r:

$$\Phi_i(\theta, t) = V_0 \sin\left[m_\theta\left(\theta_i - \omega_\mathrm{r} t\right)\right] \quad \text{with} \quad \theta_i - \frac{\Delta\theta}{2} < \theta < \theta_i + \frac{\Delta\theta}{2} \tag{6.5}$$

Here, $m_\theta = 1$ corresponds to a dipole drive, while $m_\theta = 2$ represents a quadrupole drive. Typically, a rotating dipolar potential is applied by a four-segmented electrode, but we plan to also test the efficiency of a quadrupolar potential on our eight-fold segmented electrode. In general, for a predefined multipole potential, a larger number of segments is preferred as the impact of higher spatial harmonics gets reduced when the sine wave is approximated smoother [176].

For a steady confinement, the torque has to compensate the background torque, i.e. $\mathcal{T}_\mathrm{r} + \mathcal{T}_\mathrm{b} = 0$, leading to a fixed value of the angular momentum and therefore of the mean square radius of the plasma. However, it is also possible to increase the torque of the rotating field by increasing the amplitude of the rotating potential or by varying the frequency of the drive. If $\mathcal{T}_\mathrm{r} > \mathcal{T}_\mathrm{b}$, the magnitude of the angular momentum is increased, leading to a reduction of $\langle\rho^2\rangle$ and therefore to an overall compression of the plasma. In addition, the rotating electric field spins-up the bulk rotation rate of the plasma around the trap center axis from the $\vec{E}\times\vec{B}$-drift rate up to the rotating field frequency ω_r. Following the modeling of the background and drag torque as defined in [175] with the current bulk rotation rate ω and two constant scaling parameters η and β as

$$\mathcal{T}_\mathrm{r} = \eta\frac{\omega_\mathrm{r} - \omega}{\omega}V_0^2 \qquad \text{and} \qquad \mathcal{T}_\mathrm{b} \cong -\frac{\beta}{\omega}. \tag{6.6}$$

We can conclude that the torque of the rotating electric field decreases with increasing rotation rate ω. In addition, we can determine the steady state rotation rate ω_eq, at which the sum of both torques is zero. It is given by

$$\omega_\mathrm{eq} = \omega_\mathrm{r} - \frac{\beta}{\eta V_0^2} \tag{6.7}$$

As the scaling parameters β and η depend on the trap properties, i.e. the vacuum level, the temperature, the alignment of the electrodes and precision of the machining, their values have to be determined experimentally.

Following the modeling of the torque of the electric field in equation (6.6), any sufficiently high rotating field frequency $\omega_\mathrm{r} > \omega$ should lead to a plasma compression if the background drag is negligibly small. Such a behavior has also been observed in several experiments and is summarized under the term of the "strong drive regime" [175, 176]. All these experiments have in common that they used rather high amplitudes in the range of a few Volts for the rotating potential. However, there are also a number of experiments with a lower voltage amplitude, and in these cases a radial compression of the plasma can only be observed at certain discrete frequencies [145, 146]. These frequencies couple with plasma wave frequencies, which correspond to the eigenfrequencies of collective excitations of the plasma. These modes have been described as Trivelpiece-Gould (TG) modes in an infinitely long charged cylinder in an axial magnetic field. These TG modes have been defined initially for the electron component of a neutral plasma, but the concept has been extended to non-neutral plasmas. Based on the collision-less drift-kinetic equation, each TG mode can be characterized by a set of three mode numbers (m_Θ, m_z, m_r) (compare Fig. 6.9) as well as a related dispersion relation for the mode frequency ω_TG [146]:

$$\omega_\mathrm{TG} - m_\Theta \omega_{E\times B} \simeq A \omega_\mathrm{p} R_\mathrm{p} k_\mathrm{z} \left[1 + \frac{3}{2}\left(\frac{\bar{v}}{v_\Phi}\right)^2\right]. \tag{6.8}$$

Here, $v_\Phi = (\omega - m_\Theta \omega_{E\times B})/k_\mathrm{z}$ is the axial phase velocity, R_p is the plasma column radius and $\bar{v} \simeq \sqrt{\frac{8 k_\mathrm{B} T}{\pi m}}$ is the average thermal velocity for the ensemble temperature T. The coefficient A depends on the azimuthal and the radial mode number m_θ, m_r and is given by:

$$A = \begin{cases} \sqrt{\frac{1}{2}\ln\left(\frac{R_w}{R_p}\right)} & \text{for} \quad m_\theta = 0 \\ \pm\frac{1}{j_{m_\theta m_r}} & \text{for} \quad m_\theta > 0 \end{cases} \tag{6.9}$$

where $j_{m_\Theta m_r}$ is the m_r-th zero of the m_Θ-th Bessel function. The sign of A depends on the mode frequency compared to the current plasma rotation frequency. If the mode rotates faster, the sign is positive; and for a slower mode rotation the sign is negative.

The description of the plasma modes based on the concept of TG modes is precise, when the plasma is very elongated with a very high aspect ratio α, but there is a large discrepancy if the spheroidal plasma approximates a spherical shape. For this case, Dubin derived a dispersion relation for azimuthally symmetric plasma waves in a generalized spheroidal plasma [169], which is now characterized by two mode numbers l and m:

$$1 - \frac{\omega_\mathrm{p}^2}{\omega_2^2} = \frac{k_2}{k_1}\frac{P_2(k_1) Q_2'^0(k_2)}{P_2'(k_1) Q_2^0(k_2)}. \tag{6.10}$$

Here, P_l and Q_l^m are the (associated) Legendre functions of first and second kind, and the primes denote the differentiation with respect to the argument. The parameters

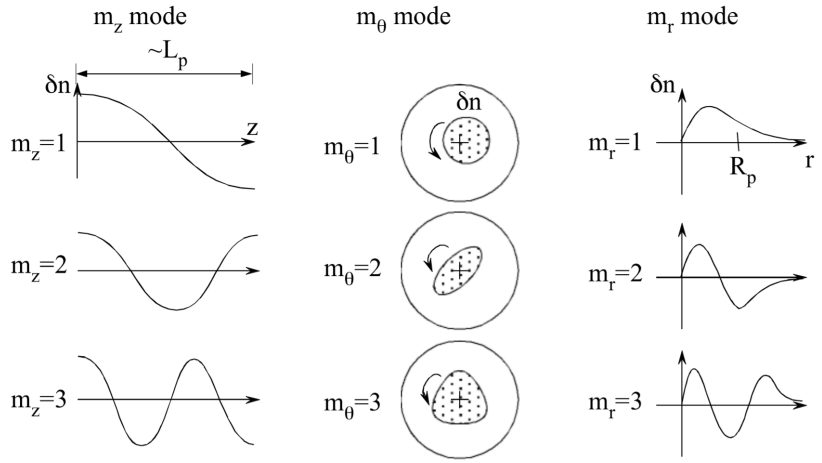

Figure 6.9: Schematic drawing of the plasma density pertubations δn for different axial, azimuthal and radial mode numbers (m_z, m_θ, m_r) [176].

k_1 and k_2 are given by:

$$k_1 = \frac{\alpha}{\sqrt{\alpha^2 - 1 + \omega_\mathrm{p}^2/\omega_2^2}} \qquad \text{and} \qquad k_2 = \frac{\alpha}{\sqrt{\alpha^2 - 1}}. \tag{6.11}$$

This dispersion relation is valid for all spheroidal plasmas and approximates the results of the TG modes in the limit of very high aspect ratios. To apply the rotating wall technique, a (l, $m \neq 0$) mode has to be excited, since modes with $m = 0$ are azimuthally symmetric, leading to no azimuthal net effect on the plasma, i.e. not torque transfer. However, the $m = 0$ modes are very useful for the plasma diagnostics, as specified in the following section. For the case of PUMA we would like to investigate if our traps can be operated in the strong drive regime, since the frequency-independent compression is more flexible and easier to handle.

Even though the rotating wall technique provides the possibility to confine the particles radially for infinite time by compressing the plasma, it has the negative side effect of heating up the plasma [144, 146]. Due to the continuous and time-dependent energy input in the plasma, the kinetic energy of each particle increases over time, leading to an significant increase of the plasma temperature. Due to the temperature-dependence of the Debye length, this increase of temperature leads to an increase of the plasma diffuseness at its edge. By this, some particles get transported to large radii outside the bulk plasma, where the motion is not guided by the plasma properties anymore. This effect leads eventually to particle loss and has to be compensated by a suitable cooling mechanism.

For a large number of antiprotons, the simplest cooling mechanism is the sympathetic cooling, i.e. that the antiprotons are cooled by a second particle species

which is cooled directly. This can be self-cooling electrons [160]. In this case, the electrons in the strong magnetic field cool themselves by the emission of cyclotron radiation according to the Larmor formula, leading to an exponential decay of the temperature down to the trap temperature with a decay time constant τ_s given by:

$$\tau_s = \frac{6\pi\epsilon_0 m c^3}{e^2\omega_c^2} = \frac{6\pi\epsilon_0 m^3 c^3}{e^4 B^2} \approx 0.3 \text{ s} \quad \text{for} \quad B = 4 \text{ T}. \tag{6.12}$$

Neglecting the heating induced by the electric field, the temperature evolution of the antiproton and the electron fraction of the mixed plasma is given by:

$$\frac{\partial T_{\bar{\text{p}}}}{\partial t} = -\frac{1}{\tau_{\bar{\text{p}}}} \left(T_{\bar{\text{p}}} - T_{\text{e}}\right) \tag{6.13}$$

$$\frac{\partial T_{\text{e}}}{\partial t} = \frac{1}{\tau_{\bar{\text{p}}}} \frac{N_{\bar{\text{p}}}}{N_{\text{e}}} \left(T_{\bar{\text{p}}} - T_{\text{e}}\right) - \frac{1}{\tau_{\text{e}}} \left(T_{\text{e}} - T_{\text{amb}}\right) \tag{6.14}$$

In these equations, $\tau_{\bar{\text{p}}}$ represents the sympathetic cooling time constant, which depends on the current temperatures T_{e} and $T_{\bar{\text{p}}}$ and densities n_{e} and $n_{\bar{\text{p}}}$ [177]. In cgs units, it is given by:

$$\tau_{\bar{\text{p}}} = \frac{3 m_{\bar{\text{p}}} m_{\text{e}} c^3}{8\sqrt{2\pi}\, n_{\text{e}} e^4 \ln\Lambda} \cdot \left(\frac{\text{k}_\text{B} T_{\text{e}}}{m_{\text{e}} c^2} + \frac{\text{k}_\text{B} T_{\bar{\text{p}}}}{m_{\bar{\text{p}}} c^2}\right)^{3/2} \tag{6.15}$$

The expression $\ln\Lambda$ represents the Coulomb logarithm, which is a measure for the impact parameter of the electron-antiproton Coulomb collisions. It depends on the temperatures of both species and is given by

$$\ln\Lambda = 23 - \ln\left(n_{\text{e}}^{1/2} T_{\text{e}}^{-3/2} Z\right), \qquad \text{if } T_{\bar{\text{p}}} \cdot \frac{m_{\text{e}}}{m_{\bar{\text{p}}}} < T_{\text{e}} \text{ with Z=1} \tag{6.16}$$

$$\ln\Lambda = 16 - \ln\left(n_{\bar{\text{p}}}^{1/2} T_{\bar{\text{p}}}^{-3/2} Z^2 \mu\right), \quad \text{if } T_{\text{e}} < T_{\bar{\text{p}}} \cdot \frac{m_{\text{e}}}{m_{\bar{\text{p}}}} \text{ with Z=1 and } \mu = \frac{m_{\bar{\text{p}}}}{m_{\text{p}}} = 1 \tag{6.17}$$

Typically, the cooling of the antiprotons takes about a few seconds until their temperature arrives at the ambient temperature for our typical conditions, an electron density of $n_e \sim 10^8$ / cm^3 and an antiproton density of $n_{\bar{\text{p}}} \sim 10^7$ / cm^3. This cooling time is small enough to fit into the 100 s gap between two consecutive antiproton bunches at ELENA. The equations (6.13) get more complicated, if some antiprotons have already been cooled and stored in the trap and a new bunch of hot antiprotons is delivered into the trap, but due to the larger storage of cold particles the total cooling time per bunch decreases and the capturing efficiency increases over time. This behavior has already been investigated by ATRAP, where they observed an increasing fraction of cooled and stacked antiprotons for a higher number of already stacked antiproton bunches [136].

The electrons are provided by a cold field-emission point (FEP) which is located at the end of the storage trap, mounted on a frame together with the Faraday cup.

The field-emission point will be positioned off-axis, as the Faraday cup should occupy the area around the center axis to detect all trapped particles (compare Fig. 6.8). By the use of an acceleration electrode the electrons gain enough energy to overcome the potential edge on the end of the storage trap. This edge is slightly reduced to second potential edge on the opposite end of the storage trap to allow the electrons to enter into the trapping region. Electrons are trapped at the minimum of potential well by loosing the energy themselves. We plan to adjust the electron cloud position and diameter by applying the rotating wall at the end of the trap. The electron cloud will be controlled to maximize the overlap with antiproton cloud, and thus the efficiency of sympathetic cooling.

The compression of an antiproton plasma by the rotating wall technique in combination with sympathetic electron cooling has already been established at other ELENA experiments. As an example, ALPHA investigated the compression of about 3×10^4 antiprotons with about 1.2×10^8 electrons and observed, that they achieve significant compression by a factor of $\sim$ 4 - 5 based on the strong drive regime (see Fig. 6.10) [149]. Similar observations have also been made at AEGIS [150], where the compression was achieved through coupling to the TG modes. These observations contradict each other on the compression regime. A further investigation of this transition between the different rotating wall regimes will also be investigated in the course of our development.

In summary, it is necessary to apply the rotating wall technique together with the sympathetic electron cooling to store the antiprotons for a long period of time. In order to accumulate bunched antiprotons in the most efficient manner, it will be necessary to carefully tune an appropriate frequency of the rotating electric field. A suitable scheme will be developed to accumulate the antiprotons proportional to the number of incoming bunches. In addition, we will investigate the optimum number of electrons for efficient cooling of incoming bunched antiprotons.

6.3.1 Non-destructive mode diagnostics

Characterizing the properties of non-neutral plasma is of high interest. Because they are lost when measured destructively, a non-destructive way of measuring the plasma density n, the aspect ratio α and the total number of charges N is needed.

The axial frequency ω_z is related to the density n and the aspect ratio α by

$$\frac{\omega_\mathrm{z}^2}{\omega_\mathrm{p}^2} = \frac{1}{\alpha^2 - 1} Q_1^0 \left(\frac{\alpha}{\sqrt{\alpha^2 - 1}} \right) \qquad \text{with the plasma frequency } \omega_\mathrm{p} = \sqrt{\frac{nq^2}{\epsilon_0 m}}. \quad (6.18)$$

Q_1^0 is the (associated) Legendre function of second kind, m is the mass and q the charge of the particle.

By measuring the frequencies ω_l of the (1,0) dipole and the (2,0) quadrupole plasma mode, one can extract the plasma density n and the aspect ratio α.

In a harmonic trap, the frequency ω_1 is that of a single particle motion along the z axis

$$\omega_1 = \omega_z. \quad (6.19)$$

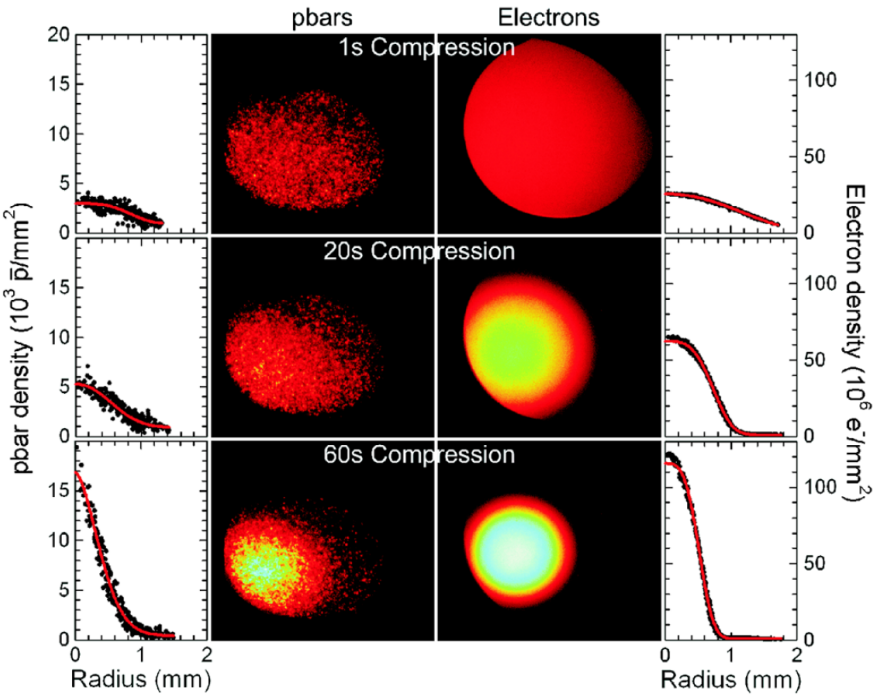

Figure 6.10: Compression of a mixed antiproton-electron plasma at ALPHA. The densities of both the electron as well as the antiproton fraction have been increased by a factor of about 5 within 60 s [149].

For a plasma with cyclotron frequency much higher than the plasma frequency (highly magnetised), the frequency of the dipole mode is given by the dispersion relation [169]

$$1 - \frac{\omega_p^2}{\omega_2^2} = \frac{k_2}{k_1} \frac{P_2(k_1) Q_2'^0(k_2)}{P_2'(k_1) Q_2^0(k_2)}. \tag{6.20}$$

P_l and Q_l^m are the (associated) Legendre functions of first and second kind, primes denote the differentiation with respect to the argument. Also

$$k_1 = \frac{\alpha}{\sqrt{\alpha^2 - 1 + \omega_p^2/\omega_2^2}} \tag{6.21}$$

$$k_2 = \frac{\alpha}{\sqrt{\alpha^2 - 1}}. \tag{6.22}$$

By measuring ω_1 and ω_2 and combining equations 6.18, 6.19 and 6.10 one can extract the plasma density n and the aspect ratio α. It is important to note here, that the $(1,0)$ and $(2,0)$ frequencies (and also higher orders) do not depend on the total number of particles, but only the density n and the aspect ratio α.

To get the total number of charges N, another parameter is needed, since N satisfies the following relationship:

$$N = 4\pi n z_p^3 / 3\alpha^2. \tag{6.23}$$

The ATHENA collaboration developed a model for determining the total number of charges N in the trap [178]. A radio frequency is applied to the plasma near resonance and the response of the plasma is analysed (see Fig. 6.11). The width of the resonance peak, which corresponds to a quality factor of equivalent RLC circuit, is connected to the plasma properties such as the plasma length z_{p}.

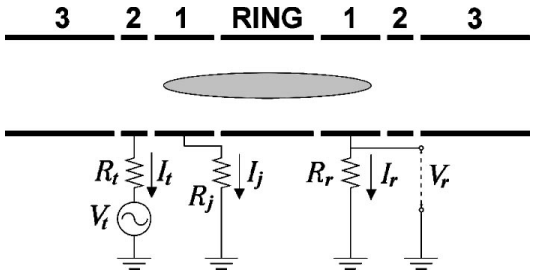

Figure 6.11: The radio frequency is applied to the transmission electrode and the signal is picked up by the receiver electrode. R_j denotes the resistance of electrodes not used for detection. Figure from [178].

The proposed non-destructive diagnostics for PUMA uses resonant plasma modes. To measure the plasma density n and the aspect ratio α, one has to find the frequencies ω_l of the plasma modes. A way to do this is to sweep the frequency range around the expected resonance frequency and record the response of the system.

This can be done by connecting a vector network analyzer to two of the electrodes. The network analyzer supplies a driving signal to one electrode and records the amplitude and phase of the signal induced on another electrode relative to the driving signal. This leads to a spectrum like the one shown in Fig. 6.12. From the peaks one can deduce the resonance frequency.

We are considering a Rohde & Schwarz Vektor Network Analyzer ZNB4 (2 ports, 9 kHz - 4.5 kHz) with an extended power range down to -80 dBm (ZNB4-B22).

The driving voltages are low ($\sim$ 100 µV) compared to the trap potential ($\sim$ 100 V). The excited motion of the plasma will therefore be small compared to the trap dimensions, and the effect of the non-destructive diagnostics on the overall evolution of the plasma can be neglected [180]. Table 6.1 gives frequencies for the (1,0) dipole mode for particles in the PUMA trap. The values are estimated via

$$\omega_1 = \omega_{\mathrm{z}} = \sqrt{\frac{qU}{md^2}} \tag{6.24}$$

with the on-axis potential $U = 250\,\mathrm{V}$ and characteristic trap size $d^2 = 1.35{\times}10^{-3}\,\mathrm{m}^2$. Rough values for the (2,0) quadrupole mode can be obtained by looking at the solution of the dispersion relation (eq. 6.10) in Fig. 6.13. The ATRAP collaboration developed a similar approach to measure the total number of charges with resonant plasma modes [154].

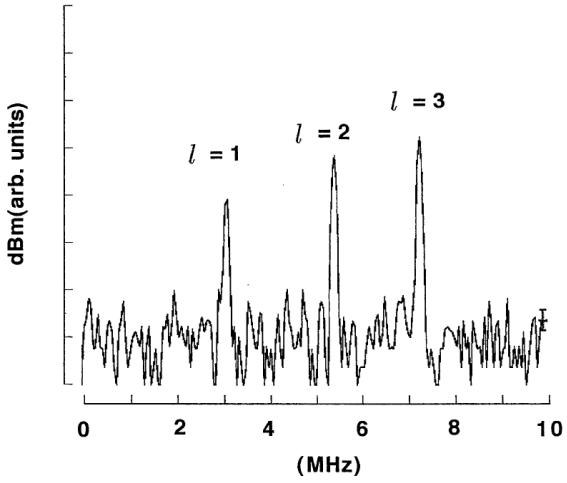

Figure 6.12: The spectrum of several plasma modes. Here, three plasma modes are excited. The peaks correspond to the indicated modes. Figure from [179].

Table 6.1: Rough estimates on the expected (1,0) dipole plasma frequencies for different particles.

Particle	(1,0) dipole frequency f_1	(2,0) quadrupole frequency f_2
e^-	29 MHz	44 MHz
$p, \bar{p}$	670 kHz	1 MHz
He^+	335 kHz	500 kHz

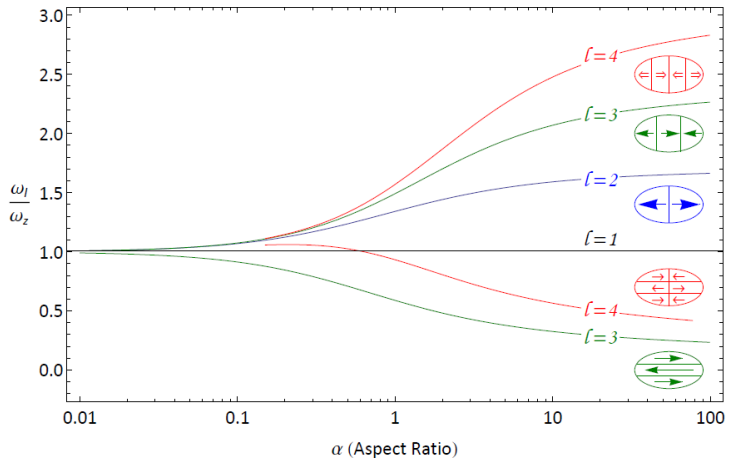

Figure 6.13: Ratio of the mode frequency ω_l to ω_z as a function of the aspect ratio α. Figure adapted from [181].

6.4 Ancillary Equipment

In addition to the electrodes and a superconducting magnet, a number of ancillary components are needed to conduct the experiment. Detectors to monitor annihilation rate and determine the number of trapped charged particles are needed for the actual measurement.

6.4.1 Cold Field-Emission Electron Source

An electron source is needed for PUMA to cool the antiprotons. Electrons can also be used to test the basic operations of the trap offline without using antiprotons. To produce the electrons, a cold field-emission electron source will be used. Such an electron source was first proposed by Crewe et al. in 1968 [182]. It is based on the principle of cold field-emission. In contrast to conventional electron sources that produce electrons via a hot filament, a field emission electron source does not introduce a heat source into the cryogenic environment. This is important as the PUMA trap will be cooled to 4.2 K. In return, the cold field emission requires ultra high vacuum in the order of 10^{-9} mbar, already provided in the PUMA design. To emit an electron out of a metal surface, the electron has to be given energy at least equal to the corresponding work function ϕ of the metal. In an electron source with a hot filament this is provided via thermal energy. To use field emission, a sufficient voltage is applied between a sharp point of the metal and an extraction electrode, so that the potential drops outside the metal. This makes it possible for the electrons to tunnel out of the material.

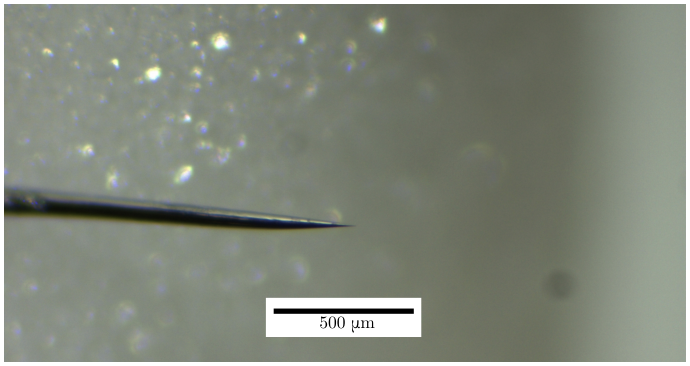

Figure 6.14: A field emission point examined with a light microscope.

With a field emission point (see Fig. 6.14) currents between 10 nA and 100 nA can be extracted with an applied voltage of between 0.5 kV and 1.5 kV [183]. The electrons are emitted from the field emission point with energies close to the Fermi energy [184, 185], and therefore their energy is dominated by the voltage applied to the tip. The electron gun has been designed, but the production of the field emission points requires further development to achieve sufficient sharpness of the tip.

6.4.2 Faraday Cup

To measure the total charge, and therefore the number of charges of the sample, a very simple destructive measurement can be done by using a Faraday cup. Here, the charges are collected on a metal plate and amplified in a charge sensitive preamplifier (AmpTek A250CF CoolFET). The output signal can be read with an oscilloscope. While an absolute measurement of the number of antiprotons is difficult, as the annihilation products may carry away charge [186], a relative measurement is possible. The Faraday cup, as well as the electron source will be located at the end of the storage trap.

6.4.3 Micro-Channel Plate

A way to get the radial distribution of the antiproton cloud is to use a micro-channel plate (MCP). An MCP consists of one or more plates with micro channels that have a diameter $d \sim$10 µm and a small ($5 \ldots 15°$) bias angle to an axis perpendicular to the plate surface. In each channel the incoming charge hits the wall and releases secondary electrons, leading to amplification. The amplification factor can be set by changing the voltage applied between the MCP's surfaces. By stacking two or more MCPs the amplification gain can be increased. For this, the channels are angled in the opposite way, so the channels form a V shape. This configuration is called Chevron type. A standard MCP assembly with two plates has a gain of up to 10^7. The multiplied charges can be converted to light with a phosphor screen and then imaged with a CCD camera. The AEGIS collaboration achieved a resolution of 14 µm [187].

Using an MCP in a strong magnetic field requires additional considerations. The magnetic field significantly reduces the gain of the MCP [161, 188]. Also the MCP assembly must be made of non-magnetic material. Some MCPs can be used in magnetic fields up to 2 T. In order to keep sufficient gain, small MCP channels and small bias angles ($< 15°$) are recommended [188]. We choose a channel diameter of 6 µm and a bias angle of 12 degrees. The charged particles extracted from the trap follow the magnetic field lines. Because the MCP will be located outside of the solenoid at the entrance of the trap, the extracted particles will be guided along the diverging magnetic field. This leads to a magnification of the radial profile of the plasma.

In the case of PUMA, the particles start at a magnetic field of 4 T and hit the MCP at about T. The MCP will be placed on a movable ladder at the entrance of the collision trap and pumping barrier.

An estimation of the number of electrons produced on the optical sensor of the read-out camera (Thorlabs CS505MU) shows that a single particle can be detected. Considered were the MCP gain, the conversion factor of the phosphor screen (phosphor type P47), the collection efficiency of the optics and the quantum efficiency of the camera.

6.5 Cryogenic apparatus

The whole PUMA trap tower must be kept at a temperature of 4 K to achieve XHV conditions, and thus to store antiprotons for several months. PUMA proposes to built the system completely free of cryogenic liquids to ease safety conditions during transportation. Cryogen-free system has additional advantage to reduce cost of exhausting liquid helium. The cryostat is cooled by two 4 K pulsed-tube cryocoolers provided by SUMITOMO industries, SRP-182B2S and SRP-082B2. The first stage of the pulsed-tube cryocoolers have a cooling power of 1.5 W and 1 W at 4 K respectively. The pulsed-tube type cryocoolers can suppress vibrations transmitted to the cryostat compared to GM type cryocooler. The PUMA trap is inserted into a 4 K vacuum chamber made of Cu-OFHC connected to the first stage of the cryocoolers. The 4 K chamber is surrounded by 70 K thermal shield made of aluminum connected to the second stage of the cryocooler. Thermal insulator foils made of aluminized mylar will be additionally used to cut radiation from 300 K. Each stage of the cryostat will be supported by the low thermal insulating material such as Kevlar, titanium, and G10. A similar cryostat was developed by the BASE collaboration [189]. The cryocoolers will be supplied with cooling water from the water-to-air heat exchanging chiller during transportation.

6.6 The trap prototype at TU Darmstadt

The trap prototype will be the main tool for the upcoming developments at TU Darmstadt. The key idea of this setup is to investigate the properties of a non-neutral plasma in a trap which is similar to the storage trap in our final apparatus. To do so, we plan to start with a single-species plasma consisting of electrons, which are provided by a cold field emission point (FEP). The prototype will have the same construction as the storage trap. We plan to develop the trap at 300 K as a first step and then proceed to cool down the to 4 K. The ring electrode and insulators are made of cryogenic compatible material, namely Cu-OFHC and pure sapphire. A 3-T superconducting solenoid has been installed at TU Darmstadt, with warm-bore diameter of 30 cm and axial length of 50 cm. The solenoid has a homogeneity of 2 % within cylinder of axial length 50 cm and 30 cm diameter. This makes our prototype ideal to test the properties of non-neutral plasmas and to gain experience handling such devices in Darmstadt with the group.

6.6.1 Foreseen developments

- align the trap relative to the magnetic field low-energy electrons
- accumulate as many electrons as possible in a predefined trap potential
  - add electrons to the trap, while a loss of the stored particles is minimized
  - measure the total charge of the stored plasma by transporting the plasma from the trap onto the Faraday cup.

  - transportation has to be adiabatic to avoid heating, which might distort the plasma shape

- test the manipulation of the electron plasma in the trap
  - fractional extraction from the non-neutral plasma
  - optimise amplitude and frequency of rotating wall technique
  - determine the relevant mode frequencies for the non-destructive diagnostics
  - compare the plasma properties to measurements with the destructive diagnostics

- investigate the behaviour of mixed-species plasmas by introducing light and positively-charged ions
  - nested potential for oppositely charged particles
  - derive the lifetime of the mixed plasma considering charge recombination

- transport test of the filled final trap
  - estimate the impact of vibrations during the entire operation

Chapter 7

Detection

7.1 Overview

The detection system previewed for PUMA is made up of two parts: One for the storage zone and one for the collision zone. Both parts are within the 4–Tesla PUMA solenoid. The signals are transported via low capacitance cables to a common data acquisition system with the front and back end electronics being housed outside the magnetic field.

The detection system in the collision zone consists of a Time Projection Chamber (TPC) around the collision trap, surrounded by a barrel made up of scintillator axial plastic bars read out by Silicon Photomultipliers (SiPMs). A sketch of the proposed setup is presented in Fig. 7.1. After the annihilation takes place in the collision trap, energetic pions are produced. The charged particles traverse the gas volume of the TPC and ionize the atoms of the gas mixture along their trajectory. The released electrons drift towards the anode plane driven by an electric field applied between the endplates of the TPC. At the anode plane, the electrons are collected on the readout pads which are oriented facing the drift direction. Because the electron signal from the primary ionization process is very low, it is amplified before collection by means of a Micromegas detector with a resistive Kapton layer [190, 191].

In addition to the system described in the collision region, a detection system in the storage region monitors the antiproton decay rate: it allows a measure of the pressure in the zone and it will also measure the position of the decay. The system consists of two plastic barrels surrounding the storage zone. The detection of the pions in the inner and outer barrel for each decay will provide information of the position of the decay.

In order to optimize the geometrical acceptance and the detection efficiency, simulations based on the Geant4 toolkit [192] as well as the analysis using the ROOT framework [193] have been carried out. They consist of three main blocks:

- The simulation of the detector and the generation of the pions corresponding to realistic events in the trap.
- The drift of the ionization electrons towards the pad plane.

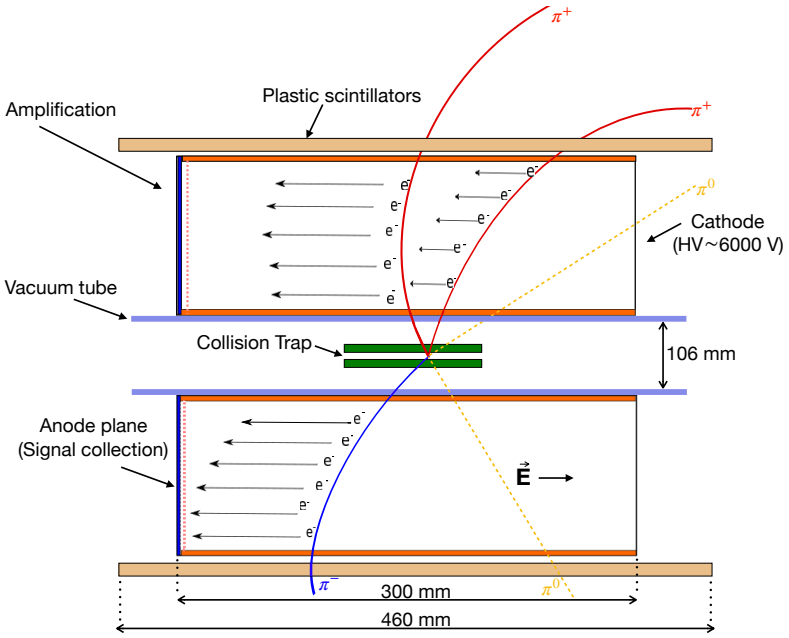

Figure 7.1: Sketch of the detection system. The trap cryostat and vacuum chambers are not shown.

- The identification of the vertex and the charge of the pions by the bending of the tracks in the magnetic field, based on the method validated by the MINOS collaboration [194, 195].

Details are described in the following sections.

7.2 Efficiencies and resolution

7.2.1 Event generator

Each event produced in the simulation consists of a set of pions randomly generated according to the appropriate branching ratios of antiproton–neutron [196] and antiproton–proton [197] annihilations. The total kinetic energy that satisfies energy conservation is isotropically shared among final–state pions. The energy distribution of the pions at the creation vertex, obtained from the simulation, is depicted in Fig 7.2.

Afterwards, the energy loss of the particles in the TPC (10–15 keV with a track-length of ∼15 cm) as well as the interaction points of the particles in the gas are calculated with Geant4, information used to implement the electron drift. Fig. 7.3 presents a typical event in the collision trap surrounded by the TPC and the plastic barrel.

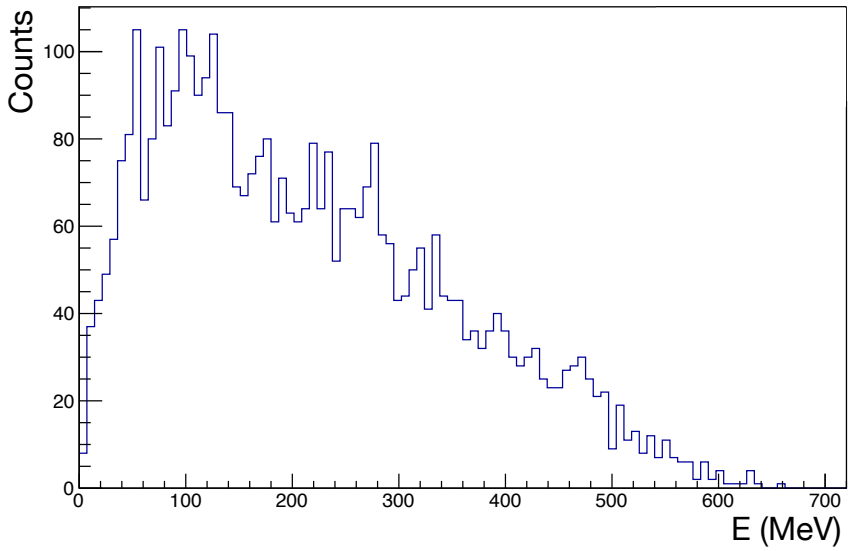

Figure 7.2: Kinetic energy distribution of charged pions at the vertex.

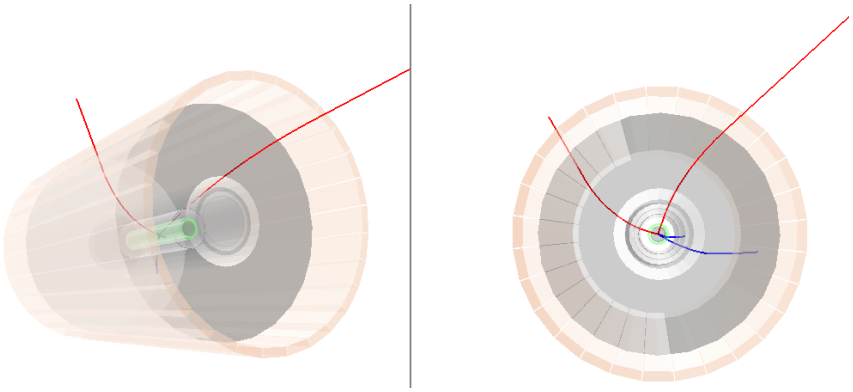

Figure 7.3: Typical event simulated with the Geant4 toolkit. The blue line corresponds to a π^- and the red ones to π^+.

7.2.2 Drift of electrons

In the active volume of the TPC, the energy loss is calculated at each interaction point of a charged particle with the sensitive gas. The number of primary ionization electrons at a given point is randomly generated following a Gaussian distribution centered in the ratio of the energy loss at that point over the mean energy of an electron–ion pair creation. The variance is given by the mean value multiplied by the fano factor, which varies according to the gas used [198].

The final position of each of these primary electrons in the anode plane (XY plane) also follows a Gaussian distribution, centered at the creation point (x_0,y_0,z_0):

$$P_i = \frac{1}{\sqrt{2\pi}\sigma_T} e^{-\frac{(i-i_0)^2}{2\sigma_T^2}}$$

Where $i = x, y$, $\sigma_{\mathrm{T}} = \mathrm{D_T}\sqrt{z_0}$ and $\mathrm{D_T}$ is the transverse diffusion coefficient.

Similarly, along the drift direction (Z), the probability distribution considers instead the longitudinal diffusion coefficient D_L, with $\sigma_L = D_L\sqrt{z_0}$

$$P_z = \frac{1}{\sqrt{2\pi}\sigma_L} e^{-\frac{(z-z_0)^2}{2\sigma_L^2}}$$

The transport parameters used in this simulation (namely the drift velocity, D_T and D_L) were calculated beforehand with Magboltz [199] in the conditions of the experiment for different gas mixtures (see section 7.2.5).

Each electron amplified in the Micromegas detector is simulated considering a random gain following a Polya distribution [200] with a mean value corresponding to the expected gain for each gas mixture simulated. In the case where the resistive foil is included, the amplified charge is diffused over the foil (which is glued to the anode plane), following the Telegraph equation [201] (see section 7.4.1).

The anode plane is segmented into rectangular pads of constant size in which the response of the electronics system is simulated. The model used was developed and validated in the MINOS experiment [194]. The signal is sampled in time and a noise corresponding to the capacitance of the cable length of 1 m (60 pF) is added to each sample. A threshold is applied to select pads for which the signal is larger than five times the σ r.m.s. of the noise, estimated tentatively to 2500 electrons.

7.2.3 Tracking method

The correct determination of the charge of the pions is key to determine which type of nucleon was annihilated on the surface of the nuclei ($\bar{p}p$ or $\bar{p}n$). Charged particles in an electromagnetic field experience a curvature in their trajectory following the Lorentz force

$$\mathbf{F} = q(\mathbf{E} + \mathbf{v} \times \mathbf{B}).$$

If a uniform magnetic field $\mathbf{B}$ perpendicular to the velocity $\mathbf{v}$ of the particle is applied, then the force $\mathbf{F}$ will be orthogonal to both quantities at each instant, making its trajectory circular. The direction of motion will only depend on the charge q of the particle, making it possible to differentiate π^+ from π^-. If, in addition, an electric field $\mathbf{E}$ parallel to $\mathbf{B}$ is applied, the final motion of the charged particle will become helical.

For this reason, a track reconstruction software to determine the direction of the particle's trajectory in the XY plane is implemented. To that end, each track is fitted with the circle equation using the MINUIT tool with the MIGRAD minimizer [202]: The data points considered are the center of each pad that was hit weighted by the charge it collected. An additional constraint for the minimization is that the track should arrive from the center of the trap, meaning that the XY origin is an extra point added to every track. Figure 7.4 shows an example of a fitted track.

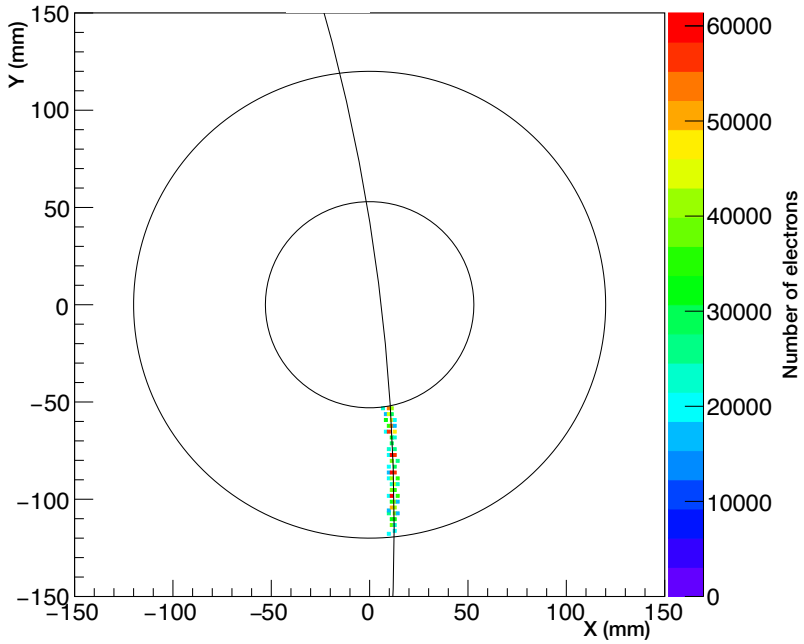

Figure 7.4: Two-dimensional charge distribution collected of one track after the drift of electrons following an event. The vertical line represents the fitted curve (a section of a circle) on the track.

7.2.4 Efficiencies

The TPC geometry needed to maximize the detection is explored considering three main parameters: the TPC external radius R, its length L and the pads size.

We define the total efficiency as

$$\varepsilon_{\text{tot}} = \varepsilon_{\text{TPC}} \cdot \varepsilon_{\text{ID}}$$

where ε_{TPC} corresponds to the ratio of the number of pions that deposited energy in the TPC with respect to those that were generated in the trap (in other words, they were within the TPC's geometrical acceptance and not absorbed by the surrounding materials). The variable ε_{ID} is the ratio of the number of particles whose charge was correctly identified by the analysis software implemented over the total number of tracked pions.

TPC length

Figure 7.5 displays the efficiencies ε_{tot} (triangles), ε_{TPC} (squares) and ε_{ID} (circles) obtained as a function of the length of the TPC after the simulation of 1500 events per point, corresponding to roughly 3500 pions. The material from which the trap is made of as well as the rest of the components surrounding the trap (such as the electrodes and the aluminum shields, described in Chapter 6) were simulated. The external radius of the TPC used for this simulation was R=140 mm and a point-like

plasma cloud was used. The pads dimensions used were 3 mm of height and 2 mm of width. The resistive foil was not considered.

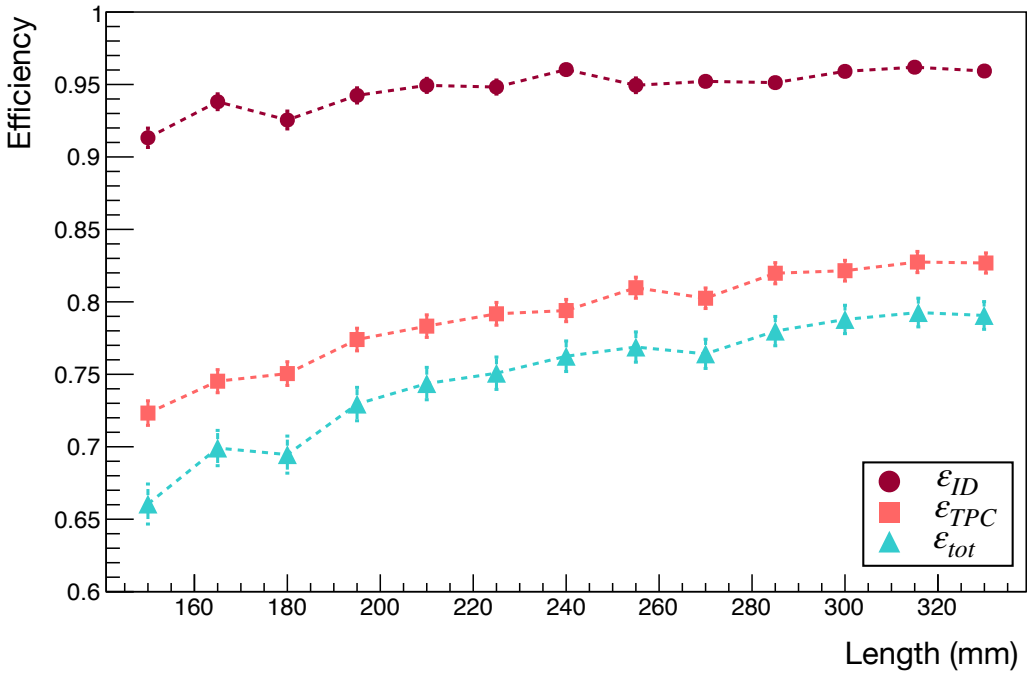

Figure 7.5: Efficiencies ε_{tot} (triangles), ε_{TPC} (squares) and ε_{ID} (circles) as a function of the length of the TPC. The error bars correspond to statistical uncertainty from the simulation.

It is observed that the determination of the pion's charge (ε_{ID}) under this conditions is ∼95% and the limiting quantity in this case is ε_{TPC}. A plateau beyond ∼280 mm is observed, therefore we consider that the total efficiency of ∼78% reached for a TPC of 300 mm length is close on an optimal value.

TPC external radius

The TPC internal radius R_{int}=53 mm is fixed by the dimensions of the trap. Simulating the detection efficiency as a function of its external radius is relevant for the evaluation of the dimensions of the plastic barrel as well as for reducing costs.

Figure 7.6 shows the efficiencies obtained in the same conditions as for the length study, considering a length L=300 mm. The red curve (squares) corresponds to the aforementioned ε_{TPC} which, as expected, remains constant. The absorption probability of a pion depends only on the materials the particle traverses during its path towards the TPC sensitive gas, and the geometrical acceptance only depends on its length. An increase is observed on the charge identification efficiency ε_{ID} (circles) due to an increase of the track length as the radius enlarges. A plateau is

reached at R∼110 mm, which determines the minimum radius that the TPC should have, and the value under consideration is R=120 mm.

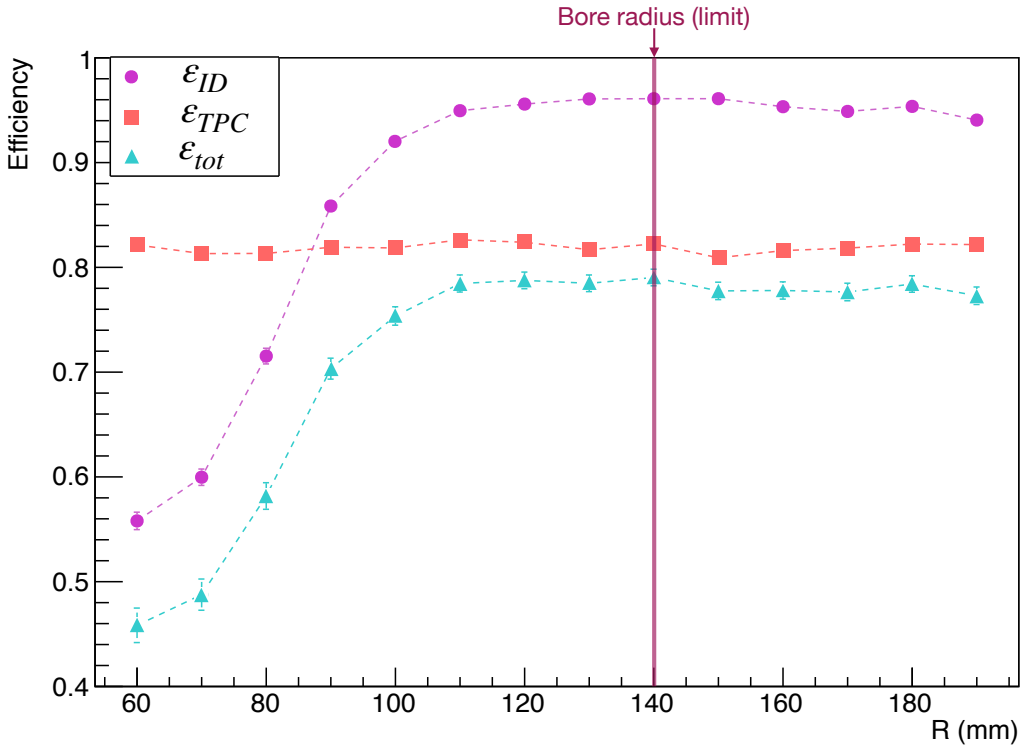

Figure 7.6: Efficiencies ε_{tot} (triangles), ε_{TPC} (squares) and ε_{ID} (circles) as a function of the external radius of the TPC. The error bars correspond to statistical uncertainty from the simulation.

Pad size

The choice of the pad size should be a compromise between the TPC performance and the number of channels foreseen to be used in terms of available space for connectors. Considering that the geometry of the pads will be rectangular, Fig. 7.7 shows the total efficiency ε_{tot} obtained for pad sizes from 2×2 to 5×5 mm^2, where each curve is the pad length in the direction parallel to the radial axis of the TPC (called *dr*) and its perpendicular direction (*dl*). The error bars correspond to statistical error.

It is observed that the largest difference in dl is ∼ 5%, at dr=3, and in *dr* is ∼ 2%, at dl=4 and that the efficiency increases at smaller sizes. Taking this into account, the pad sizes considered from this study are dl=2mm×dr=4 mm, dl=3mm×dr=3 mm, dl=3mm×dr=4 mm and dl=3mm×dr=5 mm which would correspond to 4269, 3955, 2844 and 2324 channels respectively, for a TPC with an external radius of 120 mm.

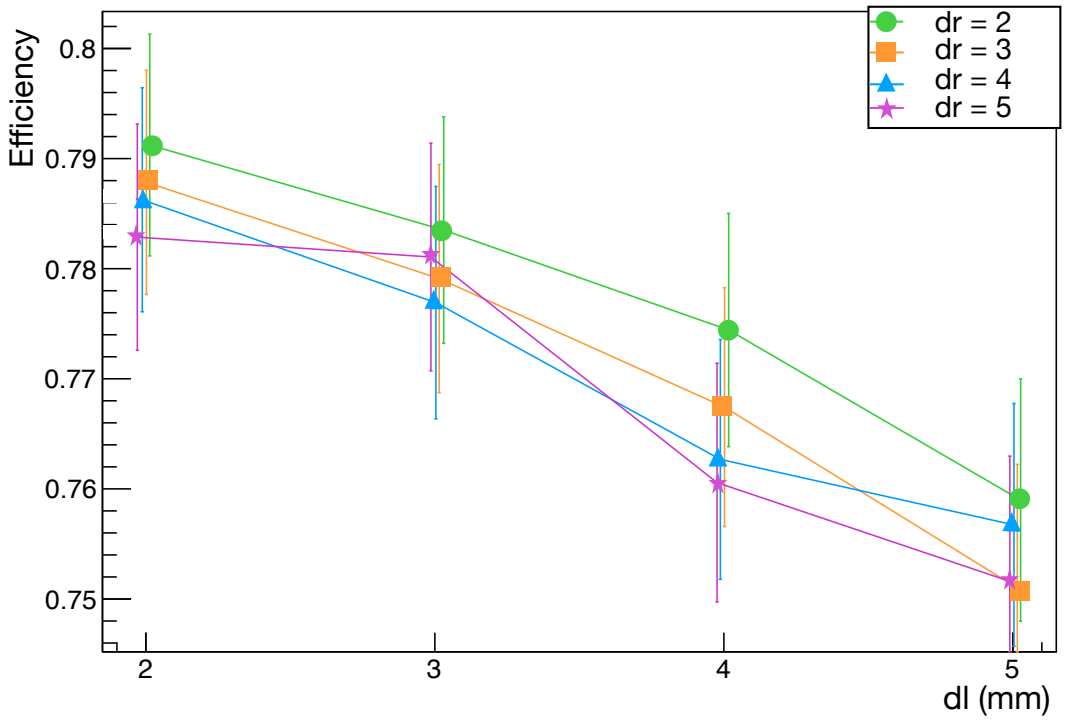

Figure 7.7: Efficiency obtained for different pad sizes.

7.2.5 Choice of gas

The choice of the gas for the TPC is a trade-off between electron transverse and longitudinal diffusions, electron drift velocity and maximum reachable gain. From the mentioned parameters, PUMA's event rate (10-100 Hz) does not require an ambitiously high drift velocity. Instead, more importance is given to the gain in the amplification step and the transverse diffusion coefficient, which is relevant for the centroid determination given the strong magnetic field of PUMA. Both parameters can also be influenced by the addition of a resistive layer glued to the anode plane (see section 7.4.1).

As a general rule, a noble gas is used as the 'carrier' which is mixed with a 'quencher' [203]. Mixtures of gases used in existing experiments were introduced in the simulation under the conditions of the PUMA experiment, namely a 4–Tesla magnetic field and atmospheric pressure:

- The gas mixture used for ALICE, $Ne/CO_2/N_2$ (85.7/9.5/4.8), provides low radiation length and hence low multiple scattering. As CO_2 is a weaker quencher than the most commonly used CH_4, N_2 is added to increase the stable gain limit. This ALICE mixture, however, requires an electric field several times higher than that required for Ar/CH_4 mixtures to achieve a similar drift velocity [204].

- The T2K mixture (Ar/CF_4/isobutane - 95/3/2) offers a high drift velocity at a moderate electric field, a relatively low longitudinal diffusion con-

stant of 250 µm/$\sqrt{\text{cm}}$ and a transverse diffusion coefficient of ∼20 µm/$\sqrt{\text{cm}}$ at 5 T [205].

- The MINOS experiment used the same mixture as T2K but with different proportions (82/15/3). Argon, for its low average energy required to produce one ion/electron pair (26 eV); CF_4 to speed up the electron drift velocity and lower the diffusions in the 200–300 V/cm electric field range; and Isobutane for its known quencher capabilities for the amplification avalanche [194].

Fig. 7.8 shows the total efficiency ε_{tot} obtained for these three gas mixtures as a function of the aforementioned parameter, *dl*, with a fixed length, $dr = 3$ mm.

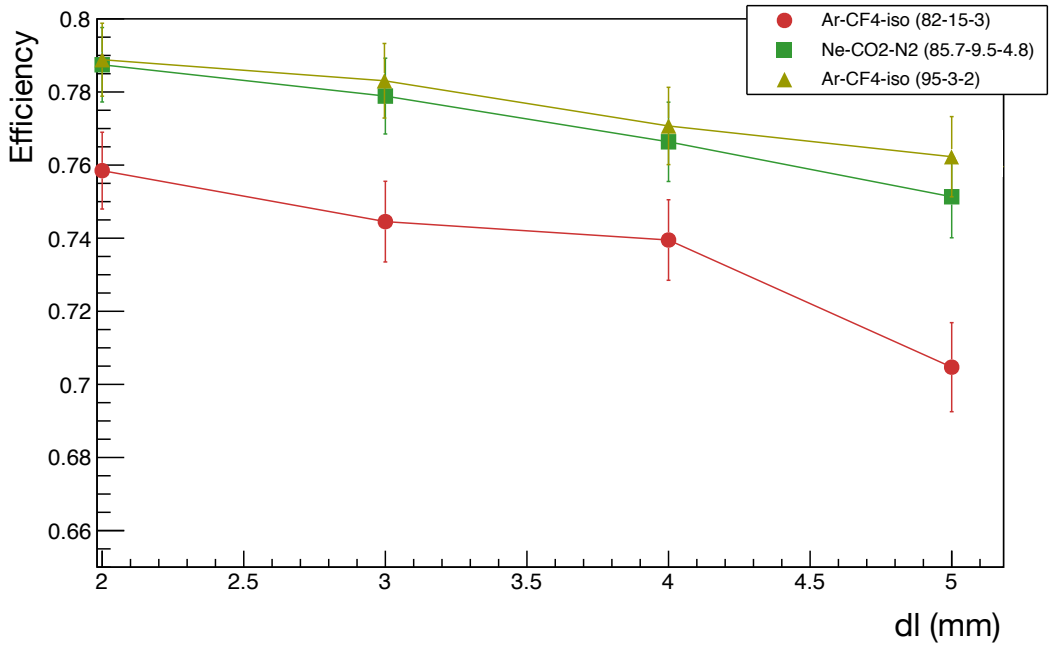

Figure 7.8: Detection efficiency obtained for the three different gas mixtures as a function of the pad width, *dl*, at a fixed pad length $dr = 3$ mm. The error bars correspond to statistical uncertainty.

It is observed that both the ALICE and the T2K gas mixtures provide a similar output, although the performance using the MINOS gas is slightly lower. In the following, we will consider a similar gas mixture to the one used for T2K.

7.3 Background rejection

The influence of atmospheric muons, product cosmic ray showers in the atmosphere, is investigated. Simulations with Geant4 have been made to determine their rate

and the rejection capabilities of PUMA.

7.3.1 Event generator

The simulation of atmospheric muons was done using the Cosmic Ray Shower library (CRY) integrated in Geant4, in which cosmic ray showers are generated from data tables and show good agreement with cosmic rays measurements [206]. The library allows to choose a set of parameters (altitude, latitude and date -to account for the eleven year, sunspot cycle-) to adjust the particle distributions to the conditions in which the experiment will work. Cosmic particles are generated in an area of $3{\times}3$ m^2 at 2 m above the detector.

7.3.2 Rate of atmospheric muons

From the simulations, the rate of muons expected to cross the TPC is $\sim$2 sec^{-1}. However, $\sim$90 % of them are rejected by adding the constraint that their track should also pass through the collision zone of the trap: In this case, after a simulation of 3 million muons, the expected rate is 8 ± 0.5 min^{-1}. Figure 7.9 shows the energy deposit in the TPC by the muons compared to that of the pions assuming a rate of 10 min^{-1} real events, where a clear cut can be seen at $\sim$30 keV and only less than 1% of the pions will have an energy deposit in the TPC similar to the muons. In addition, muons will only pollute the channels of multiplicity M = 1 and 2, which represent 30% of the total branching ratios. Considering all of these factors, it is estimated that at least 99.7% of the muons will be rejected. Moreover, it is expected to further reject muons from the track reconstruction in the z-axis during the analysis process and the measurement and subtraction of the background before the ions are introduced.

7.4 Time projection chamber design

The PUMA-TPC is being conceptually designed in collaboration with CEA-Saclay and MPGD laboratories (Section EP-DT-EF). The MPGD laboratory will build the TPC, except for the cathode which will be designed at CEA-Saclay. The TPC will be delivered functional in terms of tensions (anode, cathode and field cage) and gas seals. Testing with cosmics will be done at TU Darmstadt as of July 2020.

An important consideration with the conceptual design of the PUMA detection is the long reliability factor that is required. The reason is that the dismantling after integration and alignment to the system would entail breaking the extremely high vacuum. Hence the TPC design includes additional features when it comes to the gas supply, HT stability, mechanical stability, choice of connectors and redundancy measurements. This is seen in the field cage construction, choice of MPGD amplification, connectors, SiPM readout, etc.

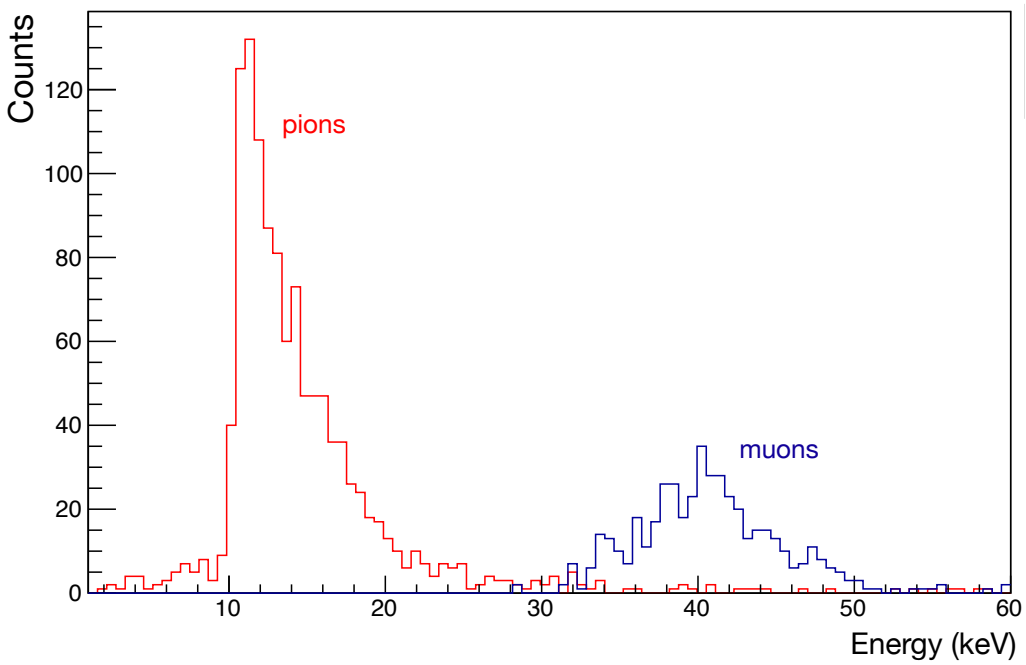

Figure 7.9: Comparison of the energy deposit in the TPC by muons and pions.

7.4.1 Micromegas amplification

A signal amplification is needed when using a TPC [203]. One of the standard options, the Micromegas detector, consists of a micromesh separated typically by 100 µm from the anode plane, where the amplification takes place by creating a strong field of ∼tens of kV/cm in this gap. As a consequence, the ionization electrons that arrive to the micromesh are accelerated and produce an avalanche of electrons, which induce a signal in the pad plane before being collected.

In particular, the technique chosen for PUMA, called the resistive Micromegas technology, contains an additional feature: it consists of gluing a thin resistive foil to the readout plane [191] (typically Kapton) and, as a result, the avalanche produced in the amplification gap will be diffused in the resistive foil following the Telegraph equation

$$\rho(r,t) = \frac{RC}{2t} e^{-r^2 RC/(4t)}$$

where RC are the resistance and capacitance respectively, determined by the spacing between the anode and the readout pads, and the dielectric constant of the glue. This provides a number of advantages:

- The resistive coating will reduce the spark frequency and hence increase the lifetime of the detector electronics. This feature is especially important since we do not intend to unmount the detector from the system once it is integrated into the trap.
- The pre-amplification stages of the electronics do not need to be protected if this technique is used.

- With the high suppression of transverse diffusion in strong magnetic fields, the track ionization charge clusters arriving at the pad plane will be confined to a single pad, therefore resulting in loss of resolution. However, the spread of the signal over a larger number of pads will enable a more accurate centroid determination.

A standard 128 µm gap between the mesh and the resistive foil will be used for amplification. Simulations of the electron amplification and diffusion in the resistive foil with typical values of R and C (R ∼1 MΩ and C ∼ a few pF) have been made, showing a small improvement of the order of 1% in the charge identification efficiency, which was already higher than 95 %, as shown in Sec. 7.2.4.

7.4.2 Field cage and mechanics

One of the challenges for the TPC is the field adjustments between the Anode and field cage so as to keep a satisfactory uniformity in the electric field, in order to eliminate the distortion in the drift velocity over all the active volume. This complexity is due to the small volume of the TPC and the relatively small available volume inside the magnet. Hence the active anode-to-field cage interface is very close (2-3 mm). A prototype was built and it is shown in Fig. 7.10. Adjustment to the final rings on the field cage might be necessary in the 'real' detector. These tests will be undertaken once the electronics have been implemented on the TPC using cosmic rays. The field cage and pad plane allows modification of the field through accessible resistors. Further resolution and stability measures will be undertaken with the full barrel cover of the TPC over approximately three months. Resolution measurements and efficiency measurements using cosmic rays will be performed.

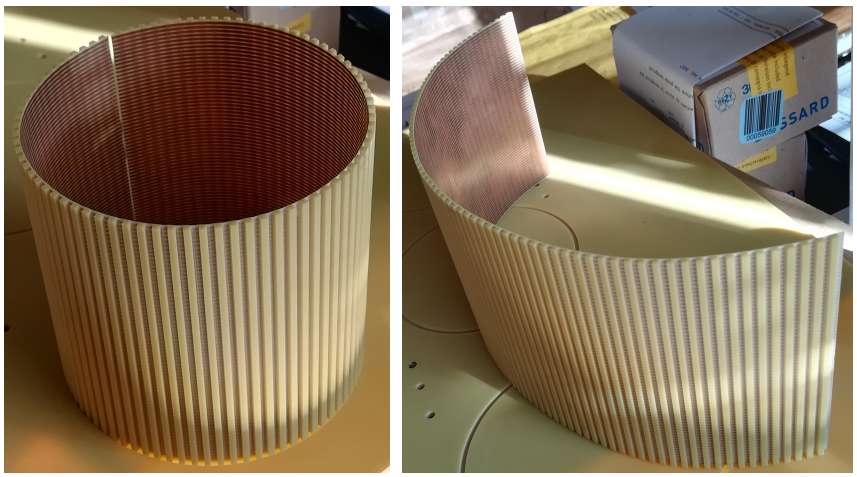

Figure 7.10: Prototype of the field cage.

7.4.3 Gas handling system

The gas system is an open-loop system where the premixed gas is provided from a standard B50 bottle. The final composition still needs to be chosen to be in

accordance with the safety regulations at CERN. In addition, the safety of the gas handling will be discussed with the safety division of CERN.

The gas flow is regulated from a flowmeter in series between the regulator of the bottle and the TPC. The pressure in the TPC relative to atmospheric pressure is kept constant with better than 0.1 mbar precision. Oxygen and water are removed from the gas with cartridges filled with a copper catalyzer. Ten l/h of mixed gas continuously flows through the TPC which has a volume of 16 l. A small amount of gas is exhausted through an analysis line which provides a measurement of the O_2 and H_2O contaminants. The exhaust will be combined with an oil-filled bubbler to avoid air back-flow. The system, schematically shown in Fig. 7.11, is arranged in functional modules distributed on shells of the frame system and on the floor of the PUMA frame. A Programmable Logic Controller (PLC) will control the system with a user interface based on National Instrument software and modules.

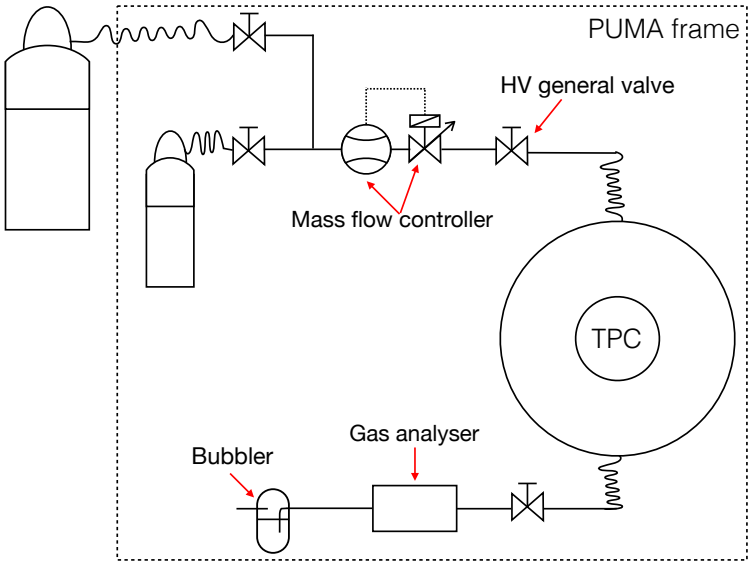

Figure 7.11: Schematic view of the gas handling system.

During transportation, the main gas bottle will be disconnected from the system and, to avoid contamination of the TPC volume during this phase, the gas system will run on a (smaller) backup gas supply attached to the frame.

7.4.4 Electronics

The PUMA detection system consists of a TPC ($<$ 5000 channels) with a plastic barrel which is read by 112 SiPMs. The storage zone is surrounded by two concentric barrels. Tests with sample cables from the Barrels and TPC are programmed, however experience from MINOS [194] at RIKEN largely covers the difficulties associated with the cable lengths needed. The trigger rate expected for PUMA is

in the range of 10 to 100 Hz. The electronics system considered suitable for such requirement relies on existing developments for TPCs [194, 207].

TPC Front-end electronics

The front-end electronics basically consist of the Front-End Cards, ARC, shown in Fig. 7.12 in its electromagnetic shield. ARC collects the analog signal from the pads through four readout Application Specific Integrated Circuits (ASICs) which is sampled in an analog memory (511-bucket switched capacitor array) and converted into digital format using a 4 channel (one per ASIC), 25 MHz 12-bit multi-channel analog-to-digital converter (ADC).

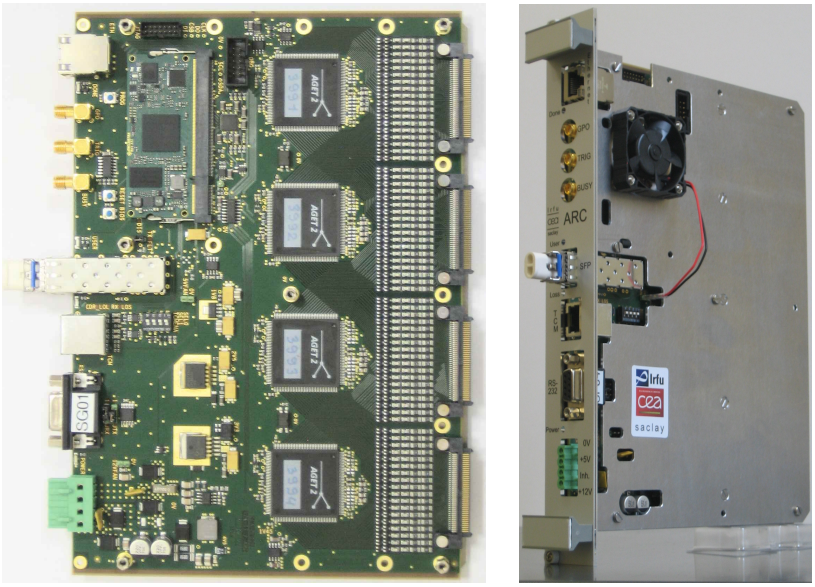

Figure 7.12: (Left) ARC front end card equipped with four AGET chip. (Right) ARC front card with the electromagnetic shield and a fan.

The system can operate with three ASIC developed at IRFU, namely AFTER [207], AGET [208] and now ASTRE [209]. All three allow for pulse shape readout up to 100 MHz. We will be deploying the last generation, ASTRE, which has recently been tested and is operational. These newer generations of chips contain 64 channels where the maximum charge, the peaking time (50 ns to 1 µs), and the sampling frequency are programmable. Additionally, AGET and ASTRE provide the possibility of self-trigger, with a discriminator in each channel for multiplicity building that allows only hit channels to be read-out, accordingly reducing dead-time. Another advantage is that charge sensitive preamplifier (CSA) has a variable gain to support the dynamic range of 120 fC to 10 pC for event rates of up to 1 kHz, which is adjustable for each channel.

Although both AGET and ASTRE are suitable for PUMA, ASTRE includes a few improvements such as radiation hardness, addition of a gain in the multiplicity

signal (2, 4 or 8 times larger) which accounts for better discrimination of the different levels, hindered before by noise fluctuations [210]. Flat cables give the input from the TPC and SiPMs. Outputs, numeric data, clock, and trigger are optically carried to the Trigger and Data Concentrator Module (TDCM) and the switch. Hence the system is reasonably well protected from electromagnetic disturbances. An assembly in crate is shown in Fig.7.13. Firmware and software codes will be tested before pre-assembly in the magnet.

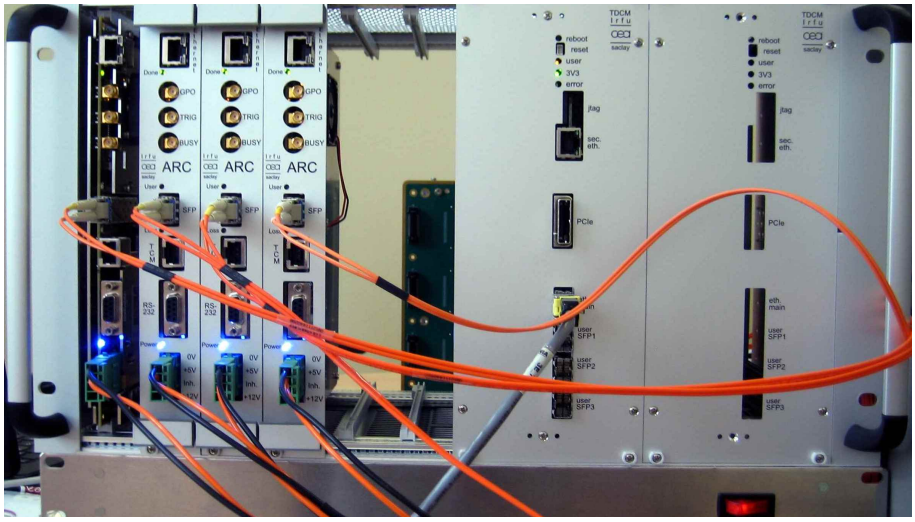

Figure 7.13: Front-end and back-end cards set within an enclosure.

Back-End electronics

The data of each detector module is transported to the back-end unit by optic fibers. The back-end consists of a TDCM, seen in Fig. 7.14, which distributes a primary reference clock to the set of front-end cards as well as a common trigger signal and global synchronization of the front-ends [211]. The TDCM is composed of two mezzanine cards (custom made board that can house up to 16 small form factor pluggable optical transceivers (SFP)) that are plugged into the carrier board of the back-end unit, a Field Programmable Gate Arrays (FPGA) module (the Mercury ZX1 commercially available from Enclustra [212]), and a main carrier board designed to carry the FPGA module and the mezzanine cards. A test setup is currently under preparation at TU Darmstadt.

For an average of 4000 pads to be read (according to the estimation made in Sec. 7.2.4), 63 chips contained in 16 front-end cards would be needed. Regarding the back-end, One TDCM module would suffice since it can host up to 8000 channels (16 front end boards per mezzanine card) A diagram of the electronics system is shown in Fig. 7.15.

Here we have not included a detailed description of the ARC+TDCM system as it has been largely documented in FEMINOS [213]. However it is important to note that ARC+TDCM is a second generation of FEMINOS and we thus expect

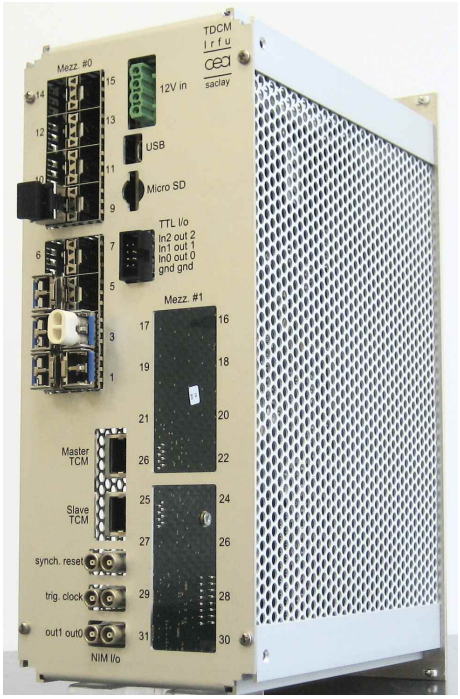

Figure 7.14: Back-end TDCM.

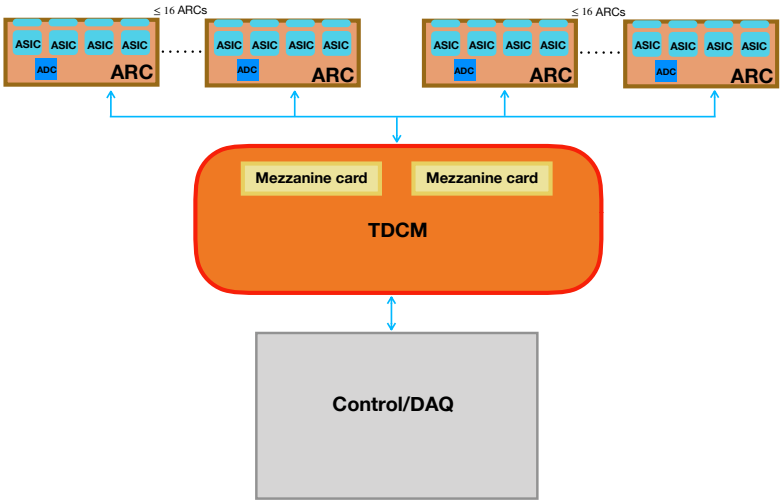

Figure 7.15: Diagram of the electronics architecture.

an enhanced performance with this novel system even though the PUMA project is less demanding both in coupling with other subsystems and in rates.

SiPM and Front-end electronics

To investigate which electronics is to be used, tests were done at CEA-Saclay where SiPMs have been coupled directly to the AGET chips, showing satisfactory results. Therefore, it is probably not necessary to introduce an external pre-amplifier to the

AGET chip. Tests with appropriate sources will confirm the choice, and preamplifiers that adapt to AGET are available on the market if necessary.

7.5 Plastic barrels

Present estimates indicate that 28 longitudinal bars will be used for the barrel surrounding the TPC and the number of bars for the two barrels in the storage zone have to be optimized. Every scintillator bar will be read off by two Silicon Photomultipliers (SiPMs) at either end.

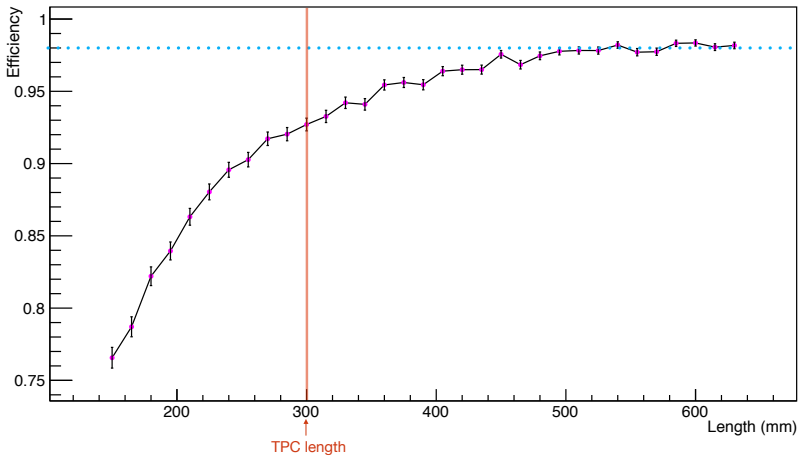

Figure 7.16: Acceptance obtained for simulated events detected in the plastic scintillators. The red vertical line shows the length of the TPC. The dotted line shows that the maximum acceptance is 0.98 from ∼450 mm, on.

The choice of plastics, geometry and SiPM are relatively standard. Nevertheless, at this stage of the project, samples of two types of plastic are being considered. Machined Trapizodial sectioned polished bars of 5 mm and 8 mm thickness bars are being purchased. Teflon and aluminised mylar will be deployed to allow minimum light cross-talk and to reach optimal light capture. Two types of sample SiPM will be tested that couple well with the plastics in terms of wavelength response. They will be glued on tapered bar and rings. Once satisfactory performance is reached, an order for the 3 barrels will be issued. The three barrels will require approx 240 channels of electronics each. The wrapping and gluing of the plastics and assembly mechanics, as well as the testing of the assembled barrels (as mentioned previously, using pulses, lasers, cosmic and sources) will be done at TU Darmstadt.

The curve presented in Fig. 7.16 corresponds to the study of the plastic's acceptance. The efficiency, in this case, is defined as 1 each time at least one particle of a given event that deposited energy in the TPC, also deposits energy in a plastic.

Considering a TPC of 300 mm long, the maximum efficiency is reached for length of ∼450 mm.

7.6 Foreseen developments

- TPC will be built at the EP-DT-EF (CERN) laboratory (R. de Oliviera) and will be ready in July 2020.
- A prototype test will be done using cosmic muons for approximately 3 months to establish reliability and performance in 2020.
- The online acquisition software will be fully developed by the end of 2019.
- Further study and simulations to evaluate the influence of resistive Micromegas.
- Development of the gas system and control.
- Electronics system for the barrels and the prototype.
- Investigation on the capabilities of studying X-rays and recoil residue detection.

Chapter 8

Operation at ELENA

8.1 Possible locations

As suggested by the SPSC in its minutes of the 131^{st} meeting [8], options for the location of the experiment have been explored. The details and costs estimates are reported in the dedicated Engineering Change Request [214]. At the time the ECR was written, it was unclear if the AEgIS experiment would change location. Two options of sites at ELENA that fulfill the requirements of PUMA were investigated:

- At experimental area LNE51, currently occupied by a portion of the ASACUSA laser room, located close to the GBAR bunker.
- At the current AEgIS location (LNE02) if the AEgIS experiment is relocated.

It is now clear that the AEgiS collaboration will not request a change of location in the near future [215]. We therefore only detail in the following the option of installing PUMA in the new experimental area LNE51.

The LNE51 experimental area is the only possibility available at present (Fig. 8.1). The location is suited for the PUMA experiment and to the specific case of a movable experiment: it is indeed the closest location to the transfer gate allowing a one-step crane operation and a fast transfer.

In Figure 8.1, the wall on the left hand side of the proposed experimental area is the GBAR perimeter wall, which already exists. However, the right and front walls including the main experimental zone entrance door still need to be built with standard concrete blocks. Presently, on the right hand side of the proposed zone, the ASACUSA laser hut occupies a fraction of the surface. The laser hut would, therefore, have to be modified to leave space for the new experimental zone and space for a controlled access to the ELENA ring. The work is already started, and a new extension of the ASACUSA laser hut is already operational. About two meters of the present ASACUSA laser room still need to be removed from the new experimental area, and a new access control to be made. A possible layout of the PUMA experiment can be seen in the CAD representation in Fig. 8.2.

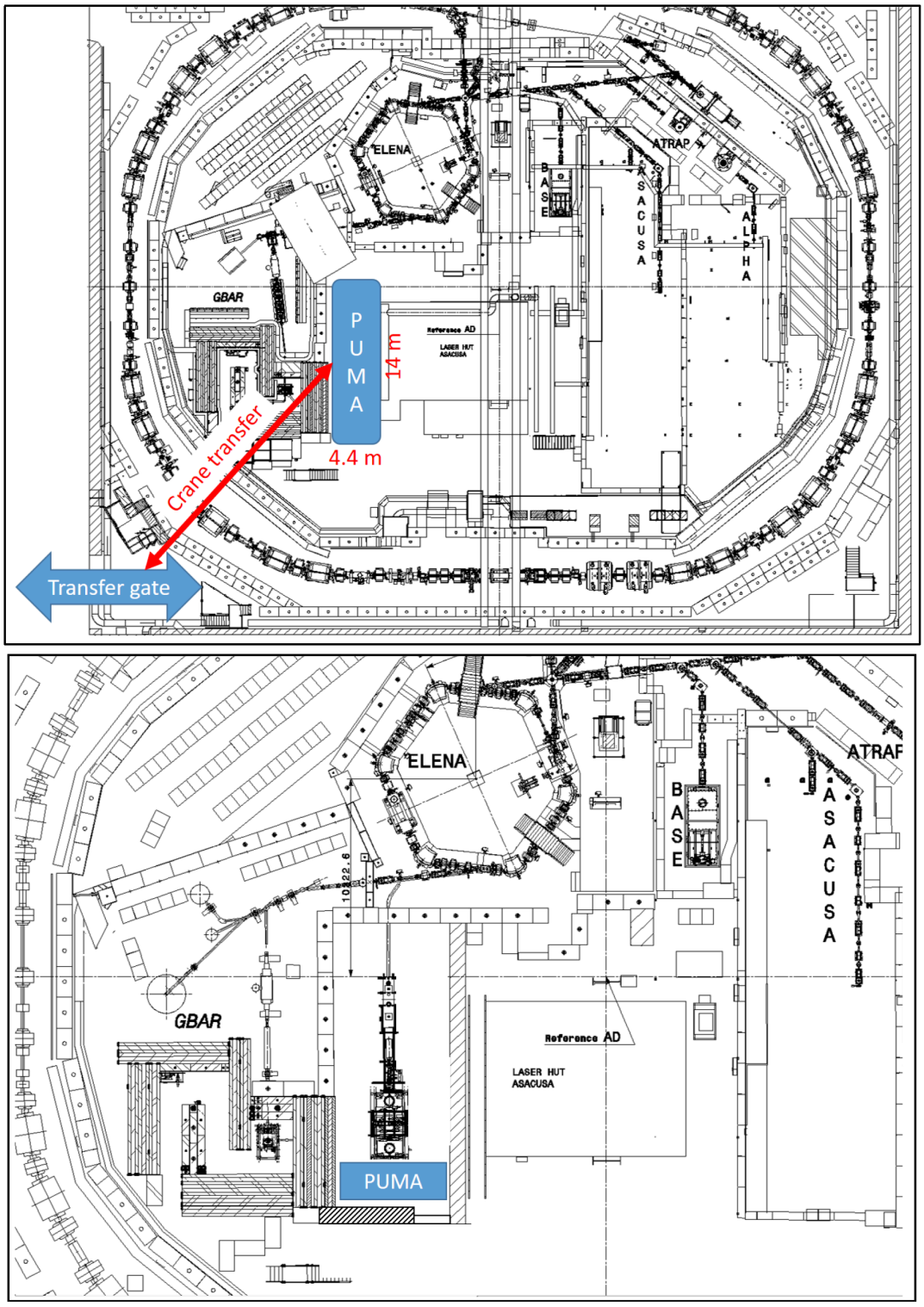

Figure 8.1: (Top) First option for PUMA at ELENA: the LNE51 zone. The available space for experiments is 14-meter long and 4.4-meter wide. (Bottom) Zoom of the LNE51 zone with a representation of PUMA on site.

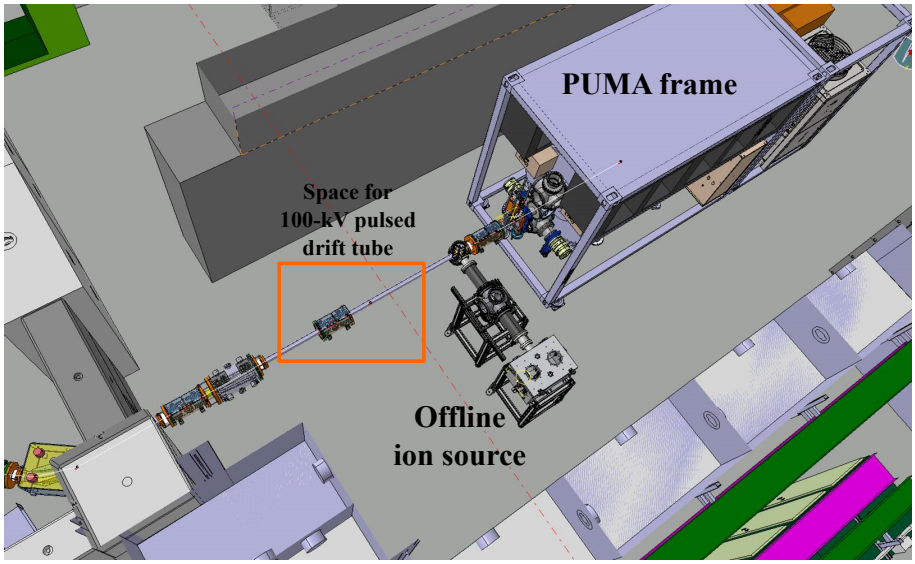

Figure 8.2: CAD drawing of the conceptional positioning of the PUMA setup at the AD.

8.2 Infrastructure

8.2.1 Electrical distribution

The PUMA experiment will have the specificity to move back and forth between the AD and ISOLDE, typically twice per year. In the AD, the trap will be transported by the 50-ton crane onto a truck located at the loading platform in front of the transfer gate. During these transport operations, a number of systems must be powered without interruption. The requirements are therefore the following:

- While sitting in the experimental area and suspended from the crane: 70 kW (40 kW at 400 V - 3 phases, and 30 kW 240 V - 1 phase).
- Vital apparatus which cannot suffer any short power outage (trap electrodes, control circuit for the solenoid) will rely on a 80 kW UPS in series with the main power grid. It is important that the disconnection and connection operations are totally transparent to the apparatus in terms of power supply since any power shortage would lead to the instantaneous loss of the antiprotons.

It is foreseen that the UPS is attached to the PUMA apparatus at all times, that would be connected either to the AD mains, to the truck generator or to the ISOLDE mains. Discussions with EL group point to a single UPS of 100 kVA attached to the PUMA apparatus at all time, that would be connected either to the AD mains, to the truck generator or to the ISOLDE mains. This UPS would then be the interface to the various power supplies and would guarantee no glitches at disconnection and connection operations. The cost of this solution is evaluated in the ECR.

8.2.2 Cooling water

Cooling water will be needed for the experiment, in particular for the cryo-coolers. The total cooling capacity required is estimated to 50 kW. The water flow will be set to 40 liters per minute and the maximum temperature of the cooling water should be limited to 29° Celsius. In case of power outage, it is foreseen that the chiller will start automatically, providing the necessary cooling for the PUMA operation.

8.2.3 Control room

A new control room is expected to be provided for the PUMA collaboration. A 45 m^2 spare room had been planned and so far kept free in 93-1-031 for new experiments at ELENA.

8.2.4 Developments and storage space

The experiment needs additional space for the storage and preparation of trap and detection parts. Two modules of 15 m^2 each are requested for PUMA developments and storage of small equipment. Additional storage capacity (70 m^2) should be accommodated somewhere else on the Meyrin site, as there is no more capacity at AD. The storage zone should allow delivery and storage of objects up to one ton and of height up to three meters.

8.3 Beamline

8.3.1 Beam from ELENA

At CERN, antiprotons are produced by colliding a 26 GeV/c proton beam onto an iridium target. A fraction of the protons interact via the reaction $p+p \rightarrow p+p+p+\bar{p}$. Collected and injected into the AD at the most favourable momentum of 3.6 GeV/c, they are then successively decelerated and cooled down to an energy of 5.3 MeV. A typical AD cycle lasts around 110s. The new Extra Low ENergy Antiproton ring (ELENA) is crucial for PUMA since a high trapping efficiency, and therefore a low-emittance low-energy bunched antiproton beam is required to store 10^9 antiprotons in a timescale of one week.

In 2018, before the second long shut down (LS2) of the LHC, ELENA successfully demonstrated the feasibility to further decelerate antiproton bunches down to 100 keV before ejection toward experiments. The ELENA ring will be able to provide up to 6×10^6 $\bar{p}$ to four experiments at the same time.

In the following of this section, the beam parameters are assumed to be consistent with those referred in Ref. [216][1]. The layout of the new line presented

[1]The momentum spread in the extraction line is taken to $\frac{\Delta p}{p} = 5.10^{-3}$. The value presented

here is similar to a layout once considered for the AEgIS relocation. The needs of PUMA are slightly different, although the main elements will remain identical. In the baseline design for LNE50 to GBAR experiment, sufficient space was allocated to install a fast switch and deflector to service other experimental stations on another beamline. Along with the integration constraints in the hall, this switch serves as the starting point for the design of the LNE51 line. To satisfy the integration constraints and match the beam to the PUMA experiment at the end of the line, four extra quadrupole units (ZQNA) are needed along with a 37.7 degree standalone deflector and the standard ZDFA-ZDSA switching unit integrated in LNE50. Two beam profile devices (SEM or BSGWA) are proposed to be installed in the LNE51 line. The last profiler should be placed immediately upstream of the vacuum valve at the handover point. The layout of the LNE51 beam line is shown schematically in Fig. 8.3.

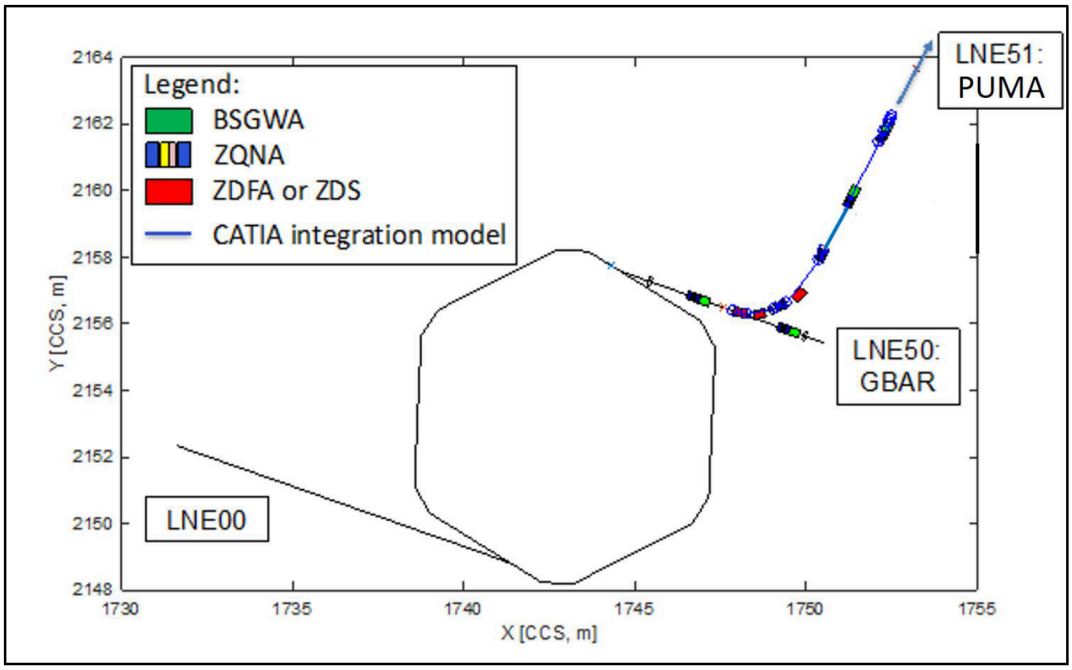

Figure 8.3: Vizualisation (CATIA integration model) of beam elements to implement between ELENA and the handover point of LNE51.

8.3.2 The pulsed drift tube (PDT)

The antiprotons from ELENA will be decelerated from 100 keV to 3 keV using the same pulsed drift tube (PDT) technique as employed by the GBAR experiment.

in Ref. [216] is assumed inside the ELENA ring and does not fit with the expected value in the LNE51 line.

This technique relies on the electrostatic deceleration of the antiprotons pulses by switching a drift tube from -97 kV to ground while particles are travelling through.

At CERN, antiparticle beams are transported at ground potential. When a beam with a kinetic energy E_i arrives in the vicinity of the drift electrode polarized at a potential V, the electric gradient at the entrance decelerates the charged particles. Inside the drift tube, antiprotons travel through with a remaining energy of $E_f = E_i - \frac{V}{e}$. Since the longitudinal potential in the tube is flat, the pulse feels no gradient of potential. The voltage applied on the drift tube can then be switched from -97 kV to ground. When exiting the tube, the decelerated antiprotons do not feel any re-accelerating gradient.

The ELENA technical design report specifies an antiproton beam emittance of 4π mm.mrad on the vertical axis and 6π mm·mrad on the horizontal one. According to Louville's theorem, the emittance of the beam will blow up during the deceleration process. To counterbalance the increase of the emittance at the tube entrance, upstream optics are necessary. The GBAR experiment uses a six electrodes pre-decelerating system designed for more flexibility in the potential shape at the entrance. Based on a similar system, simulations [217] have shown that a much simpler design based on telescopic optics should be enough. In this proposal, we propose to implement a simple and compact Einzel lens-based design at the entrance of the drift tube. A first design of the pulsed drift tube for PUMA is shown in chapter 4, Fig. 4.11.

A deceleration down to 3 keV results in an increase of the emittance of a factor 6. The PUMA project proposes a two step deceleration: first, in a dedicated apparatus, from 100 keV to 3 keV for a better beam definition and, second, using a smaller pulsed drift tube in the solenoid field from 3 keV to few hundreds of eV taking advantage of the magnetic field for the radial confinement of the antiprotons.

Past experience with pulsed tube deceleration has shown very good efficiency up to 80% with heavy ion beams [218, 219]. Such efficiency is achievable in the framework of the PUMA project.

The current preliminary design of the Pulsed Drift Tube (PDT) integrates an injection Einzel lens, the drift tube electrode and a second refocusing Einzel lens. Both Einzel lenses' electrodes have a diameter of 100 mm. Such a diameter is necessary to accept the decelerated beam without suffering incorrigible edge effects.

However, the wide opening of the electrodes requires applying higher voltages to generate a potential on the optical axis high enough to act in the desired way on the beam. According to preliminary simulations, a potential of maximum 90 kV on the optical axis is necessary to guarantee an optimal operation of the injection Einzel lens. The length is chosen as a compromise between the total length of the system and the maximum applicable voltage on the electrode. Standard electrical vacuum

feedthroughs could support until 100 kV, the length of the electrode should not be below 100 mm to generate until 90 kV potential on the optical axis. Preliminary simulations have shown that that gap size between the injection Einzel lens and the PDT has a negligible effect on the emittance downstream. The gap between the injection Einzel lens and the PDT is then taken to its minimum.

The refocusing Einzel lens is less sensitive to technical considerations since the potential applied on it is small with respect to the injection one. A simple design based on 30-mm-long cylindrical electrodes spaced by 10-mm gaps is implemented.

According to [216], the bunch length is expected to be 300 ns at 100 keV. It corresponds to a bunch length of 1.3 m. When decelerated to 5 keV, the bunch length shrinks to 29 cm. The bunch length is small compared to the 700 mm drift tube. We consider here the displacement of the ion when switching the tube[2] which represents a displacement of 20 cm and margin zones of 10 cm on each side of the tube to limit the effects induced by the edge of the potential plateau.

8.3.3 The pulsed ion source system

In order to investigate the injection conditions into the PUMA trap, we propose here to develop a pulsed ion source system. This source will offer the possibility to perform reference measurements with protons, He isotopes and other stable ions as a crucial step before the transport operations.

A hot filament source will generate ions from the ionization of different gases injected into the plasma chamber. The ionization process in the plasma chamber requires a vacuum level of the order of 10^{-3} mbar which is not compatible with the PUMA trap operation. We purchased a commercial deferentially pumped source (model IEQ 12/38 from SPECS) leading to a vacuum of about 10^{-8} mbar at the extraction of the source. The extraction potential of the source is tunable up to 5 kV. It offers a sub-millimetre beam spot at a tunable focal position.

Such ion sources do not generate a single-species beam. Other undesired ion isotopes must be separated from the ions of interest. The desired isotopes will be selected by using a Wien filter or a Multi-reflection time-of-flight mass separator (MR-ToF MS). The Wien filter selects the velocity of the particles by the association of a magnetic field and a transverse electric field. When the magnetic field tends to bend the charged particle trajectory, the electric field counterbalance this effect. It is then possible to select the desired species according its charge over mass ratio q/m and its momentum. The resolution in the species selection downstream depends largely on the shape and size of the optics. For this purpose, we propose a compact design based on the use of strong neodymium permanent magnets to generate the magnetic field. Such type of Wien filter is currently used on the GBAR

[2]A basic falling-time of 200 ns is considered as observed on 150 kV Behlke switches.

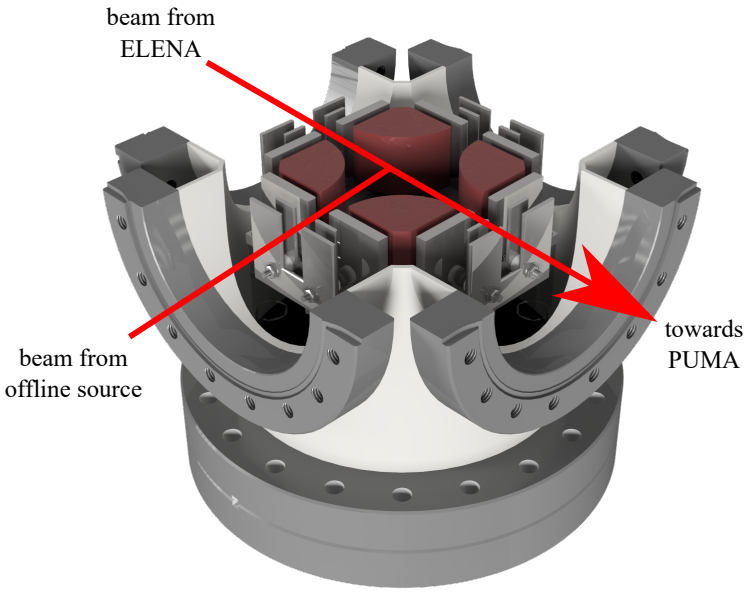

Figure 8.4: CAD representation of a quadrupole bender which is planned to be used for the implementation of the offline ion source of PUMA while being located at ELENA.

proton source system.
For a more versatile approach, an MR-ToF system will be installed in which a bunched beam from a reference ion source can be injected. The flight-path of the ions will be prolonged significantly due to the use of electrostatic mirrors. The ions are then separated in their time-of-flight because of their mass difference and a single ion species can then be extracted from it [220].

The ion source operates in a continuous beam mode which is not exploitable as such for the PUMA experiment. That is why we propose to design a beam chopper and buncher made of three meshes placed on the beam path. The outermost meshes will be kept at ground potential when the intermediate mesh will be held at a potential high enough to stop the beam. By successively turning on and off the potential applied on the intermediate mesh, the system operates as an electrostatic gate for the beam, namely a chopper. The possibility to improve the transmission efficiency into the trap is conceivable by applying a time-varying potential on the intermediate mesh following the formula $V = V_0(1 - (t/\mathrm{T})^{\mathrm{k}})$ [38] with k, the time-bunching factor; T, the half-period of the bunching pulse and V_0, the maximum potential applied.

When exiting the ion source, a fraction of the ions suffer recombination processes. This neutral component of the beam would have a damaging effect on the trapped antiproton plasma and must be removed. For this purpose, we propose to implement the pulsed source system perpendicularly to the main antiproton line. An electrostatic quadrupole bender (see Fig. 8.4) bends the ion trajectory with a 90-degree angle. Such device eliminates the residual neutral species from the beam

since only charged particles undergo the 90-degree bending. In addition, such electrostatic quadrupole will offer the opportunity to supply the PUMA trap with two different types of particles without any mechanical operations. When the electrodes of the bender are not polarized, the antiproton beam coming from ELENA will pass through it without being affected. Reversely, when the electrodes are polarized, the PUMA trap will be supplied with the ions coming from the pulsed source system.

Chapter 9

Transport and Handling

9.1 Transport from ELENA to ISOLDE

PUMA is a transportable experiment with the specific requirement to remain under operation during the transport phase since the storage of antiprotons requires the full operation of the Penning trap. The transfer of PUMA will take place between the ELENA experimental area (building 193) and the ISOLDE experimental zone (building 170).

The foreseen itinerary is 2 km long and is shown in Fig. 9.1. The heavy weight of the experiment and the expected length of the convoy prevent from considering a shorter itinerary. The current itinerary implies slopes up to 6 % in both directions.

The power consumption of PUMA is estimated to 70 kW in operation during transport (20 kW of chiller power consumption to be added to the 50 kW of on-site operation of the system). The transport time from ELENA to ISOLDE is estimated to last one to two hours. A powering exclusively from batteries is excluded. PUMA will always be connected to an external source of power.

A first operation is the transfer of the PUMA experimental from its experimental location at ELENA (see Chapter 8) to the trailer. This operation will be performed by the overhead crane. The AD hall is equipped with 50-ton cranes which are suited for this operation. The power of PUMA will be switched from the grid to a powering from the crane (see next section). Providing a 70 kW power from the crane requires a modification of the present equipment.

Once PUMA is loaded on the trailer and during transport, the experiment will be powered by an external diesel generator. A sketch of a possible truck configuration is shown in Fig. 9.2. So far, a solution that allows to compensate the road inclination along the itinerary is investigated. A simpler solution with no compensation will also be considered. The frame will be equipped to record the acceleration and vibration history of PUMA during the transport. Transport of fragile large-size objects, such as accelerating cavities, have been often performed at CERN. Note

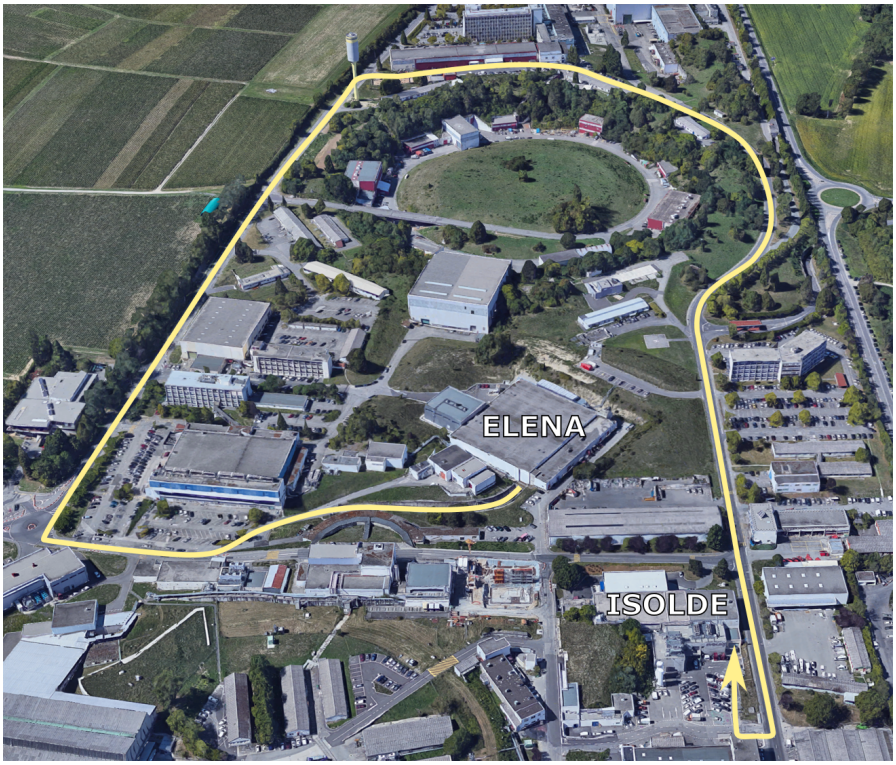

Figure 9.1: Itinerary of PUMA from ELENA to ISOLDE.

that the demonstration of transporting trapped charged particles was made more than twenty years ago: an electron cloud in a Penning trap was transported by truck over 5000 kilometers from the west coast to the east cost of the USA [221].

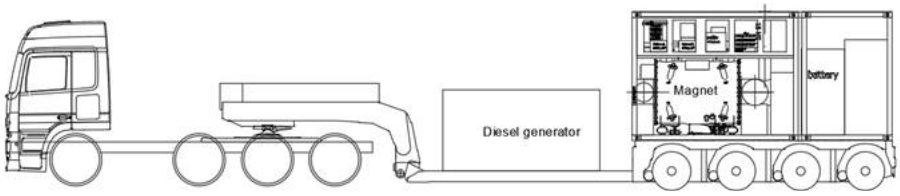

Figure 9.2: Sketch of a possible truck configuration for the transport from ELENA to ISOLDE.

9.2 Handling

The attachment system on the PUMA frame will be developed to be compatible with the cranes at ELENA and ISOLDE. The handling of PUMA has been investigated and bottlenecks have been identified:

- The maximum height available for the crane operation is limited to 3.5 m at ELENA (available space over the AD ring shielding),

- the maximum length of the PUMA frame is limited by the delivery zone at ELENA (6 meters) and by the insertion of PUMA in the ISOLDE hall.

The foreseen PUMA frame and its attachments for crane operations will fit these requirements. A preliminary study was performed for the delivery at ISOLDE (see Fig. 9.3). Before transporting antiprotons, a mock-up test with the full PUMA apparatus from ELENA to ISOLDE will be performed. Additional information on the handling and crane operation can be found in a dedicated presentation given at the PUMA collaboration workshop [222].

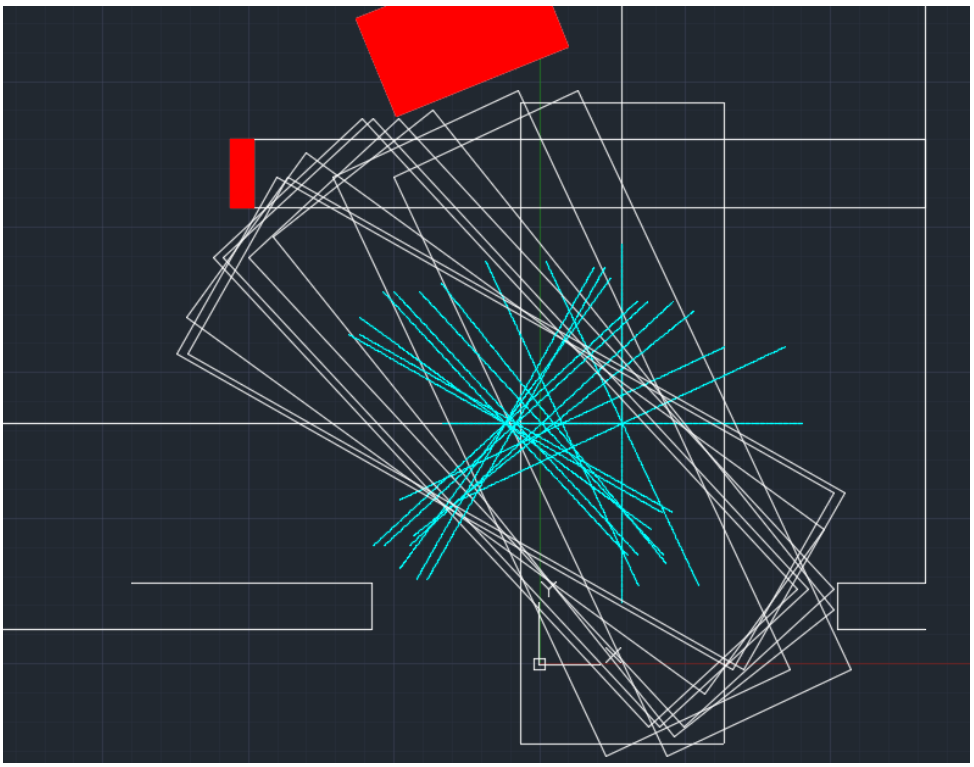

Figure 9.3: Introduction of the PUMA frame inside the ISOLDE experimental hall. The dimensions of the PUMA frame have been checked to be compatible with a safe delivery to the ISOLDE hall.

9.3 Powering scheme

The powering scheme of PUMA requires particular care since the experiment will be powered successively by five different power sources: (i) power grid of ELENA on the experimental site, (ii) power grid of ELENA from the crane during extraction to the truck, (iii) generator on the truck, (iv) power grid of ISOLDE from the crane during installation to experimental zone, (v) power grid of ISOLDE on the experimental site. In addition, PUMA requires a protection against power shortage. In 2018, many power shortage occurred at the AD, among which three were longer than 500 ms. It is worth noticing that among these three two were longer than

2 hours. The foreseen PUMA power UPS is not capable of protecting the experiment against such events. The option of connecting PUMA to the diesel generator (located in a dedicated site still to be found) within few minutes is being considered.

The PUMA powering scheme relies on an integrated UPS of 100 kW for a lifetime of 10 minutes. The UPS allows a AC-DC-AC conversion which solves any phase offset between two AC power sources. The UPS will adsorb power shortages from the grid. In addition, it provides a power buffer in case of extra transient consumption. The powering scheme is illustrated in Fig. 9.4.

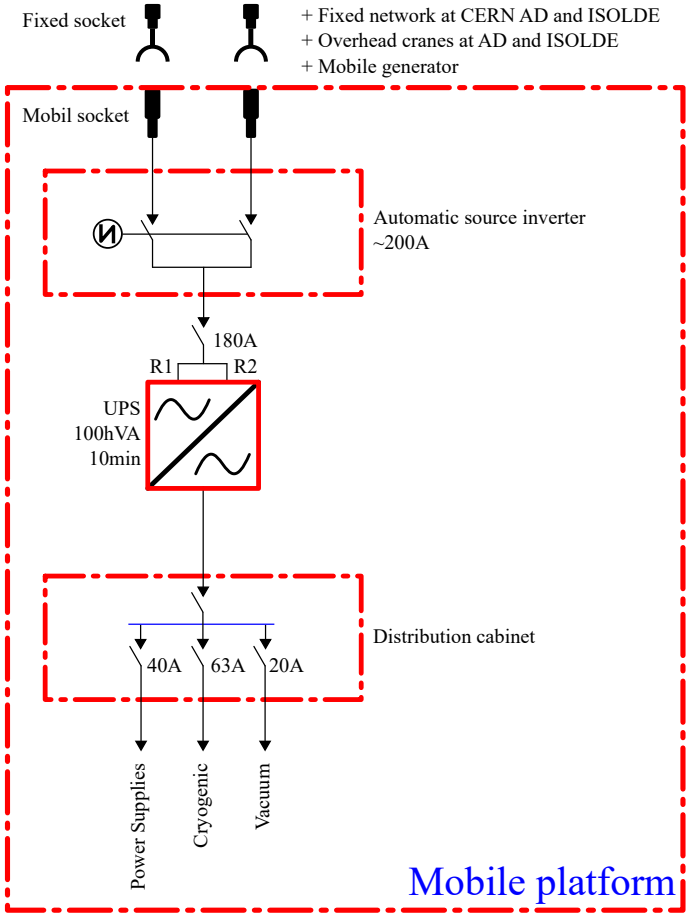

Figure 9.4: Powering scheme for the PUMA experiment. The UPS will be integrated inside the PUMA frame.

9.4 Safety and radio-protection aspects

Contacts have been taken with the Safety and Radio-protection teams of CERN to review all related aspects in PUMA. The following aspects should be considered:

- cryogenics: PUMA is free of cryogenic fluids. It is therefore considered as safe with respect of over-pressure following an unexpected warm up of the system.

- magnetic field: A moving high-field magnet can cause strong forces on magnetic material or be subject to such strong forces. We took particular care in the design of the magnet to minimize fringe fields outside the solenoid through active and passive shielding (see chapter 5). Ferromagnetic objects can become harmful projectiles if the magnetic field is above the limit where the force induced by the magnetic field overcomes the gravitational force. This limit is defined as
$$B_z \frac{\partial B_z}{\partial z} \sim 2 \times 10^{-3}\,\mathrm{T}^2 \cdot \mathrm{m}^{-1}. \tag{9.1}$$
In the case of PUMA, this condition is always satisfied outside the solenoid cryostat, while fulfilled beyond 25 cm from the cryostat edge. The condition is satisfied everywhere outside the frame of PUMA.
- high voltages: The last stage of deceleration of antiprotons at ELENA and ions at ISOLDE will be performed using pulse drift tubes on high-voltage (HV) plateforms at 100 kV and 30 kV, respectively. The access to the HV plateforms will be restricted by locked faraday cages. Access and operation procedures will follow the safety rules as applied, for example, to the HV plateform of the GBAR pulse drift tube [223].
- antimatter: No regulation exists so far for the transport of antimatter. Discussions with the radio-protection (RP) group of CERN were started, and extreme cases where all 10^9 antiprotons are lost at the same time are being investigated. First RP calculations were performed. Safe distance from the annihilation site and RP protocols are being investigated. At an unshielded distance of one meter from the annihilation of 10^9 antiprotons, the dose would be below 100 µSv [224]. A simulated fluence spectrum of particles following antiproton annihilation with iron at one meter distance is shown in Fig. 9.5.

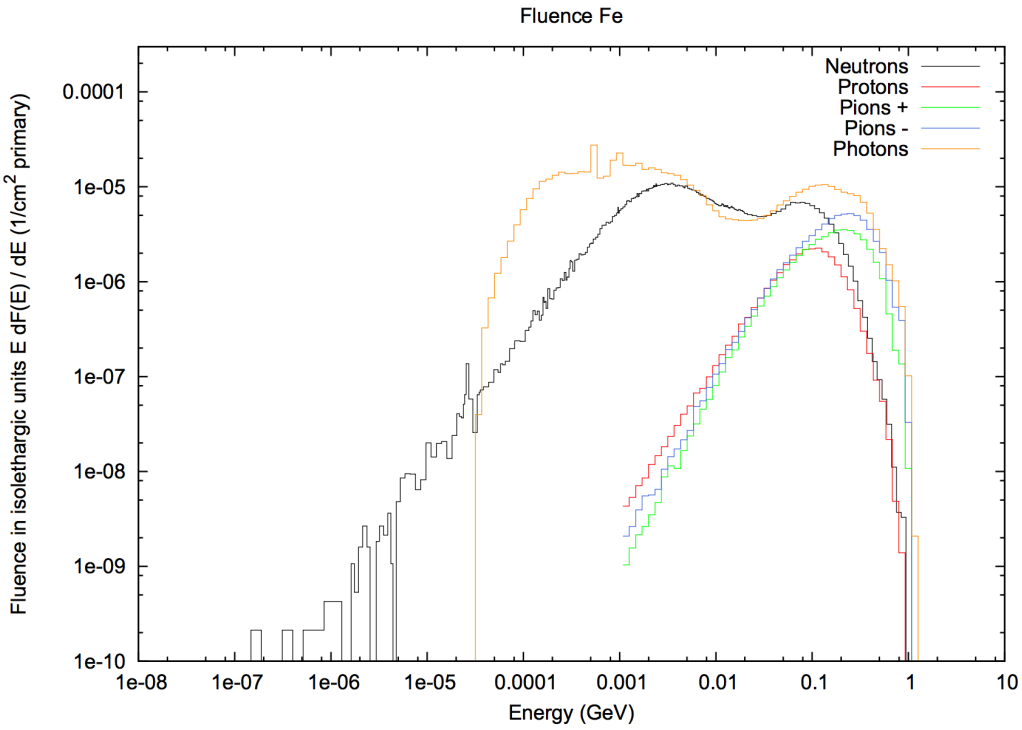

Figure 9.5: FLUKA simulation of fluence spectra of neutrons, protons, π^+, π^- and photons at one-meter distance from the annihilation point from the collision of an antiproton low-energy beam with an iron sphere.

Chapter 10

Operation at ISOLDE

In the following a brief description of ISOLDE is given and the production rates of the radioactive isotopes proposed as first physics cases for PUMA are given. The beam energy, time structure, purity and emittance requirements for PUMA are demanding. They are summarized in Tab. 10.1. These requirements can be achieved with a system similar to the ongoing MIRACLS [225, 226] project downstream the ISCOOL buncher [227]. The two apparatus are introduced, and their current status of development given. It has not been decided yet at what place PUMA will be positioned at ISOLDE. Instead, we present a currently-under-discussion location and a schematic layout which would fulfill the requirements of the PUMA experiment.

Isotopic purity	> 95 %
Beam diameter	< 5 mm
Transverse emittance at 30-60 keV	$< 50\ \pi$ mm mrad
Energy	1 - 2 keV
Energy spread	± 30 eV
Bunch length	< 15 cm
Longitudinal emittance (^{18}Ne@2 keV)	< 30 us $\cdot$ eV

Table 10.1: Requirements for the radioactive ions beams at the entrance of PUMA.

10.1 Radioactive beams at ISOLDE

The on-line isotope separation (ISOL) technique is a powerful method to produce pure low energy radioactive ion beams. In this method, high-energy light particles from accelerators or nuclear reactors impinge onto a thick heavy-ion production target. Many different isotopes are then created from several reaction mechanisms such as fission, fragmentation or spallation. The reaction products are stopped in the bulk of the target material. They then diffuse and effuse out of the heated target to an ion source section where they are ionized. Each element, with its specific chemical properties, requires an optimisation of the production target ensemble and

of the ionisation process.

ISOLDE at CERN has been a worldwide leading facility in the production of radioactive ion beams using the ISOL technique [228,229]. At ISOLDE, the radioactive isotopes are produced from the interaction of a 1.4-GeV proton beam delivered by the PS Booster at a maximum intensity of 3.2×10^{13} protons per pulse. The repetition rate is typically on the order of one Hz. Today, at ISOLDE, about 600 isotopes of more than 60 elements are available. Radiochemical methods and ionisation techniques have been developed for the majority of them. These radioactive ion beams with half-lives down to a few milliseconds can be delivered in intensities ranging from 10^{11} to 0.1 per second. In addition to the advantage of being close to ELENA, the unique range of low energy radioactive isotopes and highly competitive beam intensities make ISOLDE a perfectly suited facility where the PUMA physics program can be carried out.

ISOLDE has two on-line isotope separators with independent target-ion source systems that deliver 60-keV mass separated radioactive ion beams with a typical emittance of 25 to 35 πmm mrad [230]. The high-resolution separator (HRS) is theoretically able to separate the isotopes of interest from unwanted ions with a mass resolving power of up to 1.5×10^4 [231]. Since PUMA requires isotopically-pure beams at a level of a percent, this separation is not enough for medium-mass nuclei. This aspect is further discussed in the following. The beam intensities for the isotopes of interest to be studied with PUMA at ISOLDE are presented in Tab. 10.2.

Nuclei	Yield (ions/μC)	Target
^{6,8}He	5.4×10^7 / 4.7×10^5	BeO - UC_x
^{7,9,11}Li	8.2×10^9 / 3.9×10^6 / 1.4×10^3	UC_x
^{8}B	300	C
^{17,18}Ne	4.5×10^3 / 3.5×10^6	MgO
...	...	...
^{26,27}Ne	4.9×10^4 / 200	UC_x
$^{28,...,33,34}$Mg	3.6×10^7 / ... / 3×10^3 / 140	SiC_x / UC_x
$^{19-22}$O	1.3×10^5 / 3.4×10^4 / 7×10^3 / 1.3×10^3	UC_x
^{105}Sn	8×10^4	LaC
...	...	...
^{136,137,138}Sn	4×10^3 / 100 / 2.5	UC_x

Table 10.2: Radioactive ion beam yields and primary target material at ISOLDE facility [232] for isotopes targeted by PUMA.

With the above yields, the measurements are feasible. Note that few isotopes of particular interest are not reachable at ISOLDE: the hypothetical *p-wave* halos ^{31}Ne and ^{37}Mg are currently not sufficiently produced since their expected rates are less

than 1 s^{-1}. PUMA will benefit from any future improvement of rates at ISOLDE.

10.2 The ISCOOL buncher

In order to comply with PUMA requirements, the ISOLDE beam parameters need to be further optimized after the magnetic separation. In particular, they need to be bunched and purified, accordingly to the requirements of PUMA (see Tab. 10.1). The bunching will be performed by the existing ISCOOL cooler and buncher [227]. ISCOOL is a general purpose RFQ ion trap, located in the HRS beamline and constructed to improve the emittance of the incoming radioactive ion beams and to deliver them as bunches to the experiments. It is presented in Fig. 10.1.

The system consists of a linear Paul Trap filled with a buffer gas in which the ions thermalize through collisions with the buffer gas while the oscillating quadrupole field of the trap rods provides radial confinement [233]. The buffer gas is chosen as a noble gas to minimise charge transfer to the radioactive ions. For an efficient cooling, the mass of the buffer gas atoms should be smaller than the mass of the nuclei to cool. Light ions have to be cooled with helium or even hydrogen as a buffer gas. Currently, the ISCOOL is not able to use hydrogen as a buffer gas since specific safety considerations have to be taken into account which are envisaged in the future. In the case of PUMA, these light mass gasses causes a particular difficulty since it is difficult to remove them with vacuum pumps. The vacuum system will therefore be dimensioned and thought for Helium, together with other gases, see chapter 4. The gas volume of ISCOOL is isolated from the beam-line by two differential pumping sections which guarantee a vacuum better than 10^{-6} mbar both upstream and downstream. These vacuum conditions set the constrain for the dedicated differential pumping system for PUMA which aims at reduction better than 10^5, from 10^{-6} to better than 10^{-11} mbar at the entrance of the PUMA cryostat.

ISCOOL provides the possibility to deliver bunches of a few microseconds length, reduced energy spread ($\sim$1 eV for slow extraction) and reduced transverse beam emittance (less than 3π mm mrad at 60 keV), which allows the experiments to have a better injection of the beam into the experimental setups [235, 236] and to gate on the time structure of the beam to reduce unwanted background. In the case of PUMA, these parameters are well within the requirements except that a faster extraction is needed for light ions to provide shorter bunches (at 2 keV, a 10-cm ion bunch has a time length of 500 ns for ^{8}He, 2 μs for ^{132}Sn) suited for an efficient trapping. Such developments are considered at ISOLDE for the near future and first tests have been performed but have not been finalized yet. The different ejection methods are schematically shown in Fig. 10.2.

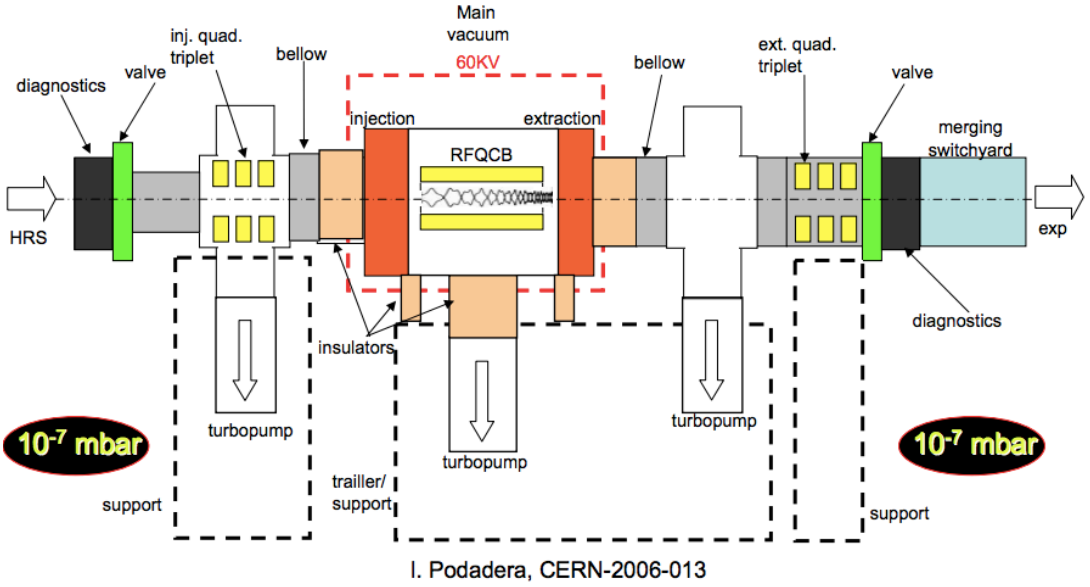

Figure 10.1: Sketch of the ISCOOL buncher. A differential pumping maintain a vacuum better than 10^{-6} mbar upstream and downstream the buncher despite the gas flow in the RFQ. Figure from [234].

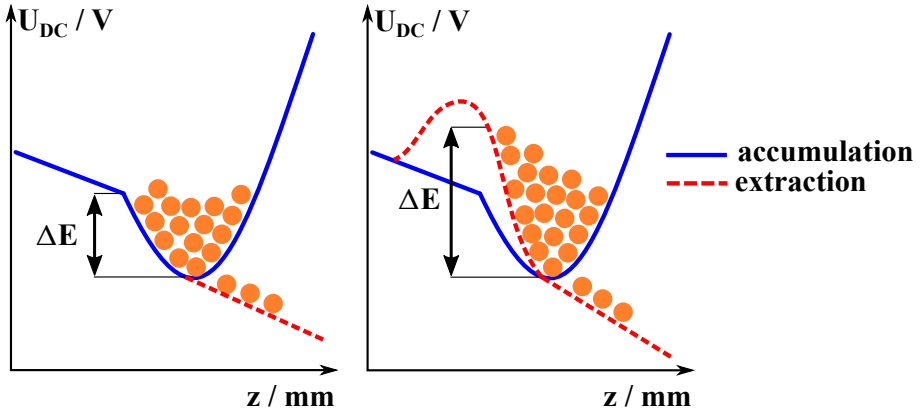

Figure 10.2: Ion extraction procedures from an RFQ: slow extraction (left) and fast extraction, also called *push-pull* extraction (right). Figure adopted from [234].

10.3 The MIRACLS project

A multi-reflection time-of-flight mass separator (MR-ToF MS) for ions at high energy (up to 30 keV) is under development at ISOLDE by the MIRACLS and the ISOLDE collaboration. An MR-ToF device is a component of typically one meter length which consist of a field free drift section surrounded by two electrostatic mirrors. Charged ions can be injected into and ejected from the MR-ToF MS by fast switching the so called in-trap lift [237] or parts of the mirror electrodes [238]. Once trapped between the mirrors of the MR-ToF MS, the ions are separated in time as a function of their mass.

The Multi Ion Reflection Apparatus for Collinear Laser Spectroscopy (MIRACLS) experiment is a new setup aiming at enhancing the sensitivity of collinear laser spectroscopy (CLS) for short-lived radioactive nuclei by a factor 20-600 in order to probe rare isotopes out of reach with current techniques [239]. This is achieved by storing ion bunches of radionuclides in an MR-ToF device. While the ions are bouncing back and forth between the electrostatic mirrors, the ion bunch interacts with the spectroscopy laser during each revolution in MIRACLS, compared to only once in conventional CLS. This increased laser-ion interaction time results in an improved sensitivity. In order to maintain the high resolution of CLS, MIRACLS MR-ToF device will operate at an ion beam energy of 30 keV, compared to a few keV in state-of-the-art instruments. In order to meet the requirements of CLS (low energy spread) and MR-ToF operation (narrow bunch width), MIRACLS will prepare the ion bunch in a cryogenic Paul trap to obtain an optimal ion-bunch emittance. The combination of improved emittance and increased ion beam energy in the MR-ToF device at MIRACLS are also very beneficial for fast and highly selective mass separation in an MR-ToF device. It is planned to develope the respective techniques within MIRACLS for a future general purpose 30 keV MR-ToF device at ISOLDE. An illustration of the MIRACLS setup is shown in Fig. 10.3.

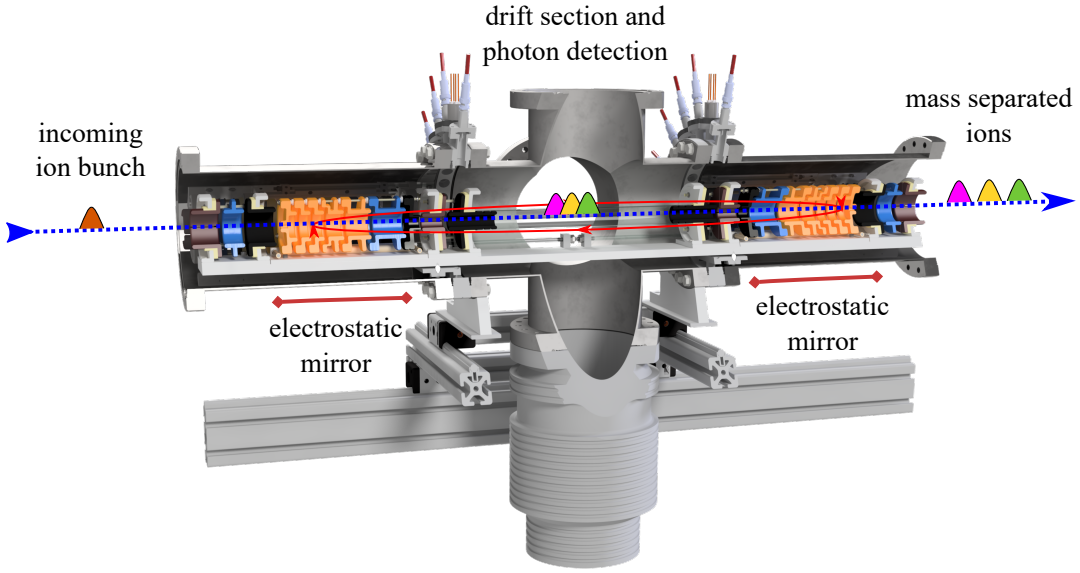

Figure 10.3: Sketch of an MR-ToF device similar to the one in development for the MIRACLS experiment.

The mass separation capability of an MR-TOF MS, its emittance requirements and its bunched working condition fit very well with the demands of PUMA. In the concept of PUMA at ISOLDE, it is expected that a MR-ToF system similar to MIRACLS will be located few meters upstream of PUMA. It will be possible to supply the beam with high purity and low energy that is needed. In addition, the MR-ToF MS will also allow to tackle the more challenging isotopes in terms of required mass

resolving power and initial beam emittance from the target ion source arrangement. It will also be possible to lower the beam energy to few keV by using the in-trap lift technique [237] together with the mirror ejection technique [238].

The development of the experiment is divided in two phases: The first one (ongoing) is building a proof-of-principle setup with an existing MR-ToF MS operating at energies of a few keV where several tests are taking place. The second phase will consist of developing a 30-keV MR-ToF and a cryogenic Paul Trap to adjust the traversal and longitudinal emittance of the beam entering the MR-ToF MS, leading to an improved turnaround-time of the ions and a lower energy spread. Designs and simulations are ongoing. It is expected that the MIRACLS equipment will be commissioned for laser spectroscopy with radioactive beams in 2021. The first purified beams are expected to be provided from late 2021 or 2022, in line with the PUMA schedule.

So far the MIRACLS project is on schedule and the technical details for the realization of this new high voltage device are feasible. The risks of failure or significant delay of MIRACLS are estimated to be low. A close collaboration is expected between the PUMA and the MIRACLS teams.

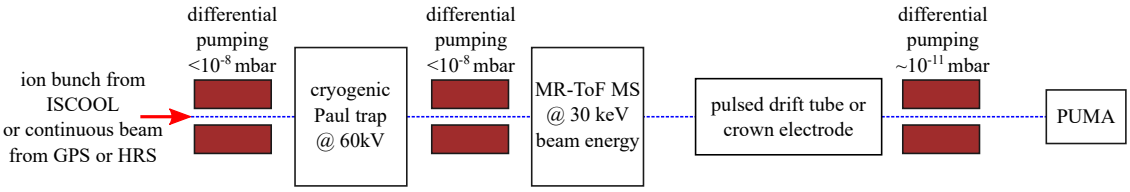

Figure 10.4: Schematic layout for the PUMA beam line at ISOLDE. Focusing elements and pumping elements are not shown.

The kinetic energy of the ions after MIRACLS is expected to reach 30 keV, which is too high for PUMA to trap them. For this reason, we are currently considering a dedicated pulse drift tube, following a similar design of the one developed for ELENA, which will allow us to slow the beam down to the desired energy of 1-2 keV, if the ejection using the in-trap lift of the MR-ToF MS at lower energies will not be possible. A sketch of a possible beam line layout at ISOLDE for PUMA is shown in Fig. 10.4.

10.4 Possible location and schematics

So far, there is no defined site to host PUMA at ISOLDE. Several options have been discussed. Taking into account the crane operation, the size of PUMA and the combination with a MR-ToF MS to provide pure, low-emittance bunched beams to PUMA, one location is considered adequate. The new beam outlet is considered to be placed as an extension of the RXC10 section in the part of the hall where also the

MINIBALL setup is placed. This will give enough space to place the PUMA setup and additionally reduce the effort to bring the PUMA setup into place as soon as it will arrive from the AD. The beam line extension will require additional beam optics which can be standard ISOLDE quadrupole triplets paired with pumping barriers and injection optics just before the PUMA setup.A layout of ISOLDE is shown in Fig. 10.5.

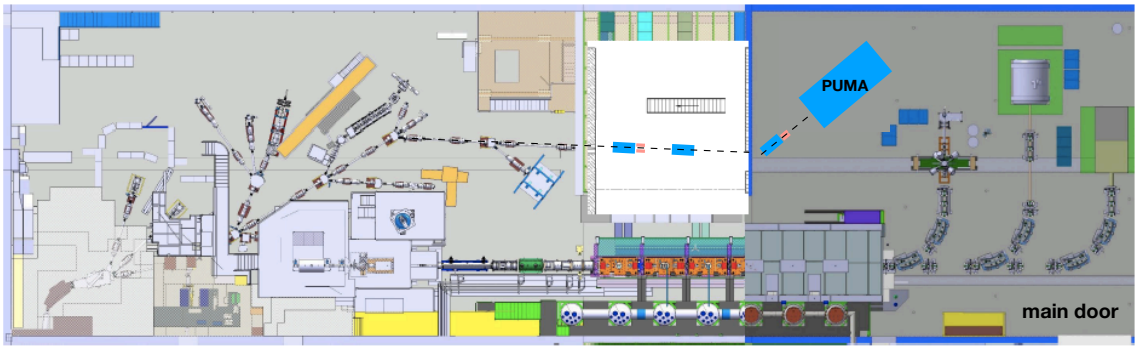

Figure 10.5: Layout of the ISOLDE experimental zone. The left part is dedicated to low-energy experiments while the more recent experimental zone (on the right) is dedicated to high energy experiments after re-acceleration by the HIE-ISOLDE linear accelerator. A possible layout of the PUMA beam line is schematically represented.

10.5 Operation mode at ISOLDE

The experimental program with PUMA at ISOLDE will be submitted in the form of a physics proposals for evaluation to the INTC, as it is the case for all experiments at ISOLDE.

Low-energy nuclear physics experiments are typically one-week long. The foreseen measurements with PUMA are estimated to last from half a day to a week, depending on the lifetime of the nucleus of interest and the corresponding yield available at ISOLDE.

Due to the very peculiar specificity of PUMA, i.e. a limited lifetime of the antiproton plasma, the experiments at ISOLDE should be scheduled in campaigns of few measurements in a row. The beam time should also be scheduled just after the antiproton trapping phase at ELENA.

10.6 Foreseen developments

The first installation at ISOLDE is foreseen in 2022 (see Chapter 12 for a detailed schedule). Beforehand, several tasks are foreseen:

- determine within the ISOLDE collaboration a location to host PUMA in the ISOLDE hall
- design an ion optics beam line according to the requirements for PUMA and to the specifications of ISCOOL and MIRACLS. The design and optics simulations will be developed in close collaboration with the ISOLDE technical coordinator and the MIRACLS team.
- finalize the development of MIRACLS
- build and test a beam line downstream MIRACLS or the future general purpose ISOLDE MR-ToF device matching the requirements of PUMA
- trap radioactive ions delivered by MIRACLS or ISOLDE MR-ToF device in PUMA in the ISOLDE hall
- design, build and test a differential pumping system with off-axis conductance-reduction pipes to prevent beaming

Chapter 11

Infrastructure at TU Darmstadt

11.1 Laboratory

A new laboratory at TU Darmstadt is planned. It will be located in the building S2|10 of the University, 100 meters away from the Institut für Kernphysik (IKP) of TU Darmstadt. The new laboratory will be composed of a clean room for detector developments (room 08, 32 m^2), a room for detector tests (room 017, 20 m^2), a laboratory for electronics and chemical treatments (room 016, 11 m^2), a multi-purpose zone (room 014, 60 m^2) equipped with a 1-ton crane and an area used as a workshop and storage (40 m^2). The crane will be used for maintenance and installation of devices inside the frame of PUMA. It is foreseen that PUMA will be slide on wheels to the outside of the building to then be loaded on a truck with a movable crane when transportation is scheduled. In addition to the laboratory space, office space equipped with 15 desks will be made available. The design of the laboratory is currently being finalized by the architects. Drawings of the ground floor are shown in Fig. 11.1 and Fig. 11.2.

All foreseen equipment of the new laboratory will be used for PUMA. In particular, the floor of room 014 has been reinforced and has been designed to withstand the 7 tons of PUMA. Despite the low ceiling (4.0 m), the room and equipment have been made to allow all operations relevant to PUMA: floor at the street level for delivery, crane system for maintenance. It is foreseen that the frame and solenoid of PUMA will be moved outdoors and indoors on multiple roller skids. Electrical power and cooling water have been scaled to the needs of PUMA. In room 014, PUMA will be installed for tests and developments during periods without beam at ELENA and ISOLDE. During the tests at the University, PUMA will be connected to a beamline composed of an ion source and a bunching device to trap and store ions as a benchmark.

The laboratory is currently under design. The safety rules for all rooms have been defined and the related documentation validated by the safety officer. The drawings and last details should be finalized in 2019. Construction should start in 2020 and the building is expected to be ready beginning of 2021. In the meanwhile,

TU Darmstadt will provide a temporary laboratory.

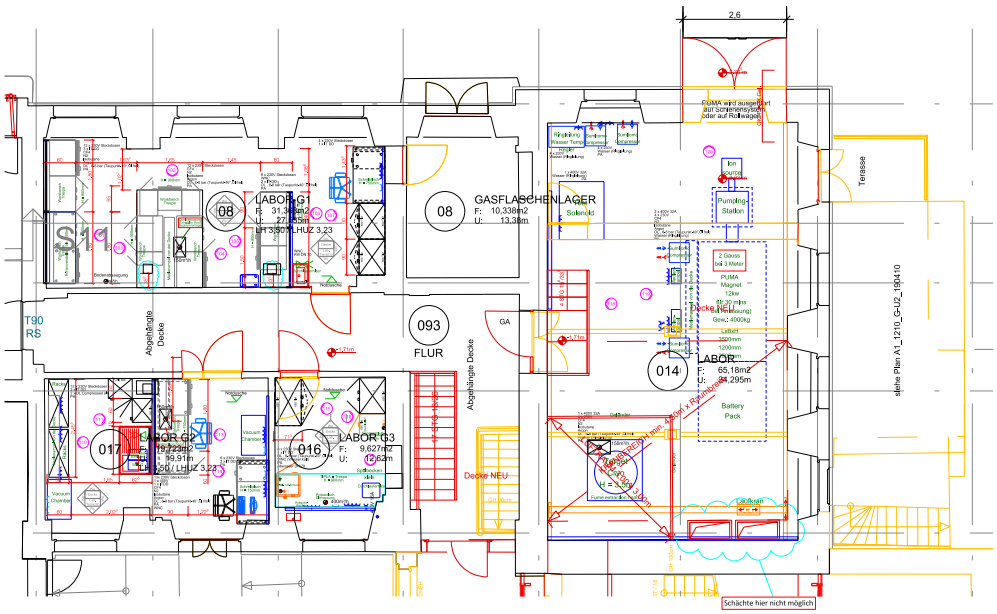

Figure 11.1: Drawing of the ground floor of the future laboratory in building S2|10 at TU Darmstadt. Most equipment of the laboratory will benefit to the development of PUMA.

11.2 Temporary laboratory

The temporary laboratory will be available from May 2020 at the expected delivery time of the PUMA solenoid from the supplier, Bilfinger Noell, until the new laboratory is ready. It is located in building S1|09 of the university, only five-minutes walking distance from the IKP. It is a 35×10-m^2 large hall with a 6-meter high ceiling and equipped with a three-ton crane. 70 kW of electrical power will be made available. A chiller with 50 kW cooling power will be installed outside the building to cover the needs of PUMA.

11.3 Transport

Contrary to CERN, no crane able to lift PUMA will be available on site. The PUMA frame will be delivered with a trailer equipped with a 10-ton crane.
PUMA will be moved inside the laboratories (temporary and final) on wheels with a dedicated transport trolley as often for heavy devices.

Different possibilities are considered for example the electric-powered trolley as offered by different companies [240, 241]. One such device is shown in Fig. 11.3.

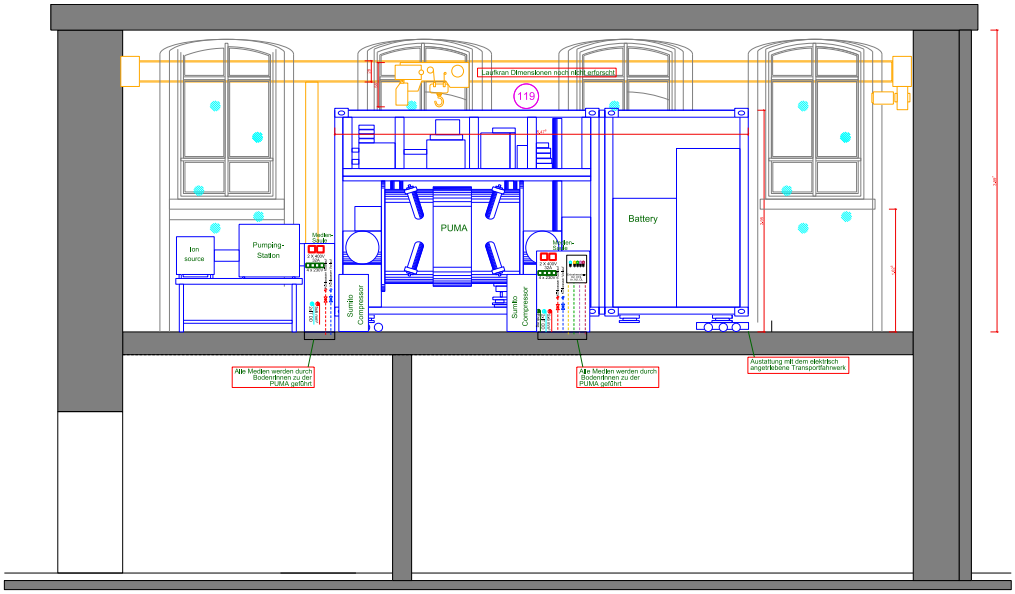

Figure 11.2: Artistic view of the main experimental hall of the S2|10 laboratory at TU Darmstadt. A 1-ton low-headroom crane will allow the management of most heavy individual components of PUMA. The (full) PUMA frame will be moved with a dedicated transport trolley. The basement of the laboratory will be used as workshop and storage.

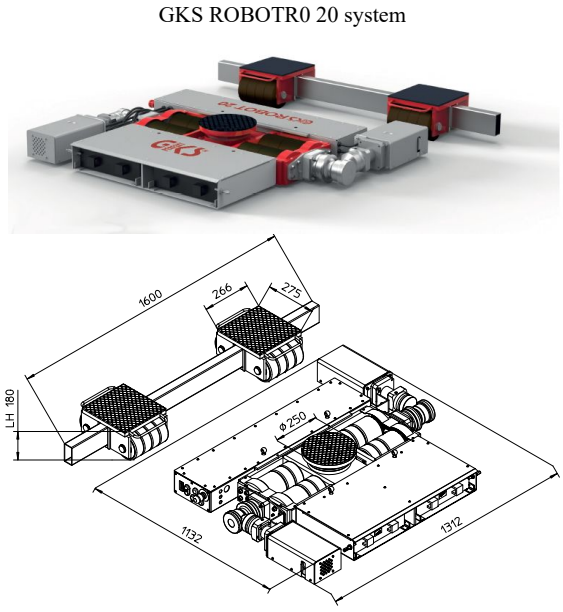

Figure 11.3: Electric-powered trolley used to handle heavy equipment in tight spaces. Figure adopted from [240].

With such a system the on-sight transport at TU Darmstadt and at CERN will be safely and reliably possible. The installation of the transport trolley requires to lift the PUMA frame by additional five centimeters compared to the on-feet position.

The lift will be performed with six 10-ton hydraulic jacks synchronized by a synchronous pressure unit.

The extraction of PUMA from the laboratory will be performed following the time-reversed procedure.

Figure 11.4: (Left) Facade of the temporary PUMA laboratory at TU Darmstadt. (Right) Inside of the laboratory. The laboratory will be equipped for 90 kW electric power grid and is equipped with a 3-ton crane.

Chapter 12

Organization, cost estimate and time line

12.1 Collaboration

At the date of the submission of the proposal (September 30$^{\text{th}}$, 2019), the PUMA collaboration is composed of 38 permanent researchers (professor, staff or engineer), 6 postdocs, 4 PhD students (two of them will start from 11/2019) from 12 universities or laboratories. The collaboration includes 40 members on the experimental side and 8 theorists. Currently, the collaboration members are :

T. Aumann[10], W. Bartmann[2], A. Bouvard[2], O. Boine-Frankenheim[10], A. Broche[2], F. Butin[2], D. Calvet[1], J. Carbonell[4], P. Chiggiatto[2], H. De Gersem[10], R. De Oliveira[2], T. Dobers[2], F. Ehm[2], J. Ferreira Somoza[2], J. Fischer[10], M. Fraser[2], E. Friedrich[10], J.-L. Grenard[2], G. Hupin[4], K. Johnston[2], Y. Kubota[10], M. Gomez-Ramos[10], P. Indelicato[6], R. Lazauskas[3], S. Malbrunot-Ettenauer[2], N. Marsic[10], W. Müller[10], S. Naimi[9], N. Nakatsuka[10], R. Necca[2], G. Neyens[2], A. Obertelli[10], Y. Ono[11], S. Pasinelli[2], N. Paul[6], E. C. Pollacco[1], D. Rossi[10], H. Scheit[10], R. Seki[8], A. Schmidt[10], L. Schweikhard[12], S. Sels[2], E. Siesling[2], T. Uesaka[9], M. Wada[5], F. Wienholtz[10], S. Wycech[7], S. Zacarias[10]

[1] CEA, IRFU, France
[2] CERN, Switzerland
[3] Institut Hubert Curien, CNRS, France
[4] Institut de Physique Nucléaire, Orsay, CNRS, France
[5] KEK, Japan
[6] Laboratoire Kastler Brossel, CNRS, France
[7] National Centre for Nuclear Research, Poland
[8] RCNP, Osaka, Japan
[9] RIKEN Nishina Center, Japan
[10] Technische Universität Darmstadt, Germany
[11] The Open University of Japan, Japan
[12] University of Greifswald, Germany

The collaboration covers all domains of expertise necessary for the successful realisation of PUMA. PUMA will benefit from the experience in Extreme High Vacuum (XHV) and cryogenic systems from CERN. The TE-VSC (Vacuum, Surfaces and Coatings) group at CERN has long experience in vacuum simulation, design and commissioning of XHV systems [109, 242]. For the development of LHC beam screens, the TE-VSC group has a wide experience measuring isotherms and designing cryopumped systems [110, 124, 243]. The PUMA vacuum system will rely on a vacuum better than 10^{-11} mbar at the entrance of the trap. This pressure is achieved in several CERN facilities like LEAR and ELENA [242, 244]. The PUMA collaboration will count on the direct involvement of Paolo Chiggiato, TE-VSC group leader at CERN, with ample experience in materials and treatments for ultra-high vacuum, in particular non-evaporable getters and Jose A. Ferreira, vacuum engineer at CERN, responsible of the vacuum operation in PS complex with experience in the design, installation and commissioning of vacuum systems and the use of different computational tools for vacuum design and simulation (MATLAB, MOLFLOW, COMSOL, LTSpice).
The optimization of the solenoid with active and passive shield has been studied by TEMF at TU Darmstadt (N. Marsic, W. Müller, and H. De Gersem) in close collaboration with the solenoid manufacturer (Bilfinger Noell). A simulation for the non-neutral antiproton plasma is been developed at TU Darmstadt (O. Boine-Frankenheim and A. Schmidt).
The PUMA collaboration has gathered a broad expertise in the design, installation and use of Penning trap systems (F. Wienholtz, L. Schweikhard, S. Malbrunot-Ettenauer). The low energy ion source and MR-ToF system, which will be used at ELENA, will be developed in close collaboration with the group of L. Schweikhard in Greifswald.
The PUMA time projection chamber has been designed at CEA Saclay (E.C. Pollacco) in conjunction with the MPGD laboratory at CERN (Section EP-DT-EF), where it will be built (R. De Oliveira). E.C. Pollacco and A. Obertelli have past experience in the development and operation of TPCs [194]. The electronics of PUMA is based on a recent development performed at CEA (D. Calvet) for the T2K experiment. The scintillator barrels for trigger and plasma diagnostics will be developed at TU Darmstadt (T. Aumann, D. Rossi and H. Scheit). The overall mechanics, simulations and cosmic-ray test bench will be taken care at TU Darmstadt (S. Zacarias, F. Wienholtz).
The design of the trap system is based on the integration of the PUMA project in the AD hall and on a new ELENA beam transfer line will be assured by the EN/EA group (F. Butin, O. Choisnet, D. Brethoux), already in charge of the general AD and ELENA technical coordination. The integration in the AD beams operation scheme will benefit from the BE/OP expertise (S. Pasinelli, L. Ponce, T. Erikson). The transports aspects will be taken care of by the EN/HE group (J.-L. Grenard) which has a vast expertise in all sorts of handling and transports of delicate physics apparatus.
The technical coordinator of ISOLDE (E. Siesling) is member of the collaboration,

as well as the spokesperson of MIRACLS (S. Malbrunot-Ettenauer). Nuclear physicists of the collaboration, in particular members of the ISOLDE collaboration with experience in carrying experiments at ISOLDE (S. Malbrunot-Ettenauer, K. Johnston, G. Neyens, S. Sels, F. Wienholtz), will ensure a smooth operation at ISOLDE. The analysis method is being developed at TU Darmstadt (Y. Kubota, A. Obertelli) and will be followed by full simulations of the physics cases to be measured (S. Zacarias). The machine learning and statistical aspects of the method under development are supported by Y. Ono. Methods and predictions will be developed together with S. Wycech, one of the leader theorists who interpreted stable-nuclei studies with antiprotons performed at LEAR. New developments on antiproton capture cross sections are foreseen (M. Gomez) and the decay of the antiprotons atoms will benefit from the expertise of R. Seki and P. Indelicato. Ab initio few-body predictions for nucleus-antiproton annihilations are being developed at IPN Orsay (J. Carbonell, G. Hupin) and IPHC (R. Lazauskas). Once bridged with microscopic predictions, effective methods as performed in the past with LEAR data (S. Wycech) will be used. Later on, specific collaborations with nuclear structure theorists outside the collaboration are foreseen, in particular at TU Darmstadt (H.-W. Hammer, R. Roth, A. Schwenk). New nuclear-physics ideas for PUMA (Y. Kubota, S. Naimi, N. Nakatsuka, A. Obertelli, N. Paul, T. Uesaka) will be investigated in parallel.

12.2 Work packages and work organisation

The PUMA project is divided into 8 work packages (WP), focusing on the physics program and analysis methods (WP 1), the vacuum (WP 2), the trap and solenoid (WP 3), its operation including diagnostics (WP 4) and the detection of annihilation products (WP 5). The infrastructure (WP 6) and beam optics (WP 7) for the operation of PUMA at CERN constitute two additional operational packages. The organisation (WP 8) is composed of a spokesperson and resource manager (A. Obertelli, TUDa), a technical coordinator and planning officer (F. Butin, CERN), a safety officer (E. Friedrich, TUDa), a quality officer (S. Zacarias, TUDa) and contact persons at ELENA (F. Butin, CERN) and ISOLDE (S. Ettenauer, CERN).

The description of the different work packages, WP and task leaders are given in Tab. 12.2. The WP leaders define the organization of their WP, in agreement with the spokesperson and technical coordinator. The work organization and communication among the collaboration members is structured into specific events: (1) collaboration meetings (in person, twice a year), (2) WP-leader meetings (monthly), (3) spokesperson and project manager (weekly), (4) WP meetings (at the discretion of the WP leader, typically weekly).

The quality control of PUMA is extremely important for a proper following of the technical evolution of the project and for the decision taking. Minutes will be issued after all meetings and will be transferred to participants for review. Minutes

and shown slides will be archived and made accessible to all collaboration members in the CERN Indico. The share of documents and archiving will be performed via the Engineering Data Management System (EDMS) server of CERN. We foresee to finalize the Technical Design Report of PUMA in 2020. For a proper operation of PUMA, detailed notes and manuals will be issued for every task and system.

Table 12.1: Workpackage and task break-out of PUMA.

WP	Task	Description	Leader	Institute
1		**Physics**	Y. Kubota	TUDa
	1.1	Simulations	S. Zacarias	TUDa
	1.2	Data analysis, tools, method	Y. Kubota	TUDa
	1.3	Theory	(tbc)	
2		**Vacuum**	A. Obertelli	TUDa
	2.1	Simulations, vacuum design	J. A. Ferreira Somoza	CERN
	2.2	Materials, surface treatment	P. Chiggiatto	CERN
	2.3	Prototyping, procurement, tests	J. A. Ferreira Somoza	CERN
	2.4	Control, monitoring	(tbc)	CERN
	2.5	Isotherm measurements	(tbc)	CERN
3		**Trap**	N. Nakatsuka	TUDa
	3.1	Design & assembly	F. Wienholtz	TUDa
	3.2	HV, control (hardware)	Y. Kubota	TUDa
	3.3	Mechanics, support	F. Wienholtz	TUDa
	3.4	Thermal calculations	F. Wienholtz	TUDa
	3.5	Solenoid operation	N. Nakatsuka	TUDa
	3.6	Frame assembly procedure	N. Nakatsuka	TUDa
	3.7	Field mapping, trap alignment	E. Friedrich	TUDa
	3.8	Magnetic field calculations	N. Marsic	TUDa
4		**Plasma**	F. Wienholtz	TUDa
	4.1	Trap operation	A. Schmidt	TUDa
	4.2	Diagnostics	J. Fischer	TUDa
	4.4	Electron gun	J. Fischer	TUDa
	4.5	Ion source operation, buncher	F. Wienholtz	TUDa
	4.6	Simulations	A. Schmidt	TUDa
5		**Annihilation detection**	E. C. Pollacco	CEA
	5.1	Design	E. C. Pollacco	CEA
	5.2	TPC realisation	R. De Oliveira	CERN
	5.3	Simulations	S. Zacarias	TUDa
	5.4	Mechanics	F. Wienholtz	TUDa
	5.5	Cosmic ray and source validation	S. Zacarias	TUDa
	5.6	Electronics	D. Calvet	CEA
	5.7	Scintillator barrels	D. Rossi	TUDa
	5.8	DAQ	Y. Kubota	TUDa
6		**Infrastructure**	F. Butin	CERN

Table 12.1: Part 2.

WP	Task	Description	Leader	Institute
	6.1	Transport and handling	J.-L. Grenard	CERN
	6.2	ELENA	A. Bouvard	CERN
	6.3	ISOLDE	E. Siesling	CERN
	6.4	TU Darmstadt	F. Wienholtz	TUDa
	6.5	Beam lines	W. Bartmann	CERN
	6.6	Alignement	T. Dobers	CERN
	6.7	Power	R. Necca	CERN
	6.8	Cooling water	A. Broche	CERN
	6.9	Controls	(tbc)	CERN
	6.10	Timing	F. Ehm	CERN
7		**Beam optics**	F. Wienholtz	TUDa
	7.1	Simulations	E. Siesling	CERN
	7.2	Beam tuning @ ELENA	(tbc)	
	7.3	Pulsed drift tube @ ELENA	F. Wienholtz	TUDa
	7.4	Beam tuning @ ISOLDE	F. Wienholtz	TUDa
	7.5	Beam diagnostics	J. Fischer	TUDa
8		**Organisation**		
		Spokesperson / resource manager	A. Obertelli	TUDa
		Project manager / planning officer	F. Butin	CERN
		Safety officer	E. Friedrich	TUDa
		Quality control, documentation	S. Zacarias	TUDa
		ISOLDE contact person	S. Malbrunot-Ettenauer	CERN
		ELENA contact person	F. Butin	CERN

12.3 Cost estimate

The PUMA project has been funded by the European Research Council (ERC Consolidator grant) on a 5-year grant from 01/2018 to 12/2022. The ERC covers the construction of the PUMA device as well as 8 years of postdoc (N. Nakatuska, 5 years, and Y. Kubota, 3 years). TU Darmstadt covers the depreciation costs of the investment of PUMA not covered by the ERC. In addition to this core support, the new laboratory created at TU Darmstadt is being equipped (test solenoid, electronics and core laboratory devices) with funds from a Alexander von Humboldt professorship grant, started on 10/2018. The Alexander von Humboldt grant will in addition support four PhD students on PUMA as well as investments at ELENA (beam line and vacuum elements after the handover point and pulsed drift tube). An additional application to the BMBF (Germany ministry of research) for manpower (a PhD and a postdoc) to work on beam optics at ELENA and ISOLDE and on the differential pumping section for ISOLDE have been submitted.

With this proposal, the necessary infrastructure at ELENA and ISOLDE is requested to CERN. In the Engineering Change Request (ECR) of ELENA related to PUMA, costs have been estimated to 693 kCH (640 k€), including 15% contingency. A dedicated ECR for ISOLDE is in preparation. The following is requested to CERN:

- experimental zone suitable for PUMA at ELENA,
- transfer beamline from the ELENA ring to handover point,
- working and storage space at ELENA,
- experimental location suitable for PUMA experiments at ISOLDE,
- low-energy beamline at ISOLDE providing bunched and isotopically pure 3-keV beams,
- necessary cooling water and 70 kW power supply (including during crane operation) for the operation of PUMA at both ELENA and ISOLDE,
- usual CERN technical support in the experimental zones.

Costs estimates, status of funding and sources of funding are summarized in Table 12.2.

Table 12.2: Investment, infrastructure cost estimates and funding sources for PUMA.

Expense	Description	Cost (k€)	Funding	Period	Status
Investment	PUMA apparatus	1100 730	ERC TUDa	2018-22	secured
	lab. equipment	500	AvH	2018-23	secured
	Isolde beam optics and vacuum	100	BMBF	2020-21	under request
Infrastructure	laboratory at TUDa	u. e.†	TUDa	2019-21	secured
	ELENA	640	CERN	2020-21	under request*
	ISOLDE	u. e.††	CERN	2021-22	under request**

† Under evaluation. The current estimate is in the range 1500 - 2000 k€.
†† Under evaluation. ECR under preparation to be ready in 01/2020.
* This proposal and detailed estimates in dedicated ECR.
** This proposal and detailed estimates in future ECR.

12.4 Schedule

The agenda and milestones for each work package is given in Tab. 12.3 and summarized in a Master plan in Fig. 12.4 and 12.4. The timeline is believed to be realistic but does not contain much contingency. No risk management plan has been performed yet. We foresee two main possible sources of delay: (i) the considered isotherm extrapolation is revealed to be optimistic after low-pressure isotherm measurements implying that the necessary vacuum cannot be reached, (ii) the learning curve for storing and cooling antiprotons is slower than anticipated. Despite these risks, our objective is a first successful measurement at ISOLDE with radioactive isotopes at the end of 2022.

Table 12.3: Main tasks and milestones of PUMA for the period 2020-2023. A tentative date is given for the milestone. When the deliverable is a report or a publication, it is expected to be fulfilled within 12 months after the milestone is reached.

WP	Task	Milestone	Deliverable	Date
1	Analysis model	R_{np} sensitivity shown better than 10%	publication	06/2020
	ab initio framework for $\bar{p}$-nucleus interactions	Bridge with optical-potential-based methods established	publication	01/2022
	Physics case at ELENA	Experiment with antiprotons and stable nuclei at ELENA	publication	07/2022
	Physics case at ISOLDE	Experimental conditions to reach PUMA objectives established	proposals	01/2022
	Skins and halos at ISOLDE	Experiment with antiprotons at ISOLDE	publication	12/2022
2	Full vacuum simulations for PUMA	simulations show 10^{-17} mbar maintained for $>$ 30 days at ISOLDE	internal report	06/2020
	Measurement of H_2 isotherms	Better extrapolation of isotherm at 4.2 K on gold and carbon	publication	06/2021
	Design and construction of cryostat		delivery	11/2020
	Long term XHV	$\bar{p}$ annihilation rate consistent with lifetime of $>$ 30 days at ELENA	internal report	04/2022
		Quantify lifetime of $\bar{p}$ plasma at ISOLDE	internal report	10/2022
3	Construction of solenoid	4T with required homogeneity achieved	delivery	07/2020
	Completion of PUMA	All functions integrated in the PUMA frame	operation	02/2021
	Develop prototype storage trap	Store 10^9 electrons for a week	internal report	09/2020
	Thermal calculations for cryostat	All trap at T $<$ 4.2 K	tech. drawings	08/2020
	Development of PUMA trap	Full trap assembled and mounted inside the chamber	documentation	06/2021

Table 12.3: Part 2.

WP	Task	Milestone	Deliverable	Date
4	Establish cooling scheme for PUMA	Phase 1 (prototype): store 10^8 protons for a week	internal report	09/2021
		Phase 2: store 10^9 $\bar{p}$ for 4 weeks	publication	04/2022
5	Completion of pion detection	Validation on cosmic rays	internal report	10/2020
	Long-term operation for TPC	Quantify performance evolution over 2 months of operation	publication	01/2021
	X-ray measurements in PUMA	Quantify the feasibility of X ray measurements with PUMA	publication	06/2023
6	Transport (phase 1)	Transport solenoid under operation	internal report	01/2021
	Transport of charged particles (phase 2)	Transport protons from ELENA to ISOLDE	internal report	06/2021
	Transport of antiprotons (phase 3)	Deliver antiprotons to ISOLDE	publication	11/2022
	Power supply	Power PUMA for 5 minutes in case of power failure	test result	12/2020
7	Beam at ELENA	Trap antiprotons and insert bunched stable ions inside PUMA	publication	04/2022
	Beam at ISOLDE	Trap RI ions in PUMA with efficiency $> 50\%$	internal report	05/2022

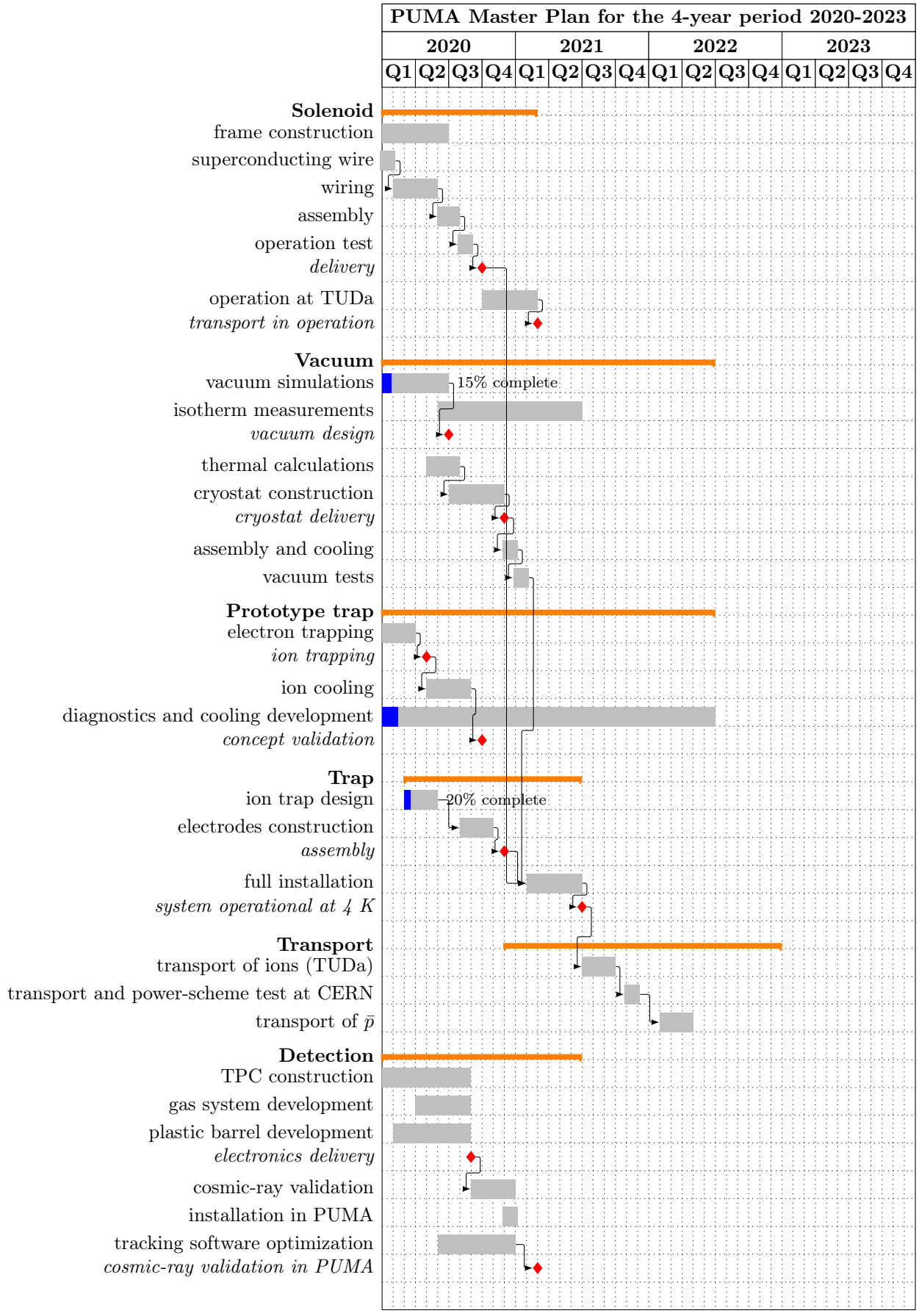
PUMA Master Plan for the 4-year period 2020-2023
2020
2021
2022
2023
Q1 Q2 Q3 Q4 Q1 Q2 Q3 Q4 Q1 Q2 Q3 Q4 Q1 Q2 Q3 Q4
Solenoid
frame construction
superconducting wire
wiring
assembly
operation test
delivery
operation at TUDa
transport in operation
Vacuum
vacuum simulations
15% complete
isotherm measurements
vacuum design
thermal calculations
cryostat construction
cryostat delivery
assembly and cooling
vacuum tests
Prototype trap
electron trapping
ion trapping
ion cooling
diagnostics and cooling development
concept validation
Trap
ion trap design
20% complete
electrodes construction
assembly
full installation
system operational at 4 K
Transport
transport of ions (TUDa)
transport and power-scheme test at CERN
transport of $\bar{p}$
Detection
TPC construction
gas system development
plastic barrel development
electronics delivery
cosmic-ray validation
installation in PUMA
tracking software optimization
cosmic-ray validation in PUMA

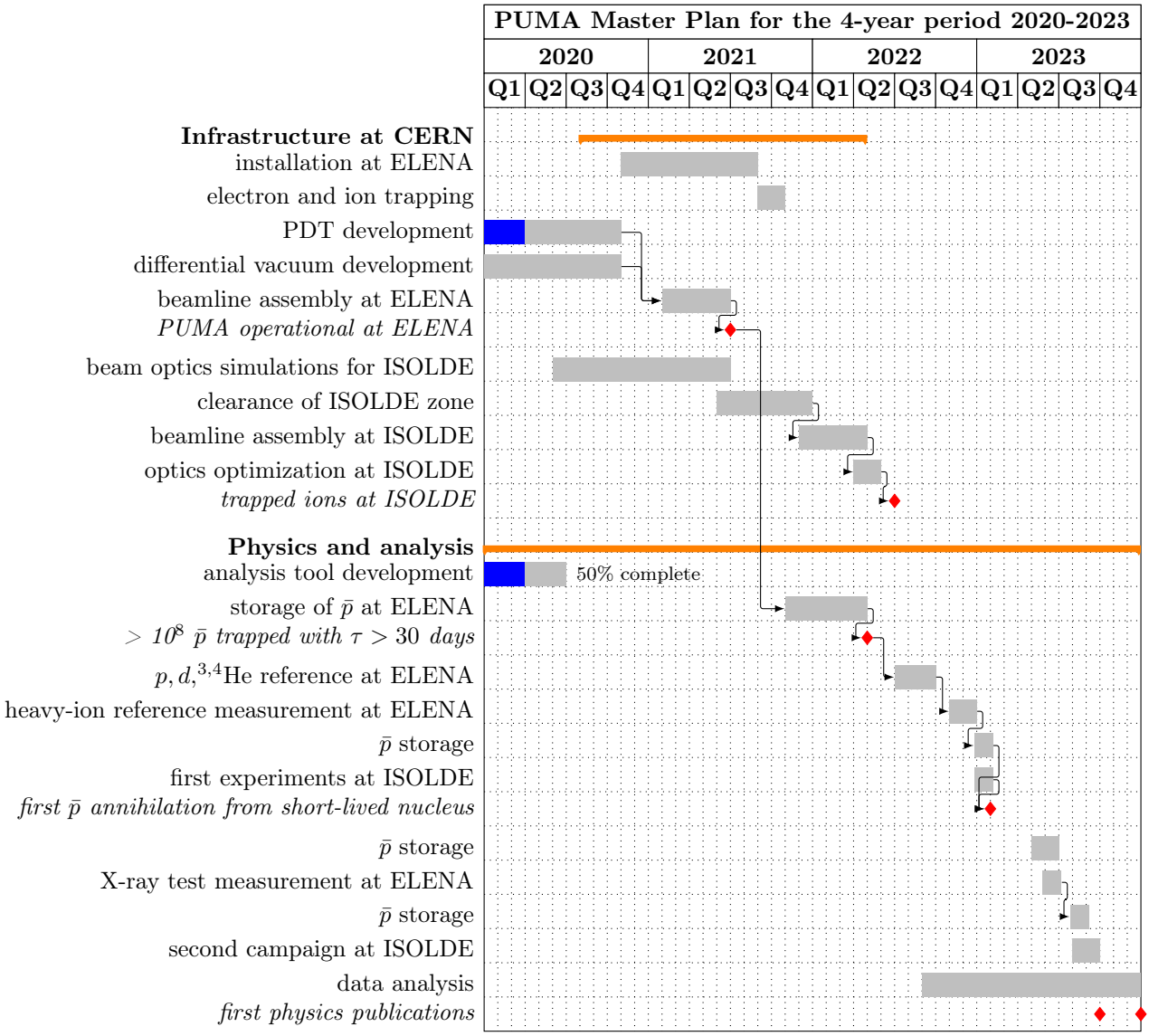
PUMA Master Plan for the 4-year period 2020-2023
2020
2021
2022
2023
Q1 Q2 Q3 Q4 Q1 Q2 Q3 Q4 Q1 Q2 Q3 Q4 Q1 Q2 Q3 Q4
Infrastructure at CERN
installation at ELENA
electron and ion trapping
PDT development
differential vacuum development
beamline assembly at ELENA
PUMA operational at ELENA
beam optics simulations for ISOLDE
clearance of ISOLDE zone
beamline assembly at ISOLDE
optics optimization at ISOLDE
trapped ions at ISOLDE
Physics and analysis
analysis tool development
50% complete
storage of $\bar{p}$ at ELENA
$> 10^8$ $\bar{p}$ trapped with $\tau > 30$ days
$p, d,{}^{3,4}$He reference at ELENA
heavy-ion reference measurement at ELENA
$\bar{p}$ storage
first experiments at ISOLDE
first $\bar{p}$ annihilation from short-lived nucleus
$\bar{p}$ storage
X-ray test measurement at ELENA
$\bar{p}$ storage
second campaign at ISOLDE
data analysis
first physics publications

Bibliography

[1] W. M. Bugg, G. T. Condo, E. L. Hart, H. O. Cohn, and R. D. McCulloch, "Evidence for a neutron halo in heavy nuclei from antiproton absorption," *Phys. Rev. Lett.*, vol. 31, pp. 475–478, Aug 1973.

[2] M. Wade and V. G. Lind, "Ratio of antiproton annihilations on neutrons and protons in carbon for low-energy and stopped antiprotons," *Phys. Rev. D*, vol. 14, pp. 1182–1187, Sep 1976.

[3] P. Lubiński, J. Jastrzębski, A. Grochulska, A. Stolarz, A. Trzcińska, W. Kurcewicz, F. J. Hartmann, W. Schmid, T. von Egidy, J. Skalski, R. Smolańczuk, S. Wycech, D. Hilscher, D. Polster, and H. Rossner, "Neutron halo in heavy nuclei from antiproton absorption," *Phys. Rev. Lett.*, vol. 73, pp. 3199–3202, Dec 1994.

[4] P. Lubiński, J. Jastrzębski, A. Trzcińska, W. Kurcewicz, F. J. Hartmann, W. Schmid, T. von Egidy, R. Smolańczuk, and S. Wycech, "Composition of the nuclear periphery from antiproton absorption," *Phys. Rev. C*, vol. 57, pp. 2962–2973, Jun 1998.

[5] A. Obertelli, S. Naimi, T. Uesaka, A. Corsi, E. C. Pollacco, and F. Flavigny, "Probing the density tail of radioactive nuclei with antiprotons," Letter of Intent SPSC-I-247, CERN, December 2017.

[6] J. Carbonell, A. Corsi, F. Flavigny, H. De Gersem, G. Hupin, Y. Kubota, R. Lazauskas, S. Malbrunot, N. Marsic, W. F. O. Muller, S. Naimi, N. Nakatsuka, A. Obertelli, P. Paul, P. Pérez, E. C. Pollacco, M. Rosenbusch, R. Seki, T. Uesaka, and F. Wienholtz, "PUMA : antiprotons and radioactive nuclei," Memorandum INTC-M-018, CERN, June 2018.

[7] "Minutes of the 59$^{\text{th}}$ Meeting of the INTC," June 2018. CERN-INTC-2018-INTC-059.

[8] "Minutes of the 131$^{\text{st}}$ Meeting of the SPSC," October 2018. CERN-SPSC-2018-033 SPSC-131.

[9] "Call for proposals for projects at the CERN Antiproton Decelerator after LS2," June 2019. CERN-SPSC-2019-028 SPSC-G-035.

[10] I. Tanihata, H. Hamagaki, O. Hashimoto, Y. Shida, N. Yoshikawa, K. Sugimoto, O. Yamakawa, T. Kobayashi, and N. Takahashi, "Measurements of interaction cross sections and nuclear radii in the light p-shell region," *Phys. Rev. Lett.*, vol. 55, pp. 2676–2679, Dec 1985.

[11] M. Freer, H. Horiuchi, Y. Kanada-En'yo, D. Lee, and U.-G. Meißner, "Microscopic clustering in light nuclei," *Rev. Mod. Phys.*, vol. 90, p. 035004, Aug 2018.

[12] P. G. Hansen and B. Jonson, "The neutron halo of extremely neutron-rich nuclei," *EPL (Europhysics Letters)*, vol. 4, p. 409, Sept. 1987.

[13] P. G. Hansen, A. S. Jensen, and B. Jonson, "Nuclear halos," *Annual Review of Nuclear and Particle Science*, vol. 45, no. 1, pp. 591–634, 1995.

[14] A. S. Jensen, K. Riisager, D. V. Fedorov, and E. Garrido, "Structure and reactions of quantum halos," *Rev. Mod. Phys.*, vol. 76, pp. 215–261, Feb 2004.

[15] K. Riisager, "Halos and related structures," *Physica Scripta*, vol. T152, p. 014001, jan 2013.

[16] C. Bertulani, H.-W. Hammer, and U. van Kolck, "Effective field theory for halo nuclei: shallow p-wave states," *Nuclear Physics A*, vol. 712, no. 1, pp. 37 – 58, 2002.

[17] T. Frederico, A. Delfino, L. Tomio, and M. Yamashita, "Universal aspects of light halo nuclei," *Progress in Particle and Nuclear Physics*, vol. 67, no. 4, pp. 939 – 994, 2012.

[18] H. P. g. Schieck, "Halo nuclei and farewell to simple radius systematics," in *Key Nuclear Reaction Experiments*, 2053-2563, pp. 5–1 to 5–6, IOP Publishing, 2015.

[19] B. Jonson, "Light dripline nuclei," *Physics Reports*, vol. 389, no. 1, pp. 1 – 59, 2004.

[20] I. Tanihata, H. Savajols, and R. Kanungo, "Recent experimental progress in nuclear halo structure studies," *Progress in Particle and Nuclear Physics*, vol. 68, pp. 215 – 313, 2013.

[21] T. Nakamura, N. Kobayashi, Y. Kondo, Y. Satou, J. A. Tostevin, Y. Utsuno, N. Aoi, H. Baba, N. Fukuda, J. Gibelin, N. Inabe, M. Ishihara, D. Kameda, T. Kubo, T. Motobayashi, T. Ohnishi, N. A. Orr, H. Otsu, T. Otsuka, H. Sakurai, T. Sumikama, H. Takeda, E. Takeshita, M. Takechi, S. Takeuchi, Y. Togano, and K. Yoneda, "Deformation-driven p-wave halos at the drip line: ^{31}Ne," *Phys. Rev. Lett.*, vol. 112, p. 142501, Apr 2014.

[22] N. Kobayashi, T. Nakamura, Y. Kondo, J. A. Tostevin, Y. Utsuno, N. Aoi, H. Baba, R. Barthelemy, M. A. Famiano, N. Fukuda, N. Inabe, M. Ishihara, R. Kanungo, S. Kim, T. Kubo, G. S. Lee, H. S. Lee, M. Matsushita, T. Motobayashi, T. Ohnishi, N. A. Orr, H. Otsu, T. Otsuka, T. Sako, H. Sakurai, Y. Satou, T. Sumikama, H. Takeda, S. Takeuchi, R. Tanaka, Y. Togano, and K. Yoneda, "Observation of a p-wave one-neutron halo configuration in ^{37}Mg," *Phys. Rev. Lett.*, vol. 112, p. 242501, Jun 2014.

[23] I. Tanihata, T. Kobayashi, O. Yamakawa, S. Shimoura, K. Ekuni, K. Sugimoto, N. Takahashi, T. Shimoda, and H. Sato, "Measurement of interaction cross sections using isotope beams of Be and B and isospin dependence of the nuclear radii," *Physics Letters B*, vol. 206, no. 4, pp. 592 – 596, 1988.

[24] T. Minamisono, T. Ohtsubo, I. Minami, S. Fukuda, A. Kitagawa, M. Fukuda, K. Matsuta, Y. Nojiri, S. Takeda, H. Sagawa, and H. Kitagawa, "Proton halo of ^{8}B disclosed by its giant quadrupole moment," *Phys. Rev. Lett.*, vol. 69, pp. 2058–2061, Oct 1992.

[25] G. Korolev, A. Dobrovolsky, A. Inglessi, G. Alkhazov, P. Egelhof, A. Estradé, I. Dillmann, F. Farinon, H. Geissel, S. Ilieva, Y. Ke, A. Khanzadeev, O. Kiselev, J. Kurcewicz, X. Le, Y. Litvinov, G. Petrov, A. Prochazka, C. Scheidenberger, L. Sergeev, H. Simon, M. Takechi, S. Tang, V. Volkov, A. Vorobyov, H. Weick, and V. Yatsoura, "Halo structure of ^{8}B determined from intermediate energy proton elastic scattering in inverse kinematics," *Physics Letters B*, vol. 780, pp. 200 – 204, 2018.

[26] W. Geithner, T. Neff, G. Audi, K. Blaum, P. Delahaye, H. Feldmeier, S. George, C. Guénaut, F. Herfurth, A. Herlert, S. Kappertz, M. Keim, A. Kellerbauer, H.-J. Kluge, M. Kowalska, P. Lievens, D. Lunney, K. Marinova, R. Neugart, L. Schweikhard, S. Wilbert, and C. Yazidjian, "Masses and charge radii of $^{17--22}$Ne and the two-proton-halo candidate ^{17}Ne," *Phys. Rev. Lett.*, vol. 101, p. 252502, Dec 2008.

[27] S. Mizutori, J. Dobaczewski, G. A. Lalazissis, W. Nazarewicz, and P.-G. Reinhard, "Nuclear skins and halos in the mean-field theory," *Phys. Rev. C*, vol. 61, p. 044326, Mar 2000.

[28] M. Grasso, S. Yoshida, N. Sandulescu, and N. Van Giai, "Giant neutron halos in the non-relativistic mean field approach," *Phys. Rev. C*, vol. 74, p. 064317, Dec 2006.

[29] J. Terasaki, S. Q. Zhang, S. G. Zhou, and J. Meng, "Giant halos in relativistic and nonrelativistic approaches," *Phys. Rev. C*, vol. 74, p. 054318, Nov 2006.

[30] V. Rotival and T. Duguet, "New analysis method of the halo phenomenon in finite many-fermion systems: First applications to medium-mass atomic nuclei," *Phys. Rev. C*, vol. 79, p. 054308, May 2009.

[31] V. Rotival, K. Bennaceur, and T. Duguet, "Halo phenomenon in finite many-fermion systems: Atom-positron complexes and large-scale study of atomic nuclei," *Phys. Rev. C*, vol. 79, p. 054309, May 2009.

[32] E. Chabanat, P. Bonche, P. Haensel, J. Meyer, and R. Schaeffer, "A skyrme parametrization from subnuclear to neutron star densities part ii. nuclei far from stabilities," *Nuclear Physics A*, vol. 635, no. 1, pp. 231 – 256, 1998.

[33] I. Hamamoto, "Dominance of low-ℓ component in weakly bound deformed single-neutron orbits," *Phys. Rev. C*, vol. 69, p. 041306, Apr 2004.

[34] I. Hamamoto, "Nilsson diagrams for light neutron-rich nuclei with weakly-bound neutrons," *Phys. Rev. C*, vol. 76, p. 054319, Nov 2007.

[35] I. Hamamoto, "Interpretation of coulomb breakup of ^{31}Ne in terms of deformation," *Phys. Rev. C*, vol. 81, p. 021304, Feb 2010.

[36] M. Dutra, O. Lourenço, J. S. Sá Martins, A. Delfino, J. R. Stone, and P. D. Stevenson, "Skyrme interaction and nuclear matter constraints," *Phys. Rev. C*, vol. 85, p. 035201, Mar 2012.

[37] M. Bender, P.-H. Heenen, and P.-G. Reinhard, "Self-consistent mean-field models for nuclear structure," *Rev. Mod. Phys.*, vol. 75, pp. 121–180, Jan 2003.

[38] J. Stone and P.-G. Reinhard, "The skyrme interaction in finite nuclei and nuclear matter," *Progress in Particle and Nuclear Physics*, vol. 58, no. 2, pp. 587 – 657, 2007.

[39] R. Sellahewa and A. Rios, "Isovector properties of the gogny interaction," *Phys. Rev. C*, vol. 90, p. 054327, Nov 2014.

[40] X. Roca-Maza, M. Centelles, X. Viñas, and M. Warda, "Neutron skin of ^{208}Pb, nuclear symmetry energy, and the parity radius experiment," *Phys. Rev. Lett.*, vol. 106, p. 252501, Jun 2011.

[41] X. Roca-Maza, X. Viñas, M. Centelles, B. K. Agrawal, G. Colò, N. Paar, J. Piekarewicz, and D. Vretenar, "Neutron skin thickness from the measured electric dipole polarizability in ^{68}Ni, ^{120}Sn, and ^{208}Pb," *Phys. Rev. C*, vol. 92, p. 064304, Dec 2015.

[42] F. J. Fattoyev, J. Piekarewicz, and C. J. Horowitz, "Neutron skins and neutron stars in the multimessenger era," *Phys. Rev. Lett.*, vol. 120, p. 172702, Apr 2018.

[43] C. A. Bertulani and J. Valencia, "Neutron skins as laboratory constraints on properties of neutron stars and on what we can learn from heavy ion fragmentation reactions," *Phys. Rev. C*, vol. 100, p. 015802, Jul 2019.

[44] W. Horiuchi, S. Ebata, and K. Iida, "Neutron-skin thickness determines the surface tension of a compressible nuclear droplet," *Phys. Rev. C*, vol. 96, p. 035804, Sep 2017.

[45] S. Abrahamyan, Z. Ahmed, H. Albataineh, K. Aniol, D. S. Armstrong, W. Armstrong, T. Averett, B. Babineau, A. Barbieri, V. Bellini, R. Beminiwattha, J. Benesch, F. Benmokhtar, T. Bielarski, W. Boeglin, A. Camsonne, M. Canan, P. Carter, G. D. Cates, C. Chen, J.-P. Chen, O. Hen, F. Cusanno, M. M. Dalton, R. De Leo, K. de Jager, W. Deconinck, P. Decowski, X. Deng, A. Deur, D. Dutta, A. Etile, D. Flay, G. B. Franklin, M. Friend, S. Frullani, E. Fuchey, F. Garibaldi, E. Gasser, R. Gilman, A. Giusa, A. Glamazdin, J. Gomez, J. Grames, C. Gu, O. Hansen, J. Hansknecht, D. W. Higinbotham, R. S. Holmes, T. Holmstrom, C. J. Horowitz, J. Hoskins, J. Huang, C. E. Hyde, F. Itard, C.-M. Jen, E. Jensen, G. Jin, S. Johnston, A. Kelleher, K. Kliakhandler, P. M. King, S. Kowalski, K. S. Kumar, J. Leacock, J. Leckey, J. H. Lee, J. J. LeRose, R. Lindgren, N. Liyanage, N. Lubinsky, J. Mammei, F. Mammoliti, D. J. Margaziotis, P. Markowitz, A. McCreary, D. McNulty, L. Mercado, Z.-E. Meziani, R. W. Michaels, M. Mihovilovic, N. Muangma, C. Muñoz Camacho, S. Nanda, V. Nelyubin, N. Nuruzzaman, Y. Oh, A. Palmer, D. Parno, K. D. Paschke, S. K. Phillips, B. Poelker, R. Pomatsalyuk, M. Posik, A. J. R. Puckett, B. Quinn, A. Rakhman, P. E. Reimer, S. Riordan, P. Rogan, G. Ron, G. Russo, K. Saenboonruang, A. Saha, B. Sawatzky, A. Shahinyan, R. Silwal, S. Sirca, K. Slifer, P. Solvignon, P. A. Souder, M. L. Sperduto, R. Subedi, R. Suleiman, V. Sulkosky, C. M. Sutera, W. A. Tobias, W. Troth, G. M. Urciuoli, B. Waidyawansa, D. Wang, J. Wexler, R. Wilson, B. Wojtsekhowski, X. Yan, H. Yao, Y. Ye, Z. Ye, V. Yim, L. Zana, X. Zhan, J. Zhang, Y. Zhang, X. Zheng, and P. Zhu, "Measurement of the neutron radius of ^{208}Pb through parity violation in electron scattering," *Phys. Rev. Lett.*, vol. 108, p. 112502, Mar 2012.

[46] C. J. Horowitz and J. Piekarewicz, "Neutron star structure and the neutron radius of ^{208}pb," *Phys. Rev. Lett.*, vol. 86, pp. 5647–5650, Jun 2001.

[47] K. Hebeler, J. M. Lattimer, C. J. Pethick, and A. Schwenk, "Equation of state and neutron star properties constrained by nuclear physics and observation," *The Astrophysical Journal*, vol. 773, p. 11, jul 2013.

[48] M. H. Mahzoon, M. C. Atkinson, R. J. Charity, and W. H. Dickhoff, "Neutron skin thickness of ^{48}Ca from a nonlocal dispersive optical-model analysis," *Phys. Rev. Lett.*, vol. 119, p. 222503, Nov 2017.

[49] C. M. Tarbert, D. P. Watts, D. I. Glazier, P. Aguar, J. Ahrens, J. R. M. Annand, H. J. Arends, R. Beck, V. Bekrenev, B. Boillat, A. Braghieri, D. Branford, W. J. Briscoe, J. Brudvik, S. Cherepnya, R. Codling, E. J. Downie, K. Foehl, P. Grabmayr, R. Gregor, E. Heid, D. Hornidge, O. Jahn, V. L. Kashevarov, A. Knezevic, R. Kondratiev, M. Korolija, M. Kotulla, D. Krambrich,

B. Krusche, M. Lang, V. Lisin, K. Livingston, S. Lugert, I. J. D. MacGregor, D. M. Manley, M. Martinez, J. C. McGeorge, D. Mekterovic, V. Metag, B. M. K. Nefkens, A. Nikolaev, R. Novotny, R. O. Owens, P. Pedroni, A. Polonski, S. N. Prakhov, J. W. Price, G. Rosner, M. Rost, T. Rostomyan, S. Schadmand, S. Schumann, D. Sober, A. Starostin, I. Supek, A. Thomas, M. Unverzagt, T. Walcher, L. Zana, and F. Zehr, "Neutron skin of ^{208}Pb from coherent pion photoproduction," *Phys. Rev. Lett.*, vol. 112, p. 242502, Jun 2014.

[50] A. Tamii, I. Poltoratska, P. von Neumann-Cosel, Y. Fujita, T. Adachi, C. A. Bertulani, J. Carter, M. Dozono, H. Fujita, K. Fujita, K. Hatanaka, D. Ishikawa, M. Itoh, T. Kawabata, Y. Kalmykov, A. M. Krumbholz, E. Litvinova, H. Matsubara, K. Nakanishi, R. Neveling, H. Okamura, H. J. Ong, B. Özel-Tashenov, V. Y. Ponomarev, A. Richter, B. Rubio, H. Sakaguchi, Y. Sakemi, Y. Sasamoto, Y. Shimbara, Y. Shimizu, F. D. Smit, T. Suzuki, Y. Tameshige, J. Wambach, R. Yamada, M. Yosoi, and J. Zenihiro, "Complete electric dipole response and the neutron skin in ^{208}Pb," *Phys. Rev. Lett.*, vol. 107, p. 062502, Aug 2011.

[51] S. Typel, "Neutron skin thickness of heavy nuclei with $\alpha-$particle correlations and the slope of the nuclear symmetry energy," *Phys. Rev. C*, vol. 89, p. 064321, Jun 2014.

[52] S. Typel, H. H. Wolter, G. Röpke, and D. Blaschke, "Effects of the liquid-gas phase transition and cluster formation on the symmetry energy," *The European Physical Journal A*, vol. 50, p. 17, Feb 2014.

[53] G. Hagen, A. Ekström, C. Forssén, G. R. Jansen, W. Nazarewicz, T. Papenbrock, K. A. Wendt, S. Bacca, N. Barnea, B. Carlsson, C. Drischler, K. Hebeler, M. Hjorth-Jensen, M. Miorelli, G. Orlandini, A. Schwenk, and J. Simonis, "Neutron and weak-charge distributions of the ^{48}Ca nucleus," *Nature Physics*, vol. 12, pp. 186 EP –, Nov 2015. Article.

[54] P. Kienle, "Medium energy antiproton absorption, a tool to study neutron halo nuclei," *Nuclear Instruments and Methods in Physics Research Section B: Beam Interactions with Materials and Atoms*, vol. 214, pp. 191 – 195, 2004. Low Energy Antiproton Physics (LEAP'03).

[55] W. M. Bugg, G. T. Condo, E. L. Hart, H. O. Cohn, and R. D. McCulloch, "Evidence for a neutron halo in heavy nuclei from antiproton absorption," *Phys. Rev. Lett.*, vol. 31, pp. 475–478, Aug 1973.

[56] J. Eades and F. J. Hartmann, "Forty years of antiprotons," *Rev. Mod. Phys.*, vol. 71, pp. 373–419, Jan 1999.

[57] S. Wycech, J. Skalski, R. Smolańczuk, J. Dobaczewski, and J. R. Rook, "Antiprotonic studies of nuclear neutron halos," *Phys. Rev. C*, vol. 54, pp. 1832–1842, Oct 1996.

[58] R. Schmidt, F. J. Hartmann, B. Ketzer, T. von Egidy, T. Czosnyka, J. Jastrzębski, M. Kisieliński, P. Lubiński, P. Napiorkowski, L. Pieńkowski, A. Trzcińska, B. Kłos, R. Smolańczuk, S. Wycech, W. Pöschl, K. Gulda, W. Kurcewicz, and E. Widmann, "Composition of the nuclear periphery from antiproton absorption using short-lived residual nuclei," *Phys. Rev. C*, vol. 60, p. 054309, Oct 1999.

[59] B. Kłos, A. Trzcińska, J. Jastrzębski, T. Czosnyka, M. Kisieliński, P. Lubiński, P. Napiorkowski, L. Pieńkowski, F. J. Hartmann, B. Ketzer, P. Ring, R. Schmidt, T. v. Egidy, R. Smolańczuk, S. Wycech, K. Gulda, W. Kurcewicz, E. Widmann, and B. A. Brown, "Neutron density distributions from antiprotonic ^{208}Pb and ^{209}Bi atoms," *Phys. Rev. C*, vol. 76, p. 014311, Jul 2007.

[60] A. Trzcińska, J. Jastrzębski, P. Lubiński, F. J. Hartmann, R. Schmidt, T. von Egidy, and B. Kłos, "Neutron density distributions deduced from antiprotonic atoms," *Phys. Rev. Lett.*, vol. 87, p. 082501, Aug 2001.

[61] E. Widmann, "Low-energy antiprotons physics and the FLAIR facility," *Physica Scripta*, vol. T166, p. 014074, nov 2015.

[62] E. Kugler, D. Fiander, B. Johnson, H. Haas, A. Przewloka, H. Ravn, D. Simon, and K. Zimmer, "The new CERN-ISOLDE on-line mass-separator facility at the PS-booster," *Nuclear Instruments and Methods in Physics Research Section B: Beam Interactions with Materials and Atoms*, vol. 70, no. 1, pp. 41 – 49, 1992.

[63] J. S. Cohen, "Capture of antiprotons by some radioactive atoms and ions," *Phys. Rev. A*, vol. 69, p. 022501, Feb 2004.

[64] E. Fermi, E. Teller, and V. Weisskopf, "The decay of negative mesotrons in matter," *Phys. Rev.*, vol. 71, pp. 314–315, Mar 1947.

[65] K. Sakimoto, "Cross sections for antiproton capture by helium ions," *Phys. Rev. A*, vol. 82, p. 012501, Jul 2010.

[66] N. H. Kwong, J. D. Garcia, and J. S. Cohen, "Classical-quantal coupling in the capture of muons by hydrogen atoms," *Journal of Physics B: Atomic, Molecular and Optical Physics*, vol. 22, pp. L633–L638, nov 1989.

[67] J. S. Cohen, "Capture of negative exotic particles by atoms, ions and molecules," *Reports on Progress in Physics*, vol. 67, pp. 1769–1819, aug 2004.

[68] R. Schmidt, F. J. Hartmann, T. von Egidy, T. Czosnyka, J. Iwanicki, J. Jastrzębski, M. Kisieliński, P. Lubiński, P. Napiorkowski, L. Pieńkowski, A. Trzcińska, J. Kulpa, R. Smolańczuk, S. Wycech, B. Kłos, K. Gulda, W. Kurcewicz, and E. Widmann, "Nucleon density of ^{172}Yb and ^{176}Yb at the nuclear periphery determined with antiprotonic x rays," *Phys. Rev. C*, vol. 58, pp. 3195–3204, Dec 1998.

[69] J. S. Cohen, "Capture of negative muons and antiprotons by noble-gas atoms," *Phys. Rev. A*, vol. 65, p. 052714, May 2002.

[70] J. S. Cohen, "Multielectron effects in capture of antiprotons and muons by helium and neon," *Phys. Rev. A*, vol. 62, p. 022512, Jul 2000.

[71] R. Callies, H. Daniel, F. Hartmann, and W. Neumann, "Detection of muonic Auger electron lines from silver," *Physics Letters A*, vol. 91, no. 9, pp. 441 – 443, 1982.

[72] R. Bacher, P. Blüm, D. Gotta, K. Heitlinger, M. Schneider, J. Missimer, L. M. Simons, and K. Elsener, "Degree of ionization in antiprotonic noble gases," *Phys. Rev. A*, vol. 38, pp. 4395–4404, Nov 1988.

[73] Gotta, D., Rashid, K., Fricke, B., Indelicato, P., and Simons, L. M., "X-ray transitions from antiprotonic noble gases," *Eur. Phys. J. D*, vol. 47, no. 1, pp. 11–26, 2008.

[74] M. Leon and R. Seki, "Determination of the neutron halo from antiproton absorption," *Physics Letters B*, vol. 48, no. 3, pp. 173 – 175, 1974.

[75] J. Desclaux, "Relativistic multiconfiguration Dirac-Fock package," *Methods an Techniques in Computational Chemistry*, 1993.

[76] T. Ishiwatari, G. Beer, A. Bragadireanu, M. Cargnelli, C. C. (Petrascu), J.-P. Egger, H. Fuhrmann, C. Guaraldo, P. Kienle, T. Koike, M. Iliescu, K. Itahashi, M. Iwasaki, B. Lauss, V. Lucherini, L. Ludhova, J. Marton, F. Mulhauser, T. Ponta, L. Schaller, R. Seki, D. Sirghi, F. Sirghi, P. Strasser, and J. Zmeskal, "Kaonic nitrogen x-ray transition yields in a gaseous target," *Physics Letters B*, vol. 593, no. 1, pp. 48 – 54, 2004.

[77] E. Friedman, A. Gal, and J. Mareš, "Antiproton–nucleus potentials from global fits to antiprotonic X-rays and radiochemical data," *Nuclear Physics A*, vol. 761, no. 3, pp. 283 – 295, 2005.

[78] C. Dover, T. Gutsche, M. Maruyama, and A. Faessler, "The physics of nucleon-antinucleon annihilation," *Progress in Particle and Nuclear Physics*, vol. 29, pp. 87 – 173, 1992.

[79] G. Ghesquière, "An inclusive view on $\bar{p}p \to \pi$ at rest," 1974. in *Symposium on Antinucleon-Nucleon Interactions*.

[80] S. Orfanidis and V. Rittenberg, "Nucleon-antinucleon annihilation into pions," *Nuclear Physics B*, vol. 59, no. 2, pp. 570 – 582, 1973.

[81] D. Mancusi, S. Lo Meo, N. Colonna, A. Boudard, M. A. Cortés-Giraldo, J. Cugnon, J.-C. David, S. Leray, J. Lerendegui-Marco, C. Massimi, and V. Vlachoudis, "On the role of secondary pions in spallation targets," *The European Physical Journal A*, vol. 53, p. 80, May 2017.

[82] J. Cugnon, S. Wycech, J. Jastrzębski, and P. Lubiński, "Geometrical effects in antiproton annihilation on nuclei," *Phys. Rev. C*, vol. 63, p. 027301, Jan 2001.

[83] M. Wada and Y. Yamazaki, "Antiprotonic radioactive atom for nuclear structure studies," *AIP Conference Proceedings*, vol. 793, no. 1, pp. 233–241, 2005.

[84] M. Abadi, A. Agarwal, P. Barham, E. Brevdo, Z. Chen, C. Citro, G. S. Corrado, A. Davis, J. Dean, M. Devin, S. Ghemawat, I. Goodfellow, A. Harp, G. Irving, M. Isard, Y. Jia, R. Jozefowicz, L. Kaiser, M. Kudlur, J. Levenberg, D. Mané, R. Monga, S. Moore, D. Murray, C. Olah, M. Schuster, J. Shlens, B. Steiner, I. Sutskever, K. Talwar, P. Tucker, V. Vanhoucke, V. Vasudevan, F. Viégas, O. Vinyals, P. Warden, M. Wattenberg, M. Wicke, Y. Yu, and X. Zheng, "TensorFlow: Large-scale machine learning on heterogeneous systems," 2015. Software available from tensorflow.org.

[85] F. Chollet *et al.*, "Keras." `https://keras.io`, 2015.

[86] D. P. Kingma and J. Ba, "Adam: A method for stochastic optimization," 2014.

[87] M. Cahay, J. Cugnon, and J. Vandermeulen, "Low-energy antiproton annihilation in nuclei," *Nuclear Physics A*, vol. 393, no. 3, pp. 237 – 251, 1983.

[88] J. Cugnon, P. Deneye, and J. Vandermeulen, "Multipion dynamics following antiproton annihilation on nuclei," *Nuclear Physics A*, vol. 500, no. 3, pp. 701 – 730, 1989.

[89] J. Cugnon, P. Deneye, and J. Vandermeulen, "Antiproton annihilation at rest on light nuclei: Rescattering, strange-particle yield and B = 1 annihilation," *Nuclear Physics A*, vol. 517, no. 3, pp. 533 – 553, 1990.

[90] J. Cugnon, T. Mizutani, and J. Vandermeulen, "Equilibration in relativistic nuclear collisions. a Monte Carlo calculation," *Nuclear Physics A*, vol. 352, no. 3, pp. 505 – 534, 1981.

[91] A. Boudard, J. Cugnon, S. Leray, and C. Volant, "Intranuclear cascade model for a comprehensive description of spallation reaction data," *Phys. Rev. C*, vol. 66, p. 044615, Oct 2002.

[92] A. Boudard, J. Cugnon, J.-C. David, S. Leray, and D. Mancusi, "New potentialities of the Liège intranuclear cascade model for reactions induced by nucleons and light charged particles," *Phys. Rev. C*, vol. 87, p. 014606, Jan 2013.

[93] C. B. Dover and J. M. Richard, "Elastic, charge exchange, and inelastic $\overline{p}p$ cross sections in the optical model," *Phys. Rev. C*, vol. 21, pp. 1466–1471, Apr 1980.

[94] M. Kohno and W. Weise, "Proton-antiproton scattering and annihilation into two mesons," *Nuclear Physics A*, vol. 454, no. 3, pp. 429 – 452, 1986.

[95] B. El-Bennich, M. Lacombe, B. Loiseau, and S. Wycech, "Paris $N\overline{N}$ potential constrained by recent antiprotonic-atom data and $\overline{n}p$ total cross sections," *Phys. Rev. C*, vol. 79, p. 054001, May 2009.

[96] L.-Y. Dai, J. Haidenbauer, and U.-G. Meißner, "Antinucleon-nucleon interaction at next-to-next-to-next-to-leading order in chiral effective field theory," *Journal of High Energy Physics*, vol. 2017, p. 78, Jul 2017.

[97] O. D. Dalkarov, J. Carbonell, and K. V. Protasov, "Baryon-antibaryon states: Spectra, production, decay," *Il Nuovo Cimento A (1965-1970)*, vol. 107, pp. 2409–2414, Nov 1994.

[98] J. Carbonell, K. Protasov, and O. Dalkarov, "On a possible near threshold lambda-lambda state," *Physics Letters B*, vol. 306, no. 3, pp. 407 – 410, 1993.

[99] J. Carbonell, G. Ihle, and J. M. Richard, "Protonium annihilation in optical models," *Zeitschrift für Physik A Atomic Nuclei*, vol. 334, pp. 329–341, Sep 1989.

[100] R. Lazauskas and J. Carbonell, "Testing nonlocal nucleon-nucleon interactions in four-nucleon systems," *Phys. Rev. C*, vol. 70, p. 044002, Oct 2004.

[101] R. Lazauskas, "Solution of the $n - ^4$He elastic scattering problem using the Faddeev-Yakubovsky equations," *Phys. Rev. C*, vol. 97, p. 044002, Apr 2018.

[102] P. Navrátil, S. Quaglioni, G. Hupin, C. Romero-Redondo, and A. Calci, "Unified ab initio approaches to nuclear structure and reactions," *Physica Scripta*, vol. 91, p. 053002, apr 2016.

[103] A. Calci, P. Navrátil, R. Roth, J. Dohet-Eraly, S. Quaglioni, and G. Hupin, "Can ab initio theory explain the phenomenon of parity inversion in ^{11}Be?," *Phys. Rev. Lett.*, vol. 117, p. 242501, Dec 2016.

[104] S. Wycech, F. Hartmann, H. Daniel, W. Kanert, H. Plendl, T. von Egidy, J. Reidy, M. Nicholas, L. Redmond, H. Koch, A. Kreissl, H. Poth, and D. Rohmann, "Antiprotonic atoms with heavy nuclei," *Nuclear Physics A*, vol. 561, no. 4, pp. 607 – 627, 1993.

[105] C. Batty, E. Friedman, and A. Gal, "Strong interaction physics from hadronic atoms," *Physics Reports*, vol. 287, no. 5, pp. 385 – 445, 1997.

[106] F. G. Bracci, L and O. Pitzurra, "Protonium formation in flight," *Phys. Lett., B; (Netherlands)*, vol. 85:2-3, Aug 1979.

[107] X. Fei, *Trapping Low Energy in an Ion Trap*. PhD thesis, Harvard University, 1990.

[108] E. Butler, *Antihydrogen formation, dynamics and trapping*. PhD thesis, Swansea University, 2011.

[109] C. Benvenuti, "Extreme vacua: Achievements and expectations," *Physica Scripta*, vol. T22, pp. 48–54, jan 1988.

[110] *Vacuum Performance of Amorphous Carbon Coating at Cryogenic Temperature with Presence of Proton Beams*, no. 7 in International Particle Accelerator Conference, (Geneva, Switzerland), JACoW, June 2016. doi:10.18429/JACoW-IPAC2016-THPMY007.

[111] P. Chiggiato, *Vacuum Technology for Ion Sources*. CERN, 2014.

[112] F. Chill, S. Wilfert, and L. Bozyk, "Cryopumping of hydrogen on stainless steel in the temperature range between 7 and 18 K," *Journal of Vacuum Science & Technology A*, vol. 37, Mar. 2019.

[113] P. A. Redhead, J. P. Hobson, and E. V. Kornelsen, *The Physical Basis of Ultrahigh Vacuum*. AIP-Press, 1 ed., 1993.

[114] K. Jousten, *Handbook of Vacuum Technology*. Wiley-VCH Verlag, 2016.

[115] H. Freundlich *Kapillarchemie (Leipizig)*, vol. I, 1930.

[116] S. Brunauer, P. H. Emmett, , and E. Teller, "Adsorption of gases in multimolecular layers," *American Chemical Society*, vol. 60, pp. 309–319, Feb. 1938.

[117] D. M. Young and A. D. Crowell, *Physical Adsorption of Gases*. Butterworths, 1962.

[118] M. M. Dubinin *Russian Journal of Physical Chemistry*, vol. 39, no. 487, 1965.

[119] M. M. Dubinin *Journal of Colloid and Interface Science*, vol. 23, no. 487, 1967.

[120] M. M. Dubinin and L. V. Radushkevich *Proceedings of the USSR Academy of Sciences*, vol. 55, no. 327, 1947.

[121] M. G. Kaganer *Proc. Acad. Sci. U.S.S.R.*, vol. 116, no. 603, 1957.

[122] M. Polanyi *Z. Electrochem.*, vol. 26, no. 371, 1920.

[123] R. A. Haefer, *Cryopumping: Theory and Practice*. Oxford University Press, Sept. 1989.

[124] E. Wallén, "Adsorption isotherms of He and H_2 at liquid He temperatures," *Journal of Vacuum Science & Technology A*, vol. 15, no. 2, pp. 265–274, 1997.

[125] CERN, *Basics and applications of cryopumps*, CAS - CERN Accelerator School and ALBA Synchrotron Light Facility: Course on Vacuum in Accelerators, May 2007.

[126] A. Güntherschulze, H. Betz, and H. Kleinwächter, "Die diffusion von wasserstoff und deuterium durch eisen," *Zeitschrift für Physik*, vol. 111, pp. 657–679, Sep 1939.

[127] K. Kiuchi and R. McLellan, "The solubility and diffusivity of hydrogen in well-annealed and deformed iron," *Acta Metallurgica*, vol. 31, no. 7, pp. 961 – 984, 1983.

[128] J. P. Hobson, "Theoretical isotherms for physical adsorption at pressures below 10^{-10} torr," *Journal of Vacuum Science and Technology*, vol. 3, no. 281, 1966.

[129] Molflow+: A test-particle Monte-Carlo simulator for ultra-high-vacuum systems developed at CERN, see https://molflow.web.cern.ch/ (last accessed August 1, 2019).

[130] R. Kersevan and J.-L. Pons, "Introduction to MOLFLOW+: New graphical processing unit-based Monte Carlo code for simulating molecular flows and for calculating angular coefficients in the compute unified device architecture environment," *Journal of Vacuum Science & Technology A*, vol. 27, no. 1017, 2009.

[131] COMSOL Multiphysics: A finite element analysis, solver and multiphysics simulation software developed by COMSOL Inc.

[132] J. N. Chubb, L. Gowland, and I. E. Pollard, "Condensation pumping of hydrogen and deuterium on to liquid-helium-cooled surfaces," *Journal of Physics D: Applied Physics*, vol. 1, pp. 361–370, mar 1968.

[133] K. Kanazawa, "Analysis of pumping down process," *Journal of Vacuum Science & Technology A*, vol. 7, no. 3361, 1989.

[134] A. Hobl, "PUMA Functional Design Report," tech. rep., Bilfinger Noell GmbH, 2019.

[135] N. Marsic, A. Obertelli, W. Müller, and H. De Gersem, "Three-stage procedure for optimizing a superconducting solenoid magnet with active and passive shields," *submitted for publication*, 2019.

[136] ATRAP Collaboration. `http://gabrielse.physics.harvard.edu/`.

[137] Alpha Collaboration. `http://alpha.web.cern.ch`.

[138] AEgIS Collaboration. `https://aegis.web.cern.ch/aegis/`.

[139] BASE Collaboration. `http://base.web.cern.ch`.

[140] ASACUSA Collaboration. `http://asacusa.web.cern.ch/ASACUSA/`.

[141] ELENA project. `https://espace.cern.ch/elena-project/SitePages/Home.aspx`.

[142] G. Gabrielse, N. Bowden, P. Oxley, A. Speck, C. Storry, J. Tan, M. Wessels, D. Grzonka, W. Oelert, G. Schepers, T. Sefzick, J. Walz, H. Pittner, T. Hänsch, and E. Hessels, "Stacking of cold antiprotons," *Physics Letters B*, vol. 548, no. 3, pp. 140 – 145, 2002.

[143] A. W. Trivelpiece and R. W. Gould, "Space charge waves in cylindrical plasma columns," *Journal of Applied Physics*, vol. 30, no. 11, pp. 1784–1793, 1959.

[144] X.-P. Huang, F. Anderegg, E. M. Hollmann, C. F. Driscoll, and T. M. O'Neil, "Steady-state confinement of non-neutral plasmas by rotating electric fields," *Phys. Rev. Lett.*, vol. 78, pp. 875–878, Feb 1997.

[145] F. Anderegg, E. M. Hollmann, and C. F. Driscoll, "Rotating field confinement of pure electron plasmas using trivelpiece-gould modes," *Phys. Rev. Lett.*, vol. 81, pp. 4875–4878, Nov 1998.

[146] E. M. Hollmann, F. Anderegg, and C. F. Driscoll, "Confinement and manipulation of non-neutral plasmas using rotating wall electric fields," *Physics of Plasmas*, vol. 7, no. 7, pp. 2776–2789, 2000.

[147] R. G. Greaves and C. M. Surko, "Inward transport and compression of a positron plasma by a rotating electric field," *Phys. Rev. Lett.*, vol. 85, pp. 1883–1886, Aug 2000.

[148] J. R. Danielson and C. M. Surko, "Torque-balanced high-density steady states of single-component plasmas," *Phys. Rev. Lett.*, vol. 94, p. 035001, Jan 2005.

[149] G. B. Andresen, W. Bertsche, P. D. Bowe, C. C. Bray, E. Butler, C. L. Cesar, S. Chapman, M. Charlton, J. Fajans, M. C. Fujiwara, R. Funakoshi, D. R. Gill, J. S. Hangst, W. N. Hardy, R. S. Hayano, M. E. Hayden, R. Hydomako, M. J. Jenkins, L. V. Jørgensen, L. Kurchaninov, R. Lambo, N. Madsen, P. Nolan, K. Olchanski, A. Olin, A. Povilus, P. Pusa, F. Robicheaux, E. Sarid, S. Seif El Nasr, D. M. Silveira, J. W. Storey, R. I. Thompson, D. P. van der Werf, J. S. Wurtele, and Y. Yamazaki, "Compression of antiproton clouds for antihydrogen trapping," *Phys. Rev. Lett.*, vol. 100, p. 203401, May 2008.

[150] S. Aghion, C. Amsler, G. Bonomi, R. S. Brusa, M. Caccia, R. Caravita, F. Castelli, G. Cerchiari, D. Comparat, G. Consolati, A. Demetrio, L. Di Noto, M. Doser, C. Evans, M. Fanì, R. Ferragut, J. Fesel, A. Fontana, S. Gerber, M. Giammarchi, A. Gligorova, F. Guatieri, S. Haider, A. Hinterberger, H. Holmestad, A. Kellerbauer, O. Khalidova, D. Krasnický, V. Lagomarsino, P. Lansonneur, P. Lebrun, C. Malbrunot, S. Mariazzi, J. Marton, V. Matveev, Z. Mazzotta, S. R. Müller, G. Nebbia, P. Nedelec, M. Oberthaler, N. Pacifico, D. Pagano, L. Penasa, V. Petracek, F. Prelz, M. Prevedelli, B. Rienaecker, J. Robert, O. M. Røhne, A. Rotondi, H. Sandaker, R. Santoro, L. Smestad, F. Sorrentino, G. Testera, I. C. Tietje, E. Widmann, P. Yzombard, C. Zimmer, J. Zmeskal, N. Zurlo, and M. Antonello, "Compression of a mixed antiproton

and electron non-neutral plasma to high densities," *The European Physical Journal D*, vol. 72, p. 76, Apr 2018.

[151] G. Gabrielse, W. S. Kolthammer, R. McConnell, P. Richerme, J. Wrubel, R. Kalra, E. Novitski, D. Grzonka, W. Oelert, T. Sefzick, M. Zielinski, J. S. Borbely, D. Fitzakerley, M. C. George, E. A. Hessels, C. H. Storry, M. Weel, A. Müllers, J. Walz, and A. Speck, "Centrifugal separation of antiprotons and electrons," *Phys. Rev. Lett.*, vol. 105, p. 213002, Nov 2010.

[152] M. Amoretti, C. Amsler, G. Bonomi, A. Bouchta, P. D. Bowe, C. Carraro, C. L. Cesar, M. Charlton, M. Doser, V. Filippini, A. Fontana, M. C. Fujiwara, R. Funakoshi, P. Genova, J. S. Hangst, R. S. Hayano, L. V. Jørgensen, V. Lagomarsino, R. Landua, D. Lindelöf, E. L. Rizzini, M. Macrí, N. Madsen, G. Manuzio, P. Montagna, H. Pruys, C. Regenfus, A. Rotondi, G. Testera, A. Variola, and D. P. van der Werf, "Positron plasma diagnostics and temperature control for antihydrogen production," *Phys. Rev. Lett.*, vol. 91, p. 055001, Jul 2003.

[153] M. Amoretti, G. Bonomi, A. Bouchta, P. D. Bowe, C. Carraro, C. L. Cesar, M. Charlton, M. Doser, A. Fontana, M. C. Fujiwara, R. Funakoshi, P. Genova, J. S. Hangst, R. S. Hayano, L. V. Jørgensen, L. V.rgensen, V. Lagomarsino, R. Landua, E. L. Rizzini, M. Macrí, M., N. Madsen, G. Manuzio, G. Testera, A. Variola, and D. P. van der Werf, "Complete nondestructive diagnostic of nonneutral plasmas based on the detection of electrostatic modes," *Physics of Plasmas*, vol. 10, no. 8, pp. 3056–3064, 2003.

[154] A. Speck, G. Gabrielse, P. Larochelle, D. L. Sage, B. Levitt, W. Kolthammer, R. McConnell, J. Wrubel, D. Grzonka, W. Oelert, T. Sefzick, Z. Zhang, D. Comeau, M. George, E. Hessels, C. Storry, M. Weel, and J. Walz, "Density and geometry of single component plasmas," *Physics Letters B*, vol. 650, no. 2, pp. 119 – 123, 2007.

[155] M. Amoretti, C. Amsler, G. Bonomi, A. Bouchta, P. Bowe, C. Carraro, M. Charlton, M. Collier, M. Doser, V. Filippini, K. Fine, A. Fontana, M. Fujiwara, R. Funakoshi, P. Genova, A. Glauser, D. Grögler, J. Hangst, R. Hayano, H. Higaki, M. Holzscheiter, W. Joffrain, L. Jørgensen, V. Lagomarsino, R. Landua, C. L. Cesar, D. Lindelöf, E. Lodi-Rizzini, M. Macri, N. Madsen, D. Manuzio, G. Manuzio, M. Marchesotti, P. Montagna, H. Pruys, C. Regenfus, P. Riedler, J. Rochet, A. Rotondi, G. Rouleau, G. Testera, D. P. van der Werf, A. Variola, T. Watson, T. Yamazaki, and Y. Yamazaki, "The athena antihydrogen apparatus," *Nuclear Instruments and Methods in Physics Research Section A: Accelerators, Spectrometers, Detectors and Associated Equipment*, vol. 518, no. 3, pp. 679 – 711, 2004.

[156] P. Richerme, *Trapped Antihydrogen in Its Ground State*. PhD thesis, Harvard University, Cambridge, Massachusetts, USA, May 2012.

[157] C. Amole, G. Andresen, M. Ashkezari, M. Baquero-Ruiz, W. Bertsche, P. Bowe, E. Butler, A. Capra, P. Carpenter, C. Cesar, S. Chapman, M. Charlton, A. Deller, S. Eriksson, J. Escallier, J. Fajans, T. Friesen, M. Fujiwara, D. Gill, A. Gutierrez, J. Hangst, W. Hardy, R. Hayano, M. Hayden, A. Humphries, J. Hurt, R. Hydomako, C. Isaac, M. Jenkins, S. Jonsell, L. Jørgensen, S. Kerrigan, L. Kurchaninov, N. Madsen, A. Marone, J. McKenna, S. Menary, P. Nolan, K. Olchanski, A. Olin, B. Parker, A. Povilus, P. Pusa, F. Robicheaux, E. Sarid, D. Seddon, S. S. E. Nasr, D. Silveira, C. So, J. Storey, R. Thompson, J. Thornhill, D. Wells, D. van der Werf, J. Wurtele, and Y. Yamazaki, "The alpha antihydrogen trapping apparatus," *Nuclear Instruments and Methods in Physics Research Section A: Accelerators, Spectrometers, Detectors and Associated Equipment*, vol. 735, pp. 319 – 340, 2014.

[158] C. Smorra, A. Mooser, K. Franke, H. Nagahama, G. Schneider, T. Higuchi, S. Gorp, K. Blaum, Y. Matsuda, W. Quint, J. Walz, Y. Yamazaki, and S. Ulmer, "A reservoir trap for antiprotons," *International Journal of Mass Spectrometry*, vol. 389, pp. 10 – 13, 2015.

[159] G. Gabrielse, J. Estrada, J. Tan, P. Yesley, N. Bowden, P. Oxley, T. Roach, C. Storry, M. Wessels, J. Tan, D. Grzonka, W. Oelert, G. Schepers, T. Sefzick, W. Breunlich, M. Cargnelli, H. Fuhrmann, R. King, R. Ursin, J. Zmeskal, H. Kalinowsky, C. Wesdorp, J. Walz, K. Eikema, and T. Hänsch, "First positron cooling of antiprotons," *Physics Letters B*, vol. 507, no. 1, pp. 1 – 6, 2001.

[160] D. S. Hall and G. Gabrielse, "Electron cooling of protons in a nested penning trap," *Phys. Rev. Lett.*, vol. 77, pp. 1962–1965, Sep 1996.

[161] G. Testera, S. Aghion, C. Amsler, A. Ariga, T. Ariga, A. Belov, G. Bonomi, P. Braunig, J. Bremer, R. Brusa, L. Cabaret, M. Caccia, R. Caravita, F. Castelli, G. Cerchiari, K. Chlouba, S. Cialdi, D. Comparat, G. Consolati, S. Curreli, A. Demetrio, H. Derking, L. D. Noto, M. Doser, A. Dudarev, A. Ereditato, R. Ferragut, A. Fontana, S. Gerber, M. Giammarchi, A. Gligorova, S. Gninenko, S. Haider, S. Hogan, H. Holmestad, T. Huse, E. J. Jordan, J. Kawada, A. Kellerbauer, M. Kimura, D. Krasnický, V. Lagomarsino, S. Lehner, C. Malbrunot, S. Mariazzi, V. Matveev, Z. Mazzotta, G. Nebbia, P. Nedelec, M. Oberthaler, N. Pacifico, L. Penasa, V. Petracek, C. Pistillo, F. Prelz, M. Prevedelli, L. Ravelli, C. Riccardi, O. M. Røhne, S. Rosenberger, A. Rotondi, H. Sandaker, R. Santoro, P. Scampoli, L. Semeria, M. Simon, M. Spacek, J. Storey, I. M. Strojek, M. Subieta, E. Widmann, P. Yzombard, S. Zavatarelli, J. Zmeskal, and (AEgIS Collaboration), "The AEgIS experiment," *Hyperfine Interactions*, vol. 233, pp. 13–20, Aug 2015.

[162] T. Mohamed, "Compression features of high density electron plasma in a long harmonic trap using a rotating wall technique," *Physics Letters A*, vol. 382, pp. 2459 – 2463, 07 2018.

[163] J. M. A. Repp, *The setup of the high-precision Penning trap mass spectrometer PENTATRAP and first production studies of highly charged ions*. PhD thesis, Ruprecht-Karls-Universität Heidelberg, 2012.

[164] Z. Andelkovic, *Setup of a Penning trap for precision laser spectroscopy at HITRAP*. PhD thesis, Johannes Gutenberg-Universität Mainz, 2012.

[165] Lake Shore Cryotronics, Inc., *Appendix I: Cryogenic Reference Tables*.

[166] G. W. Hart, "The effect of a tilted magnetic field on the equilibrium of a pure electron plasma," *Physics of Fluids B: Plasma Physics*, vol. 3, no. 11, pp. 2987–2993, 1991.

[167] GBAR collaboration. `https://gbar.web.cern.ch/GBAR/public/index.html`.

[168] J. H. Malmberg and J. S. deGrassie, "Properties of nonneutral plasma," *Phys. Rev. Lett.*, vol. 35, pp. 577–580, Sep 1975.

[169] D. H. E. Dubin, "Theory of electrostatic fluid modes in a cold spheroidal nonneutral plasma," *Phys. Rev. Lett.*, vol. 66, pp. 2076–2079, Apr 1991.

[170] A. Mohri, H. Higaki, H. Tanaka, Y. Yamazawa, M. Aoyagi, T. Yuyama, and T. Michishita, "Confinement of Nonneutral Spheroidal Plasmas in Multi-Ring Electrode Traps," *Japanese Journal of Applied Physics*, vol. 37, p. 664, Feb. 1998.

[171] S. A. Prasad and T. M. O'Neil, "Finite length thermal equilibria of a pure electron plasma column," *The Physics of Fluids*, vol. 22, no. 2, pp. 278–281, 1979.

[172] T. M. O'Neil and R. A. Smith, "Stability theorem for off-axis states of a nonneutral plasma column," *Physics of Fluids B: Plasma Physics*, vol. 4, no. 9, pp. 2720–2728, 1992.

[173] T. M. O'Neil, "A confinement theorem for nonneutral plasmas," *The Physics of Fluids*, vol. 23, no. 11, pp. 2216–2218, 1980.

[174] D. J. Wineland, J. J. Bollinger, W. M. Itano, and J. D. Prestage, "Angular momentum of trapped atomic particles," *J. Opt. Soc. Am. B*, vol. 2, pp. 1721–1730, Nov 1985.

[175] J. R. Danielson, C. M. Surko, and T. M. O'Neil, "High-density fixed point for radially compressed single-component plasmas," *Phys. Rev. Lett.*, vol. 99, p. 135005, Sep 2007.

[176] F. Anderegg, *Trapped Charged Particles*. World Scientific, 2016.

[177] G.-Z. Li, S. Guan, and A. G. Marshall, "Sympathetic cooling of trapped negative ions by self-cooled electrons in a fourier transform ion cyclotron resonance mass spectrometer," *Journal of the American Society for Mass Spectrometry*, vol. 8, no. 8, pp. 793 – 800, 1997.

[178] M. Amoretti, G. Bonomi, A. Bouchta, P. D. Bowe, C. Carraro, C. L. Cesar, M. Charlton, M. Doser, A. Fontana, M. C. Fujiwara, R. Funakoshi, P. Genova, J. S. Hangst, R. S. Hayano, L. V. Jørgensen, V. Lagomarsino, R. Landua, E. L. Rizzini, M. Macrí, N. Madsen, G. Manuzio, G. Testera, A. Variola, and D. P. van der Werf, "Complete nondestructive diagnostic of nonneutral plasmas based on the detection of electrostatic modes," *Physics of Plasmas*, vol. 10, no. 8, pp. 3056–3064, 2003.

[179] H. Higaki and A. Mohri, "Wall and temperature effects on electrostatic oscillations of spheroidal non-neutral electron plasmas in the multi-ring electrode trap," *Japanese Journal of Applied Physics*, vol. 36, pp. 5300–5305, aug 1997.

[180] M. Amoretti, C. Amsler, G. Bonomi, A. Bouchta, P. D. Bowe, C. Carraro, C. L. Cesar, M. Charlton, M. Doser, V. Filippini, A. Fontana, M. C. Fujiwara, R. Funakoshi, P. Genova, J. S. Hangst, R. S. Hayano, L. V. Jørgensen, V. Lagomarsino, R. Landua, D. Lindelöf, E. L. Rizzini, M. Macrí, N. Madsen, G. Manuzio, P. Montagna, H. Pruys, C. Regenfus, A. Rotondi, G. Testera, A. Variola, and D. P. van der Werf, "Positron plasma diagnostics and temperature control for antihydrogen production," *Phys. Rev. Lett.*, vol. 91, p. 055001, Jul 2003.

[181] M. D. Tinkle, R. G. Greaves, C. M. Surko, R. L. Spencer, and G. W. Mason, "Low-order modes as diagnostics of spheroidal non-neutral plasmas," *Phys. Rev. Lett.*, vol. 72, pp. 352–355, Jan 1994.

[182] A. V. Crewe, D. N. Eggenberger, J. Wall, and L. M. Welter, "Electron gun using a field emission source," *Review of Scientific Instruments*, vol. 39, no. 4, pp. 576–583, 1968.

[183] S. Ulmer, *First Observation of Spin Flips with a Single Proton Stored in a Cryogenic Penning Trap*. PhD thesis, Ruperto-Carola University of Heidelberg, 2011.

[184] J. E. Henderson and R. K. Dahlstrom, "The energy distribution in field emission," *Phys. Rev.*, vol. 55, pp. 473–481, Mar 1939.

[185] J. W. Gadzuk and E. W. Plummer, "Field emission energy distribution (feed)," *Rev. Mod. Phys.*, vol. 45, pp. 487–548, Jul 1973.

[186] G. B. Andresen, W. Bertsche, P. D. Bowe, C. C. Bray, E. Butler, C. L. Cesar, S. Chapman, M. Charlton, S. S. El Nasr, J. Fajans, M. C. Fujiwara, D. R. Gill, J. S. Hangst, W. N. Hardy, R. S. Hayano, M. E. Hayden, A. J. Humphries, R. Hydomako, L. V. Jørgensen, S. J. Kerrigan, L. Kurchaninov, R. Lambo,

N. Madsen, P. Nolan, K. Olchanski, A. Olin, A. P. Povilus, P. Pusa, E. Sarid, D. M. Silveira, J. W. Storey, R. I. Thompson, D. P. van der Werf, Y. Yamazaki, and A. Collaboration, "Antiproton, positron, and electron imaging with a microchannel plate/phosphor detector," *Review of Scientific Instruments*, vol. 80, no. 12, p. 123701, 2009.

[187] P. Lansonneur, *Moiré Deflectometry with a Low-Energy Ion Beam for the AEGIS Experiment.* PhD thesis, Université de Lyon, 2017.

[188] Hamamatsu Photonics K.K., *MCP Assembly: Technical Information.*

[189] C. Smorra, K. Blaum, L. Bojtar, M. Borchert, K. Franke, T. Higuchi, N. Leefer, H. Nagahama, Y. Matsuda, A. Mooser, M. Niemann, C. Ospelkaus, W. Quint, G. Schneider, S. Sellner, T. Tanaka, S. Van Gorp, J. Walz, Y. Yamazaki, and S. Ulmer, "Base – the baryon antibaryon symmetry experiment," *The European Physical Journal Special Topics*, vol. 224, pp. 3055–3108, Nov 2015.

[190] Y. Giomataris, P. Rebourgeard, J. Robert, and G. Charpak, "MICROMEGAS: a high-granularity position-sensitive gaseous detector for high particle-flux environments," *Nucl. Instrum. Meth. Phys. Res. Sect. A Accel. Spectrometers, Detect. Assoc. Equip.*, vol. 376, no. 1, pp. 29–35, 1996.

[191] M. S. Dixit, J. Dubeau, J. P. Martin, and K. Sachs, "Position sensing from charge dispersion in micro-pattern gas detectors with a resistive anode," *Nucl. Instrum. Meth. Phys. Res. Sect. A Accel. Spectrometers, Detect. Assoc. Equip.*, vol. 518, no. 3, pp. 721–727, 2004.

[192] S. Agostinelli *et al.*, "Geant4 - a simulation toolkit," *Nucl. Instrum. Meth.*, vol. 506, no. 3, pp. 250 – 303, 2003.

[193] R. Brun and F. Rademakers, "Root - an object oriented data analysis framework," *Proceedings AIHENP'96 Workshop, Lausanne, Sep. 1996, Nucl. Inst. & Meth. in Phys. Res. A*, vol. 389, pp. 81–86, 1997.

[194] A. Obertelli *et al.*, "MINOS: A vertex tracker coupled to a thick liquid-hydrogen target for in-beam spectroscopy of exotic nuclei," *The European Physical Journal A*, vol. 50, p. 8, Jan 2014.

[195] C. Santamaria, A. Obertelli, S. Ota, M. Sasano, E. Takada, L. Audirac, H. Baba, D. Calvet, F. Château, A. Corsi, A. Delbart, P. Doornenbal, A. Giganon, A. Gillibert, Y. Kondo, Y. Kubota, C. Lahonde-Hamdoun, V. Lapoux, D. Leboeuf, C. Lee, H. Liu, M. Matsushita, T. Motobayashi, M. Niikura, M. Kurata-Nishimura, H. Otsu, A. Peyaud, E. Pollacco, G. Prono, H. Tokieda, T. Uesaka, and J. Zenihiro, "Tracking with the MINOS time projection chamber," *Nuclear Instruments and Methods in Physics Research Section A: Accelerators, Spectrometers, Detectors and Associated Equipment*, vol. 905, pp. 138 – 148, 2018.

[196] S. Orfanidis and V. Rittenberg, "Nucleon-antinucleon annihilation into pions," *Nuclear Physics B*, vol. 59, no. 2, pp. 570 – 582, 1973.

[197] C. Ghesquiere, "An inclusive view on $p\bar{p} \to n\pi$ at rest," *Symposium on Antinucleon-Nucleon Interactions, CERN*, 1974.

[198] W. Leo, *Techniques for Nuclear and Particle Physics Experiments: A How-to Approach*. Springer-Verlag., 1 ed., 1987. ISBN 978-3-642-57920-2.

[199] S. Biagi, "Monte carlo simulation of electron drift and diffusion in counting gases under the influence of electric and magnetic fields," *Nucl. Instrum. Meth. Res. Sect. A: Accel., Spectr., Detect. Assoc. Equip.*, vol. 421, no. 1, pp. 234 – 240, 1999.

[200] T. Zerguerras, B. Genolini, F. Kuger, M. Josselin, A. Maroni, T. Nguyen-Trung, J. Pouthas, P. Rosier, O. Şahin, D. Suzuki, and R. Veenhof, "Understanding avalanches in a Micromegas from single-electron response measurement," *Nuclear Instruments and Methods in Physics Research Section A: Accelerators, Spectrometers, Detectors and Associated Equipment*, vol. 772, pp. 76 – 82, 2015.

[201] M. Dixit and A. Rankin, "Simulating the charge dispersion phenomena in micro pattern gas detectors with a resistive anode," *Nuclear Instruments and Methods in Physics Research Section A: Accelerators, Spectrometers, Detectors and Associated Equipment*, vol. 566, pp. 281–285, 06 2006.

[202] F. James and M. Winkler, "MINUIT User's Guide," *INSPIRE*, 2004.

[203] H. J. Hilke, "Time projection chambers," *Reports on Progress in Physics*, vol. 73, no. 11, p. 116201, 2010.

[204] R. Veenhof, "Choosing a gas mixture for the ALICE TPC," *ALICE-INT-2003-29*, 2003.

[205] N. Abgrall *et al.*, "Time projection chambers for the T2K near detectors," *Nuclear Instruments and Methods in Physics Research Section A: Accelerators, Spectrometers, Detectors and Associated Equipment*, vol. 637, no. 1, pp. 25 – 46, 2011.

[206] C. Hagmann, D. Lange, and D. Wright, "Cosmic-ray shower generator (CRY) for monte carlo transport codes," in *2007 IEEE Nuclear Science Symposium Conference Record*, vol. 2, pp. 1143–1146, 2007.

[207] P. Baron *et al.*, "After, an asic for the readout of the large T2K time projection chambers," in *2007 IEEE Nuclear Science Symposium Conference Record*, vol. 55, pp. 1865 – 1872, 01 2008.

[208] S. Anvar *et al.*, "AGET, the GET front-end ASIC, for the readout of the time projection chambers used in nuclear physic experiments," in *2011 IEEE Nuclear Science Symposium Conference Record*, pp. 745–749, Oct 2011.

[209] D. Baudin, D. Attié, P. Baron, D. Bernard, D. Calvet, A. Delbart, Y. Geerebaert, and P. Gros, "ASTRE: ASIC with switched capacitor array (SCA) and trigger for detector readout electronics hardened against single event latchup (SEL)," *Nuclear Instruments and Methods in Physics Research Section A: Accelerators, Spectrometers, Detectors and Associated Equipment*, vol. 912, pp. 66 – 69, 2018. New Developments In Photodetection 2017.

[210] Pascal Baron, "ASTRE: The upgraded version of AGET ASIC." URL: `https://indico.in2p3.fr/event/17431/contributions/65827/attachments/50808/65007/ASTRE-GWS-bordeaux_.pdf`, 10 2018.

[211] D. Calvet, "Trigger & data concentrator module reference manual," *CEA Saclay*, 2019.

[212] Enclustra, "Mercury ZX1 SoC module user manual," *Enclustra, FPGA solutions*, 2018.

[213] D. Calvet, "A versatile readout system for small to medium scale gaseous and silicon detectors," *IEEE Transactions on Nuclear Science*, vol. 61, pp. 675–682, Feb 2014.

[214] F. Butin and A. Obertelli, "An Experimental Area at AD for PUMA," Engineering Change Request (ECR) AD-LJ-EC-0011, CERN, June 2019.

[215] M. Doser, 2019. Private communication.

[216] M.-E. Angoletta, P. Belochitskii, J. Borburgh, H. Breuker, M. Buzio, O. Capatina, P. Chiggiato, L. Ducimetière, T. Eriksson, T. Fowler, M. Hori, J.-M. Lacroix, G. LeGodec, P. Lelong, S. Maury, D. Möhl, A. Newborough, D. Nisbet, W. Oelert, S. Pasinelli, B. Puccio, L. Sermeus, L. Soby, D. Tommasini, G. Tranquille, and A. Vorozhtsov, "ELENA – an updated cost and feasibility study," Tech. Rep. CERN-BE-2010-029, CERN, November 2010.

[217] A. Husson, *Deceleration of antiprotons from CERN's ELENA synchrotron and transport of antimatter beams through the GBAR experiment.* PhD thesis, CSNSM, Université de Paris-Sud, 2018. Thèse de doctorat dirigée par Lunney, David Physique Paris Sud-Paris Saclay 2018.

[218] D. Lunney, C. Bachelet, C. Guénaut, S. Henry, and M. Sewtz, "COLETTE: A linear paul-trap beam cooler for the on-line mass spectrometer mistral," *Nuclear Instruments and Methods in Physics Research Section A: Accelerators, Spectrometers, Detectors and Associated Equipment*, vol. 598, no. 2, pp. 379 – 387, 2009.

[219] F. Herfurth *et al.*, "A Linear radiofrequency ion trap for accumulation, bunching, and emittance improvement of radioactive ion beams," *Nucl. Instrum. Meth.*, vol. A469, pp. 254–275, 2001.

[220] R. Wolf, F. Wienholtz, D. Atanasov, D. Beck, K. Blaum, C. Borgmann, F. Herfurth, M. Kowalska, S. Kreim, Y. A. Litvinov, D. Lunney, V. Manea, D. Neidherr, M. Rosenbusch, L. Schweikhard, J. Stanja, and K. Zuber, "ISOLTRAP's multi-reflection time-of-flight mass separator/spectrometer," *International Journal of Mass Spectrometry*, vol. 349-350, pp. 123 – 133, 2013. 100 years of Mass Spectrometry.

[221] C. H. Tseng and G. Gabrielse, "Portable trap carries particles 5000 kilometers," *Hyperfine Interactions*, vol. 76, pp. 381–386, Dec 1993.

[222] J.-L. Grenard and R. Rinaldesi, "PUMA transport and handling," PUMA meeting Indico https://indico.cern.ch/event/834338, CERN, July 2019.

[223] A. Husson, "GBAR decelerator lockout procedure," Safety document GBAR-DECEL-LOCKOUT, CERN, August 2018.

[224] R. Froeschl and S. Lohmann, "Radiation fields due to anti-proton annihilation, prompt dose rates and induced activity in the AD experimental areas," Technical report CERN–RP–2013–084–REPORTS–TN, EDMS 223 1312195, CERN, 2013.

[225] S. Sels, P. Fischer, H. Heylen, V. Lagaki, S. Lechner, F. M. Maier, P. Plattner, M. Rosenbusch, F. Wienholtz, R. N. Wolf, W. Nörtershäuser, L. Schweikhard, and S. Malbrunot-Ettenauer, "First steps in the development of the multi ion reflection apparatus for collinear laser spectroscopy," *Nuclear Instruments and Methods in Physics Research Section B: Beam Interactions with Materials and Atoms*, 2019.

[226] F. M. Maier, P. Fischer, H. Heylen, V. Lagaki, S. Lechner, P. Plattner, S. Sels, F. Wienholtz, W. Nörtershäuser, L. Schweikhard, and S. Malbrunot-Ettenauer, "Simulations of a proof-of-principle experiment for collinear laser spectroscopy within a multi-reflection time-of-flight device," *Hyperfine Interactions*, vol. 240, p. 54, May 2019.

[227] I. Podadera, T. Fritioff, A. Jokinen, J. F. Kepinski, M. Lindroos, D. Lunney, and F. Wenander, "Preparation of cooled and bunched ion beams at ISOLDE-CERN," *The European Physical Journal A - Hadrons and Nuclei*, vol. 25, pp. 743–744, Sep 2005.

[228] M. J. G. Borge and B. Jonson, "ISOLDE past, present and future," *Journal of Physics G: Nuclear and Particle Physics*, vol. 44, no. 4, p. 044011, 2017.

[229] M. J. G. Borge and K. Blaum, "Focus on exotic beams at ISOLDE: A laboratory portrait," *Journal of Physics G: Nuclear and Particle Physics*, vol. 45, p. 010301, 11 2017.

[230] F. Wenander, J. Lettry, and M. Lindroos, "Transverse emittance investigation of the ISOLDE target-ion sources," *Nuclear Instruments and Methods*

in Physics Research Section B: Beam Interactions with Materials and Atoms, vol. 204, pp. 261 – 266, 2003. 14th International Conference on Electromagnetic Isotope Separators and Techniques Related to their Applications.

[231] E. Kugler, "The ISOLDE facility," *Hyperfine Interactions*, vol. 129, pp. 23–42, Dec 2000.

[232] Manuela Turrion and Urszula Herman-Izycka. `http://isoyields-classic.web.cern.ch/helium_isotopes_orig.html`.

[233] R. Catherall, W. Andreazza, M. Breitenfeldt, A. Dorsival, G. J. Focker, T. P. Gharsa, G. T. J, J.-L. Grenard, F. Locci, P. Martins, S. Marzari, J. Schipper, A. Shornikov, and T. Stora, "The ISOLDE facility," *Journal of Physics G: Nuclear and Particle Physics*, vol. 44, p. 094002, aug 2017.

[234] ISOLDE collaboration, "HIE-ISOLDE: the technical options," report CERN-2006-013, CERN, November 2006.

[235] A. Herlert, "The ISOLDE facility," *Nuclear Physics News*, vol. 20, no. 4, pp. 5–12, 2010.

[236] E. Mané, J. Billowes, K. Blaum, P. Campbell, B. Cheal, P. Delahaye, K. T. Flanagan, D. H. Forest, H. Franberg, C. Geppert, T. Giles, A. Jokinen, M. Kowalska, R. Neugart, G. Neyens, W. Nörtershäuser, I. Podadera, G. Tungate, P. Vingerhoets, and D. T. Yordanov, "An ion cooler-buncher for high-sensitivity collinear laser spectroscopy at ISOLDE," *The European Physical Journal A*, vol. 42, pp. 503–507, Dec 2009.

[237] R. N. Wolf, G. Marx, M. Rosenbusch, and L. Schweikhard, "Static-mirror ion capture and time focusing for electrostatic ion-beam traps and multi-reflection time-of-flight mass analyzers by use of an in-trap potential lift," *International Journal of Mass Spectrometry*, vol. 313, pp. 8 – 14, 2012.

[238] S. Knauer, P. Fischer, G. Marx, B. Schabinger, L. Schweikhard, and R. Wolf, "Multi-reflection time-of-flight mass spectrometry with combined in-trap lift capture and mirror-switch ejection," *International Journal of Mass Spectrometry*, vol. 423, pp. 46 – 53, 2017.

[239] MIRACLS collaboration, "Benchmarking of a multi ion reflection apparatus for collinear laser spectroscopy of radionuclides," *Letter of Intent to the ISOLDE and Neutron Time-of-Flight Committee*, 2017.

[240] GKS-Perfekt / DIGI.sys GmbH, "type ROBOT 10," tech. rep., 2019.

[241] JUNG Hebe- und Transporttechnik GmbH, "JLA-e ," tech. rep., 2019.

[242] R. Kersevan, "the vacuum system of the extra-low energy antiproton decelerator elena at cern,"

[243] G. Moulard, B. Jenninger, and Y. Saito, "Industrial surfaces behaviour related to the adsorption and desorption of hydrogen at cryogenic temperature," *Vacuum*, vol. 60, no. 1, pp. 43 – 50, 2001. The Sixth European Vacuum Conference.

[244] M. Chanel, "LEIR: the low energy ion ring at CERN," *Nuclear Instruments and Methods in Physics Research Section A: Accelerators, Spectrometers, Detectors and Associated Equipment*, vol. 532, no. 1, pp. 137 – 143, 2004. International Workshop on Beam Cooling and Related Topics.